Three dimensional simulation of rubber profile extrusion on the basis of in-line rheometry.

Rippl, Andreas P

Civil and Computational Engineering Centre
University of Wales Swansea

Three Dimensional Simulation of Rubber Profile Extrusion on the Basis of In-Line Rheometry

Andreas P. Rippl
Dipl.-Ing. (FH)

Thesis Submitted to the University of Wales in Candidature
for the Degree of Doctor of Philosophy

August 2004

DECLARATION

This work has not previously been accepted in substance for any degree and is not being concurrently submitted in candidature for any degree.

Candidate: _____

Date: 30/11/2004

STATEMENT 1

This dissertation is being submitted in partial fulfilment of the requirements for the degree of Doctor of Philosophy in the School of Engineering.

Candidate: _____

Date: 30/11/2004

STATEMENT 2

This dissertation is the result of my own independent work/investigation, except where otherwise stated. Other sources are acknowledged by footnotes giving explicit references. A bibliography is appended.

Candidate: _____

Date: 30/11/2004

STATEMENT 3

I hereby give consent for my dissertation, if accepted, to be available for photocopying and for inter-library loan, and for the title and summary to be made available to outside organisations.

Candidate: _____

Date: 30/11/2004

Summary

The work presented in this thesis is concerned with the accurate determination of material parameters and their use in three dimensional numerical simulation of the flow of rubber compounds through complex profile dies. In a first step, results from a study, based on classical rheometry conducted at the University of Wales Aberystwyth, are reviewed together with literature data. In conclusion of a comprehensive literature review, it is found that the existing literature on rubber compound material behaviour does not account for the separation of the different phenomena, i.e. in the most common case, wall slip effects are not separated from the shear behaviour and extensional viscosity is often neglected.

The design of a novel in-line rheometer is presented, as classical laboratory rheometry is not considered adequate for taking into account the deformation history of the material as it proceeds through the extruder located upstream of the profile die. Extensive results gathered with this rheometer are used in an inverse material parameter determination scheme to obtain the parameters for the shear thinning, wall slip and extensional behaviour of the material. Subsequently, the new material parameters are used in the numerical study of a generic profile die especially designed for this purpose in order to display the various flow problems occurring in the real extrusion process.

The design and instrumentation of trials on a profile production line at the industrial collaborators site (Cooper Standard Products Ltd., Maesteg) for the aforementioned generic profile die are described.

Experimental results for the flow distribution between the various limbs of the profile are compared with simulations. It is concluded, that the inclusion of extensional viscosity effects in the simulation is required, as a preliminary to the use of simulations in a computational optimisation scheme for profile dies.

Acknowledgements

First, I would like to express my sincere gratitude to my supervisors, *Dr. John F.T. Pittman* and *Dr. Johann Sienz*, who made this cooperation possible and whose support and guidance, through uncounted discussions, were crucial to the completion of this work.

During the years that lead to the accomplishment of this work, I met a number of people here in The School of Engineering at the University of Wales Swansea, many of whom became close friends. These people have also contributed to this work through discussions concerning many topics in relationship to this study. While far too numerous to name, I'd like to mention *Wulf Dettmer, Holger Ettinger, José Fonseca, Scott Langley, Chenfeng Li, Antonio Orlando, Andreij Polynkin, Miguel Rodriguez, Paul Saunders* and *Sava Slijepčević.*

This work would not have been possible without the financial support from the *Engineering and Physical Sciences Research Council*, EPSRC, under the project 'Computer Aided Optimisation of Extrusion Die Design' (EPSRC GR/M 95820).

Finally, and most importantly, I would like to express my sincere gratitude to my *parents* and my *brother* for being who they are and to *Nadège* for her endless patience.

to Nadège, and her profound

understanding of life

Contents

List of Figures

List of Tables

NOMENCLATURE

$dp, \Delta p$	Pressure drop in the capillary
ΔT	Temperature difference
δ	Phase angle
δ_{ij}	Kronecker delta
$\dot{\gamma}$	Shear strain rate
$\dot{\gamma}_a$	Apparent shear strain rate
$\dot{\gamma}_w$	Wall shear strain rate
$\dot{\omega}_{ij}$	Rate of vorticity
$\dot{\varepsilon}_{ij}$	Rate of strain
$\dot{V}$	Flow rate
ϵ_{ijk}	Alternating tensor
η	Dynamic viscosity
η'	Real part of the complex viscosity
η''	Imaginary part of the complex viscosity
η^*	Complex viscosity
η_0	Zero shear viscosity
η_c	Combined shear and extensional viscosity
η_e	Elongational viscosity
η_s	Shear viscosity
γ_0	Amplitude of the complex strain
κ_0'	Modified wall slip bulk material parameter
κ_0	Wall slip bulk material parameter
λ	Second coefficient of viscosity
μ	Newtonian viscosity
μ_0	Power law bulk material parameter (fluid consistency)
μ_e	Extension bulk material parameter
μ_y	Bulk material parameter (Bingham plastic and Herschel-Bulkeley model)
Ω	Computational domain
ω	Angular frequency
ω_{ij}	Vorticity
$\overline{x}$	Mean value
∂_0	Partial derivative with respect to time $\left(\frac{\partial}{\partial t}\right)$
ρ	Density
σ_{ij}	Stress tensor
τ'	Real part of the complex stress
τ''	Imaginary part of the complex stress

τ_0'	Bulk material parameter (extended wall slip law)
τ^*	Complex stress
τ_0	Amplitude of the complex stress
τ_w	Wall shear stress
τ_y	Yield stress
τ_{crit}	Critical wall shear stress
τ_{ij}	Viscous (deviatoric) stress tensor
τ_{ij}	Viscous stress tensor
τ_{rz}	Shear stress
ε_{ij}	Strain
A_{exit}	Exit area of the profile die
A_{ij}	Finite element stiffness matrix
b	Power law temperature coefficient
c	Wall slip law temperature coefficient
c_p	Specific heat capacity
C_{ijlm}	Coefficient tensor
CV	Coefficient of variation
D	Capillary die diameter
d	Extension law temperature coefficient
E	Youngs modulus
f_i	Body forces
f_j	Force vector
f_{obj}	Objective function value
G'	Storage modulus (real part of the complex shear modulus)
G''	Loss modulus (imaginary part of the complex shear modulus)
G^*	Complex shear modulus
I_ε	First Invariant of the strain rate tensor
II_ε	Second Invariant of the strain rate tensor
III_ε	Third Invariant of the strain rate tensor
L	Capillary die length
L^1	Norm of the residual
m	Wall slip index
n	Power law index
n_{el}	Number of elements
p	Extension law index
p	Thermodynamic pressure
P_{cap}	Capillary pressure drop
P_{ent}	Entry pressure drop
P_{exit}	Exit pressure drop
R	Capillary die radius
r, θ, χ	Spherical coordinates
R_a	Average roughness
Re	Reynolds number
Re_n	Non-Newtonian Reynolds number
s	Standard deviation

S_Ω	Surface area of the computational domain
T	Temperature
t_i	Surface forces
t_r	Residence time
T_{ref}	Reference temperature
Tr	Trouton ratio
v_n	Normal velocity at the wall
v_s	Slip velocity
v_t	Tangential velocity at the wall
v_x, v_y	Velocities normal to flow direction
v_z	Velocity in flow direction
V_Ω	Volume of the computational domain
v_{in}	Inlet velocity
v_i	Velocity vector
W	Weighting of the combined shear and extensional viscosity
EPDM	Ethylene Propylene Diene Monomer
pphr	Parts per hundred of rubber
PTT	Passenger Tire Tread
SBR	Styrene Butadiene Rubber

Chapter 1

Introduction

1.1 Background

Over the last 20 years, the numerical simulation of engineering problems has seen a transition from its beginnings in an academic environment to widespread application in many fields of industry. Today, a large number of problems is solved adequately through the use of numerical methods, either in areas where an analytic solution is not obtainable, or where such a solution is not efficient due to the complexity of the problem at hand. Once a numerical solution is determined, various procedures are available for finding an improved design, the most prominent being automated optimisation schemes. The combination of numerical simulation and automated optimisation allow for a fully integrated design process, completely carried out in a virtual domain.

At the time of writing, numerical methods are spreading towards more complex problems, due to advances in the theoretical field, but also especially due to rapidly increasing computational power. It is obvious, that areas with a high potential in cost-saving have priority in the application of numerical simulation.

One such area is found in the production of endless rubber profiles, where the traditional design process for a new profile die is a tedious and lengthy procedure. Starting from an initial guess, the die, produced by wire erosion, is trialled on the production line and then manually adapted for an improved flow rate balance at the die exit. This iterative cycle is terminated once a satisfactory configuration is found. As each trial incurs a down-time of the production line in addition to the manufacturing cost for the improved die, this design process is very cost intensive. In contrast, an implementation in a numerical simulation is faster and

complements the intuition of the die designer.

When considering the simulation of a rubber compound, special attention has to be given to the polymeric nature of the material, which differs to a large degree from commonly known Newtonian fluids with a constant viscosity. This behaviour is further complicated due to a high degree of filler content (mainly carbon black), present to modify the physical properties of the compound and for cost saving reasons. Significant differences in behaviour are observed when comparing an unfilled EPDM and a fully formulated compound.

1.2 Scope of the Work

With regard to the aforementioned requirements, several main aspects can be identified as crucial for the basis of an accurate simulation of the material flow in a complex profile die.

- An adequate material model has to be identified, which is able to accurately represent the material flow through the die, yet is acceptable in terms of computational cost. The latter requirement is imposed by the complexity of the computational domain.
- Once a material model is determined, accurate parameters have to be obtained. As the flow behaviour is highly dependent on the material composition and on the upstream deformation history, the use of an in-line capillary rheometer is recommended.
- A trial scheme, including different dies and extrusion conditions, will have to be devised in order to obtain raw flow parameters (Pressure drop ΔP, flow rate $\dot{V}$ and temperature T).
- This basic data can subsequently be used in an inverse material parameter optimisation. An analytic solution including all the relevant phenomena will have to be derived, which can be used in an iterative scheme to minimise the error of an objective function. One such function could be based on the difference between the experimental flow rate on one hand and the analytical solution of the flow rate under use of the corresponding experimental pressure and one specific set of material parameters on the other.
- The results of this study will then have to be critically compared with the current state of rubber rheology as found in the literature; consistencies and differences will have to be analysed carefully.

- The optimal set of parameters will be used in a number of simulations, with a generic die exhibiting all the typical features of a complex rubber profile die, under varying extrusion conditions.
- A comparison with actual extrusion samples will be made possible by comparison of the simulation results with trials conducted on the same geometry.

With the verification of the simulation results, a solid basis for the automatic optimisation of the die geometry will have been established.

1.3 Layout of the Thesis

It is the aim of this work to provide a solid foundation for the automated optimisation of rubber profile dies. In order to clarify the procedure followed here, it proves useful to present the material covered by the various chapters present in this work.

Introduction

A general introduction is given, illustrating the need for an automated profile die design cycle and especially an accurate material description at its basis.

Problem Definition

The subject of rubber profile extrusion is covered in more detail. The requirements of rubber sealing profiles are presented, together with the rubber composition. Furthermore, the extrusion process is described, split into its main components, extruder, die area and curing line.

The current die development process is shown and an improved design cycle is presented, based on an automated optimisation scheme.

Fluid Mechanics

The classic conservation equations are derived together with a set of constitutive equations. These two are combined to form a set of equations of change as employed in the current work.

Rheology

The difference between viscous and visco-elastic flow is defined and the need for a viscous description of the present problem is pointed out. Various non-Newtonian material laws are introduced and a separation of shear and extensional effects is presented. The different rheometrical instruments are introduced with regard to their use in rubber processing. Finally, the concept of wall slip and its analytical determination and description are given.

Parameter Determination

Starting with rheological experiments carried out at the University of Wales Aberystwyth, classical oscillatory and capillary methods are used for the material categorisation. Based on these results, the need for in-line data is confirmed and an in-line rheometer for use in the actual extrusion line is designed. Extensive experiments are carried out with this rheometer.

Two generic dies exhibiting typical extrusion problems are manufactured, one with an unoptimised shape, the other with manual improvements for better balancing of the material flow. Further trials are used for the collection of data on these profile dies.

Various optimisation techniques are applied to the rheometrical data in order to extract a valid set of material parameters for shear viscosity, extensional viscosity and wall slip, each of them including temperature dependence. As a result, the inverse parameter determination yields a set of parameters.

These parameters are compared critically with literature values, a review which reaches the conclusion that special care has to be taken in separating the various flow phenomena.

Simulation

The pre-processing of the numerical model is described together with an overview of the simulation code and of the physical problem. Various verifications, including a mesh size study are presented for the validation of the model. A simplified material model is used to display the transition from wall stick to wall slip in the profile die.

Both the unoptimised and the manually optimised generic die are used in simula-

tions at different processing conditions. The results of these simulations are used in a comparison between experiment and simulation.

Conclusion

Main achievements are summarised and conclusions are drawn before future work is pointed out.

Chapter 2

Problem Definition

2.1 Product Description

2.1.1 The Profile

Rubber profiles are found in a wide variety of applications. Their primary purpose is the sealing of contact surfaces and edges as a protection against adverse conditions such as water and wind. Additionally, rubber profiles have a function in covering sharp edges of sheet metals, providing improved user safety and as ornamental details.

One of the major application fields of rubber profiles is found in the automotive industry, where rubber seals are extensively used in all situations where moving elements need to be sealed against a contact surface. The same is true in house-building, where all doors and windows are sealed against draught by rubber profiles.

Modern product requirements result in the complex shape of today's rubber profiles as seen in Figure 2.1. In 2.1 a), a simple profile of uniform properties is shown, contrasted by Figure 2.1 b), which has a support for transport on the conveyor belt to curing attached in the lower part. This support is torn off afterwards. Figures 2.1 c) and d) show examples of profiles with metal inserts and different types of sealing lips. As a result of the product specification, different physical properties are needed in different parts of the profile. In areas where sealing qualities are desired, namely the contacts between two parts that are sealed against each other, high elasticity is needed, whereas the fixation of seals on the base material calls for strong and rigid attachment. Two main options are available for

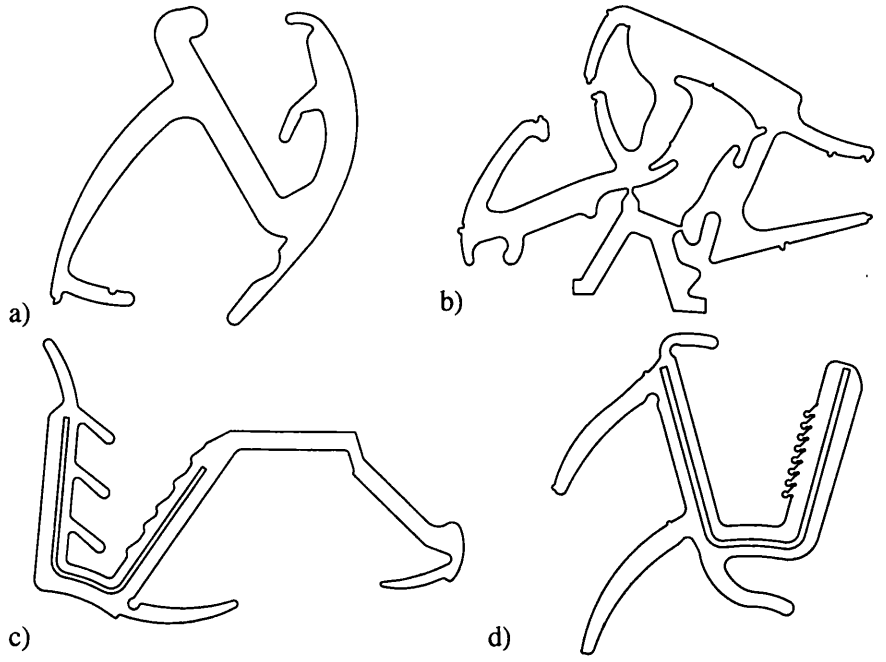

Figure 2.1: Typical profiles in automotive industry.

realising a variation of the physical properties: metal inserts and multiple rubber compounds. The former are an excellent method for clamping seals on to the base material as the plastic deformation of the insert ensures a safe attachment of the seal. Multiple rubber compounds are typically brought together by different extruders, each conveying one compound. These are brought together and allowed to weld together in the so called cross-head, a section of the flow-path specifically designed for this purpose (see Section 2.2.1).

The variety of rubber compounds ranges from rubbers of different hardness to sophisticated foamed rubbers, which form a sponge-like structure when cured. In an attempt at cost reduction and recycling, cheaper grades of rubber are sometimes used for non-visible sections of a profile. To increase the optical appeal of visible surfaces, often a textured pattern is imprinted by a roller just after the profile leaves the die.

Additional enhancements include glued-on felt linings to prevent adherence to surfaces, as seen in car window seals. In the same way, self-adhering layers can be added.

2.1.2 Rubber Composition

In order to understand the flow behaviour of rubber, it is necessary to investigate the composition of a typical rubber compound. In its pure state, EPDM (Ethylene Propylene Diene Monomer) does not display satisfactory properties for use in practical applications, as its yield strength is not adequate. Therefore, a wide range of additional materials is mixed into a compound; for a typical example see Figure 2.2. Nowadays, the main ingredient of an EPDM compound is not

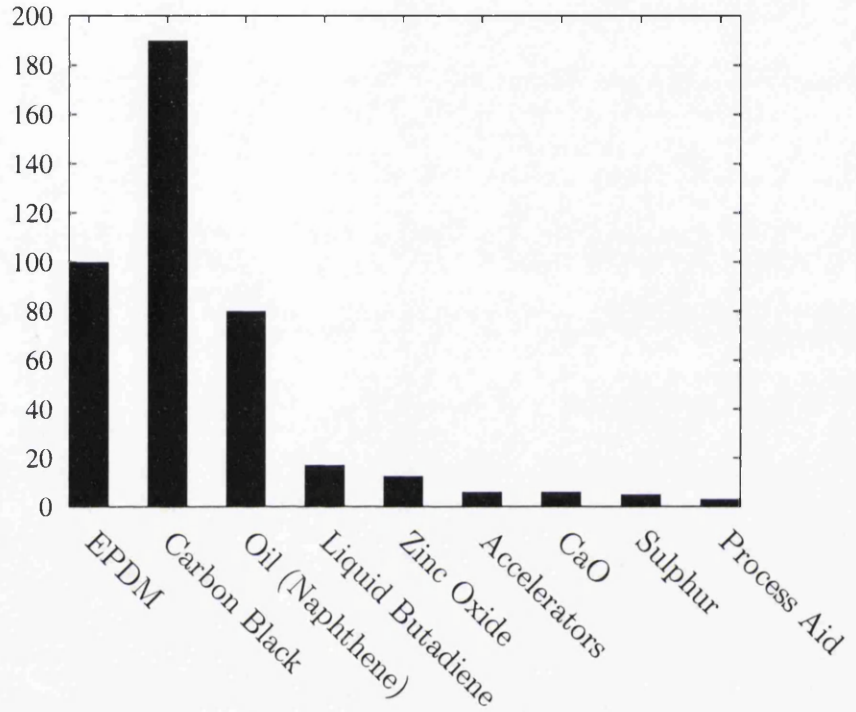

Figure 2.2: Contents of a typical rubber compound in parts per hundred rubber - E8246.

rubber, but carbon black, which, together with all other added materials, leads to an EPDM percentage of only around 25%. Made by burning oil or natural gas, carbon black greatly increases the tensile strength of the final product when added to rubber. The original channel process of carbon black production was made obsolete by the oil furnace process as it is much cheaper, at the cost of increased particle size. Over the years, the percentage of carbon black filler which is added to compounds has steadily increased as a result of design requirements and economic considerations. In the beginning, commercial rubber compounds incorporated a carbon black ratio of 30 pphr (parts per hundred rubber, by weight), contrasted by modern ratios of up to 200 pphr. The main difference in the quality of carbon blacks consists in the particle size as shown in Table 2.1.

Another major component of any industrial rubber compound is mineral oil,

Designation	Nitrogen adsorption surface area $[m^3/g]$	Ultimate particle diameter $[10^{-10}m]$	Old designation
N110	143	200-250	SAF
N220	119	240-330	ISAF
N234	126		
N326	84		
N330	83	280-360	HAF
N339	96		
N375	100		
N550	42	390-550	FEF
N660	35		

Table 2.1: Properties of different grades of carbon black [8].

which serves several purposes. Its main effect is to regulate the hardness of the vulcanised product as well as to aid in the dispersion of carbon black. As a processing aid it improves the material flow through the extrusion line. Another positive side effect is a cost reduction for base materials if oil is added to the compound. This technique for lowering costs is known as oil extension.

The main component responsible for the vulcanisation is sulphur. The theory of rubber curing is explained in detail in Section 2.2.2. Used on its own, vulcanisation times for sulphur based curing are very long. Historically, this circumstance soon lead to an increased activity in the development of accelerators. Certain chemicals were found to increase the rate of rubber vulcanisation when used in conjunction with sulphur. Modern accelerators are highly optimised mixtures adapted to a specific product. In conjunction with accelerators, activators have to be mentioned as they improve the performance of accelerators. The most common activator is zinc-oxide.

There are several other components such as desiccant, but the focus in this work is laid on the ones mentioned above as they define the flow behaviour of the final product. In comparison with other sources [2, 8], the compounds used in the present work contain high levels for both carbon black and mineral oil. These numbers back the trend towards higher levels of additives as rubber mixing technology improves.

2.2 Process Description

The extrusion of rubber is only one step in the complete process of rubber profile manufacturing. After the profile leaves the die cavity, the profile is lead towards the conveyor belt in a free surface flow where it is hauled-off to curing.

Curing may be realised in several ways, with the most common being simple heating in an oven. The curing of other rubber compounds is activated by microwaves. In this way, different curing times for different areas of a profile can be achieved.

2.2.1 Extrusion

The fabrication of rubber seals by extrusion is a continuous process, where a rubber compound is forced through a die in order to obtain a specific profile shape. The pressure required to ensure a satisfactory rubber flow rate is provided either by a screw or by a ram piston. As a continuous process cannot be maintained by a ram type extruder and the majority of large scale applications use screw type extrusion, the focus of this work will be laid on this type of process. In Figure 2.3, a typical setup of two extruders is shown with the extruders oriented sideways, the cross-head in the centre and the material being extruded towards the front.

Figure 2.3: Extrusion line (Cooper Standard Products Ltd.).

The typical schematic layout of a modern extrusion line incorporating different compounds as well as a metal insert is detailed in Figure 2.4. Up to four extruders are feeding a so-called 'cross-head' which unites and bonds together the rubber streams into one well balanced flow. For this purpose, it is necessary to use an optimised cross-head. From the back, an optional metal insert may be fed to reinforce the profile as described in Section 2.1.1. After exiting the confined extrusion block through the die exit, the profile is hauled off on conveyor belts towards curing with a haul off speed equal to the extrusion velocity.

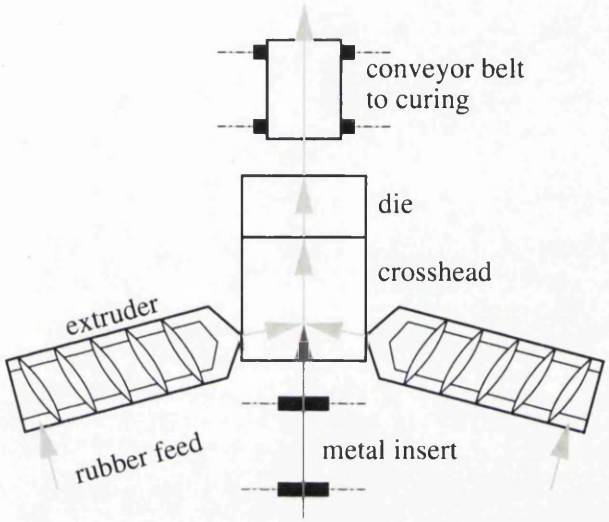

Figure 2.4: Extrusion layout.

Process control is provided through sensors for different process variables indicating the current level of the value inside the process window. In older equipment, adjustments are made manually whereas modern machinery includes automatic control mechanisms. In a well-designed extrusion line, there should be thermocouples and pressure transducers in all the crucial parts of the extruder and die section. These will give an immediate image of the current status of the extrusion line. An introduction on sensors typically found in an extrusion environment is given in Section 5.2.3. An indirect, but nonetheless very important indicator for the performance of the extruder are its electrical readings. A direct dependence between the heat generation inside the extruder and the power consumption is established, as most of the electrical energy is converted into heat by friction. Concerning the extrusion speed, adjustments are made by regulation of the rotational speed of the screw. This speed is coordinated with the speed of the conveyor belt after extrusion, to eliminate differences. In special cases it might be desirable to set a slightly higher speed for the conveyor belt to reduce die swell effects and prevent any jams of the process line from the die onwards.

Screw Design

In order to understand the mastication process, it is necessary to have a closer look at the design of extrusion screws, examples of which are shown in Figure 2.5. The constant root diameter is a typical feature of rubber extrusion screws (Figures 2.5 a) and c)), contrary to screws used in the extrusion of other materials, where varying root diameters along the screw length as shown in Figure 2.5 b), are commonly found. Nowadays, the lead length, that is the distance between two adjacent flights of the screw, is variable, with more narrow flights at the extruder exit where the material is undergoing additional compression, leading to better mastication and lower air content in the final extrudate (see Figure 2.5 c)).

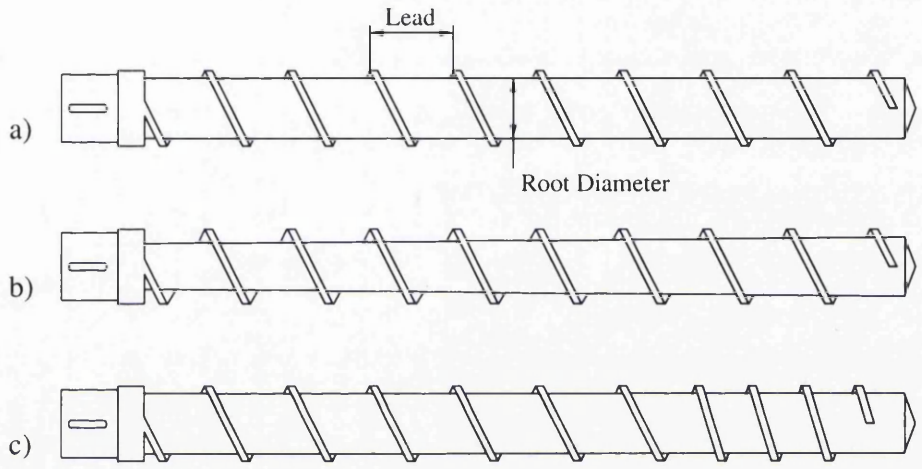

Figure 2.5: Typical extrusion screws.

Various other techniques are known to improve the plastification process, such as metering sections at the end of the varying root diameter screw, in order to reach a stabilised flow at the extruder exit. In other cases, sections cleared of screw flights are used to disturb a laminar flow for the sake of better mixing. Many companies have filed patents addressing problems in the extrusion of rubber.

The manufacturing of extrusion screws is a complicated process, as the final product is subject to high load. Inspection intervals of more than one year are not uncommon, with typical uptimes of around 24 hours between changes of rubber compound. The flight land, the contact zone between extruder screw and barrel, is an area of special interest for several reasons. The gap in this area is subject to rigid tolerances of significantly less than $1/10\,mm$, as bad fits will incur a backward oriented material flow, resulting in long residence times with all negative consequences. To ensure proper function, these faces are consequently heat treated to create a hard contact surface.

Functionality

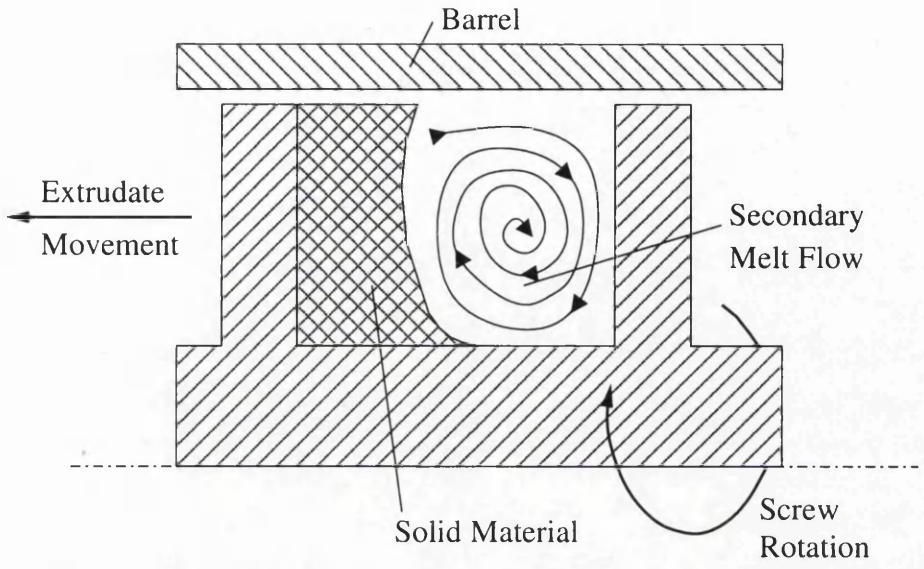

Figure 2.6: The liquefaction process [1].

An extrusion screw has to fulfil several roles correctly as it is a basic requirement for a product without defects [1].

- The rubber is fed to the extruder in long bands of raw, uncured compound, which is the preferred method, unlike many other industries where pelletised material is used as a basis.
- Once inside the extruder, the material is first chopped into increasingly small pieces and subsequently masticated to form a homogeneous flow of rubber.
- During the transport of material towards the exit, a huge amount of heat is generated due to friction. According to Muccio [1], 85% to 90% of the energy needed for the process are created by friction. This heat leads to increased levels of liquefaction as the material is advancing (Figure 2.6).
- By applying the techniques shown in Figures 2.5 b) and c), further compression and devolisation of the extrudate is achieved. It is important to allow for proper mixing of the molten material in the final stage of the extruder, to avoid the formation of inhomogeneities in the final product.

2.2.2 Curing

Rubber in its natural state is a soft substance with highly plastic properties. Only by subjecting it to the process of curing can a tough, elastic state be reached. The contents of the rubber used in this work are listed in Figure 2.2. Though only listed at five parts per 100 parts EPDM, sulphur is an important component of the rubber compound, as it triggers the vulcanisation: cross-links are established between polymer chains. The details of the vulcanisation of rubber are a highly complex mechanism which has only been unravelled in recent years.

Figure 2.7 shows the possibilities of cross-linking between chains of rubber. The only way of improving the elastic properties of a compound is shown in Figure 2.7 a): the connection exists between two distinct chains of rubber. A variety of sulphides, ranging from mono- and di- to polysulphides is able to build this connection. Figure 2.7 b) shows a dead end where no connection is achieved at all and Figures 2.7 c) and d) show cyclic connections for mono- and disulphides respectively.

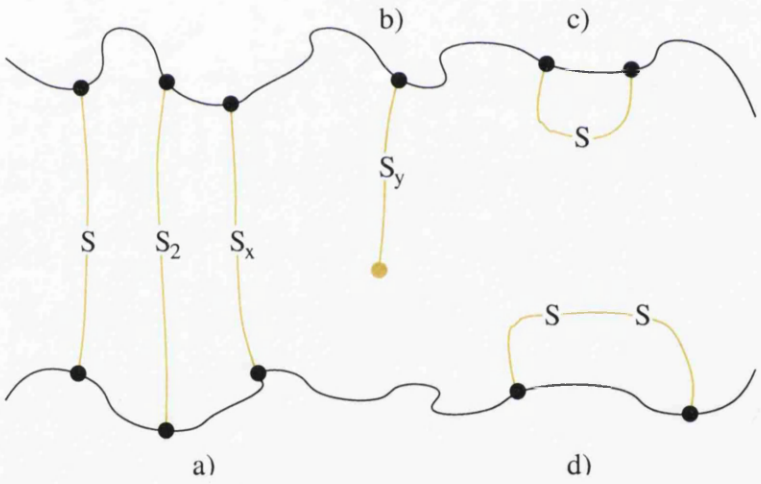

Figure 2.7: Chemical structure of sulphur cross-links [2].

The vulcanisation starts off with a reaction between the sulphur and the accelerator to form a zinc-perthio salt which reacts with the rubber hydrocarbon RH in the following way:

$$XS_xZnS_xX + RH \rightarrow XS_xR + ZnS + HS_{x-1}X$$

where X stands for a component resulting from the accelerator. The sulphur content will decrease, but the resulting component itself may be active again,

reducing the level of sulphidity steadily. In another step, the XS_xR group reacts with a second rubber hydrocarbon chain to form a constant cross-link:

$$XS_xR + RH \rightarrow RS_{x-1}R + XSH$$

Further application of heat results in a decrease of polysulphidity leading to a more stable connection. At the same time, excessive temperatures or curing times can lead to compound decomposition, resulting in optimum curing times and temperatures for a specific compound.

2.2.3 Process Parameters

In the present extrusion, there is a number of parameters which are used to control the process. In order to create a reasonable simulation, these have to be identified and a process-window for defining a range of typical values for each parameter has to be specified. The parameters found on a typical production line can be grouped in two main categories: extrusion and curing values. In this project, we are concerned only with the first group, as the curing has no direct effect on the form of the profile leaving the die. It is arguable that the curing has a profound influence on the final shape of the profile and should therefore be included in the simulation. However, as the chemical process of rubber curing requires a completely different set of governing equations compared to the physical phenomenon of fluid flow, it is excluded here.

The available sensors in the present extrusion are several thermocouples along the extruder wall in addition to a pressure transducer at the exit of the extruder, which together give an indication of processing conditions. The power input of the extruder as a means of estimating the work input into the rubber is dismissed here as too indirect for drawing any meaningful conclusions. The extruder screw speed on the other hand is a very useful value for indicating the extrusion speed as it is not otherwise determined. In addition to these values which are gathered at some distance from the die itself, a number of sensors for pressure and temperature will be introduced into the flow in a non-intrusive way, as shown in Chapter 5. These will provide the necessary data for the determination of material parameters as derived in Chapter 4.

A wealth of material is available on the processing of polymeric materials. Relevant references include, amongst others, White [8], Blow [2], Muccio [1], Tadmor [11] and Bernhardt [12].

2.3 State of the Art in Die Design

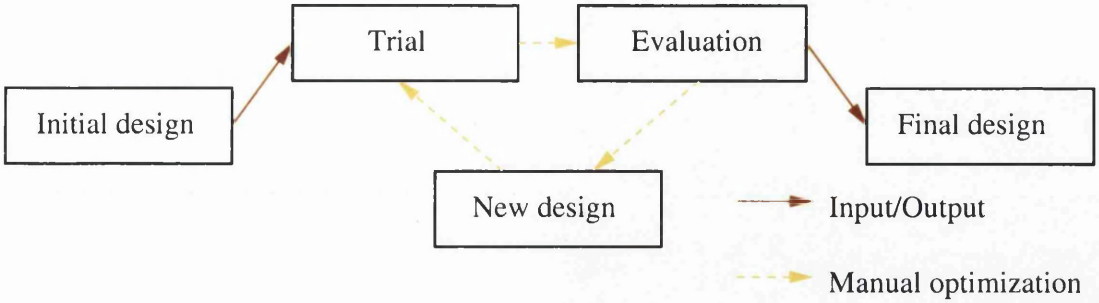

Figure 2.8: Manual optimisation of die design.

The current die design process involves an iterative cycle based on practical experience and intuition (see Figure 2.8). A team of senior designers starts with a best guess of the flow region shown in Figure 2.9 a) regarding a reasonable die geometry, where a profile as shown in Figure 2.1 is opened up in the upstream section according to Figure 2.9 b). The parallel section is never touched as it is needed for stabilising the flow before the die exit.

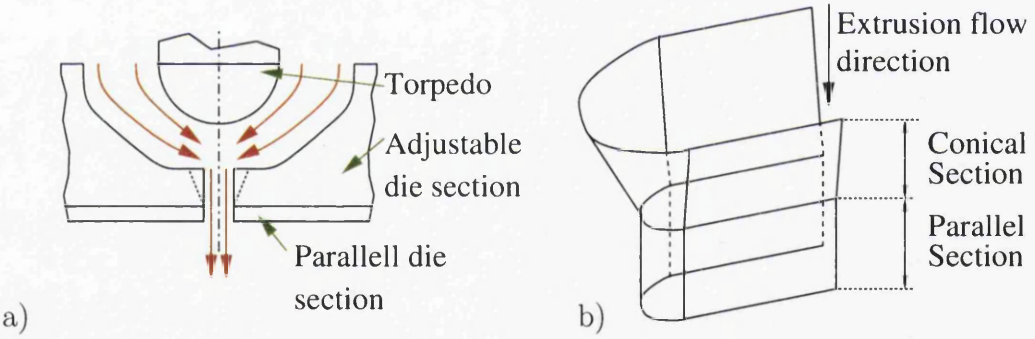

Figure 2.9: a) Flow regions of interest, b) parallel and conical section of the optimised die.

The die is actually manufactured and tested in a trial to determine its performance in terms of cross sectional area and extrusion velocity in different sections of the die. A first indication of the die performance is given by the straightness of the extrudate. The exact evaluation is usually performed by cutting slices out of the profile and comparing the outline manually to the profile specification. The conical die sections which need to be opened or closed are identified and integrated into a new version of the die. These iterations are repeated until a well-balanced die is found, which can be used for production purposes with an average number of iterations of five to six.

2.4 Proposition for an Optimised Design Cycle

There are several drawbacks in the conventional approach to die design. Time and cost are two main factors which spring to mind as areas of improvement. The manual iterative optimisation of the die is labour intensive and requires a significant number of resources as the die is manufactured by wire erosion. In addition, the downtime due to running trials is not negligible. A further disadvantage of the conventional method of die design is found in its reduced degree of repeatability. The final changes to a specific die design are often made manually, thus circumventing any procedures installed for the compliance with a transparent design process.

In the light of ever increasing computational power, a modern design cycle, where as many of the steps described in Section 2.3 as possible are replaced by virtual tasks in a computer, has to be the goal of an improvement in the design of profile dies. A scheme according to Figure 2.10 will enable the designer to significantly reduce the time to production. The bulk of the remaining manual work will be

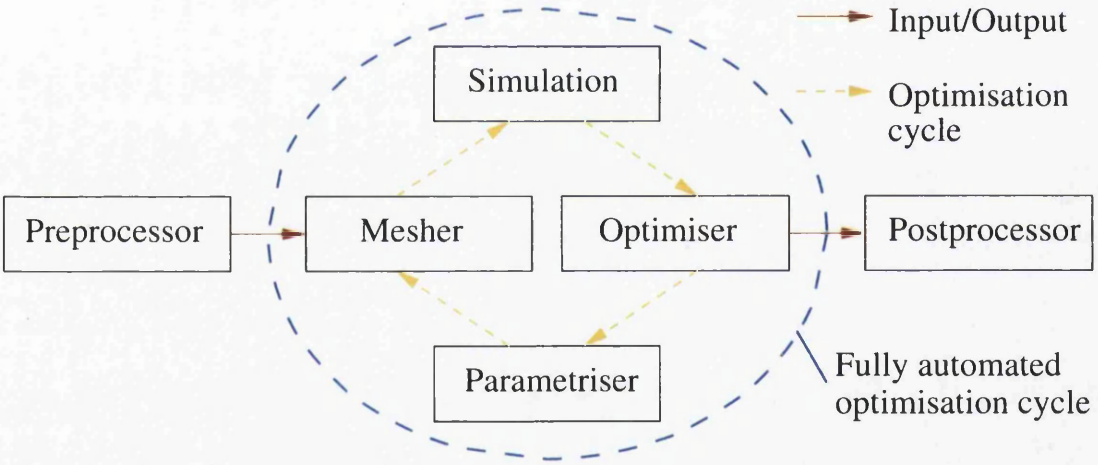

Figure 2.10: Proposed automated optimization cycle.

located at the start of the design process at the pre-processing level, where a CAD model of the die has to be prepared for the automated cycle by cleaning up (de-featuring) and parametrising it. After this step is completed, a fully autonomous optimization cycle will compute an optimum solution for the flow distribution over the exit cross sections, with alternative optimisation goals imaginable. This cycle, shown as the centrepiece of Figure 2.10, is launched by meshing the existent CAD file and the application of a set of boundary conditions suitable for use in the following simulation. The results, more specifically the average output flow rates in different sections of the die, are passed on to an optimisation module

which calculates an objective function value that is used to estimate the quality of the result. Once the relative deviation from the average flow rate in each partition is known, a parametriser can be invoked with the goal of computing a new set of values for the various design variables. These new design variables are incorporated into an updated CAD file and the cycle is closed by creating a new mesh.

After a threshold for the deviation from the average flow rate predetermined in the optimization module has been crossed, the loop is exited and the final version of the CAD model, as well as post-processing information for verification purposes, is written by the post-processing module. As a result, the human interaction in the design process will be limited to pre- and post-processing, thus eliminating the dependence on intuition on the developers side. Such knowledge will instead complement the automatic process which is able to generate high-performance solutions in new applications quickly and at greatly reduced cost.

A potential problem area which cannot be neglected is the incompleteness of realistic material behaviour models in the extruder and die. If the material model does not reflect the reality, a numerical optimisation will give a balanced solution which will not yield a viable die. For this reason, emphasis is laid on obtaining a realistic material flow model as introduced in Chapter 4. Also, at this point we have to mention a discrepancy between the manual and the numerical optimization which can not be easily avoided. In the manual optimization process, the design team uses its intuition gathered over many design cycles to predict the deformation of the extrudate due to die swell and curing effects. As these mechanisms are based on fundamentally different principles (elastic effects and chemical reactions respectively), we are not able to predict any implications due to these effects in our simulation code. It is however thought, that the die designer will be able to introduce the necessary adaptations into the numerically optimised die without major changes.

On the numerical side, it can already be estimated that the simulation of a complex real-world die will take considerable computational effort. As the optimisation will be constituted of a multitude of simulations, it is imperative to keep the number of simulations as small as possible by making use of an advanced parametrisation scheme (see e.g. [13]) and to restrict the number of design variables as far as possible.

Chapter 3

Fluid Mechanics

3.1 Conservation Equations

In the following, we will give a brief summary of the different conservation equations which govern the flow of any material under non-relativistic conditions. This material is covered in a wide range of books (see e.g. [14, 15, 16, 17, 18]), from which the present material is gathered. The conservation equations are applied to the mass, linear momenta, angular momenta and to the energy of a control volume. A further axiom is the entropy inequality or the second law of thermodynamics, which is of no immediate use in this place.

3.1.1 Mass

In an arbitrary volume of fluid, no creation or destruction of mass is effected, assuming that no chemical processes take place,

$$\frac{\mathrm{d}}{\mathrm{d}t}\int_{V(t)} \rho \mathrm{d}V = 0. \tag{3.1}$$

By transformation through Leibniz's and Gauss's theorem we get

$$\int_{V(t)} \left[\frac{\partial \rho}{\partial t} + \partial_i \left(\rho v_i\right)\right] \mathrm{d}V = 0. \tag{3.2}$$

As Equation (3.2) is independent of the chosen frame of reference, we can state that

$$\frac{\partial \rho}{\partial t} + \partial_i \left(\rho v_i\right) = 0, \tag{3.3}$$

which is the well known continuity equation. It can be further simplified for the case of constant density, for which the time derivative vanishes,

$$\frac{\partial v_j}{\partial x_j} = 0. \tag{3.4}$$

3.1.2 Linear Momenta

This axiom is derived from Newtons second law of motion, $F = m \cdot a$, applied to an arbitrary volume

$$\frac{\mathrm{d}}{\mathrm{d}t}\int_{V(t)} \rho v_i \mathrm{d}V = \int_{V(t)} \rho f_i \mathrm{d}V + \int_{S(t)} t_i \mathrm{d}S, \tag{3.5}$$

where the left hand side represents the linear momentum and the right hand side the body forces f_i and surface forces t_i.

By application of the theorems of Leibniz and Gauss, we can expand the left hand side

$$\frac{\mathrm{d}}{\mathrm{d}t}\int_{V(t)} \rho v_i \mathrm{d}V = \int_{V(t)} \frac{\partial}{\partial t}\left(\rho v_i\right) + \partial_j\left(\rho v_j v_i\right) \mathrm{d}V. \tag{3.6}$$

The surface traction vector t_i can be related to the stress tensor T_{ji} via the normal vector n_j by stating

$$t_i = n_j T_{ji}. \tag{3.7}$$

The surface integral in Equation (3.5) can be subjected to Gauss in the same way as seen before, effectively resulting in one integral over the volume

$$\int_{V(t)} \left(\partial_0\left(\rho v_i\right) + \partial_j\left(\rho v_j v_i\right) - \rho f_i - \partial_j T_{ji}\right) \mathrm{d}V = 0. \tag{3.8}$$

By making use of the possibility of arbitrary volumes, we can simplify Equation (3.8) to yield

$$\partial_0\left(\rho v_i\right) + \partial_j\left(\rho v_j v_i\right) - \rho f_i - \partial_j T_{ji} = 0. \tag{3.9}$$

In a final step, by using the definition of the viscous stress tensor τ_{ij}

$$T_{ij} = -p\delta_{ij} + \tau_{ij}, \tag{3.10}$$

we can write

$$\partial_0\left(\rho v_i\right) + \partial_j\left(\rho v_j v_i\right) - \rho f_i + \partial_i p - \partial_j \tau_{ji} = 0 \tag{3.11}$$

or

$$\partial_0\left(\rho v_i\right) + \partial_j\left(\rho v_j v_i\right) = \rho f_i - \partial_i p + \partial_j \tau_{ji}. \tag{3.12}$$

3.1.3 Angular Momenta

This axiom is useful in that it can supply the proof of the symmetry of the stress tensor, as will be shown in Section 3.2.1. We start with the vector of the angular momentum

$$L = r \times (mv)) = \rho \epsilon_{ijk} r_j v_k \mathrm{d}V \tag{3.13}$$

and the outer momenta of the body forces

$$M = r \times F, \tag{3.14}$$

which can be split into momenta due to body forces

$$M_b = r \times f \left(\rho \mathrm{d}V\right) = \rho \epsilon_{ijk} r_j f_k \mathrm{d}S \tag{3.15}$$

and momenta due to surface forces

$$M_s = r \times t \mathrm{d}S = \epsilon_{ijk} r_j n_p T_{pk} \mathrm{d}V. \tag{3.16}$$

The term resulting from angular momenta such as the Coriolis force is negligible under the studied conditions. Thus, we get the angular momenta axiom in its basic form

$$\frac{\mathrm{d}}{\mathrm{d}t} \int_{V(t)} \rho \epsilon_{ijk} r_j v_k \mathrm{d}V = \int_{V(t)} \rho \epsilon_{ijk} r_j f_k \mathrm{d}V + \int_{S(t)} \epsilon_{ijk} r_j n_p T_{pk} \mathrm{d}S. \tag{3.17}$$

By applying Leibniz's theorem to the left hand side, we get

$$\int_{V(t)} \frac{\partial}{\partial t} \left(\rho \epsilon_{ijk} r_j v_k\right) \mathrm{d}V + \int_{S(t)} \epsilon_{ijk} \rho r_j v_k n_p v_p \mathrm{d}S = \int_{V(t)} \rho \epsilon_{ijk} r_j f_k \mathrm{d}V + \int_{S(t)} \epsilon_{ijk} r_j n_p T_{pk} \mathrm{d}S \tag{3.18}$$

and by applying the theorem of Gauss

$$\int_{V(t)} \frac{\partial}{\partial t} \left(\rho \epsilon_{ijk} r_j v_k\right) \mathrm{d}V + \int_{V(t)} \epsilon_{ijk} \partial_p \left(\rho r_j v_k v_p\right) \mathrm{d}V = \int_{V(t)} \rho \epsilon_{ijk} r_j f_k \mathrm{d}V + \int_{V(t)} \epsilon_{ijk} \partial_p \left(r_j T_{pk}\right) \mathrm{d}V. \tag{3.19}$$

Again, use is made of the independence on the frame of reference to eliminate the integrals

$$\epsilon_{ijk} \left(\partial_0 \left(\rho r_j v_k\right) + \partial_p \left(\rho r_j v_p v_k\right) - \rho r_j f_k - \partial_p \left(r_j T_{pk}\right)\right) = 0. \tag{3.20}$$

3.1.4 Energy

The last of the relevant conservation equations is the energy equation derived from the first law of thermodynamics:

$$\frac{\mathrm{d}E}{\mathrm{d}t} = \frac{\mathrm{d}Q}{\mathrm{d}t} - \frac{\mathrm{d}W}{\mathrm{d}t} \tag{3.21}$$

where Q denotes the thermal energy and W the work. Considering the total energy of an arbitrary fluid particle we get

$$dE = \rho \left(e + \frac{1}{2} v_j v_j \right) \mathrm{d}V \tag{3.22}$$

with a contribution from the internal energy e and the kinetic energy. The work term is derived from the definition of work as

$$dW = d\mathbf{x}^{\mathbf{T}} \cdot \mathbf{F} \tag{3.23}$$

or the rate of work as

$$\frac{\mathrm{d}W}{\mathrm{d}t} = \mathbf{v}^{\mathbf{T}} \cdot \mathbf{F}. \tag{3.24}$$

By separating body and surface forces, we get

$$(\rho \mathrm{d}V)\,(f_i)\,v_i \tag{3.25}$$

for the body forces and

$$((n_j T_{ji})\,\mathrm{d}S)\,v_i \tag{3.26}$$

for the surface forces as the two contributions of the work term in Equation (3.21). The third term of Equation (3.21), the heat transfer term, is introduced by means of the heat flux vector q_i. For heat transfer from a body we have

$$dQ = n_i q_i \mathrm{d}S \tag{3.27}$$

and for heat transfer to a body we get

$$dQ \doteq -n_i q_i \mathrm{d}S. \tag{3.28}$$

Equations (3.22), (3.25), (3.26) and (3.28) can now be substituted into Equation (3.21) to yield

$$\frac{\mathrm{d}}{\mathrm{d}t}\int_{V(t)}\rho\left(e+\frac{1}{2}v_jv_j\right)\mathrm{d}V = -\int_{S(t)}n_iq_i\mathrm{d}S+\int_{S(t)}n_iT_{ij}v_j\mathrm{d}S+\int_{V(t)}\rho f_iv_i\mathrm{d}V. \tag{3.29}$$

By applying the theorems to convert surface integrals to volume integrals (see Section 3.1.2) and by assuming independence of the frame of reference we end up with

$$\partial_0\left(\rho\left(e+\frac{1}{2}v_jv_j\right)\right)+\partial_i\left(\rho v_i\left(e+\frac{1}{2}v_jv_j\right)\right) = -\partial_iq_i-\partial_i\left(pv_i\right)+\partial_i\left(\tau_{ij}v_j\right)+\rho v_if_i \tag{3.30}$$

which completes our set of conservation equations.

Equations (3.4), (3.12), (3.20) and (3.30) represent a complete set of equations that can be used to describe the behaviour of any material, solid or liquid, under the influence of outer forces and energy fluxes. As the number of unknowns in the above equations is higher than the number of equations, it is now necessary to introduce a set of constitutive equations which describe the behaviour of a specific material.

3.2 Constitutive Equations

3.2.1 Stresses and Strains

Definition of the Stress Tensor

In an arbitrary volume $\mathrm{d}V$, any stresses can be classified according to Figure 3.1. The stresses τ_{11}, τ_{22} and τ_{33} are the normal stresses acting perpendicular to a surface while all other stresses are shear components. These shear stresses are not independent of each other. This can be shown by applying Greens theorem to the angular momentum balance for any given domain V (see Equation (3.17)) under exclusion of temporal changes.

$$\int_V\epsilon_{ijk}r_jf_k\mathrm{d}V+\int_S\epsilon_{ijk}r_jn_p\tau_{pk}\mathrm{d}S=0 \tag{3.31}$$

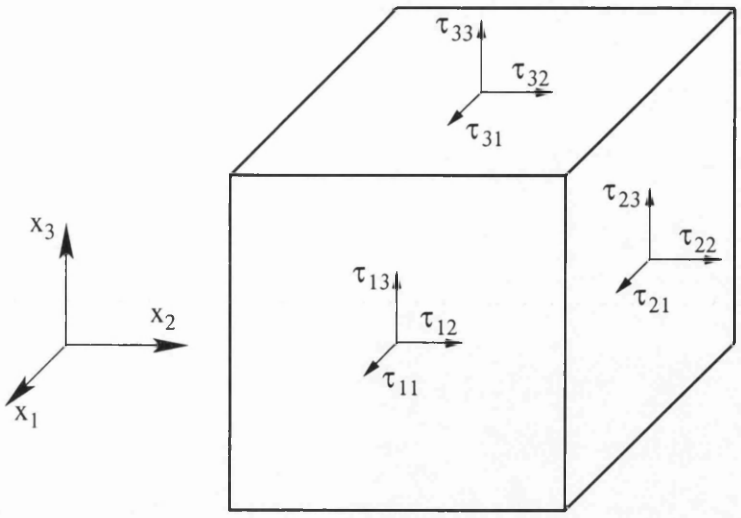

Figure 3.1: Components of the stress tensor.

becomes

$$\begin{aligned}\int_S r_j \tau_{kl} n_l \mathrm{d}S &= \int_V \left(r_j \tau_{kl}\right)_{,l} \mathrm{d}V \\ &= \int_V \left(\delta_{jl}\tau_{kl} + r_j \tau_{kl,l}\right) \mathrm{d}V \\ &= \int_V \left(\tau_{kj} + r_j \tau_{kl,l}\right) \mathrm{d}V.\end{aligned}$$

which is substituted into the original Equation (3.31) to form

$$\int_V \epsilon_{ijk} \left[r_j \left(f_k + \tau_{kl,l}\right) + \tau_{kj}\right] \mathrm{d}V = 0. \tag{3.32}$$

As the local equilibrium has to be respected, Equation (3.32) can be simplified to

$$\int_V \epsilon_{ijk} \tau_{kj} \mathrm{d}V = 0. \tag{3.33}$$

Because Equation (3.33) has to be correct for any domain, it follows that

$$\epsilon_{ijk} \tau_{kj} = 0 \tag{3.34}$$

which can be expanded to

$$\tau_{ij} = \tau_{ji}. \tag{3.35}$$

Thus, the number of independent stress components reduces from nine to six. Apart from the three normal stresses τ_{11}, τ_{22} and τ_{33}, the three shear stresses $\tau_{12} = \tau_{21}$, $\tau_{13} = \tau_{31}$ and $\tau_{23} = \tau_{32}$ have to be determined.

Relation between Stress and Strain

In any fluid, the inherent stress field is composed of two components: the surrounding thermodynamic pressure and a component due to any movement occurring in the fluid, the viscous stress tensor, also called deviatoric stress tensor.

$$\sigma_{ij} = -p\delta_{ij} + \tau_{ij} \tag{3.36}$$

For a fluid at rest, the deviatoric stress vanishes and the fluid is only under hydrostatic stress. Otherwise, additional stresses which depend on the velocity gradient in the fluid and on material properties arise. The common assumption for relating shear stresses to velocity gradients is formulated as

$$\tau_{ij} = C_{ijlm}\frac{\partial v_l}{\partial x_m}. \tag{3.37}$$

For Newtonian fluids such as air or water, the coefficient tensor C_{ijlm} is generally composed of up to 81 constants. However, for isotropic fluids which do not display different material properties according to orientation in space, the coefficients of Equation (3.37) reduce to two: η and λ.

$$\tau_{ij} = \eta\left(\frac{\partial v_i}{\partial x_j} + \frac{\partial v_j}{\partial x_i}\right) + \lambda\frac{\partial v_l}{\partial x_l}\delta_{ij} \tag{3.38}$$

By making use of the continuity Equation (3.4) for incompressible flow, Equation (3.38) can be reduced to

$$\tau_{ij} = \eta\left(\frac{\partial v_i}{\partial x_j} + \frac{\partial v_j}{\partial x_i}\right) \tag{3.39}$$

if the fluid density is constant. Therefore, the second viscosity coefficient does not need to be specified for incompressible fluids. The velocity gradient$^{\partial v_i}/_{\partial x_j}$ is derived from two separate contributions

$$\frac{\partial v_i}{\partial x_j} = \frac{1}{2}\left(\frac{\partial v_i}{\partial x_j} + \frac{\partial v_j}{\partial x_i}\right) + \frac{1}{2}\left(\frac{\partial v_i}{\partial x_j} - \frac{\partial v_j}{x_i}\right) \tag{3.40}$$

with

$$\dot{\varepsilon}_{ij} = \frac{1}{2}\left(\frac{\partial v_i}{\partial x_j} + \frac{\partial v_j}{\partial x_i}\right) \tag{3.41}$$

being the rate of strain tensor and

$$\dot{\omega}_{ij} = \frac{1}{2}\left(\frac{\partial v_i}{\partial x_j} - \frac{\partial v_j}{x_i}\right) \tag{3.42}$$

being the vorticity tensor. It is worth noting that the Equations (3.38) and (3.39) do not depend on the vorticity which is responsible for any rigid body rotation, as no additional stresses will occur in the case of rotation. In Figure 3.2, the difference between irrotational and rotational flow is shown as the path of a finite fluid volume is tracked along a streamline ψ.

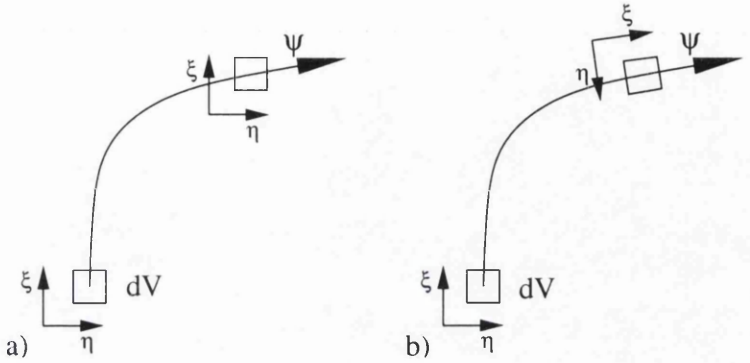

Figure 3.2: a) Irrotational and b) rotational flow.

3.3 Equations of Change

With the definition of the constitutive equations, we have a means at hand to remove the unknowns from the continuity equations. By substituting the definition of the stress tensor, Equation (3.39), into the conservation equations found in Section 3.1, we get a system of equations which can be used to solve an arbitrary fluid mechanics problem either analytically, or in the case of great complexity, numerically. Thus, we can express the general equations of change:

Mass Conservation

$$\partial_0 \rho + \partial_i (\rho v_i) = 0. \tag{3.43}$$

Linear Momenta

$$\partial_0 (\rho v_i) + \partial_j (\rho v_j v_i) = \rho f_i - \partial_i p + \partial_j \left(\eta \left(\frac{\partial v_i}{\partial x_j} + \frac{\partial v_j}{\partial x_i} \right) + \lambda \frac{\partial v_l}{\partial x_l} \delta_{ji} \right). \tag{3.44}$$

Energy

$$\partial_0\left(\rho\left(e+\frac{1}{2}v_jv_j\right)\right)+\partial_i\left(\rho v_i\left(e+\frac{1}{2}v_jv_j\right)\right)=$$
$$-\partial_i q_i-\partial_i\left(pv_i\right)+\partial_i\left(\eta\left(\frac{\partial v_i}{\partial x_j}+\frac{\partial v_j}{\partial x_i}\right)+\lambda\frac{\partial v_l}{\partial x_l}\delta_{ij}\right)+\rho v_i f_i. \tag{3.45}$$

These equations are suitable for solving arbitrary flow problems including transient problems, compressible materials and changing viscosity under non-isothermal conditions. As the focus of this study is laid on steady-state extrusion and as the present rubber compounds are considered incompressible, Equations (3.43), (3.44) and (3.45) can be simplified to yield the following system of equations.

Mass Conservation

$$\partial_i v_i=0. \tag{3.46}$$

Linear Momenta

$$\rho v_j\partial_j v_i=\rho f_i-\partial_i p+2\partial_j\left(\eta\dot{\varepsilon}_{ij}\right). \tag{3.47}$$

As the extrusion can well be approximated by an iso-thermal problem in the steady state, Equation (3.45) can be discarded. These equations are the non-Newtonian equivalent of the Navier-Stokes equations, the difference being found in the variable viscosity term. At this point, different rheological models are excluded as well as wall slip, as these concepts will be introduced in Sections 4.2 and 4.4 respectively.

Chapter 4

Rheology

The modern science of rheology is defined as the study of the deformation and flow of matter. Founded on the work of Newton, the flow of viscous materials can be described in analogy to the theory of elasticity. A solid material will respond with stresses if subjected to a strain field:

$$\sigma_{ij} = E\varepsilon_{ij}, \tag{4.1}$$

where σ_{ij} is the stress tensor, E is the Youngs modulus and ε_{ij} is the applied strain. Newton used a similar approach to describe the viscous stresses in a fluid in dependence of the strain rate tensor $\dot{\varepsilon}_{ij}$ as derived in Section 3.2.1, where Equation (3.39) shows the following relationship:

$$\tau_{ij} = \eta 2\dot{\varepsilon}_{ij}. \tag{4.2}$$

The material constant η is called the dynamic viscosity and is usually given in the unit $Pa\,s$. The full range of real-life viscosities is displayed in Table 4.1, spanning more than 45 orders of magnitude for common materials. Comprehensive listings of a wide range of viscosities are found in reference works, see e.g. [19]. Except for the simple case of inviscid flow, this material property is crucial for an accurate description of any fluid flow.

From the above equations it is possible to draw a simple distinction between solids and fluids: solid materials show limited deformation under an applied stress field, they show *elastic* behaviour. Fluids on the other hand will deform infinitely for a given stress, they display *viscous* properties.

Liquid	Approximate viscosity $\eta[Pa\,s]$
Glass	10^{40}
Molten glass ($500°C$)	10^{12}
Bitumen	10^{8}
Molten polymers	10^{3}
Golden syrup	10^{2}
Liquid honey	10^{1}
Glycerol	10^{0}
Olive oil	10^{-1}
Bicycle oil	10^{-2}
Water	10^{-3}
Air	10^{-5}

Table 4.1: Viscosity range of common materials at room temperature [9].

4.1 Viscous vs. Visco-elastic Fluids

In reality however, the border between fluids and solids is not drawn as distinctively as presented above. On the side of solids, creeping behaviour is encountered, where a solid deforms plastically, even under very small strains. For fluids, so called visco-elastic behaviour is found, where elastic components influence the flow field. Examples of this behaviour are found in the well-known effect of die swell and the Weissenberg (rod-climbing) effect. The visco-elastic behaviour of fluids is based on long-range memory effects of the deformation history of the fluid, a phenomenon whose numerical solution requires considerable computational cost. Crochet et. al. give a good introduction to the numerical analysis of non-Newtonian flows in [20]. In this place, however, visco-elastic fluids are not investigated any further, not due to a lack of relation with the subject of this study, but purely due to the excessive cost of the constitutive model.

4.2 Non-Newtonian Fluids

Even if the dynamic viscosity is often assumed to be constant for a given problem, this assumption only holds for a very limited number of cases. In reality the viscosity shows dependence on a range of physical properties which may have significant influence on the viscosity. The most important factors are listed here.

- *Temperature.* Many real processes involve changes in temperature which

can not be neglected when considering the viscosity of a given material. For Newtonian fluids, the well known equation of Arrhenius (see e.g. [21]) describes this relationship

$$\eta = A \exp^{\frac{B}{T}}, \tag{4.3}$$

with A and B as material constants and T as the absolute temperature. Another approach is the addition of an exponential modifier of the type

$$e^{b(T_{ref}-T)}, \tag{4.4}$$

with b being an additional material parameter to any of the shear dependant models. We will make use of this method in the application in Section 5.4, as it is well suited for numerical implementation while introducing only one new material parameter.

- *Pressure.* The use of lubricants in engines and gears is the classical example where a fluid's capacity to show increased viscosity under pressure is used to separate moving parts. According to Barnes [9], changes of viscosity in the order of four magnitudes are commonly found for pressure differences of around $0.5GPa$.

- *Shear rate.* Probably the most important influence on the viscosity of a fluid is exerted by the shear rate. Many non-Newtonian fluids show a high degree of sensitivity towards changes in shear rate. Therefore, a main point in building a model for the simulation of non-Newtonian fluids has to be an accurate description of this relationship, which will be covered in Section 4.2.1.

4.2.1 Shear Rate Dependency

As a restricting condition in the following chapter it is assumed that the behaviour of the examined fluids is time-independent, i.e. the shear rate does not change with the time for which an arbitrary stress has been applied to the fluid.

In general, the stress-strain curve of a fluid can be expressed as an equation of the form

$$\tau = f(\dot{\gamma}), \tag{4.5}$$

which leads to the different flow curves depicted in Figure 4.1. A closer inspection is deemed appropriate.

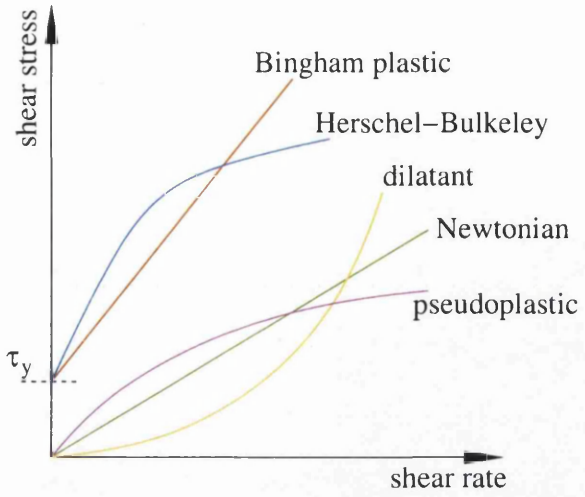

Figure 4.1: Non-Newtonian fluid behaviour.

Newtonian Fluid

The simplest conceivable case is the one of the Newtonian fluid where Equation (4.5) takes the form

$$\tau = \mu\dot{\gamma}. \tag{4.6}$$

The resulting flow curve is a straight line with a linear relationship between stress and shear rate.

Bingham Plastic

The characterising quality of a Bingham plastic is its resistance to deformation until a yield stress τ_y is reached. Below this threshold no flow will occur in this class of materials. The flow curve takes the form

$$\eta = \mu_y + \frac{\tau_y}{\dot{\gamma}} \quad for \quad \tau > \tau_y, \tag{4.7}$$

where μ_y is the bulk offset material parameter. If τ is smaller or equal τ_y, no motion is triggered. The definition of a value for the yield stress might under circumstances be considered vague, as many materials exhibit a yield stress which is so low that in practical applications it is of no importance.

Pseudoplastic

A very important category of fluids are the pseudoplastic or *shear-thinning* fluids. As shown in Figure 4.1, the shear stress - shear rate relationship is not linear and the higher the applied shear rate, the lower the increase in shear stress. This behaviour is due to a reduction in viscosity which itself is a result of various factors. The causes which have to be mentioned are the alignment of polymer particles in the flow direction and a disentanglement between different polymer chains. Most pseudoplastic fluids show a linear range in their flow curve, where the double logarithmic plot of shear rate vs. viscosity is linear. At the high and the low end of the shear rate spectrum often constant values for the viscosity can be observed. The shape of the flow curve is determined by the composition of the polymer, with narrow weight distributions giving more accurately defined curves than wide weight distributions.

There are a number of mathematical models in use to represent this shear-thinning behaviour, which have found a varying degree of popularity due to their accuracy and also their applicability:

- *Power law.* This is the most commonly found model due to its simplicity. It is expressed as derived in Chapter 4.3.2:

$$\eta = \mu_0 \dot{\gamma}^{n-1}. \tag{4.8}$$

  Its disadvantage is its restriction to the linear section of the shear thinning part of the flow curve. From a practical standpoint however, many applications are still operating within the ranges set by this approach and cut-off values for $\dot{\gamma} \to 0$ and $\dot{\gamma} \to \infty$ can be provided for in a simulation. The parameters of this model are μ_0, the fluid consistency and n, the power law index. The values for these parameters are specific to a given material and they can be determined by various rheometrical experiments which are explained in detail in Section 4.3. A common objection to the experimental character of this model is founded in the units ($Pa\,s^n$) which do not have any scientific meaning.

  For shear-thinning fluids, the power law index is always less than one, with one being the borderline case for a Newtonian fluid. Thus, it can be clearly seen that Equation (4.6) is a special case of Equation (4.8).

- *Carreau and Cross type models.* To overcome the restrictions imposed by the power law model, namely the existence of cut-off values [22], a model

was developed by various researchers which pays attention to the regions excluded from the power law. In its generic form it is expressed as

$$\eta = \frac{\eta_0}{\left[1 + \left(\frac{\eta_0}{\tau^*}\dot{\gamma}\right)^a\right]^{\frac{1-n}{a}}}, \tag{4.9}$$

with the material parameters being η_0, n, τ^*, and a. In its specific implementation, the Carreau model for $a = 2$ and the Cross model for $a = 1 - n$ should be mentioned as the most commonly found models.

Herschel-Bulkeley

A variation of the power law is the Herschel-Bulkeley model (see e.g. [21]) which combines an offset value μ_y with the power law model described above:

$$\eta = \mu_y + \mu_0 \dot{\gamma}^{n-1} \tag{4.10}$$

thus removing the restrictions of the power law model, Equation (4.8).

Dilatant

Less common than other materials types, some materials (e.g. concentrated aqueous corn starch) express dilatant or shear thickening behaviour. Especially in polymer extrusion processes, this behaviour is very rarely found. The material model most commonly used is the power law (Equation (4.8)) with a power law index n greater than one.

4.2.2 Extension Rate Dependency

Historically, the shear behaviour of materials has received much more attention than the influence of extension as tests for the former are more readily defined. In spite of this fact, many industrial processes seem to exhibit a significant degree of extensional flow. Traditionally, the Trouton ratio

$$Tr = \eta_e / \eta_s \tag{4.11}$$

for a Newtonian fluid is determined to be three. As described e.g. by Osswald [23] or Agassant [24], this result stems from the fact that the diagonal of the stress tensor under uniaxial extension (as seen in axisymmetric extrusion) is determined

from the total stress tensor - Equation (3.36) - and the deviatoric stress under uniaxial conditions

$$\tau_{ij} = \begin{bmatrix} -\eta\dot{\varepsilon} & 0 & 0 \\ 0 & -\eta\dot{\varepsilon} & 0 \\ 0 & 0 & 2\eta\dot{\varepsilon} \end{bmatrix} \tag{4.12}$$

to yield

$$\sigma_{11} = \sigma_{22} = -p - \eta\dot{\varepsilon} \tag{4.13}$$

and

$$\sigma_{33} = -p + 2\eta\dot{\varepsilon} \tag{4.14}$$

with all non-diagonal terms equal to zero. Because the outer stress is only applied in the third direction, σ_{11} and σ_{22} have to be zero leading to

$$\sigma_{33} = 3\eta\dot{\varepsilon} \tag{4.15}$$

and thus an extensional viscosity of $\eta_e = 3\eta$, the definition of the Trouton ratio for the uniaxial case. At this point it has to be noted that other extensional flows show different Trouton ratios, for example $Tr = 4$ in the case of planar extension.

For non-Newtonian fluids however, the Trouton ratio can diverge from this value to a high degree (see e.g. McGlashan [25]), the reason for the need to evaluate the Trouton ratio before deciding on whether extensional behaviour has to be modelled in the simulation.

Cogswell

Cogswell [26] was the first to derive an approximate solution for the determination of the extensional viscosity. A summary of assumptions for this analysis can be found in Sarkars work [27]:

1. incompressible fluid
2. funnel-shaped flow; no-slip ($v_z = 0$) on funnel surface
3. unidirectional flow in the funnel region
4. well developed flow upstream and downstream
5. symmetry in Θ
6. pressure drops due to shear and elongation may be calculated separately and summed to give the total entrance pressure-loss

7. neglect Weissenberg-Rabinowitch correction
8. shear stress is related to shear-rate through a power law
9. elongational viscosity is constant
10. shape of the funnel is determined by the minimum generated pressure drop
11. no effect of elasticity (shear normal stresses neglected)
12. neglect inertia

If these restrictions seem acceptable, an equation for the pressure can be expressed as

$$P_{ent} = \frac{n+1}{\dot{\gamma}}\sqrt{\frac{32}{9}\eta_e\eta_s}. \tag{4.16}$$

Binding

First described in [28], this approach aims to minimise the energy balance of the fluid on its way through the die, with both the planar and the axisymmetric case being covered. In [25], an application of this technique is given by McGlashan and Mackay. If the usual definition of the shear viscosity (Equation (4.8)) is used as the basis for a similar law for the extensional case, we can expand Cogswells model by introducing a variable elongational viscosity

$$\eta_e = \mu_e\dot{\varepsilon}^{p-1}. \tag{4.17}$$

A similar set of assumptions to Cogswell's approach is proposed:

1. incompressible fluid
2. funnel-shaped flow; no slip ($v_z = 0$) on funnel surface
3. unidirectional flow in the funnel region (see assumption 10)
4. well developed flow upstream and downstream
5. Θ-symmetry
6. shear viscosity is related to shear-rate through a power law
7. elongational viscosity is given by a power law
8. shape of the funnel is determined by the minimum work to drive flow

9. no effect of elasticity (shear normal stresses neglected)

10. the quantities $\left(\frac{dR}{dz}\right)^2$ and $\frac{d^2R}{dz^2}$, related to the shape of the funnel, are neglected; implies that the radial velocity is neglected when calculating the rate of deformation

11. neglect energy required to maintain vortex circulation

12. $\tau_{\Theta\Theta} - \tau_{rr} = 0$

13. neglect inertia

with the severest being number 3, the assumption of unidirectional flow. This restriction is not acceptable for Newtonian fluids; non-Newtonian fluids however which tend to exhibit vortices in corners are generally deemed conforming to this rule. McGlashan and Mackay [25] solve the equation for the power consumption $\dot{E}$ to result in an entry pressure drop

$$P_{ent} = \frac{16n\mu_0}{3m}\left(\frac{m+1}{n+1}\right)^2\left(\frac{\mu_e I_{mn}}{\mu_0}\frac{3n+1}{(4m)^m 4n}\right)^{\frac{1}{m+1}} \cdot \dot{\gamma}_w^{\frac{m(n+1)}{m+1}}\left(1-\left(\frac{r}{r_0}\right)^{\frac{3m(n+1)}{m+1}}\right), \tag{4.18}$$

with $\dot{\gamma}_w$ being the strain rate at the wall as introduced in Section 4.3.2 (see Equation (4.56)). The definition for r and r_0 are the orifice and the upstream radius, respectively. The Integral I_{mn} in Equation (4.18) can be solved to yield

$$I_{mn} = \frac{mn\,(m+1)\,(n+1)}{(m\,(n+1)+2n)\,((m+1)\,(n+1)+2n)}\frac{\Gamma\,(m)\,\Gamma\left(\frac{2n}{n+1}\right)}{\Gamma\left(m+\left(\frac{2n}{n+1}\right)\right)} \tag{4.19}$$

with $\Gamma\,(y) = \int_0^\infty x^{y-1}e^{-x}dx$ being the standard definition of the gamma function.

4.3 Rheometry

The determination of the material properties describing the flow of non-Newtonian fluids has historically been undertaken in various ways. Two techniques commonly found are cone-and-plate rheometers and die rheometers. The advantages of the former situate it mainly in a laboratory environment due to the possibility of widely adjustable test parameters, whereas the latter show their strength more in an industrial environment, where on-line data can be extracted from forked-off

streams of material. Another advantage is the possibility to achieve less intrusive sampling as the material stream is deformed in a similar way to the actual extrusion process.

4.3.1 Cone-and-Plate Rheometers

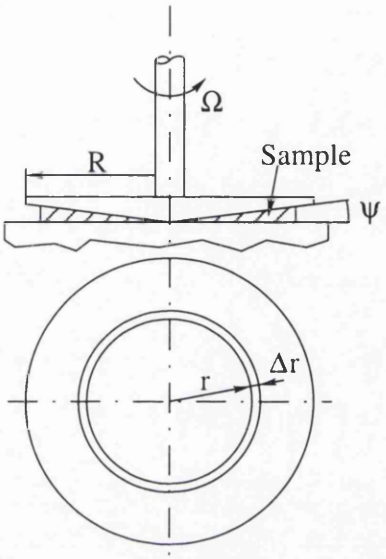

Figure 4.2: The cone-and-plate rheometer.

Figure 4.2 shows a schematic view of a typical cone-and-plate rheometer which is commonly used to determine the characteristics of a fluid in laboratory environments. A sample of the material is clamped between a fixed plate and a rotating cone. The rotation results in a shearing motion which, for small angles ψ, shows a constant shear rate over the whole radius R as

$$\dot{\gamma}(r) = \frac{\Omega r}{r \tan \psi} = \frac{\Omega}{\tan \psi} \tag{4.20}$$

and for small angles

$$\dot{\gamma} \approx \frac{\Omega}{\psi}. \tag{4.21}$$

This is the reason for reduced implementation of parallel plates in this type of rheometer.

Two kind of modes of operation have to be distinguished: uniform and oscillatory shear. As the experiments considered in this work were conducted using oscillatory shear, the remainder of this section will be focused on this type of rheometry which nowadays seems to be the dominant method.

The dynamic analysis of polymeric materials has to take into account the elastic properties as well as the viscous ones and a convenient way to manipulate the data is found in the use of complex numbers. In this context, the definition of the strain is given as (see e.g. [9, 21])

$$\gamma^*(t) = \gamma_0 e^{(i\omega t)} \tag{4.22}$$

with a derivative of

$$\dot{\gamma}^*(t) = i\omega\gamma_0 e^{i\omega t}. \tag{4.23}$$

The complex stress is defined in the same manner as

$$\tau^*(t) = \tau_0 e^{i(\omega t+\delta)}, \tag{4.24}$$

leading to a stress vector made up of a viscous and a elastic part as illustrated in Figure 4.3 b). Rewriting the general Equations (4.1) and (4.2), we can state

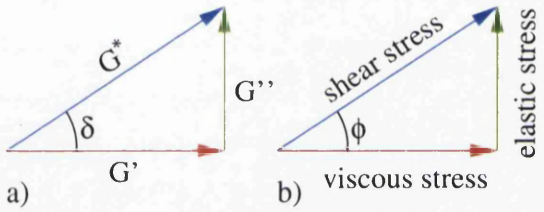

Figure 4.3: Components of a) the complex shear modulus and b) the complex stress.

$$\tau(t) = E\gamma(t) \tag{4.25}$$

for a perfectly elastic solid and

$$\tau(t) = \eta\dot{\gamma}(t) \tag{4.26}$$

for a perfectly viscous fluid.

A complex shear modulus G^* as seen in Figure 4.3 a) has to be defined for accommodating the need for split (viscous and elastic) properties by substituting Equations (4.22) and (4.24) into Equation (4.25):

$$G^* = G' + iG'', \tag{4.27}$$

which can be used to relate strain and stress

$$\tau^*(t) = G^*(\omega)\gamma(t) \tag{4.28}$$

to represent the shear stress displayed in Figure 4.3 b). In Equation (4.27), G' and G'' are denoted as the *storage modulus* and *loss modulus.* The same steps can be performed for the viscous stress, by substituting Equations (4.23) and (4.24) into the definition of the viscous fluid (Equation (4.26)):

$$\tau^*(t) = \eta^*\dot{\gamma}(t), \tag{4.29}$$

where the definition of the complex viscosity

$$\eta^* = \eta' - i\eta'' \tag{4.30}$$

is used, with η' representing the viscous part of the viscosity and η'' the elastic part, which is recovered. The viscous part η' is, in fact, the same entity as the *dynamic viscosity* found in Equation (4.2). Now, Equation (4.28) can be substituted into Equation (4.29) to yield

$$\eta^* = \frac{G^*}{i\omega} = \frac{G'' - iG'}{\omega} \tag{4.31}$$

and therefore, with Equation (4.30)

$$\eta'(\omega) = \frac{G''(\omega)}{\omega}, \qquad \eta''(\omega) = \frac{G'(\omega)}{\omega}. \tag{4.32}$$

To correlate experimental results from oscillatory cone-and-plate rheometry with these equations, the data from the rheometer, i.e. γ_0, τ_0 and the phase angle δ have to be used.

When subjected to oscillatory shear, the analysed material shows a stress response which is out of phase with the input, as seen in Figure 4.4. As this graph is based on Equations (4.22) and (4.24), δ can plainly be seen as the difference in phase angle between the strain input and the stress response. The phase angle δ relates G' and G'' as seen in Figure 4.3 a):

$$\tan\delta = \frac{G''}{G'}. \tag{4.33}$$

At this point we have to introduce the well-known Cox-Merz rule, a very useful tool for obtaining data on polymer materials. While solely based on empirical correlation, the Cox-Merz rule is widely used, as it seems to produce valid results for

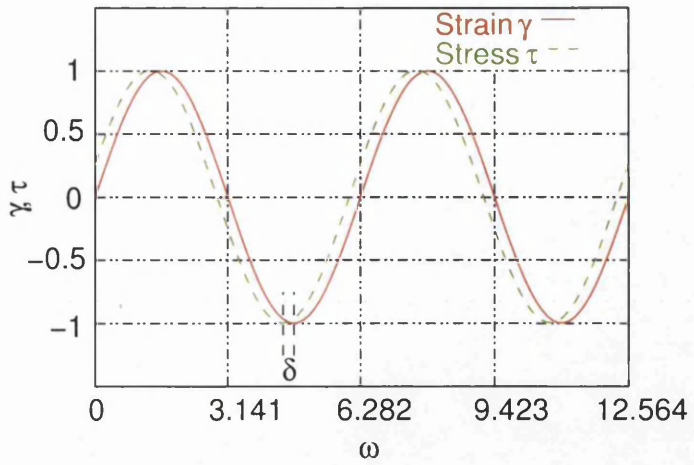

Figure 4.4: Oscillatory strain and resulting stress response in the cone-and-plate rheometer.

a wide range of materials. The Cox-Merz rule is applied in oscillatory rheometry by plotting the complex viscosity η^* over the angular frequency Ω. The resulting plot is then equated with a plot of the shear viscosity over the shear rate while the numerical values stay the same, i.e. the angular frequency is turned into the shear rate and the complex viscosity becomes the shear viscosity.

Though widely used in polymer processing, we will have to question its applicability with regard to the present range of rubber compounds.

4.3.2 Die Rheometers

As mentioned earlier, the main advantage making die rheometers very useful is the close binding of the sampling to the actual process. If a die rheometer is coupled with an extruder from the production line, a system of minimal disturbance is created which is a requirement for exact results. Due to the complexity of the material, the temperature and deformation history of the compound have to be modelled according to the flow in the production line as cone-and-plate rheometers impose their own stress history which might or might not have an influence on the measured properties.

Two main kinds of die rheometers have to be distinguished: the slit die and the capillary die rheometer. Being more flexible, the slit die rheometer is more complex to build and to operate, whereas the capillary die rheometer is a simple device which might not serve all envisaged purposes.

Both types of instrument show flow regions according to Figure 4.5, which give

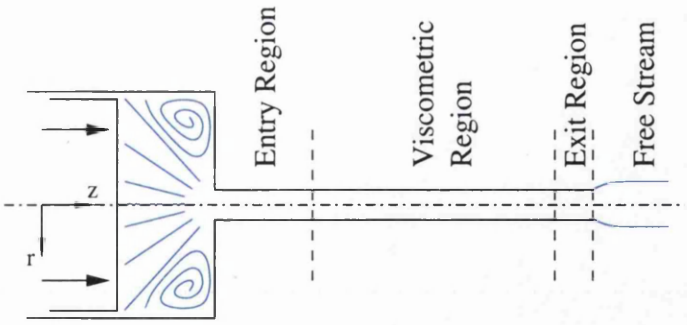

Figure 4.5: Different flow regions in die rheometers [3].

rise to several problems when evaluating the accuracy of any obtained value. Generally, we can state that

$$P_{tot} = P_{ent} + P_{cap} + P_{exit}, \tag{4.34}$$

where P_{cap} is the actual pressure drop through the die and P_{ent} and P_{exit} are the entry/exit losses, respectively. This relation will prove useful in the context of separating the entry pressure loss from the capillary pressure drop.

Slit Die Rheometer

In many situations it is desirable to have an analytical solution for the flow field in a slit die, e.g. in order to determine shear rates in a profile extrusion, not to speak of its usefulness in designing a slit die rheometer. From fluid mechanics we can state that

$$\frac{\partial p}{\partial z} = \frac{\partial \tau_{zy}}{\partial y}, \tag{4.35}$$

which integrates over y to yield

$$\frac{\partial p}{\partial z} y = \tau_{zy} \tag{4.36}$$

or (see Equation (3.39))

$$\frac{\partial p}{\partial z} y = \eta \frac{\partial v_z}{\partial y}. \tag{4.37}$$

By changing sign and substituting the power law (Equation (4.8)) into Equation (4.37), we get

$$-\frac{\partial p}{\partial z} y = \mu_0 \left(\frac{\partial v_z}{\partial y} \right)^{n-1} \frac{\partial v_z}{\partial y} = \mu_0 \left(\frac{\partial v_z}{\partial y} \right)^{n}, \tag{4.38}$$

$$v_z(y) = \frac{n}{n+1}\left(\frac{\partial p}{\partial z}\mu_0\right)^{\frac{1}{n}}\left(H^{\frac{n+1}{n}} - h^{\frac{n+1}{n}}\right). \tag{4.39}$$

Capillary Rheometer

The determination of the material properties, namely of the fluid consistency μ_0 and the power law index n, is a well known procedure for capillary dies. It is described in a number of textbooks such as [3, 21, 29, 30], which were used to compile this derivation. For the viscometric region of Figure 4.5, the equations of motion can be expressed in a cylindrical coordinate system as

$$-\frac{\partial p}{\partial z} + \frac{1}{r}\frac{\partial (r\tau_{rz})}{\partial r} = 0, \tag{4.40}$$

$$-\frac{\partial p}{\partial r} + \frac{\partial \tau_{rr}}{\partial r} + \frac{\tau_{rr} - \tau_{\theta\theta}}{r} = 0, \tag{4.41}$$

where the total stress tensor is defined as

$$\sigma_{ij} = \begin{vmatrix} -p + \tau_{zz} & \tau_{rz} & 0 \\ \tau_{rz} & -p + \tau_{rr} & 0 \\ 0 & 0 & -p + \tau_{\theta\theta} \end{vmatrix}. \tag{4.42}$$

Integration of Equation (4.40) from the centreline $r = 0$ to an arbitrary radius r gives

$$\tau_{rz} = \frac{r}{2}\frac{\partial p}{\partial z} \tag{4.43}$$

and for the shear stress at the wall

$$\tau_w = \frac{R}{2}\frac{\partial p}{\partial z}, \tag{4.44}$$

where R is the die radius. This equation is the limit of the balance of forces on a cylindrical element in the flow channel:

$$\tau_w = \frac{R\Delta P}{2L}. \tag{4.45}$$

Equations (4.43) and (4.44) can be combined to form

$$\frac{\tau_{rz}}{\tau_w} = \frac{r}{R}. \tag{4.46}$$

The flow rate $\dot{V}$ is calculated by integrating the velocity profile over the cross section of the die:

$$\dot{V} = 2\pi \int_0^R r v_z(r) \mathrm{d}r, \tag{4.47}$$

which can be integrated by parts to yield

$$\dot{V} = -\pi \int_0^R r^2 \frac{\mathrm{d}v_z}{\mathrm{d}r} \mathrm{d}r. \tag{4.48}$$

In the viscometric region, we have constant shear rates and thus

$$-\frac{\mathrm{d}v_z}{\mathrm{d}r} = \dot{\gamma}. \tag{4.49}$$

Equations (4.46) and (4.49) can be substituted into Equation (4.48) to give

$$\frac{\tau_w^3 \dot{V}}{\pi R^3} = \int_0^{\tau_w} \dot{\gamma} \tau_{rz}^2 d\tau_{rz}, \tag{4.50}$$

which can be integrated to result in

$$\dot{\gamma}_w = \frac{1}{\pi R^3} \left(\tau_w \frac{\mathrm{d}\dot{V}}{\mathrm{d}\tau_w} + 3\dot{V} \right). \tag{4.51}$$

By making use of the definition of the apparent shear rate

$$\dot{\gamma}_{app} = \frac{4\dot{V}}{\pi R^3}, \tag{4.52}$$

Equation (4.51) can be transformed into [21]

$$\dot{\gamma}_w = \frac{\dot{\gamma}_{app}}{4} \left(3 + \frac{\mathrm{d} \ln \dot{\gamma}_{app}}{\mathrm{d} \ln \tau_w} \right). \tag{4.53}$$

When expressing the power law in terms of the dependency between shear rate and shear stress

$$\tau_w = \mu_0' \dot{\gamma}_{app}^n, \tag{4.54}$$

the power law index n can be interpreted as the slope of the shear rate vs. shear stress curve in the logarithmic diagram.

$$n = \frac{\mathrm{d} \ln \tau_w}{\mathrm{d} \ln \dot{\gamma}_{app}}. \tag{4.55}$$

Equation (4.55) can now be used to simplify Equation (4.53) into

$$\dot{\gamma}_w = \frac{3n+1}{4n} \dot{\gamma}_{app}, \tag{4.56}$$

where $\frac{3n+1}{4n}$ is sometimes called the Rabinowitch correction. Equation (4.56) can subsequently be used to to express τ_w in terms of $\dot{\gamma}_w$ in Equation (4.54)

$$\tau_w = \mu_0 \dot{\gamma}_w^n. \tag{4.57}$$

The relation between μ_0 and μ_0' is thus determined by

$$\mu_0 = \mu_0' \left(\frac{4n}{3n+1} \right)^n. \tag{4.58}$$

As τ_w and $\dot{\gamma}_w$ in Equation (4.57) are defined by Equations (4.45) and (4.56), an equation is at hand which lets us relate the measured pressure drop ΔP through a capillary die to the flow rate $\dot{V}$ and thus the shear stress τ_w to the shear rate $\dot{\gamma}_w$.

With these equations, it is possible to generate plots of $\dot{\gamma}_w$ vs. τ_w as seen in Figure 4.1. An important advantage of this procedure is the fact that wall slip can be detected easily. If non-laminar flow and time-dependency can be assumed to be negligible [29], a discrepancy between the flow curves for different diameters indicates wall slip.

Equation (4.57) can be substituted into the definition of the viscosity

$$\eta = \frac{\tau_w}{\dot{\gamma}_w} \tag{4.59}$$

to give

$$\eta = \mu_0 \dot{\gamma}^{n-1}, \tag{4.60}$$

which is the well known power law for non-Newtonian fluids. A simple enhancement of this equation is the addition of a temperature dependant exponential term as proposed in Section 4.2,

$$\eta = \mu_0 e^{b(T_{ref}-T)} \dot{\gamma}^{n-1}. \tag{4.61}$$

4.4 Wall Slip

In classical fluids analysis, a fundamental assumption is the wall stick boundary condition where the fluid velocity at the wall is zero. The theory of the boundary layer - first formulated by Prandtl - explains the forming of a velocity profile which is assumed to range from $v_w = 0$ at the wall to $v = v_\infty$ at a distance δ. Boundary layer theory is covered in a number of textbooks, with an extensive

discussion found in [31]. This assumption of zero wall velocity as a reasonable approximation has found its way into the numerical simulation of a wide range of common materials such as gases and simple Newtonian liquids.

4.4.1 Determination

Experimental Determination

For complex polymers such as the present rubber formulation however, wall slip has to be considered as a major influence on the pressure drop. Mooney [32] first described a method to detect wall slip by making use of a capillary rheometer as described in Section 4.3.2 and by using different die diameters (see also [29], [33]). If the wall shear stress τ_{rz} as given in Equation (4.43) is plotted over the apparent shear rate (Equation (4.52)), as seen in Figure 4.1, a fluid without wall slip will exhibit a unique curve when plotting the data for different die diameters. If this exercise results in several different curves, wall slip can assumed to be present. Several conditions have to be met in order to result in a valid wall slip determination:

- The flow is laminar, a criterion readily met by typical rubber extrusion applications
- Time-independence can be assumed

A quantitative determination of the wall slip velocity v_s can be effected by plotting the apparent shear rate (Equation (4.52)) over the reciprocal orifice radius $1/R$ for constant wall shear rates τ_w as defined in Equation (4.45). In this graph, the gradient is interpreted as the wall slip velocity,

$$v_s = \frac{\partial\left(\frac{\dot{V}_{tot}}{\pi R^3}\right)}{\partial\left(\frac{1}{R}\right)}. \tag{4.62}$$

The difficulty in applying this approach to an inline rheometer is found to be the precision of the extruder's adjustability and the delay in the response to any adjustment.

Analytical Determination

In the following, the analytical calculation of the wall slip velocity will be presented for a non-Newtonian fluid with power law behaviour. The two-dimensional flow between two walls of infinite depth will be useful in comparing the analytical solution with the numerical implementation (see Section 6.2.2), so we choose it here to demonstrate the procedure of wall slip analysis. The mentioned problem,

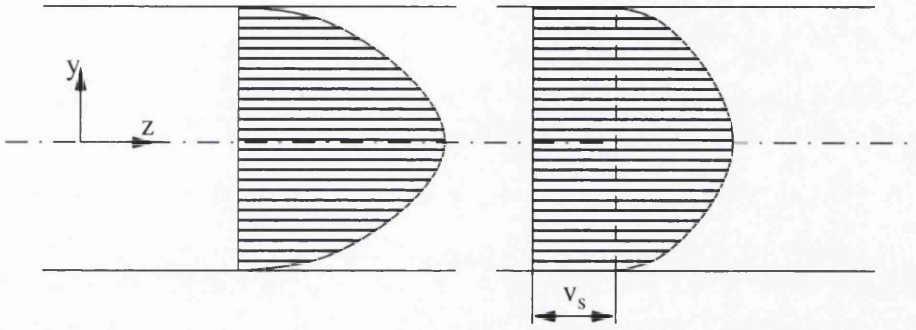

Figure 4.6: Poiseuille flow with wall stick and wall slip ($v_s > 0$).

known as Poiseuille flow, is illustrated in Figure 4.6 with $-h \leq y \leq +h$. In Section 3.3, we have presented the derivation of the equations of change, from which we can extract the pressure drop for the case of Poiseuille flow as

$$\frac{\mathrm{d}P}{\mathrm{d}z} = \mu \frac{\mathrm{d}^2 v_z}{\mathrm{d}y^2} \tag{4.63}$$

subject to the boundary conditions

$$v_z = v_s \quad \text{at} \quad y = \pm h \quad \text{and} \quad \frac{\mathrm{d}v_z}{\mathrm{d}y} = 0 \quad \text{at} \quad y = 0$$

and under the convention of defining $^{\mathrm{d}P}/_{\mathrm{d}z}$ as a negative entity. Equation (4.63) can be integrated from the wall to the centre

$$\int \frac{\mathrm{d}P}{\mathrm{d}z} \mathrm{d}y = \int \mu \frac{\mathrm{d}^2 v_z}{\mathrm{d}y^2} \mathrm{d}y$$

to give

$$\frac{\mathrm{d}P}{\mathrm{d}z} y = \mu \frac{\mathrm{d}v_z}{\mathrm{d}y}. \tag{4.64}$$

A second integration

$$\int \frac{\mathrm{d}P}{\mathrm{d}z} y \mathrm{d}y = \int \mu \frac{\mathrm{d}v_z}{\mathrm{d}y} \mathrm{d}y$$

yields

$$\frac{1}{2}\frac{\mathrm{d}P}{\mathrm{d}z}\left(h^2 - y^2\right) = \mu\left(v_s - v_z\right), \tag{4.65}$$

from which it follows that the velocity at any given point of the profile is

$$v_z\left(y\right) = v_s - \frac{1}{2\mu}\frac{\mathrm{d}P}{\mathrm{d}z}\left(h^2 - y^2\right). \tag{4.66}$$

A common implementation of the wall slip law is the non-linear term

$$\tau = \kappa_0 \left|v_s\right|^m = -\mu h \frac{\mathrm{d}P}{\mathrm{d}z} \tag{4.67}$$

with κ_0 and m as material parameters. This equation enables the rheologist to specify any slip behaviour from increased slip at elevated shear levels ($m < 1.0$) via $m = 1.0$ for the linear case to inhibited slippage for $m > 1.0$. De Gennes [34], together with Brochard [35], propose this linearised case in a simplified term as they approach the subject from the microscopic side as opposed to the continuum assumption used in fluid mechanics. The resulting general slip velocity is expressed as

$$v_s = \left(\frac{-\mu}{\kappa_0}\frac{\mathrm{d}P}{\mathrm{d}z}\right)^{\frac{1}{m}} h^{\frac{1}{m}}, \tag{4.68}$$

a result which can be inserted into Equation (4.66) to give

$$v_z\left(y\right) = \left(\frac{-\mu}{\kappa_0}\frac{\mathrm{d}P}{\mathrm{d}z}\right)^{\frac{1}{m}} h^{\frac{1}{m}} - \frac{1}{2\mu}\frac{\mathrm{d}P}{\mathrm{d}z}\left(h^2 - y^2\right). \tag{4.69}$$

4.5 Conclusions

The material model to be used has been determined as a viscous power law model, a choice which is due to the acceptable numerical cost, while maintaining the accuracy of the model. As has been pointed out previously, the complex deformation history of the material as it proceeds through the extruder, necessitates the introduction of an in-line capillary rheometer. Such an instrument will be introduced shortly, in Section 5.2.2.

Further details on industrial applications concerned with rheological problems can be found in Walters [36] or Fredrickson [37], while general coverage of rheology and rheometry is given by Cogswell [38], Walters [3] and Tanner [16].

Chapter 5

Parameter Determination

The need for experiments in the context of the optimisation of rubber extrusion can be separated into two distinct areas. First, rheological trials are needed to correctly describe the flow behaviour of the polymeric material along its flow path. This kind of experiment necessitates the use of specific instrumentation as introduced in Section 5.2.2, as the possibility to describe the flow analytically is a basic requirement for obtaining material parameters. Traditional laboratory (off-line) rheometry results are presented in Section 5.1. Section 5.2 will give details of a novel experimental setup for in-line parameter determination, while the theoretical background for the chosen approach will be dealt with in Section 5.4.

Once a suitable set of parameters has been found, a second series of experiments as described in Section 5.3 is used to verify simulation results with actual cross sections of extruded profile.

5.1 Classical Rheology at Aberystwyth

In the scope of this study, an extensive series of experiments was conducted by our collaborators at the University of Wales, Aberystwyth (see [39]). The compound under examination is E8246, the composition of which is shown in Figure 2.2. As a precautionary measure in divergence from the standard procedure, this batch did not include any added curing agent in order avoid possible detrimental effects in prolonged oscillatory experiments at elevated temperatures. Both oscillatory (see Section 4.3.1) and capillary rheometers (see Section 4.3.2) were used, with oscillatory tests being performed at different temperatures while the capillary

work was conducted at the reference temperature of 60°C. Steps of 20°C were chosen as convenient for covering the whole range of operating temperatures from 60°C to 120°C. In deviation from common practice, the present experimental setup makes use of parallel plates as has been found useful for materials displaying high levels of viscosity. In all other respects, the method described in Section 4.3.1 has been followed, with a shear strain amplitude fixed at 10^{-3}, as preliminary tests suggested a linear behaviour for the complex shear modulus G^* and the phase angle δ up to this strain.

A set of initial results is displayed in the appendix (Table A.1), showing the components of the complex shear modulus G^*, G' and G'', and the complex viscosity η^* along with its real part η' for different angular frequencies ω. Another important result of the report [39] is the viscosity vs. shear rate plot using different methods of viscosity determination as presented in Figure 5.1. This plot

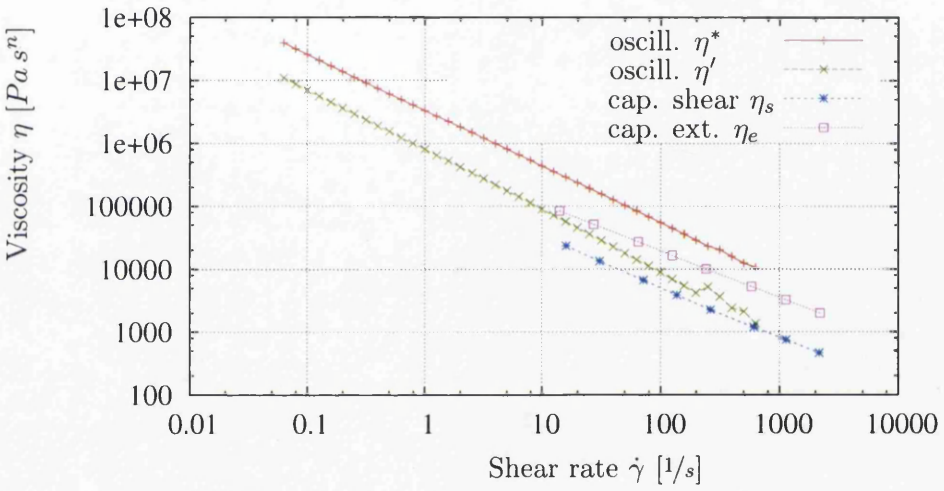

Figure 5.1: Shear rate vs. Viscosity results of experiments in Aberystwyth at $T = 60$°C.

is created using the well-known Cox-Merz rule as described in Section 4.3.1 to extract shear viscosities from oscillatory data. In this plot, η^* is generated by application of the classical Cox-Merz rule while η' is produced by making use of the real part of the complex viscosity. On the capillary side, the shear viscosity η_s and the extensional viscosity η_e are displayed.

5.1.1 Power Law Parameters

Figure 5.1 enables us to specify the power law parameters for the various determination methods by making use of a variation of Equation (4.8). By simply looking

	$\mu_0\,[Pa\,s^n]$	n
Complex oscillatory viscosity η^*	3,301,704	0.109
Real part of complex oscillatory viscosity η'	725,280	0.024
Capillary shear viscosity η_s	210,288	0.200
Capillary extensional viscosity η_e	587,942	0.259

Table 5.1: Power law parameters extracted from Figure 5.1.

at the two end-points of each graph we can set up two power law equations for two unknowns and solve them for the unknowns:

$$n = \frac{\log\left(\frac{\eta_1}{\eta_2}\right)}{\log\left(\frac{\dot{\gamma}_1}{\dot{\gamma}_2}\right)} + 1. \tag{5.1}$$

Re-substitution into one of the two original equations then yields μ_0. After extracting the power law parameters in this manner, we are left with parameters according to Table 5.1. The results show high values for the oscillatory bulk parameters with a low power law index for η^* and a very low index for η'. The capillary values for μ_0 on the other hand are much lower. From this discrepancy between the oscillatory η^* on the one hand and the capillary η_s on the other, we can conclude that either the Cox-Merz rule is not applicable for this material or that a significant amount of wall slip in the capillary case is leading to the present result.

Going one step further, the capillary rheometry results η_s and η_e can be used to estimate the Trouton ratio, defined as η_e/η_s (see Section 4.2.2). Figure 5.2 shows the Trouton ratio over the relevant deformation rate range. A surprising result is the relatively low Trouton ratio over the whole data range with other rubbers being known to display much higher ratios.

5.1.2 Temperature Dependence

In addition to these results, the oscillatory results were used to determine the temperature coefficient for μ_0, as an extensive set of data points was available at different temperatures as shown in Appendix A.2. Taking advantage of Equation (4.61), we can set up an equation to compare two viscosities at the same shear rate but different temperature:

$$b = \frac{1}{T_2 - T_1} \ln\left(\frac{\eta_1}{\eta_2}\right). \tag{5.2}$$

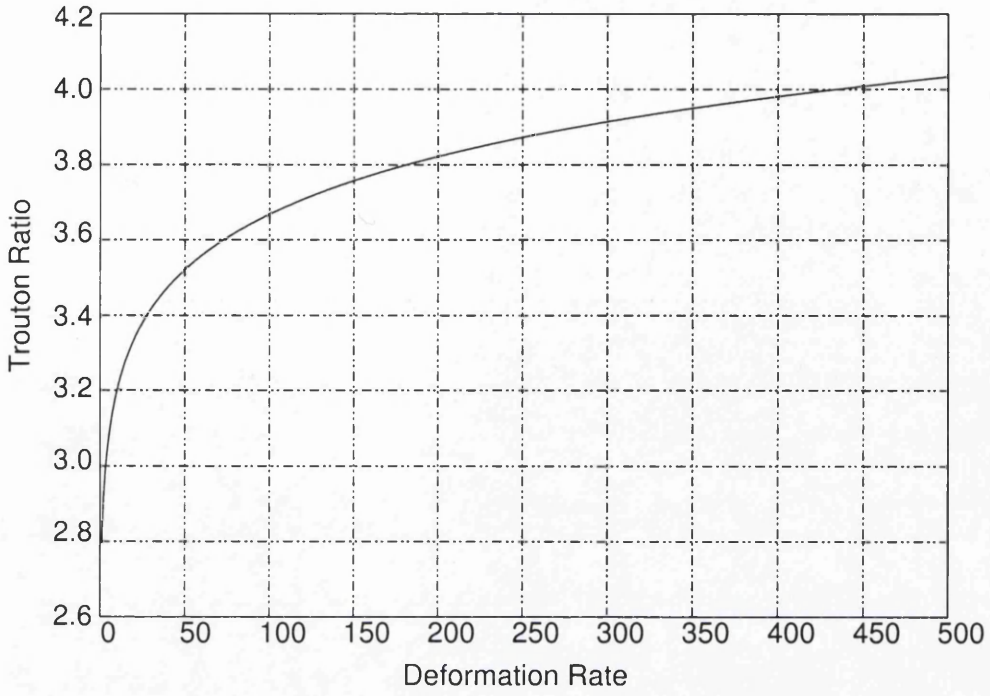

Figure 5.2: Trouton ratio from capillary experiments in Aberystwyth.

As 60°C is used as the reference temperature in [39], we can now calculate a grid of temperature dependence parameters with reference to that temperature. The results of this calculation are represented in Table 5.2. In spite of an input data

$\dot{\gamma}$ [1/s]	b [1/°C] (60 − 120°C)	b [1/°C] (60 − 100°C)	b [1/°C] (60 − 80°C)
628.3	0.0042	0.0050	0.0064
499.0	0.0049	0.0051	0.0063
396.5	0.0053	0.0055	0.0066
314.9	0.0057	0.0060	0.0071
250.1	0.0041	0.0057	0.0065
198.7	0.0054	0.0057	0.0067
157.8	0.0057	0.0059	0.0070
125.4	0.0058	0.0062	0.0072
99.6	0.0062	0.0064	0.0074
79.1	0.0062	0.0066	0.0075
62.8	0.0063	0.0068	0.0076
49.9	0.0064	0.0069	0.0077
39.7	0.0068	0.0072	0.0079
31.5	0.0069	0.0075	0.0081
25.0	0.0070	0.0076	0.0083
19.9	0.0073	0.0078	0.0084

Table 5.2: Temperature dependence calculated from data in Appendix A.2.

set which extends to much smaller shear rates, this table only lists shear rate

values relevant to the extrusion process, as the average temperature dependence at these low shear rates is of no interest in this context. Looking at the average value yields $b = 0.0065\,{}^{1}/_{°C}$, thus completing the parameter set needed for material modelling together with the capillary shear parameters at 60°C taken from Table 5.1:

μ_0 $[Pa\,s^n]$	n $[-]$	b $[{}^{1}/_{°C}]$
210,288	0.20	0.0065

These parameters will prove useful in the following when the need to estimate various processing conditions like pressure drops and flow rates arises in the design process of the proposed rheometer.

5.2 In-Line Rheometer Trials

Pure laboratory rheometry as described in the previous Section is a powerful tool for accurate determination of material parameters. One drawback however, is the question of applicability of the obtained results to a real world extrusion line, expressed e.g. in Montes' work [40]. Before passing through the die area which is relevant in this work, the rubber compound undergoes a complex deformation described in detail in Section 2.2.1. This deformation history may influence the material parameters and is not reproducible with laboratory equipment, introducing the need for in-line rheometry where a capillary or slit die rheometer is introduced directly into the material flow of the production line. As no implementation for the present extrusion line was in existence at that point, the design of a generic rheometer with a high degree of freedom regarding adjustability was necessary.

5.2.1 Torpedo Design

The original design of the extrusion line includes a so-called torpedo, shown in Figure 2.9 a), which is responsible for uniting the annular flow coming from the extruder cross-head into one solid stream of material just upstream of the converging zone into the die. This semi-spherical torpedo is replaced by a custom one of equal dimensions but including sensors to log temperature and pressure before the compound passes the die. Figure 5.3 shows the instrumented torpedo

with the two pressure sensors at locations **A** on the side and **B** at the tip and a thermocouple at **C**. As the torpedo design is held axisymmetric, it is possible to turn the whole torpedo in order to gather information about the pressure and temperature distribution at any point on the circumference. For this purpose,

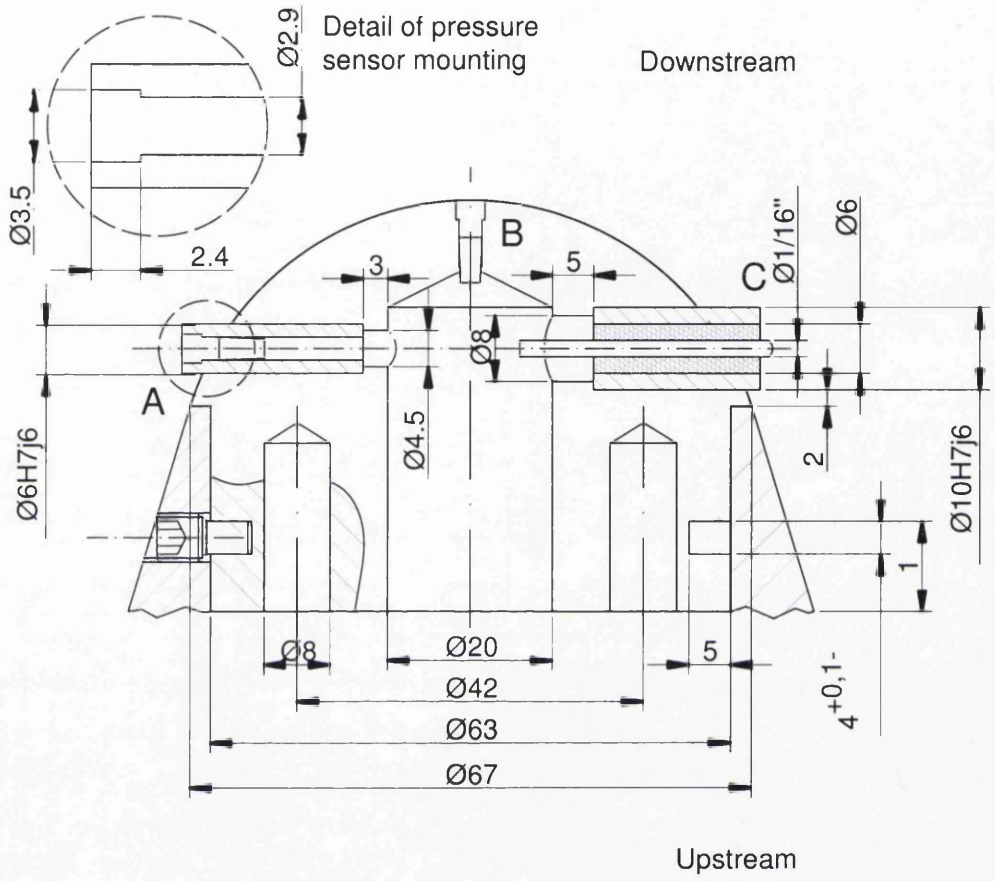

Figure 5.3: Design of instrumented torpedo.

the two off-centre holes in the back of the torpedo are provided as docking points for a rod with a forked head. The cabling of the sensors is routed through the large centre hole and the space in the cross head reserved for the feeding of any metal insert towards the back of the extrusion line as shown in Figure 2.4. As this torpedo has the same dimensions as the original one, there are no restrictions regarding its use in any possible experimental configuration.

5.2.2 In-Line Rheometer Design

There are several fundamental decisions concerning the design of the rheometer which will influence its performance. Most critically, the decision between capillary and slit die design will determine the equations that are needed to extract material parameters. In the present case, a flexible approach has been favoured,

where the actual die is located in a sliding, replaceable bar that can contain either a capillary or a slit die. Actual use was finally made of cylindrical dies. Dimensioning of these dies will be presented later in this chapter in Table 5.3, where the reader will also find a rough calculation which led to the chosen dimensions.

As processing parameters have to be kept as close to the actual processing conditions as possible, circumferential overflow valves for adjusting the back pressure before the die have been included in the design. A schematic overview of rheometer is given in Figure 5.4 while a conceptual study of the final rheometer is presented in Figure 5.5.

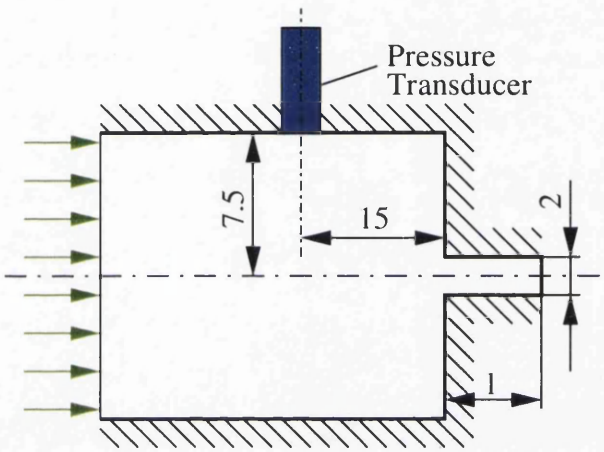

Figure 5.4: Schematic view of capillary rheometer trial showing a specific die of the interchangeable set; units in *mm*.

The flow-path is divided into an outer overflow path and an unperturbed inner material flow which leads into the rheometer orifice. The overflow valves are operated by equally tightening the circumferential screws which have a clearance fit in their lower section where they are in contact with the valve bore. The aim of this arrangement of circumferential overflow valves is to create an axisymmetric flow as found in classical capillary rheometers while retaining the possibility of setting a desired pressure level. The interchangeable die is implemented as a sliding bar as shown in detail in Appendix B, Figure B.4.

A further design constraint, which has to be considered, is the upstream reservoir diameter to capillary diameter ratio, a number which Walters [3] determines to be at least 12:1. As in the present case a ratio of 15:1 is used, we can be confident that consistent results are obtainable. Regarding the L/D ratio of the die, a compromise had to be found as classical laboratory rheometry uses very high ratios of 40:1, with some sources citing the need to go as high as 350:1. In the present study however strong emphasis is laid on reproducing the actual conditions in a profile extrusion die. The inherent disadvantage of a low L/D ratio in terms of non-

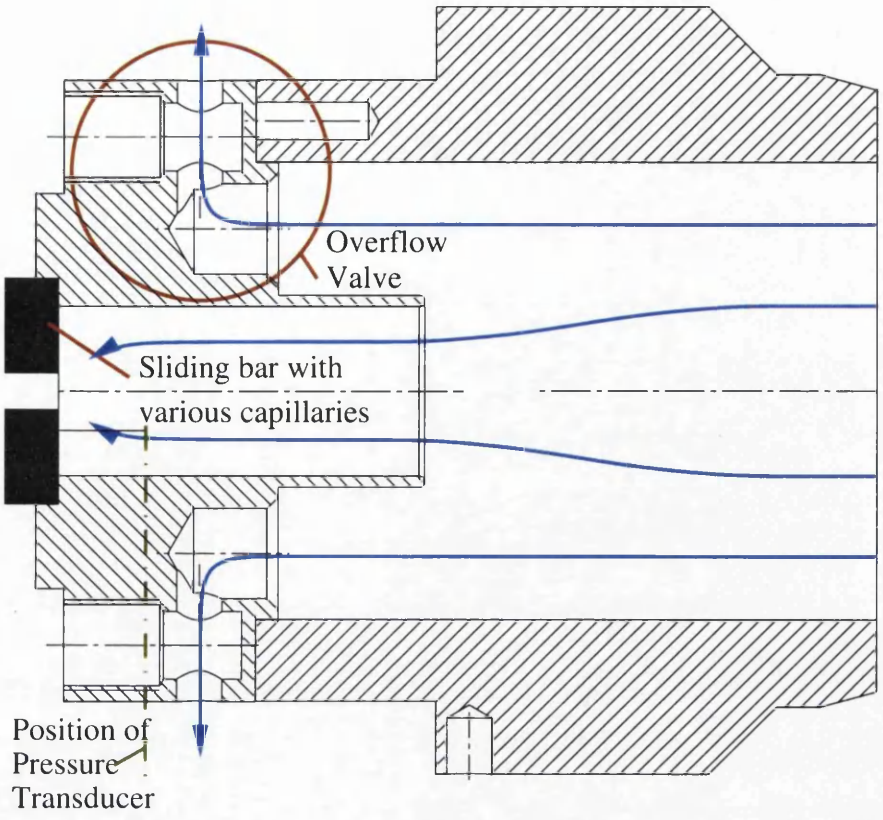

Figure 5.5: Design of capillary rheometer.

linearity in the entry region has to be accepted as no production die shows a ratio as high as 40:1.

Calculation of Rheometer Dimensions - Overflow

In order to obtain pressure drops and flow rates which are in the same region as the actual processing conditions, a rough calculation of the overflow valves and the actual rheometer orifice are necessary. By considering the material parameters found in [39], we can generate a worst case for which sufficient overflow throughput has to be ensured.

After an initial design phase, where the requirements of the rheometer such as geometrical constraints and placement of sensors were considered, a setup with six adjustable overflow valves was favoured. The equation for the calculation of the flow rate $\dot{V}$ in a cylindrical channel in dependence of the pressure and the material parameters is given to be

$$\dot{V} = 2\pi \frac{n}{n+1} \left(-\frac{\partial p}{\partial z} \frac{1}{2\mu_0 e^{b(T_{ref}-T)}} \right)^{\frac{1}{n}} \left[\left(\frac{1}{2} - \frac{n}{3n+1} \right) R^{\frac{3n+1}{n}} \right], \tag{5.3}$$

as derived in Section 5.4.2. Note that this equation is simplified by neglecting the wall slip term as it will only enhance the material flow. Using the parameters found in the study from Aberystwyth in Section 5.1 ($\mu_0 = 210288\,Pa\,s$, $n = 0.20$, $b = 0.0065\,{}^1/_{°C}$), an overflow radius of $12.5\,mm$ and a flow-path length of $56\,mm$ as the geometrical dimensions from Figure B.2 in Appendix B, we now only require a guess for the pressure drop in a typical production die. Test runs of a generic profile, which will be introduced later in this chapter, suggest $20\,bar$ to be a reasonable guess for the *minimum* pressure to be expected in accordance with our maxim of creating a worst case scenario i.e. small flow rates. With these input numbers we get a flow rate per overflow valve of $\dot{V} = 1.09 \cdot 10^{-5}\,{}^{m^3}/_s$ or $\dot{V}_{tot} = 6 \cdot \dot{V} = 6.56 \cdot 10^{-5}\,{}^{m^3}/_s$. Compared to initial tests which indicate a maximum expected extrusion flow rate of $3 \cdot 10^{-5}\,{}^{m^3}/_s$, sufficient leeway is present for other influences such as upstream resistance and the 90° deflection in the overflow path.

Calculation of Rheometer Dimensions - Shear Rates

As it is imperative to operate the rheometer at shear rates similar to the ones found in the profile extrusion process, we need to estimate the shear rates for the production case and then apply them to our rheometer. The profile die which we want to examine has an average profile half-width of ${}^d/_2 = r = 1\,mm$ and we know that for Newtonian fluids $v_{max} = 2v_{avg}$ and for highly non-Newtonian fluids $v_{max} \approx v_{avg}$. In initial test trials conducted at $20\,rpm$, we found the extrusion haul-off speed to be $v_{avg} = 0.167\,{}^m/_s$. By making use of Equation (4.52), we can calculate a first guess for the required shear rate range:

$$\dot{\gamma}_{app} = \frac{4\dot{V}}{\pi R^3} = \frac{4v}{R} = 668\,{}^1/_s.$$

By assuming a linear relationship between the extruder rpm and the extrusion velocity v_{avg}, we can expand the shear rate range to the borders of the extruders operational range, in our case five rpm to 20 rpm. If we also allow for lower fluid velocities in smaller cross sections, we end up with a relevant shear rate range of 50 to $1000\,{}^1/_s$. By combining Equations (4.44) and (4.57) we get the expression

$$\dot{\gamma} = \left(\frac{R}{2}\frac{P}{\mu_0 L}\right)^{1/n}, \tag{5.4}$$

which can be used to assess the dimensions needed to cover the aforementioned shear rate range using the rheometer. Using the capillary shear data as presented in Table 5.1 and an assumed *average* pressure drop of $50\,bar$, we can now find a suitable range of dies. Table 5.3 shows the chosen geometries which should,

according to Equation (5.4), cover a range of shear rates from $2.37\,{}^{1}/_{s}$ ($r = 1\,mm$, $l = 5\,mm$) to $7420\,{}^{1}/_{s}$ ($r = 2\,mm$, $l = 2\,mm$). The capillaries are precision drilled with an accuracy of $\pm 0.01\,mm$ and a surface roughness of $R_a = 0.8$. Together

	Die ⌀	
	1 mm	2 mm
l=5 mm	×	×
l=4 mm	×	×
l=3 mm	×	×
l=2 mm	×	×
zero length die	×	×

Table 5.3: Grid of available capillary die dimensions.

with two zero length dies which are chamfered at a 45° angle directly after the die entry in order to gather information about extensional flow into the die, a sufficiently large set of dies is thought to be available.

Calculation of Rheometer Dimensions - Estimation of Residence Time

As part of the requirements for a rheological study under real-life processing conditions, the residence time is of crucial importance, as prolonged residence of the material at high temperature in the die can significantly change its properties due to curing. We start with an estimated extrusion speed of $v = 0.167\,\frac{m}{s}$, thus finding, for a capillary of $2\,mm$ diameter, a flow rate of $\dot{V} = 5.25 \cdot 10^{-7}\,\frac{m}{s}$. The inner flow region of the divided material flow as seen in Figure B.2 in Appendix B has a length of $64\,mm$ and a volume of $4.52 \cdot 10^{-5}\,m^3$ leading to a residence time $t_r = 86\,s$. Together with the fact that curing parameters are typically in the range of several minutes at around 200°C, while in the die we typically find temperatures of 120°C, any significant curing can probably be ruled out. As a complementary technique to ensure exactly defined starting conditions, a purging procedure is introduced, where a capillary with $15\,mm$ diameter is brought into the flow between measurements in order to flush any material with a long residence time.

Calculation of Rheometer Dimensions - Screw Dimensioning

A final requirement for the rheometer is found in the dimensioning of the assembly screws which have to withstand the internal pressure generated by the extruder while connecting the main body of the rheometer to the base. The safety factor

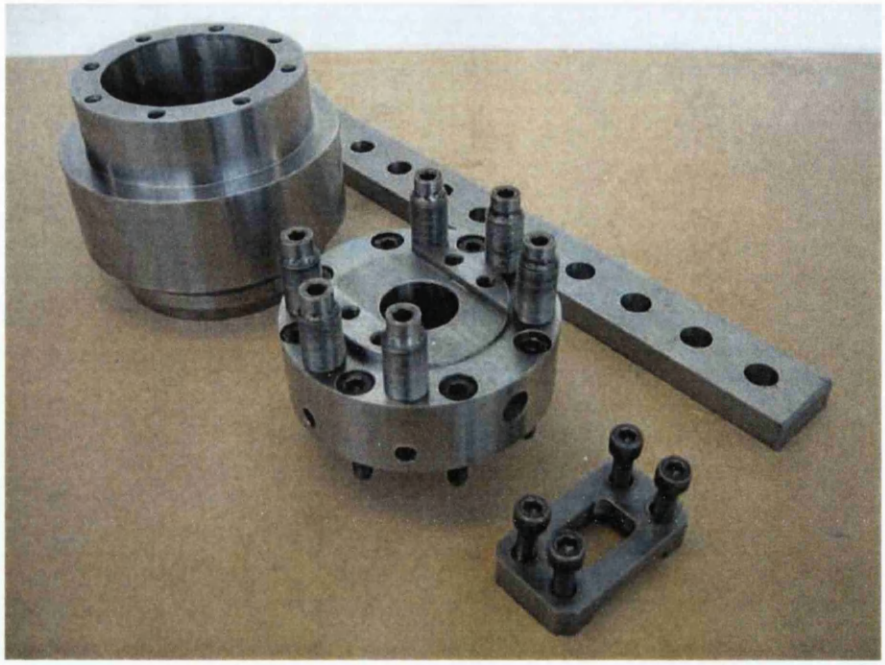

Figure 5.6: The finished rheometer.

relevant in this context is defined by

$$S = \frac{F_{s,tot}}{F_p} = \frac{nF_s}{Pr_p^2\pi}, \tag{5.5}$$

where $n = 8$ is the total number of screws, $F_s = 16\,kN$ is the maximum force to be absorbed by one screw (M8 screws of quality 12.9 are used, see [41]), $P = 120\,bar$ is the maximum pressure to be expected in the rheometer and $r = 40.5\,mm$ is the radius of the wetted flow-path. As a result we find a safety factor of $S = 2.07$ which is generally deemed sufficient for this kind of application.

A view of the finished rheometer in its disassembled state is shown in Figure 5.6, with the main rheometer body in the front and the sliding die bar in the rear.

5.2.3 Sensors

For evaluating the rheological equations derived in Chapter 4, it is necessary to collect a number of process parameters, in particular the pressure drop in the die, the flow rate and the processing temperature of the rubber compound. For pressure and temperature determination a number of industrial sensors are readily available, the choice of which is only limited by the geometrical restrictions of the application. For measuring the compound temperature, a standard thermocouple is sufficient while the pressure transducers situated in the torpedo require special

attention due to space restrictions. The pressure transducer used in the rheometer does not need any special attention as there is enough space for fitting a standard unit. As no sensors for the haul-off speed were installed on the extrusion line, the simplest and most effective solution for flow rate determination was found in simply extruding a precisely timed strip of rubber and weighing it. Together with density calculations a volumetric flow rate is easily obtainable.

Pressure Transducers

The pressure transducers located at points **A** and **B** in the instrumented torpedo (see Figure 5.3) are a miniaturised version of the regular diaphragm device. In the current design, the sensors were `Entran` models of the type `EPB-B01-350B-Z4` with a certified pressure range of up to $350\,bar$ and an excitation of $10\,V$.

The transducer used in the rheometer is an industrial standard produced by `Dynisco` under the designation `DYN-X-3M-6/18` with a maximum pressure of $3,000\,psi = 207\,bar$ and $10\,V$ excitation.

Temperature Sensors

The temperature sensor situated at **C** in Figure 5.3 is a general purpose K-type thermocouple from `Omega` under the designation `HTTC-36-K-116G-1.25` which was used in a grounded configuration.

5.2.4 Experimental Procedure

An illustration of the strategy in conducting the experiments is best given by presenting a detail of a typical data log as seen in Figure 5.7. This detail has been taken from the second rheometer trial as it is exemplary for all important phases of the trial. Cautionary mention has to be made of a drift in the pressure sensors in the torpedo (see Section 5.2.1) which is clearly visible in Figure 5.7 before the extruder is switched on at $t = 520\,s$. Besides this drift we can note the effect of the rheometer body slowly heating up. At $t = 520\,s$ we see a marked pressure spike as the pressure builds up but the temperature is not yet steady. Up to $t = 3123\,s$, the extruder speed is increased in consecutive steps from five via ten and 15 to 20 rpm. The temperature curve follows these steps, ever increasing as the extrusion screw delivers more energy to the rubber compound.

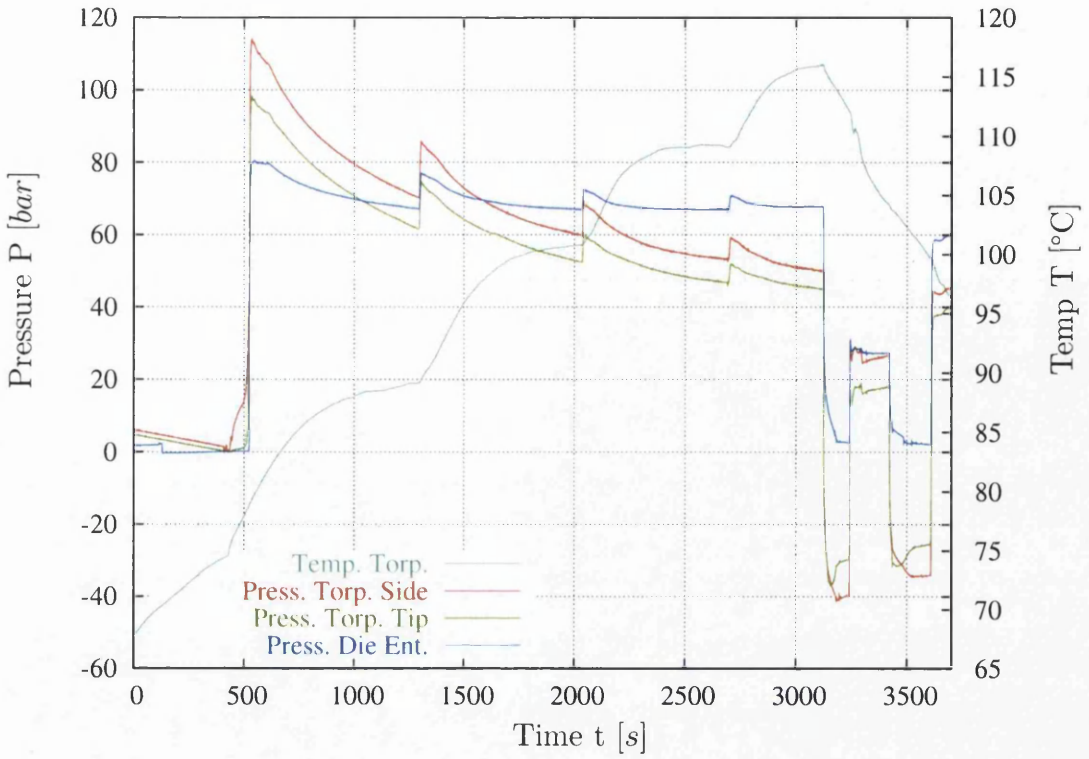

Figure 5.7: Detail of data log of rheometer Trial Nr. 2 including a purging operation.

At $t = 3123\,s$, the extruder is switched off in order to perform a purging operation that allows for well defined experimental conditions - details on the residence time for this rheometer are given in Section 5.2.2. The pressure drops almost back to atmospheric conditions, best observed in the pressure sensor at the die entry which does not show any drift. Now the die bar (see Figure B.4 in Appendix B) is changed to the centre purging hole with a diameter $d = 15\,mm$ and the extruder is switched on at $10\,rpm$ in order to replace any material with a long residence time due to the small die opening with fresh compound. After this operation, the extruder is switched off again and the next die is slid into place. The extruder is set to the desired new speed at $t = 3611\,s$ and the cycle is completed.

In Appendix C, results of the data collected during the rheometer trials is shown. In these tables, the output velocity is calculated from the length of strands of extruded material which was sampled for $120\,s$, $60\,s$ or $30\,s$, depending on the extrusion speed. In order to verify the values thus collected, samples of the purging operation were used to calculate density values in a water bath. By making use of

$$v = \frac{\dot{V}}{A} = \frac{m}{A\rho t} \tag{5.6}$$

for each sample, an alternative method of obtaining velocity data was available.

As no significant deviation from the results of the length measurements was noticed, this procedure was not pursued any further. To ensure correlation between the extrusion velocity and the pressure values in Appendix C, care was taken to extract the pressure data from the log at times corresponding to the velocity sampling.

5.2.5 Results

In this section we want to present the results of the rheometer trials conducted in the course of this study as they are essential to the understanding of the material flow through the die. A number of trials was performed with the rheometer, the design of which is described in detail in Section 5.2.2. The main goal of these trials is the collection of data sets which can be used for the determination of material properties by the inverse method described in detail in Section 5.4. In this light, the need arises for a trial matrix suitable for the use in an automated parameter optimisation. In a first series of trials, a compound named E8246, the contents of which are shown in Figure 2.2, was used to determine process parameters for a capillary of $2\,mm$ diameter and different die lengths under varying processing speeds. Due to a change of material on the production lines, this material became unavailable in the course of the trials leading to the use of a similar material. A schematic view of the experimental layout is given in Figure 5.4. The pressure transducer used in this experiment is located at a 45° angle upstream of the die entry, a distance which is considered enough to avoid the effect of any possibly existing vortex.

Trial Nr. 1

A first trial was conducted using the in-line rheometer and the same rubber compound E8246 used in the trials in Aberystwyth, with the difference that the compound is now complete, including curing agent. The capillary diameter was fixed at $2\,mm$ diameter with five different die lengths ranging from $l = 5\,mm$ to the zero length die, effectively making use of all the dies in the right column of Table 5.3. A detailed description of the available dies is given in Section 5.2.2. Each die was run at two extruder speed settings, 10 and fifteen rpm. The data gathered during this trial is shown in Figure 5.8 with detailed numerical values being represented in the tables in Appendix C.1.

The different plots present in Figure 5.8 show the data gathered from the various

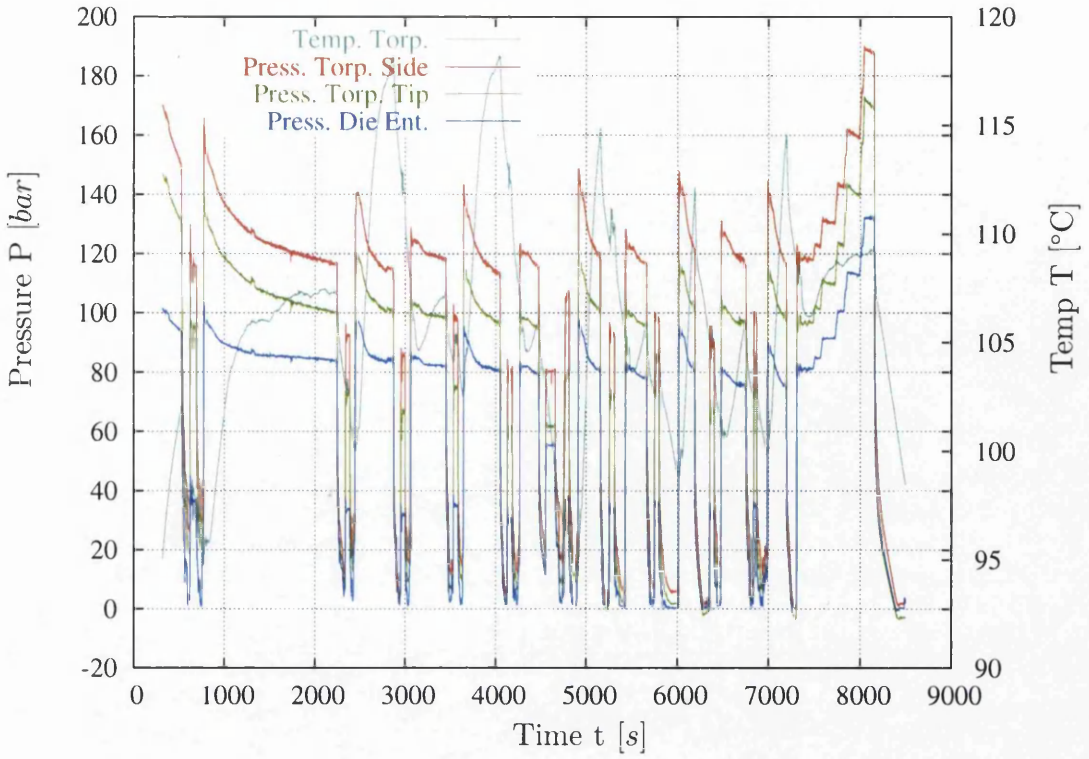

Figure 5.8: Data log of rheometer Trial Nr. 1.

sensors in the torpedo (see Section 5.2.1) plus the rheometrically crucial pressure value just above the die entrance.

One problem which was detected in the first tests of the equipment is a drift in the two ENTRAN pressure sensors presented in Section 5.2.3 which are located in the torpedo. These sensors show a drift which can be evaluated to be 0.649 $^{bar}/_{min}$ by calculating the gradient of the signal under atmospheric pressure conditions. The Dynisco pressure transducer upstream of the die entry on the other hand displays negligible drift.

Another immediate observation is the small amplitude in pressure variation between the different samples. This peculiarity is observed throughout the trials and will be discussed in detail later.

Trial Nr. 2

The second major trial makes use of a rubber of slightly different composition, internally known under the specification E7267, complete with curing agent, as shown in Figure 5.9. A trial matrix composed of four extruder settings (five, ten, 15 and 20 rpm) and four different die lengths (five, four, three *mm* and a zero

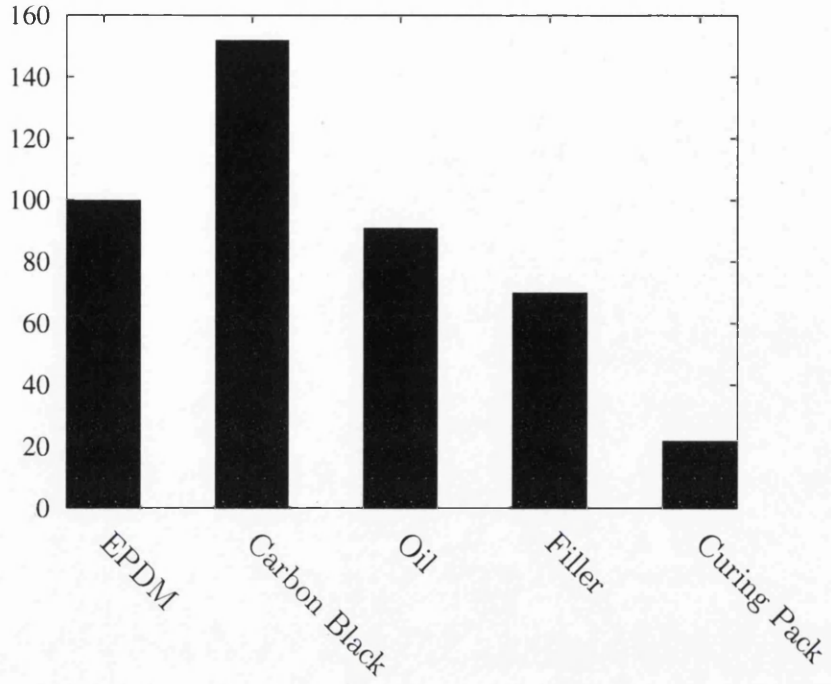

Figure 5.9: Contents of the rubber compound E7267.

length die) was used in this case, leading to 16 different processing parameter combinations. As in the previous trial, the capillary diameter was fixed at $2\,mm$. The data log for this trial is shown in Figure 5.10 and a full summary of the results for this trial is given in Appendix C.2.

A first inspection of the logged data already shows some interesting facts. When switching from lower to higher extrusion speeds (most notably at the start of the extrusion process, $t = 520\,s$), we note characteristic spikes in the pressure drop due to the temperature dependence of the material, an effect also noted by Leblanc [42]. In that work, a stabilisation time of three to four minutes is given, a figure which is estimated at around seven minutes in the present work. In another parallel to Leblanc's work, we register a fairly constant or even slightly decreasing pressure drop as we increase the extrusion velocity.

Looking at the situation after switching of the die orifice to a different length at $t = 3611\,s$ (5 to $4\,mm$), $t = 5246\,s$ (4 to $3\,mm$) and $t = 6862\,s$ ($3\,mm$ to zero length die), we see the reverse effect to that mentioned above in that the material, still being hot from the previous extrusion, cools down while the extruder is already running at a low speed again. As a result we can see the pressure rising slowly as the temperature stabilises and we can conclude that a significant temperature dependence has to exist in the rubber compound, a fact which will prove useful for judging the result of the parameter optimisation in Section 5.4.

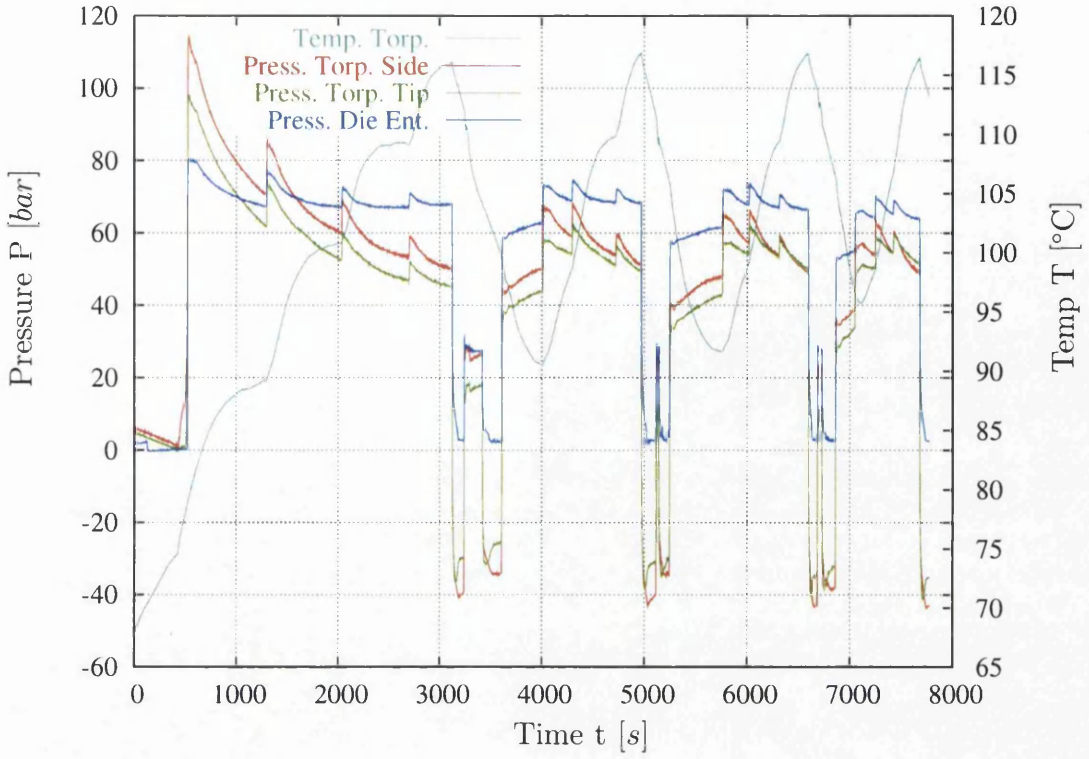

Figure 5.10: Data log of rheometer Trial Nr. 2.

When performing an initial plot of the flow rate $\dot{V}$ versus RPM, as shown in Figure 5.11 we note the non-linearity of the curves for small L/D ratios. This effect is due to differing wall slip situations which might occur in the overflow and the capillary region, deviating temperatures and especially the fact that higher L/D ratios tend to lead to more linear results as entry effects as shown in Figure 4.5 are less marked. While, in contrast with regular rheometers with one capillary orifice, this rheometer has overflow channels that account for the observed non-linearity, this effect is not detrimental in the collection of data points for a material parameter determination as we accurately take an instantaneous snapshot of all the necessary process parameters, i.e. flow rate, pressure as well as the temperature.

In the next step, we consider another plot which produces interesting results as we plot the pressure drop in the capillary die over the L/D ratio for a fixed extruder setting as seen in Figure 5.12. This plot is similar to the so-called Bagley plot with the exception that Bagley uses a constant shear rate instead of the extruder speed under controlled laboratory conditions at a fixed temperature. The deviation for the pressure values for $L/D = 2.0$, $L/D = 1.5$ and $L/D = 0.0$ in the plot for an extrusion velocity of $5\,rpm$ are explainable by the fact that these measurements were the first ones taken after a change of the die capillary (taken at $t = 4000\,s$,

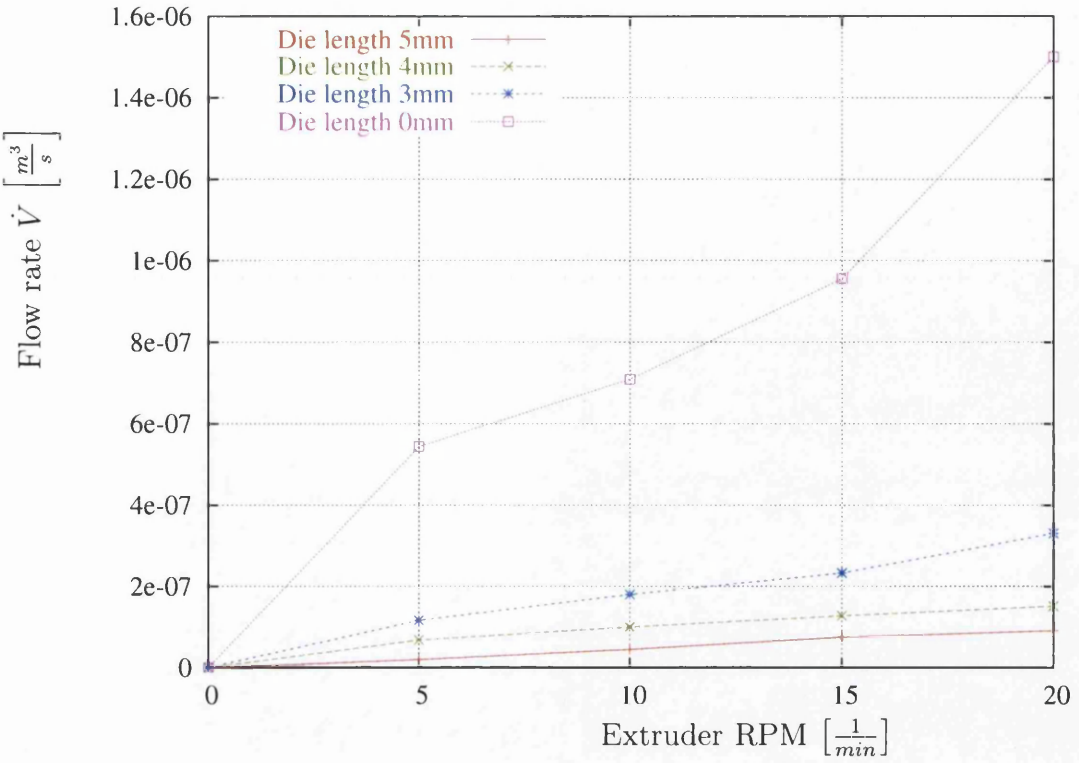

Figure 5.11: RPM versus flow rate $\dot{V}$ - Trial Nr. 2.

$t = 5753\,s$ and $t = 7035\,s$ with regard to Figure 5.10). For these measurements, the temperature has not yet stabilised as it is still falling from the die change, leading to deviating results. The measurement for $^L/_D = 2.5$, taken at $t = 1290\,s$ does not show this effect as it was taken under the same conditions as the rest of the measurements.

Ignoring the obviously inconsistent measurement for $5\,rpm$, we can state that the pressure drop including entry and exit pressure loss (which can be considered to be small compared to the entry one as observed by Leblanc [43]) is almost independent of the extrusion velocity. In fact, for the lower $^L/_D$ ratios we can even note a declining pressure drop as the rpm - and thus the shear rate - increase. Apart from the non-linear effect of the overflow valves, which can be regarded as cosmetic in this context, we can speculate that the constant or declining pressure drop for increasing extrusion velocities is a sign of wall slip even if part of this behaviour has to be attributed to decreasing viscosity due to increased temperatures. Indeed, this observation is backed by the findings of Eisele [44], Jepsen [7] and Leblanc [42] amongst others.

A very useful analysis that is commonly found in the context of material parameter determination is based on the plot of viscosity vs. shear rate as many deductions can be drawn from this plot. Since the data has not been analysed

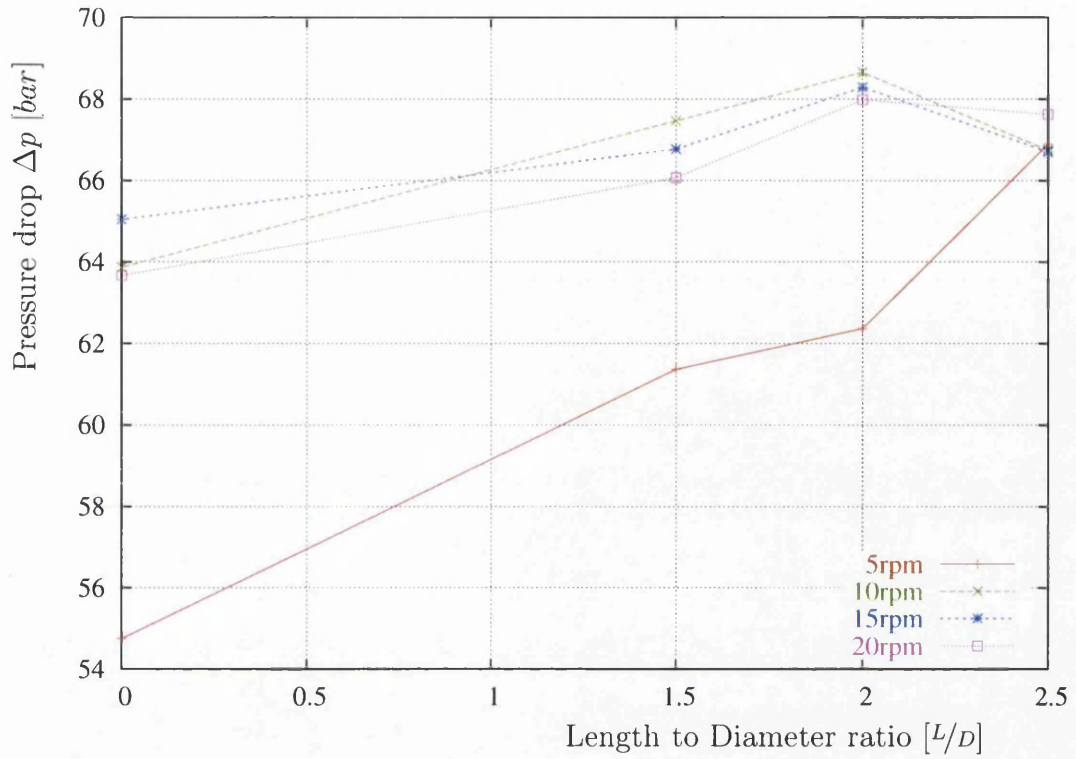

Figure 5.12: Plot of L/D ratio vs. pressure drop - Trial Nr. 2.

yet, it is preferable to use apparent values in the current context. For the present experiment, the results are shown in the lower plot in Figure 5.13 in the form of data points which correspond to the sampling points of the experiment. These data points are subsequently joined by fitting a smoothed spline through them in order to detect any trend in the material behaviour. The apparent shear rate $\dot{\gamma}_{app}$ is calculated according to Equation (4.52) while the apparent viscosity is derived from its definition, Equation (4.59) and the balance of forces (see Equation (4.45)) in the die to result in

$$\eta_{app} = \frac{R\Delta P}{2L}\frac{1}{\dot{\gamma}_{app}}. \tag{5.7}$$

As the temperature dependence is already included in the measured pressure drop, there is no need for a correction of η using the shear temperature coefficient b.

For the sake of clarity, the data is split into groups according to die length $(3, 4, 5\,mm)$, each group including all extrusion velocities for that group. While the results in a specific group are linear in the $\log/\log$-plot to the degree that can be expected in experimental data, there is a noted offset between different groups, a fact which will have to be discussed in detail in a separate paragraph below.

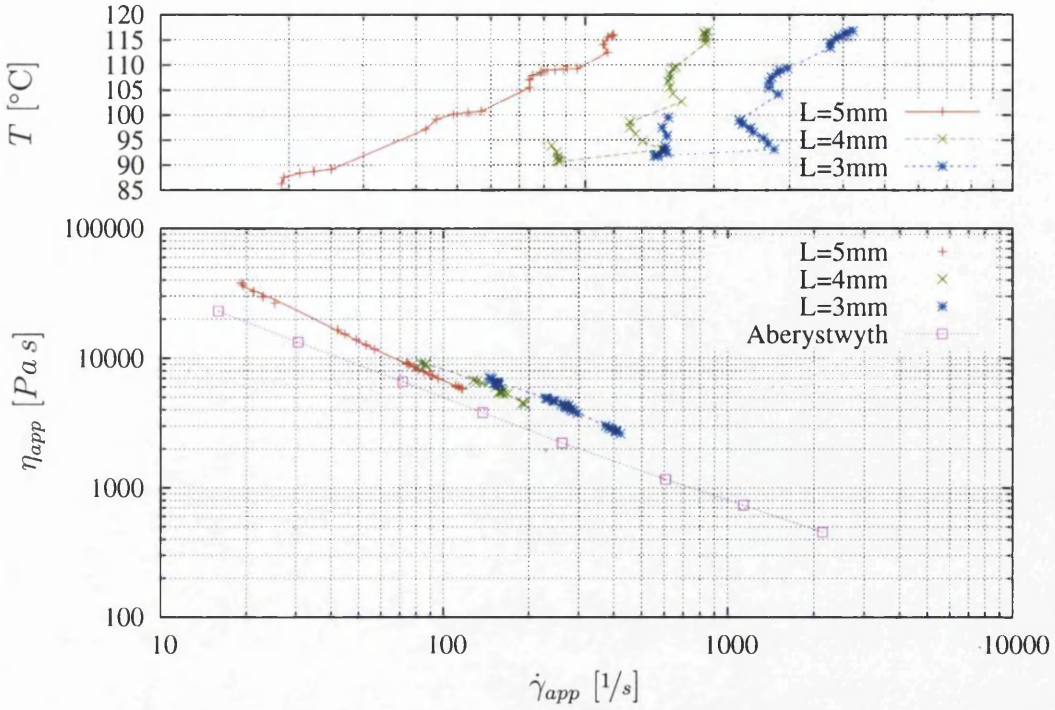

Figure 5.13: Plot of viscosity η_{app} vs. shear rate $\dot{\gamma}_{app}$ and temperature T vs. shear rate - Trial Nr. 2. The curve from Aberystwyth corresponds to the capillary data presented in Figure 5.1.

As a reference for comparison, Figure 5.13 includes the capillary data gathered in Aberystwyth [39] - already shown in Figure 5.1 - which ties in well with the present experiment considering the fact that the results from Aberystwyth were obtained at 60°C and by using a different rubber compound.

Reasons for the Offset in Figure 5.13

In a topic left to clarify, we have to analyse the reasons for the offset between different die lengths in the $\eta_{app} - \dot{\gamma}_{app}$ plot. Observable in the lower plot in Figure 5.13, it has to be attributed to several different phenomena. When looking at the corresponding temperatures in the upper plot in the same Figure, it is readily seen that for $L/D = 4\,mm$ and $L/D = 3\,mm$ the temperatures are not settled to the same degree as for $L/D = 5\,mm$ in addition to the fact that we find different temperatures for different L/D ratios. This circumstance, while not relevant in the parameter optimisation (see Section 5.4), where an instantaneous temperature value is used and an appropriate temperature dependence is introduced, will influence the linearity of the relation between $\dot{\gamma}$ and η.

Another factor in this context is the relationship between the entry pressure drop P_{ent} and the pressure drop in the capillary P_{cap}. While the entry pressure drop for a given shear rate will remain constant when changing the die length, the capillary pressure drop will increase linearly with the die length according to Equation (5.7). The resulting apparent viscosity value will, due to the inclusion of the extensional pressure drop in its calculation, show a certain degree of offset between different $^{L}/_{D}$ ratios.

Finally, differing degrees of wall slip might add to the inconsistency, as various sources claim a dependency of the wall slip velocity v_s on the die length (see e.g. Jepsen [7]). A closer examination of this phenomenon will be undertaken in Section 5.5.3. Due to the influence of these different effects, it proves difficult to determine any dominant mechanism as the cause of the offset. Having established this ambiguity however, we can state that it is not at all *needed* at this point to give a full explanation, as we are dealing with preliminary results due to the fact that the plots in Figure 5.13 are based on a total pressure drop and do not include temperature information. As such, they are only intended to give a rough idea of the material behaviour.

5.3 Profile Trials

In order to assess the accuracy of the numerical simulation of the extrusion process, a need for comparison with actual profiles arises. A procedure for comparing simulation and extrusion under well defined conditions has to be created. In this work an approach was taken where, regarding the extrusion, the cross sectional area in different partitions of the die exit is equated with the flow rate in these partitions. On the numerical side, the exit velocity profile in the aforementioned partitions is used to calculate the flow rate in the partitions by integrating over each of them.

The specification of a suitable die is determined by typical designs found in profile extrusion and by the need to reproduce a number of different flow situations that are known to create difficulties in the extrusion process. Figure 5.14 shows the generic die which was manufactured by our collaborator in Maesteg in response to these design criteria.

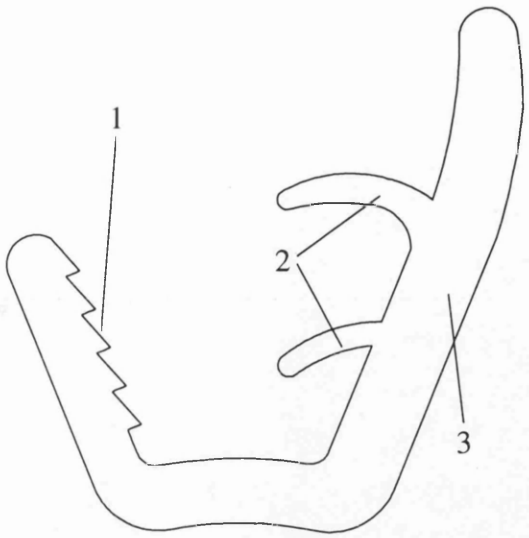

Figure 5.14: Generic extrusion profile displaying typical problem areas - 1) Contours including sharp angles, 2) fine partitions opposed to 3) large partitions.

5.3.1 Experimental Procedure

The general experimental setup is identical with standard layout of an extrusion line as detailed in Section 2.2. In the context of capillary rheometry, the curing line is of reduced interest, as the extrudate is collected directly after it leaves the capillary die for later weighing. Presumably, any transport through the curing ovens on conveyor belts would stretch the fragile rubber strand beyond usability, thus favouring direct collection of the material.

Density measurements for the first and second trial were performed by different methods. For the first trial a rough measurement method was used, by which a sample of the rubber was first weighed and then submerged in water in a measuring cylinder. From the difference in volume and the weight, the density at room temperature was then calculated.

For the second trial a more sophisticated method using a density bottle was employed. This approach also permits the determination of density values at elevated temperatures, a necessity for estimating changes in density due to temperature changes. The use of a water bath for controlled steps in temperature increase did not prove useful as the water in the density bottle started forming gas bubbles from temperatures as low as 50°C due to long residence times while heating up. The occurrence of this phenomenon could not be suppressed to a significant degree by using distilled water or boiling it beforehand. Finally a more practicable approach of taking two measurements - one a room tempera-

ture the other as close to the boiling point as possible was adopted. Preliminaries for this method include weighing the empty bottle, weighing the rubber sample and weighing the bottle filled with water at the desired temperature. Now the sample is submerged in the bottle while ensuring that the water temperature is the same as when weighing the water filled bottle. Weighing again completes the data acquisition stage. The density of the pure water can be determined from the weighed water and a density table (see e.g. [19]), which shows the exact density of water at different temperatures. Now we can calculate the density of the rubber from

$$\rho_s = \frac{m_s}{V_w - \frac{m_{w+s} - m_s}{\rho_w}}, \tag{5.8}$$

where the index s denotes the sample and w the water. The index $w + s$ refers to the weight of the combined water and sample.

The overall flow rate is determined by collecting extrudate samples over an adequate period of time - in the present experiments, sampling times from 20 seconds to one minute are used depending on the extrusion speed. These strips of profile are weighed on a precision scale and the flow rate is subsequently calculated from density, weight and sampling time.

The analysis of the flow rate in different sections of the die is based on a partitioning scheme where the die is subdivided into partitions according to Figure 5.15 a). The cured samples are cut into thin slices in order to scan them on

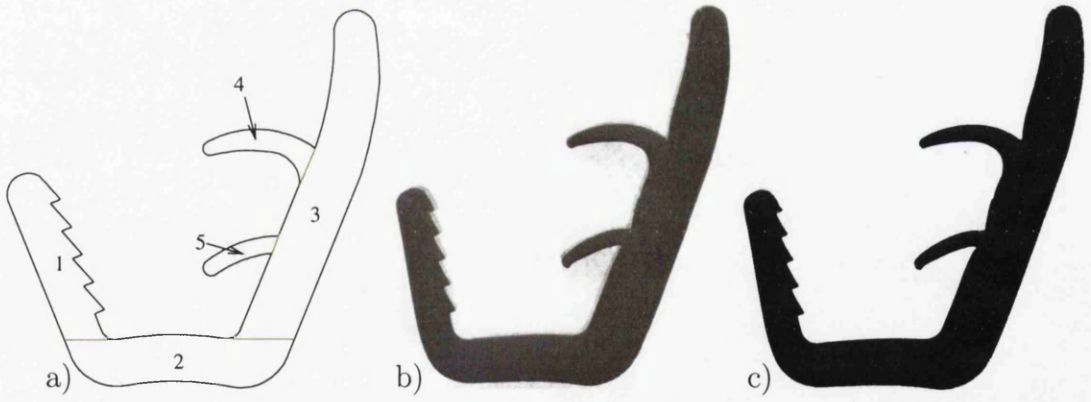

Figure 5.15: a) Partitioning for determination of flow rate in different sections of the die, b) Scanned image of the actual profile cross section in grey-scale and c) Processed image in black and white.

a flatbed scanner. As only percentages will be calculated, the resolution of the scans are not important and in this context 600 dpi were found to be a sufficient resolution to capture an accurate image of the profile. The resulting grey scale images (see Figure 5.15 b)) can be manipulated using standard image processing software to show a black and white image of the scanned profile as presented in

Figure 5.15 c). Setting up the partitions from Figure 5.15 a) in Figure 5.15 c) is achieved by simply generating white lines at the borders between the partitions. A tool for counting the black pixels in an image can then be used to get the number of black pixels in a specific partition after filling all other partitions white. By dividing by the total number of black pixels in the profile, the area percentage of each section with respect to the total can be calculated. Furthermore, these numbers can be seen as an estimate of the flow rate in each section if significant lateral flow is ruled out.

A sampling scheme used to ensure reproducibility was employed which called for three cross section samples being taken for each of the three profile samples at each speed, resulting in a number of scanned profiles equal to nine times the number of investigated extrusion speeds.

5.3.2 Results

Trial Nr. 1

In a first trial, the generic, unoptimised profile was extruded under controlled conditions in order to produce profile samples which could subsequently be used to confirm the accuracy of simulation results. The standard rubber composition E8246 including curing agent was extruded at speeds of ten, 15 and 20 rounds per minute. Section cuts were collected over a period of one minute at ten and 15 rpm, while at 20 rpm a sampling rate of 30 seconds was chosen for practical reasons due to increased material output. The minimum stabilisation time in this trial was over eight minutes. The uncured profile was collected for later flow rate determination as described in Section 5.3.1. Short strips of cured material were collected for analysis of the profile cross section and for density evaluation as the uncured material is not stable enough for these purposes.

A plot of the various data logged in the course of this experiment is shown in Figure 5.16. As in the previous trials, a drift in the pressure sensors located in the torpedo head can be observed, manifesting itself at the beginning of the trial while the extruder is still switched off. An estimate of the drift for this trial results in an average rate of $0.309\,{}^{bar}/_{min}$ at the start of the trial under atmospheric pressure. At $t = 665\,s$ the extruder is started at ten rpm. At $t = 1867\,s$ it is switched to 15 rpm and at $t = 2537$ to 20 rpm.

The raw data for all samples gathered in this trial is tabulated in Appendix D.1. In order to assess the accuracy of the partitioning scheme we have to have a closer

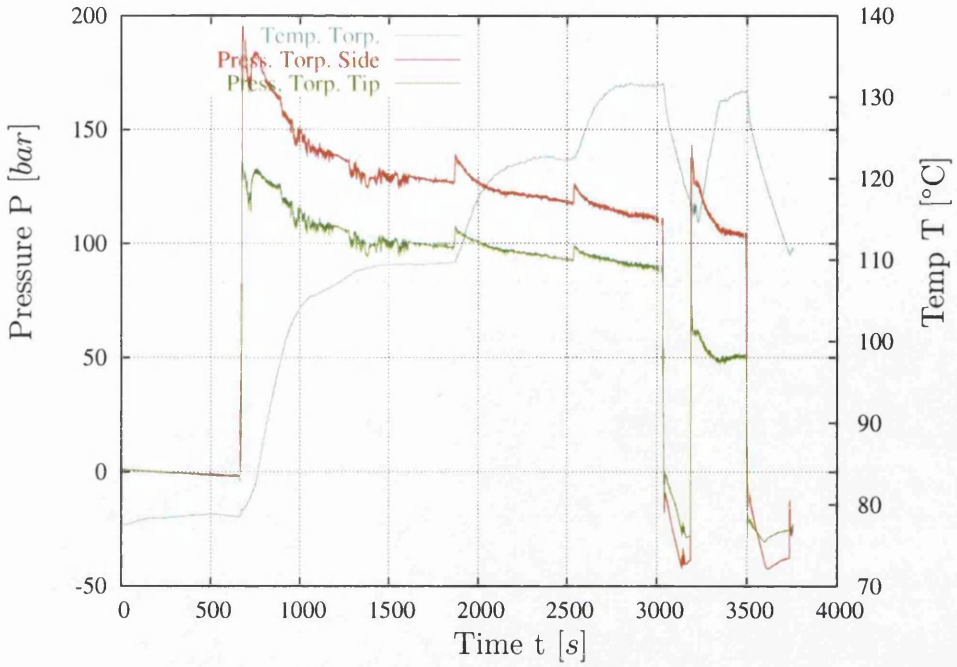

Figure 5.16: Data log of profile trial no. 1.

look at the distribution of the flow rate percentages in each partition as shown in Appendix D.1.2. By making use of the standard deviation

$$s = \sqrt{\frac{\left(\sum_{i=1}^{N} (x_i - \bar{x})^2\right)}{(N-1)}} \tag{5.9}$$

with $\bar{x}$ as the mean value, we can define a relative standard deviation, commonly named *coefficient of variation* as

$$CV = \frac{s}{\bar{x}}. \tag{5.10}$$

thus allowing us to describe the standard deviation independently from the absolute percentage for any given partition. We will now use equation 5.10 to estimate the quality of the partitioning method by applying it to the 15 rpm data for which three samples are present. The results for this operation are shown in Table 5.4. We observe a maximum of $CV_{max} = 0.0387$ in this case and an even lower value of $CV_{max} = 0.0177$ at 20 rpm. We can conclude that even for the worst case, there is a probability of 68.5 % (one standard deviation) that all values for partition one are within a range of $14.62\,\% \pm 0.57\,\%$, i.e. within a variation of 3.9 % of the mean value. As these values are obtained from three scans of the same strip of profile sample in each of the both cases, 15 and 20 rpm, an adequate repeatability is ensured.

Part. ID	$\bar{x}$	s	CV
1	14.6167	0.5662	0.0387
2	27.4367	0.5862	0.0214
3	50.0133	0.2581	0.0052
4	5.0133	0.0850	0.0170
5	2.9233	0.0208	0.0071

Table 5.4: Mean value, standard deviation s and coefficient of variation CV for the 15 rpm data in Appendix D.1.2.

The density measurement for this trial was performed in a water bath at room temperature, resulting in an average density of $\rho = 1.231\,{}^{kg}/_{dm^3}$. As the density at elevated temperatures diverged only within a range of below 5%, the density is not considered to be temperature dependent from now on. The volumetric flow rates were extracted by weighing and measuring the length of the uncured one, respectively two minute samples. Dividing by the density then yields the average volumetric flow rate given in Table 5.5.

Extruder speed $[{}^{1}/_{min}]$	Flow rate $[{}^{m^3}/_{s}]$
10 rpm	$1.34 \cdot 10^{-5}$
15 rpm	$1.99 \cdot 10^{-5}$
20 rpm	$2.62 \cdot 10^{-5}$

Table 5.5: Total volumetric flow rate for the unoptimised die (averaged from the data in Appendix D.1.1).

Table 5.6 shows the results for the three investigated extrusion speeds averaged from the data in Appendix D.1.2. Any deviation from a total of 100 percent is due to the image manipulation algorithm; however, the deviation affects all partitions equally, thus ensuring accurate measurements.

Partition Nr.				
1	2	3	4	5
% of total die exit area				
19.5	25.3	45.7	6.2	3.3
% of total extruded profile cross section at 10 rpm				
15.3	26.7	49.9	5.2	3.0
% of total extruded profile cross section at 15 rpm				
14.6	27.4	50.0	5.0	2.9
% of total extruded profile cross section at 20 rpm				
14.4	27.6	50.1	5.0	2.9

Table 5.6: Percentages of area and flow rate for experiment (averaged from the data in Appendix D.1.2).

On the numerical side, the exit velocity at the outlet of the die can be used to calculate similar values for the simulation. This procedure is described in Section 6.3.1, where the values presented here will be used as a basis for conducting a parametric study for the determination of the wall slip law parameters, Equation (4.67).

Trial Nr. 2

A second trial including an extensive range of samples was conducted with the rubber compound E7267. In contrast to the previous trial, the extrusion velocity was extended up to 30 rpm, leading to sampling points at ten, 15, 20, 25 and 30 rpm. A data log plot of the this trial is shown in Figure 5.17 and tabular data is given in Appendix D.2.

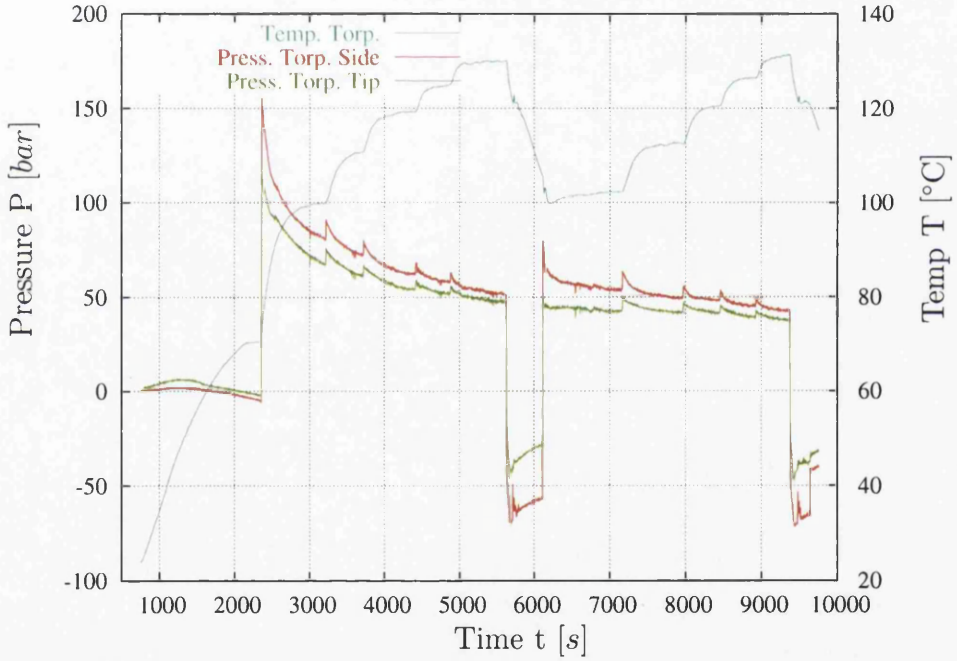

Figure 5.17: Data log of profile trial no. 2.

During this trial, two dies were used, first an unoptimised one with parallel flow channel followed by a manually optimised die. The extruder is switched on at $t = 2359\,s$ at a speed of ten rpm. Extrusion speeds of 15, 20, 25 and 30 rpm follow at $t = 3220\,s$, $t = 3721\,s$, $t = 4420\,s$ and $t = 4880\,s$. At $t = 5629\,s$, the extruder is switched off for a change of die from the unoptimised one to the manually optimised one. At $t = 6114\,s$ the extruder is switched back on, following the same velocity scheme as for the first die. The switches to a higher extrusion speed occur at $t = 7170\,s$, $t = 7970\,s$, $t = 8457\,s$ and $t = 8931\,s$. The process

data relevant to each sampling point is displayed in Appendix D.2.1.

An interesting observation can be made regarding the drift in the pressure sensors when we observe their behaviour up until the extruder is switched on at $t = 2359\,s$ and which was previously thought to be constant. As both sensors are under atmospheric pressure, the drift clearly is temperature dependent as the torpedo head and thus the sensors heat up to the temperature of the cross-head housing at around 70°C. By observing the gradient of the pressure curves we can find the point of zero drift at around $t = 1330\,s$ and at a temperature of 50.0°C.

A preliminary test to verify the consistency of the obtained results is found in the plot of the extrusion speed vs. flow rate as shown in Figure 5.18. The result of

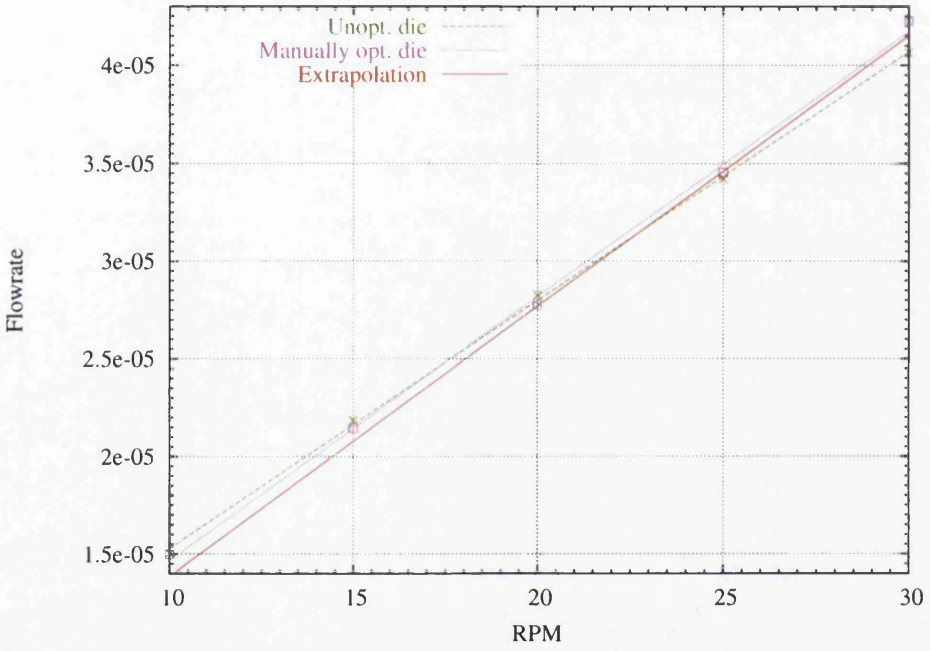

Figure 5.18: Extrusion speed vs. flow rate. The solid line represents an extrapolation from the flow rate values at 30 rpm to the origin.

this analysis is considered to be within satisfactory limits regarding the method of data acquisition for the flow rate values as described in Section 5.3.1.

The profile samples gathered during this trial can be analysed according to the scheme proposed in Section 5.3.1, resulting in flow rate percentages as presented in the table in Appendix D.2.2. This table is found to yield useful information by displaying it in graphical form - see Figure 5.19. Presented in this plot is data for the five partitions defined in Figure 5.15 a). The solid lines specify the nominal goal defined as the exit area of the die for each partition. The dashed lines show the data for the unoptimised die without any converging zone and the dotted

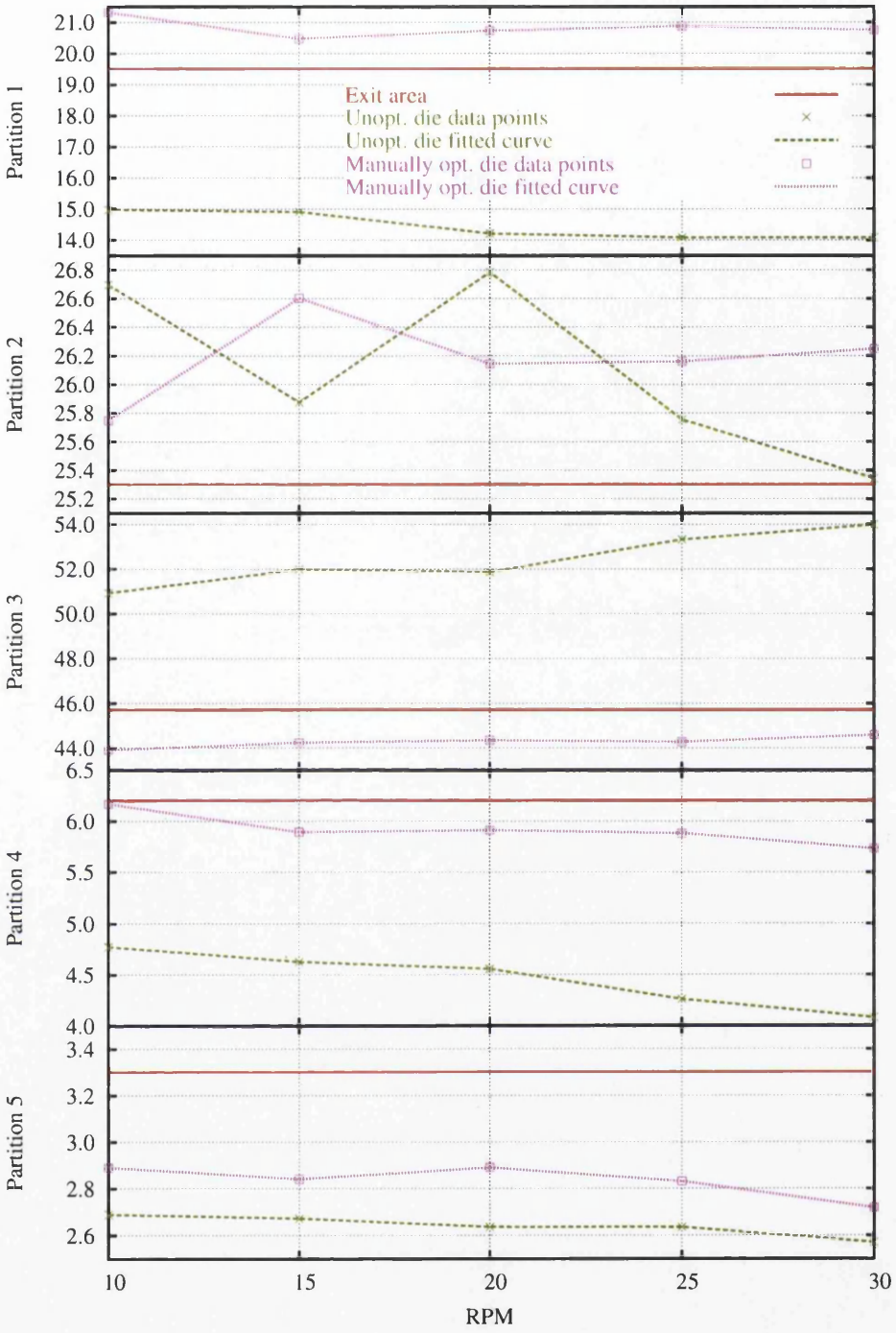

Figure 5.19: Percentage area distribution in different partitions at a range of extrusion speeds.

lines represent the manually optimised die.

Probably the most important aspect of this plot can be seen in the fact that the optimised die is insensitive to changes in extrusion speed compared to the unoptimised one. This fact is very important with respect to production line efficiency as the processing speed will not have to be constrained by profile shape

considerations. Another important observation is an imbalance for the largest partition, number three, when using the unoptimised die. A surplus in flow rate of over 5% is observed at ten rpm which increases over the sampled velocity range to almost 9%. This increase in material flow is taken from all the other partitions. As stated above, the optimised die only shows this defect to a small degree. The small partitions (number four and five) show similar behaviour for both dies, i.e. a loss of flow rate at higher extrusion speeds.

A point of concern which has to be addressed is the apparently inconsistent behaviour of the flow rate in partition two, especially for the unoptimised die. Upon close examination however, the observer will notice the small overall range of the flow rate percentage for this partition. In this light, the seemingly large deviation from the mean value is seen to be less than half a percent.

If we reduce our observations to the straight unoptimised die which displays changes in flow rate over the extrusion speed range more quickly, we can draw a number of conclusions regarding the material behaviour. Several effects which influence the flow rate have to be considered at this point. As higher extrusion speeds lead to an increase in temperature we have to consider this effect along with any changes in wall slip due to higher shear rates.

5.4 Inverse Determination of Material Parameters from In-Line Capillary Rheometry

Classical rheometry for the determination of material parameters is a useful tool in that it allows for relatively easy classification of materials, e.g. by making use of the derivation leading up to the definition of the power law, Equation (4.60). If however, a complex situation like the possibility of wall slip arises, these methods are only applicable in the calculation of combined bulk parameters. As an example we may use the present case where we want to extract shear, extensional and slip parameters from flow rate and pressure drop data extracted from various capillary dies. Due to the need of separation of the different phenomena, we can not apply the methods of classical shear parameter determination for the power law as wall slip may invalidate the result. Thus, new techniques have to be applied in order to gain an insight into the material behaviour of complex materials.

The inverse determination of material parameters is a relatively new field as it is often associated with numerical simulation, see e.g. Gupta [45], who uses a finite element model for optimisation. Apart from widespread application in the anal-

ysis of fluids, inverse determination seems to have found even more application in the analysis of solids. An interesting approach in parameter optimisation has been presented by Nouatin [46], who uses an analytic visco-elastic Phan-Thien-Tanner model with two parameters and an optimisation function based on the comparison between numerical results and birefringence flow patterns. Dal Negro [47] uses an FE-model for comparison with experimental results, but mentions the advantages of the analytical method. If an analytical solution can be obtained for a specific experimental setup, it is the preferred basis for inverse determination as it greatly reduces the computational cost of the optimisation from a complete FE analysis to calculating a single equation. Billon [48] uses a visco-plastic model to describe the blow molding of PET near the glass transition point. Mitsoulis [49] uses the K-BKZ visco-elastic model to determine the extensional viscosity of M1. Regarding solids, an interesting observation can be made, which is also applicable to fluids. Based on FE analysis, Ponthot [50] compares several optimisation algorithms and concludes that the Levenberg-Marquardt algorithm (see Section 5.4.3) yields the best results.

Upon close inspection of the material behaviour for the experiments described in Sections 5.1 and 5.2, a set of parameters can be identified, the theoretical determination of which will be detailed in the following. Due to the complexity of the material, a suitable model will have to deal with shear and extensional aspects of the flow as well as wall slip. As the temperature varies significantly over the range covered by the experiments, temperature will have to figure in each of the three elements of the model. The experiments can be classified in two categories - capillary flow with varying die length and diameter and entry flow into a zero-length die orifice.

The two governing material laws for flow in a capillary (excluding the entry pressure loss P_{ent} which is dealt with separately) are the power law, Equation (4.60), as described in Section 4.3.2 and the wall slip law, equation 4.67, presented in Section 4.4.1. Each of these two laws uses a power law model with two parameters. For the power law we have μ_0 and n, for the wall slip law κ_0 and m. Additionally, each law may incorporate a temperature dependence, b for the shear law and c for the wall slip law, resulting in six parameters describing shear flow and wall slip. Details of the analytic solution will be given in Section 5.4.2.

Regarding extensional flow, several approaches, discussed in Section 4.2.2, are available for inverse parameter determination. In this work, a modified version of Bindings theory [28] as described in Section 4.2.2 is favoured. In addition to the shear law parameters μ_0, n and b, three new parameters for the extensional

power law, μ_e, p and d will feature in the analytic solution, an in-depth discussion of which will be presented in Section 5.4.1.

5.4.1 Analytic Solution of Entry Pressure Loss due to Shear and Elongational Viscosity

In Section 4.2.2 we discussed several possibilities for determining the entry pressure drop into a die orifice. For the actual determination of material parameters, Mackays modification (see [51], [52] and [25]) of Bindings approach [28] (see Equation (5.11)) is the only suitable one as Cogswell assumes a constant elongational viscosity in the converging region.

$$P_{ent} = \frac{16n}{3p}\mu_0 e^{b(T_{ref}-T)}\left(\frac{p+1}{n+1}\right)^2\left(\frac{\mu_e e^{d(T_{ref}-T)} I_{pn}}{\mu_0 e^{b(T_{ref}-T)}}\frac{3n+1}{(4p)^p 4n}\right)^{\frac{1}{p+1}} \left(\frac{3n+1}{4n}\frac{4\dot{V}}{\pi R_0^3}\right)^{\frac{p(n+1)}{p+1}}\left(1-\left(\frac{R}{R_0}\right)^{\frac{3p(n+1)}{p+1}}\right) \tag{5.11}$$

where I_{mn} is defined in Equation (4.19). The above equation can easily be rearranged by solving for $\dot{V}$, a step which will be useful later on in Section 5.4.3,

$$\dot{V} = \frac{n\pi R_0^3}{3n+1}\left[\frac{3p\,(n+1)^2\,P_{ent}}{16n\mu_0 e^{b(T_{ref}-T)}\,(p+1)^2}\cdot \frac{1}{\left(\frac{\mu_e e^{d(T_{ref}-T)} I_{mn}(3n+1)}{\mu_0 e^{b(T_{ref}-T)}(4p)^p 4n}\right)^{\frac{1}{p+1}}\left(1-\left(\frac{R}{R_0}\right)^{\frac{3p(n+1)}{p+1}}\right)}\right]^{\frac{p+1}{p(n+1)}} \tag{5.12}$$

5.4.2 Analytic Solution of Axisymmetric Capillary Flow including Shear-Thinning and Wall Slip

Based on the concepts of fluid mechanics, introduced in Chapter 3, we will now derive an equation that relates pressure drop and flow rate in a capillary die as described in Section 5.2.2 (see Figure 5.20). We will adhere to a similar procedure as presented in Section 4.4.1. In this case we start with the basic equations expressed in terms of cylindrical coordinates (see [53]). The shear stress is defined as

$$\tau_{rz} = \mu\left(\frac{\partial v_z}{\partial r} + \frac{\partial v_r}{\partial z}\right), \tag{5.13}$$

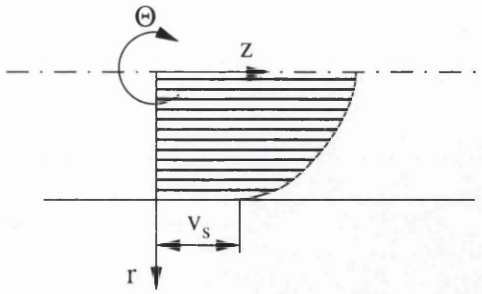

Figure 5.20: Schematic view of axisymmetric capillary flow including wall slip.

which for this special case, assuming developed capillary flow, reduces to

$$\tau_{rz} = \mu \frac{\partial v_z}{\partial r}. \tag{5.14}$$

The general equation of motion for the z-component is given as

$$\rho \left(\frac{\partial v_z}{\partial t} + v_r \frac{\partial v_z}{\partial r} + \frac{v_\Theta}{r} \frac{\partial v_z}{\partial \Theta} + v_z \frac{\partial v_z}{\partial z} \right) =$$
$$-\frac{\partial p}{\partial z} - \left(\frac{1}{r} \frac{\partial}{\partial r} (r \tau_{rz}) + \frac{1}{r} \frac{\partial \tau_{\Theta z}}{\partial \Theta} + \frac{\partial \tau_{zz}}{\partial z} \right) + \rho g_z. \tag{5.15}$$

By discarding non-existent terms for the flow given in Figure 5.20 we can reduce this equation to

$$-\frac{\partial p}{\partial z} = \frac{1}{r} \frac{\partial}{\partial r} (r \tau_{rz}). \tag{5.16}$$

An integration over r yields

$$-\frac{\partial p}{\partial z} \frac{r}{2} = \tau_{rz}. \tag{5.17}$$

The exponential temperature model chosen in Section 4.2 can now be incorporated into Equation (4.57) to yield

$$\tau_{rz} = \mu_0 \left(\left| \frac{\partial v_z}{\partial r} \right| \right)^n e^{b(T_{ref} - T)} \tag{5.18}$$

where n is assumed to be temperature independent as generally assumed by the majority of authors. The same holds for the wall slip index m which will be introduced into the velocity profile shortly. Though there is no theoretical reason for excluding these temperature dependencies, it seems prudent to avoid the excessive introduction of material parameters. Equation (5.18) can now be

be substituted into Equation (5.17) to result in

$$-\frac{\partial p}{\partial z}\frac{r}{2} = \mu_0 \left(\left| \frac{\partial v_z}{\partial r} \right| \right)^n e^{b\left(T_{ref}-T\right)}. \tag{5.19}$$

Keeping in mind that $\partial v_z/\partial r$ is a negative entity, we can remove the absolute value in Equation (5.19) by inserting a minus sign, thus resulting in a velocity distribution of

$$\frac{\partial v_z}{\partial r} = -\left(-\frac{\partial p}{\partial z}\frac{r}{2\mu_0 e^{b\left(T_{ref}-T\right)}} \right)^{\frac{1}{n}}. \tag{5.20}$$

Integrating between r and the outer boundary R

$$\int_r^R \partial v_z = -\left(-\frac{\partial p}{\partial z}\frac{1}{2\mu_0 e^{b\left(T_{ref}-T\right)}} \right)^{\frac{1}{n}} \int_r^R r^{\frac{1}{n}} dr \tag{5.21}$$

results in

$$v_s - v_z = -\frac{n}{n+1}\left(-\frac{\partial p}{\partial z}\frac{1}{2\mu_0 e^{b\left(T_{ref}-T\right)}} \right)^{\frac{1}{n}} \left(R^{\frac{n+1}{n}} - r^{\frac{n+1}{n}} \right). \tag{5.22}$$

Considering the wall slip law

$$\tau_w = \kappa_0 e^{c\left(T_{ref}-T\right)} v_s^m \tag{5.23}$$

we introduce an exponential temperature term in order to accommodate any possible temperature dependence in the wall slip law. The shear stress (Equation (5.17)) can be substituted and we can solve for v_s

$$v_s = \left(-\frac{\partial p}{\partial z}\frac{R}{2\kappa_0 e^{c\left(T_{ref}-T\right)}} \right)^{\frac{1}{m}}. \tag{5.24}$$

Inserting Equation (5.24) into equation 5.22 gives us a model for the velocity distribution in an axisymmetric tube including shear-thinning and wall slip:

$$\begin{aligned} v_z(r) = & \left(-\frac{\partial p}{\partial z}\frac{R}{2\kappa_0 e^{c\left(T_{ref}-T\right)}} \right)^{\frac{1}{m}} + \\ & \frac{n}{n+1}\left(-\frac{\partial p}{\partial z}\frac{1}{2\mu_0 e^{b\left(T_{ref}-T\right)}} \right)^{\frac{1}{n}} \left(R^{\frac{n+1}{n}} - r^{\frac{n+1}{n}} \right). \end{aligned} \tag{5.25}$$

In order to be able to compute the flow rate $\dot{V}$, we need to integrate v_z over the area

$$\dot{V} = \int_0^{2\pi}\int_0^R v_z r \, dr \, d\Theta, \tag{5.26}$$

which in turn results in

$$\dot{V} = \pi \left(-\frac{\partial p}{\partial z} \frac{R}{2\kappa_0 e^{c\left(T_{ref}-T\right)}} \right)^{\frac{1}{m}} R^2 + 2\pi \frac{n}{n+1} \left(-\frac{\partial p}{\partial z} \frac{1}{2\mu_0 e^{b\left(T_{ref}-T\right)}} \right)^{\frac{1}{n}} \left[\left(\frac{1}{2} - \frac{n}{3n+1} \right) R^{\frac{3n+1}{n}} \right]. \quad (5.27)$$

Subject to the assumptions made, Equation (5.27) provides a model which can be fitted to our experimental capillary data by adjusting our set of material parameters μ_0,n, κ_0, m, b and c. Going even one step further, we can now make use of equation 4.34 which allows us to separate the entry pressure loss due to extension from the capillary pressure drop under the assumption that $P_{ent} \gg P_{exit}$ as confirmed by Leblanc [43], leaving us with

$$P_{cap} = P_{tot} - P_{ent}. \quad (5.28)$$

As we really want to use $\partial p = P_{cap}$ in Equation (5.27) and not the total measured pressure drop P_{tot}, we can make use of Equation (5.28) by substituting

$$\partial p = P_{tot} - P_{ent} \quad (5.29)$$

into Equation (5.27), with P_{ent} being calculated from Equation (5.11). Now we can express the relationship between pressure drop and flow rate in a capillary die in its final form

$$\dot{V} = \pi \left(-\frac{P_{tot}-P_{ent}}{L} \frac{R}{2\kappa_0 e^{c\left(T_{ref}-T\right)}} \right)^{\frac{1}{m}} R^2 + 2\pi \frac{n}{n+1} \left(-\frac{P_{tot}-P_{ent}}{L} \frac{1}{2\mu_0 e^{b\left(T_{ref}-T\right)}} \right)^{\frac{1}{n}} \left[\left(\frac{1}{2} - \frac{n}{3n+1} \right) R^{\frac{3n+1}{n}} \right]. \quad (5.30)$$

In an attempt to introduce even better accuracy in fitting experimental data and numerical results, we might consider replacing the wall slip law (Equation (5.23)) with a slightly more complex expression that implements a yield value τ_0' in the same way as found in the Herschel-Bulkeley model for non-Newtonian fluids. This expression of the form

$$\tau_w = \left(\tau_0' + \kappa_0 v_s^m \right) e^{c\left(T_{ref}-T\right)} \quad (5.31)$$

can be used to replace Equation (5.23) to result in a relationship

$$\dot{V} = \pi \left(-\frac{P_{tot}-P_{ent}}{L} \frac{R}{2e^{c\left(T_{ref}-T\right)}\kappa_0} - \frac{\tau_0'}{\kappa_0} \right)^{\frac{1}{m}} R^2 + 2\pi \frac{n}{n+1} \left(-\frac{P_{tot}-P_{ent}}{L} \frac{1}{2\mu_0 e^{b\left(T_{ref}-T\right)}} \right)^{\frac{1}{n}} \left[\left(\frac{1}{2} - \frac{n}{3n+1} \right) R^{\frac{3n+1}{n}} \right]. \quad (5.32)$$

It is left to be determined in the actual inverse material parameter determination if the implementation of Equation (5.31) shows improved results in terms of the objective function compared to Equation (5.23).

5.4.3 Implementation and Determination of Parameters

Equation (5.30) is used to calculate flow rates by making use of the experimental data points listed in Appendix C. Specifically, the pressure drop, die length, die radius and temperature are experimental values inserted into Equation (5.30). Another input set is comprised of the free parameters which are going to be optimised. The objective function for a given set of free parameters μ_0, n, κ_0, m, b and c can be calculated as the sum of the differences in flow rate between experiment and analytical solution for all experimental points

$$f_{obj} = \sum_{i=1}^{nrexp} \text{abs}\left(\dot{V}_{exp,i} - \dot{V}_{ana,i} \right), \quad (5.33)$$

or alternatively

$$f_{obj} = \sum_{i=1}^{nrexp} \left(\dot{V}_{exp,i} - \dot{V}_{ana,i} \right)^2, \quad (5.34)$$

where $\dot{V}_{exp}$ are the experimental flow rates and $\dot{V}_{ana}$ the ones analytically found by applying equation 5.30. For actually finding the optimum parameters, several methods may be used ranging from simple response surface evaluation to a full optimisation making use of a mathematical analysis package which includes curve-fitting techniques. Due to the small computational cost involved in solving the analytical problem, the response surface evaluation proves to be of adequate speed for giving a first impression of the result, but is ultimately inadequate.

Response Surface Evaluation

For this technique the design space is simply subdivided for each design variable forming a grid of data sets which are subsequently inserted in Equation (5.30). If

only two design variables are used, a response surface in three dimensions can be drawn to find an optimum. This graphical approach fails for more design variables in which case the optimum is simply determined by searching for the smallest objective function value. The flow diagram of the implementation used here is given in Figure 5.21. This approach, though simple and robust in its design,

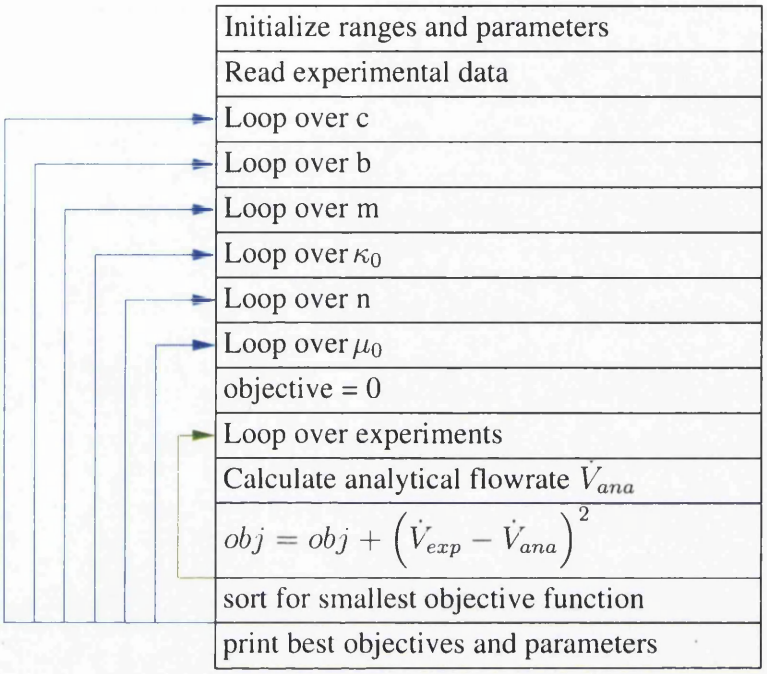

Figure 5.21: Schematic diagram of response surface calculation.

incurs several penalties which make it unsuitable for the current application. A practical drawback is the exponential growth of the computation time as design variables to loop over are added to the problem. While not considerable for two or three variables, a full set of free design variables requires a significant amount of computational time. Depending on the grid size, a response surface calculation including six design variables can easily take several hours to complete even when making use of recent processors.

The second and more important objection to response surface evaluation in this context is inherent in the present problem, not a general fault of the method. During the study of the response surface generated by the scheme as given in Figure 5.21, it soon becomes apparent that the we have to deal with a greatly varying surface gradient. To illustrate this problem, we will use a response surface generated by using two free variables, the power law parameters μ_0 and n, thus enabling us to plot the response surface. The general principle is equally applicable to higher order response surfaces.

The program for the calculation of the response surface is reproduced in Appendix

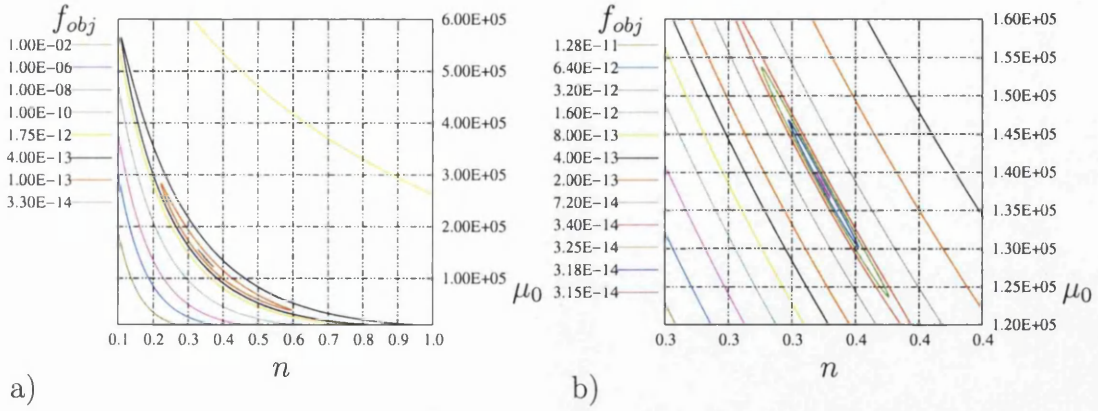

Figure 5.22: Response surface for two free parameters and wall stick a) full relevant parameter range and b) detailed view of minimum.

E.1. Figures 5.22 a) and b) show the isolines for the objective function in Figure 5.21 for fixed wall slip parameters $\kappa_0 = 1 \cdot 10^{39}$, $m = 1.0$ and $c = 0.0$, effectively simulating the classical wall stick condition. While Figure 5.22 a) shows the complete range of considered parameters - $\mu_0 = 10,000$ to $\mu_0 = 600,000$ and $n = 0.1$ to $n = 1.0$ - Figure 5.22 b) gives a detailed view of the optimum. The problem of varying gradients, as noted above, is illustrated very well by these plots. The optimum for Figures 5.22 a) and b), determined to be $f_{obj,min} = 3.149 \cdot 10^{-14}$ is situated in a long non-linear valley which stretches from $n = 0.12$ and $\mu_0 = 560,000$ to $n = 0.85$ and $\mu_0 = 10,000$. On one hand a very shallow section of the response surface stretches to the right of the minimum valley, on the other hand we see a very steep gradient to the left. The cause of this difference in gradients is found in the objective function, Equation (5.34). Analytical flow rates $\dot{V}_{ana}$ that are large compared to the experimental flow rates $\dot{V}_{exp}$ will lead to drastically increased objective function values as seen to the left of the minimum valley, while small analytical flow rates (down to the extremum of $\dot{V}_{ana} = 0$) will result in only slowly increasing objective function values, displayed in the right part of the response surface.

As a result it is possible, by choosing μ_0/n pairs lying at the bottom line of the slowly rising valley, to generate valid parameter pairs which all show acceptable objective function values. It is thus possible to generate pairs where either a high value of μ_0 is associated with with a low n value, or a low μ_0 value with a high n value. It is interesting to note that Massonis [54] examination of compression tests with regard to two variables shows a very similar response surface with a long valley and differing gradients to the sides of the valley.

While not overly expressed for the present two design variables, it is expected that the formation of the bottom of a shallow valley will intensify as more design

variables are added to the optimisation problem, a fact which could lead to numerical problems. A possible countermeasure apart from an increased sampling grid size presents itself in the form of an increase in the number of experimental data points.

For a temperature dependence of $b = 0.0065\,°C^{-1}$ as determined in Section 5.1.2, a reference temperature of 100°C and a grid size of 500 by 500 evaluation points, we find a minimum of the objective function at $\mu_0 = 138,160\,Pa\,s^n$ and $n = 0.350$. These values, while not right *per se*, are not deviating overly from the literature and the results presented in Section 5.1.1 (i.e. $\mu_0 = 210,288\,Pa\,s^n$ and $n = 0.20$), especially as we have to consider the different composition of the material used in Section 5.1.1. Because of the use of a simplified model that excludes wall slip and elongational viscosity as design variables however, we will need to undertake a closer inspection of the wall slip and elongational settings including their temperature dependence.

Least Square Optimisation using the Levenberg-Marquardt Algorithm

A more powerful approach for finding a set of parameters can be found in the basic least squares method (see [55]), expressing the objective as

$$f_{obj} = \sum_{i=1}^{nrexp} \left(\dot{V}_{exp,i} - \dot{V}_{ana,i} \right)^2 \tag{5.35}$$

as introduced in Equation (5.34). As we are dealing with highly non-linear problems in terms of the objective function (which will incorporate Equations (5.12) and (5.30)), the present algorithm uses a more sophisticated variation of the above method, the Levenberg-Marquardt algorithm [4]. This algorithm has already successfully been employed for similar purposes in many other fields (see e.g. [56]).

We start by defining the 'chi-square'

$$\chi^2 = \sum_{i=1}^{N} \left(\frac{y_i - y\left(x_i, \mathbf{a}\right)}{s_i} \right)^2, \tag{5.36}$$

which is a normal least squares error divided by the standard deviation s_i for each data point. The vector $\mathbf{a}$ is composed of the design variables. From the conjugate gradient algorithm, we can borrow the steepest descent method

$$\mathbf{a}_{n+1} = \mathbf{a}_n - \text{constant} \times \nabla\chi^2\left(\mathbf{a}_n\right) \tag{5.37}$$

and assign

$$\delta a_l = constant \times \nabla\chi^2(\mathbf{a}_n). \tag{5.38}$$

By defining

$$\beta_k = -\frac{1}{2}\frac{\partial\chi^2}{\partial a_k}; \quad \alpha_{kl} = \frac{1}{2}\frac{\partial^2\chi^2}{\partial a_k \partial a_l}, \tag{5.39}$$

we are led to a set of linear equations

$$\alpha_{kl}\delta a_l = \beta_k \tag{5.40}$$

that forms the inverse Hessian method. Some consideration of the problem of finding an adequate value for the constant in Equation (5.37) leads to

$$\delta a_l = \frac{1}{\lambda\alpha_{ll}}\nabla\chi^2, \quad \lambda\alpha_{ll}\delta a_l = \nabla\chi^2. \tag{5.41}$$

If we define a new matrix α' with the elements

$$\alpha'_{jj} = \alpha_{jj}(1+\lambda), \quad \alpha'_{jk} = \alpha_{jk}, \tag{5.42}$$

we can now unify equations 5.40 and 5.41 into one equation

$$\alpha'_{kl}\delta a_l = \beta_k, \tag{5.43}$$

which is at the centre of the Levenberg-Marquardt algorithm. The advantage of

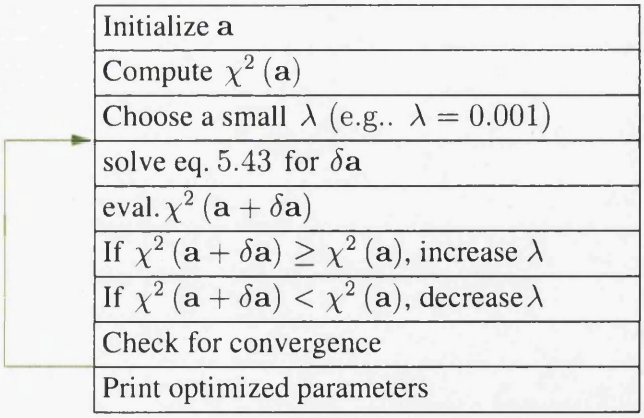

Figure 5.23: The Levenberg-Marquardt least squares algorithm [4].

this procedure is the ability to vary smoothly between equations 5.40 and 5.41 by increasing λ from very small to very large values. Typically, large values of λ are used far from the optimum, with a continuous reduction of λ occurring as the optimum is approached. A schematic overview of the algorithm is given in Figure 5.23. As this algorithm proves to be of considerate stability in practice,

it has become the standard for nonlinear least squares methods. For the actual implementation in the current context, `SciPy` [57], a package of scientific routines implemented in `Python` has been chosen due to its flexibility. Most of the routines supplied in this collection consist of wrapper functions that rely heavily on optimised `Fortran` code as a backend, while retaining the ease of use of `Python` for the interface.

Separate Evaluation of Zero Length and Capillary Equation

As it is certainly conceivable to split the optimisation problem into its two major parts, the entry flow described by Equation (5.12) and the actual flow in the die expressed by Equation (5.30), two optimisation codes have actually been implemented which enable the researcher to manually iterate between the two by passing the results of the first to the second and vice versa. Because full automation is the preferred mode of operation, this approach was abandoned as it soon became clear that a simultaneous optimisation is feasible.

Simultaneous Evaluation of Zero Length and Capillary Equation - two Design Variables

Figure 5.24 shows the data flow in a diagram of the Levenberg-Marquardt method. While starting parameters and convergence criteria have to be specified in the beginning, the algorithm itself can be treated as a black-box once the objective function is defined. A listing of the simultaneous optimisation code employed is

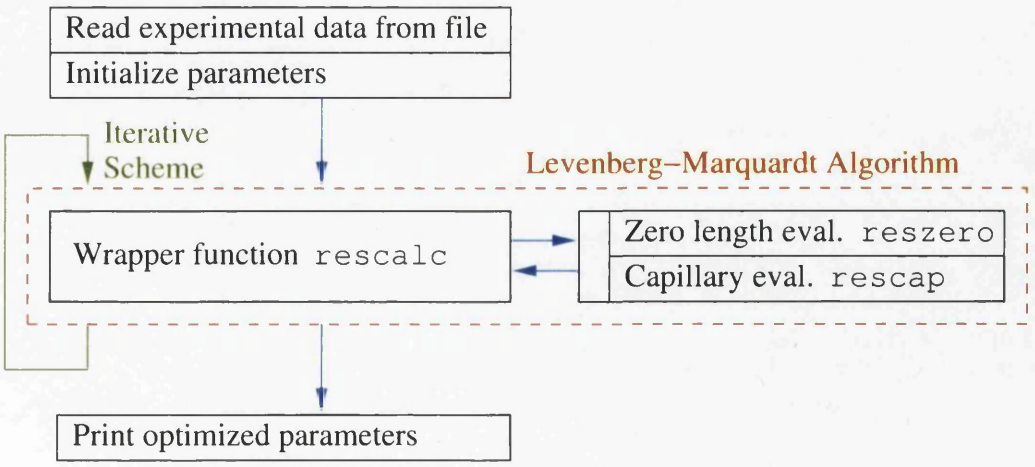

Figure 5.24: Diagram of the implementation of the Levenberg-Marquardt least squares algorithm.

reproduced in Appendix F.1. As the Levenberg-Marquardt method only requires

the definition of a function that returns the error of the result, we can define a wrapper function `rescalc`, which in turn calls two functions (`reszero` and `rescap`) with the current parameter set, in order to evaluate the zero length Equation (5.12) and the enhanced capillary Equation (5.30), which includes the pressure determination introduced in Equation (5.29). The result of the two evaluations are then passed back to `rescalc` where they are combined into one residual vector, used to obtain an updated parameter set.

The data sets chosen for this optimisation - 20 zero length and 66 capillary measurements - are taken from the trial listed in Appendix C.2, as this trial uses the most recent compound. All samples with die lengths of three, four and five mm are used for the capillary equation with all of the zero length results being reserved for the zero length calculation. The appropriate parameters for the evaluation, μ_0, n, b, μ_e, p, d for Equation (5.12), all nine design variables for Equation (5.30), are passed on separately. The results of these function calls can simply be concatenated to form one list which is returned in the list `errcomb`. The set of initial parameters for starting the optimisation loop is chosen according to Table 5.7.

Shear law	$\mu_0 = 100000$	$n = 0.5$	$b = 0.01$
Elongational law	$\mu_e = 100000$	$p = 0.5$	$d = 0.01$
Wall slip law	$\kappa_0 = 100000$	$m = 0.5$	$c = 0.01$

Table 5.7: Initial parameters for simultaneous zero length and capillary optimisation.

In a first optimisation, we want to compare the present algorithm with the response surface evaluation carried out earlier in this chapter, more specifically by using an optimisation with two design variables μ_0 and n, with $b = 0.0065\,{}^1/_{°C}$, fixed wall slip parameters $\kappa_0 = 1 \cdot 10^{39}$, $n = 1.0$ and $c = 0.0$ under exclusion of elongational influences. Due to the ability of direct comparison with the results found for the response surface evaluation and the known, visually verifiable response surface, we have an excellent method to evaluate the Levenberg-Marquardt algorithm at hand. The code shown in Appendix F.1 is modified by omitting the extensional terms and fixing the amount of wall slip at the level described above. The optimum is found after 74 iterations at $\mu_0 = 138,350$ and $n = 0.350$ with an objective function value of $f_{obj} = 3.1486 \cdot 10^{-14}$, a result which shows very good consistency in comparison with the previous results. Direct comparison shows a difference between the response surface method and the Levenberg-Marquardt algorithm of 0.14 % for μ_0 and 0.08 % for n with even these errors being considered as due mostly to the grid structure of the response surface evaluation.

Apart from the possibility to optimise problems with higher degrees of freedom, the Levenberg-Marquardt algorithm also has the considerable advantage of automation, whereas the response surface method requires manual adjustments of the design variable parameter range and the step width in order to find a shallow optimum with acceptable computational cost. Once an overview of the present literature on material parameters has been given in Section 5.5, it will be possible to classify and numerically compare the results for two design variables with the findings of other authors.

In connection with the literature review, it might also prove useful to use the optimisation with two parameters in a loop where the wall slip parameter κ_0 is varied over a range in order to simulate the transition from wall stick to pure wall slip. The resulting shear law parameters μ_0 and n can then be plotted against κ_0 as shown in Figure 5.25. It is interesting to note the rapid transition from wall

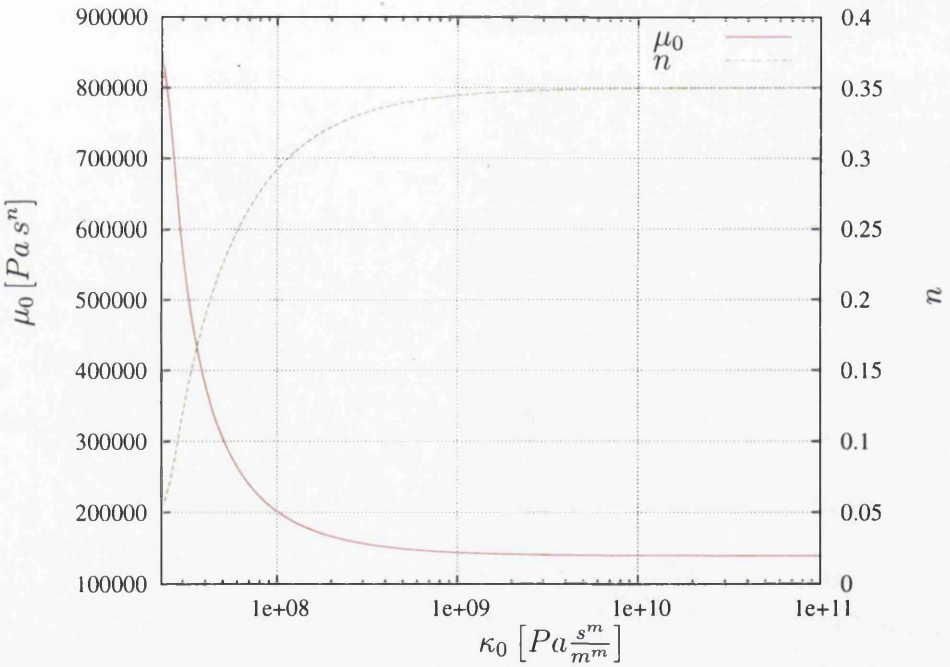

Figure 5.25: Transition of shear law parameters μ_0 and n for varying wall slip law parameter κ_0 and $m = 1.0$.

stick to wall slip, which starts at roughly $1 \cdot 10^{10}$ and results in quickly changing shear parameters towards smaller values of κ_0 and thus more wall slip.

Simultaneous Evaluation of Zero Length and Capillary Equation - Nine Design Variables

In moving on to more challenging optimisation tasks, we now want to consider a full optimisation including all nine design variables. For a prescribed error in the sum of the squares between iterations (ftol $= 1 \cdot 10^{-9}$ in this case), convergence is reached after 1028 iterations. The resulting values for the design variables are shown in Table 5.8. The values for the shear viscosity compare favourably with the available rheology data in the literature and the experiments conducted in Aberystwyth displayed in Table 5.1. It has to be noted however, that a direct comparison in terms of numerical values with the data from Aberystwyth is not possible due to the different compound used in both cases. By evaluating the exponential expression $e^{b(T_{ref}-T)}$ in Equation (5.27) for $b = -0.0047°C^{-1}$, it is evident that the variation over the relevant temperature range of $80°C < T < 120°C$ is in the range of ten percent. The overall quality of the result is estimated

Shear law	$\mu_0 = 175,726.8$	$n = 0.208$	$b = -0.0041$
Elongational law	$\mu_e = 35,172.9$	$p = 0.832$	$d = 0.0420$
Wall slip law	$\kappa_0 = 878,613.5$	$m = 0.027$	$c = 0.0148$

Table 5.8: Result of simultaneous zero length and capillary optimisation with initial parameters taken from Table 5.7 for $T_{ref} = 100°C$.

by using a variation of Equation (5.33) where the zero length and the capillary contribution are simply added together to evaluate the quality of the result,

$$f_{obj} = f_{obj}^{cap} + f_{obj}^{zero} = \sum_{i=1}^{n_{cap}} \frac{\text{abs}\left(\dot{V}_{exp,i}^{cap} - \dot{V}_{ana,i}^{cap}\right)}{\dot{V}_{exp,i}^{cap}} + \sum_{i=1}^{n_{zero}} \frac{\text{abs}\left(\dot{V}_{exp,i}^{zero} - \dot{V}_{ana,i}^{zero}\right)}{\dot{V}_{exp,i}^{zero}} \quad (5.44)$$

or equivalently

$$f_{obj} = f_{obj}^{cap} + f_{obj}^{zero} = \sum_{i=1}^{n_{cap}} \frac{\left(\dot{V}_{exp,i}^{cap} - \dot{V}_{ana,i}^{cap}\right)^2}{\dot{V}_{exp,i}^{cap}} + \sum_{i=1}^{n_{zero}} \frac{\left(\dot{V}_{exp,i}^{zero} - \dot{V}_{ana,i}^{zero}\right)^2}{\dot{V}_{exp,i}^{zero}}, \quad (5.45)$$

where n_{cap} and n_{zero} are the number of capillary and zero length experiments. In the following, we will make use Equation (5.45). In this application, we find a minimum objective of $f_{obj} = 4.362 \cdot 10^{-7}$ of which $1.252 \cdot 10^{-7}$ is contributed by the zero length term and $3.110 \cdot 10^{-7}$ by the capillary term. This discrepancy has to be judged in the light of the fact that in this optimisation 20 zero length and 66 capillary experiments have been included. Thus, we find an average contribution *per experiment* of $f_{obj}^{zero}/n_{zero} = 6.260 \cdot 10^{-9}$ for the zero length data and $f_{obj}^{cap}/n_{cap} = 4.713 \cdot 10^{-9}$ in the capillary case. Given the fact that these numbers represent

absolute data, they do not tell us anything about the accuracy of the solution, so we have to take a closer look at the significance of the statistical error to estimate the value of the present algorithm. First, however, it is advisable to highlight two features of the optimisation process.

When using Equation (5.45) as an indicator for the probability of the result, some thought has to be given to the relative importance of the two data sets. If, at the start of the iterative process, one of the data sets shows a very large deviation from the optimum ($\dot{V}_{exp} \gg \dot{V}_{ana}$ or $\dot{V}_{exp} \ll \dot{V}_{ana}$) with respect to the other set, the weight of the two contributions will be unequally distributed. If we have a look at the fitting of the curve for the first iterative step (starting parameters according to Table 5.7) as shown in Figure 5.26 a), we can see that exactly this situation occurs. At the end of the optimisation, as shown in Figure 5.26 b) (parameters in Table 5.8 are found) however, we note that the there is an adequate fit of the data points to the expected 45° exact solution. This indicates that the Levenberg-Marquardt algorithm is able to to deal with unfavourable starting parameters successfully.

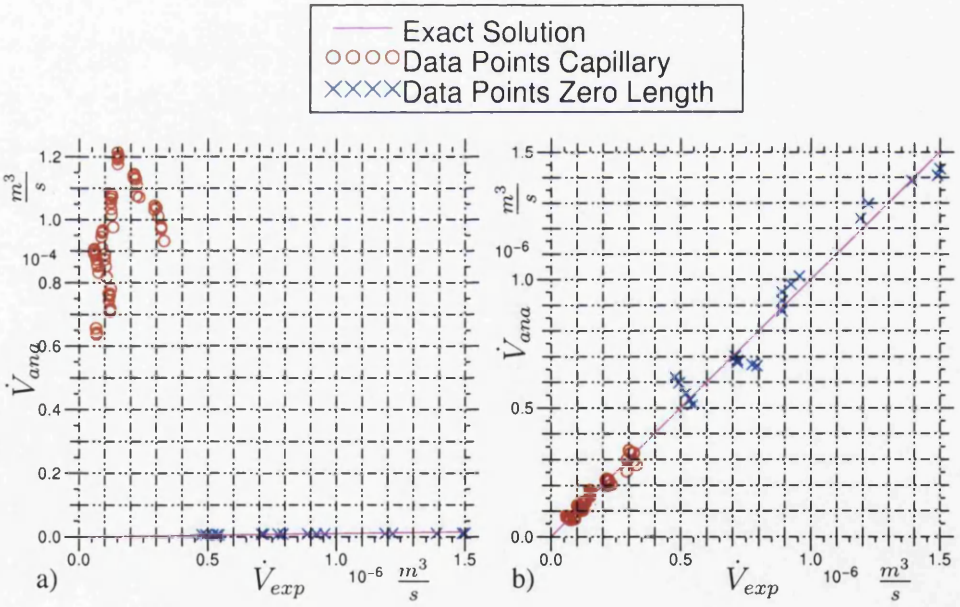

Figure 5.26: Quality of the result in the simultaneous iterative scheme a) after the first iteration, b) after the final iteration.

A more grave objection to the present algorithm is found when changing the initial parameter set, shown in Table 5.7. In the ideal case, a global minimum of the response surface exists and the optimisation algorithm is able to find the correct design variables for this optimum without the risk of diverging towards a local minimum. In the present case, we find that there exists not one unique solution independently of the initial parameters but two. After an extensive variation of

the initial parameters within meaningful boundaries - the results in Table 5.9 were obtained by setting $n = p = m = 0.45$ - we find that the objective function values for the two cases diverge only in the eighth decimal place, basically declaring them of equal validity. Upon close inspection, strong evidence for the existence of only two equally valid solutions is found and it is concluded that the optimisation converges to one of the two solutions regardless of the constellation of the starting parameters. Furthermore, we observe that in comparison with Table 5.8, some of the resulting material parameters are mirrored, i.e. n, b and m, c are exchanged between the shear law and the wall slip law, as documented in Tables 5.8 and 5.9.

Shear law	$\mu_0 = 662,855.5$	$n = 0.027$	$b = 0.0148$
Elongational law	$\mu_e = 7668.1$	$p = 1.149$	$d = 0.0283$
Wall slip law	$\kappa_0 = 1,135,577.4$	$m = 0.208$	$c = -0.0041$

Table 5.9: Result of simultaneous zero length and capillary optimisation with changed initial parameters for $T_{ref} = 100°C$.

When considering Equation (5.30), we can discern the reason for this dual minimum. As this equation is made up of two terms (the wall slip part and the non-Newtonian flow profile part), an equilibrium for $\dot{V}_{ana}$ can be found twice. It can be observed that a reduced bulk shear viscosity is qualitatively similar to increased wall slip. On the other hand, the exchange of the parameters n and m in the two solutions leads to physically different effects. From Equation (4.8), we find for $n \to 0$

$$\eta \approx \frac{\mu_0}{\dot{\gamma}}, \tag{5.46}$$

resulting in a highly shear thinning material, whereas Equation (4.67) yields

$$\tau \approx \kappa_0 \tag{5.47}$$

under the assumption of $m \to 0$, indicating a reduced influence of the wall slip velocity.

Returning to the statistical analysis of the distribution of the optimisation results, we want to choose the second optimum for an analysis, as no decision in favour of one of the two solutions has been taken yet. The distribution of the data points is the same as the one for the first optimum, given in Figure 5.26. As a result, the following statistics diverge only in the fifth decimal place when considering the two different solutions, and thus they are applicable to both optima. Considering Figure 5.26 a) and b), the initial and final errors are presented for the capillary (circles) and for the zero length data (crosses) in a plot of $\dot{V}_{ana}$ vs. $\dot{V}_{exp}$. In the following, a detailed look will be given at the distribution of the data points around the theoretical optimum, represented by the line under 45° ($\dot{V}_{ana} = \dot{V}_{exp}$)

in Figure 5.26 b). The deviation from the optimum is given as $\dot{V}_{ana}/\dot{V}_{exp} - 1$. After the final iteration, for the zero length data, a maximum signed deviation of +28.47% with a mean absolute deviation of 7.29% is found while the capillary case shows a maximum signed deviation of −38.78% and a mean absolute deviation of 16.20%. Continuing from the mean values with a look at the statistical error of the result, we find a standard deviation of $s = 9.84\%$ for the zero length data and $s = 19.41\%$ for the capillary data.

Combining these results into an overall estimate of the quality of the optimisation, we find a mean deviation of 14.13% and a standard deviation of $s = 17.61\%$, meaning that 68% of all sample points are within that error margin. The mean of the combined, signed data is $\overline{\left(\dot{V}_{ana}/\dot{V}_{exp}\right)} = 103.51\%$, which indicates a slight trend towards overestimating the analytical flow rate. Given an unknown uncertainty in the error resulting from the experimental measurements, these numbers can be classified as a result of good quality.

As both of the above solutions are equally valid and no other solution with a comparably small minimum is found, it is left to analyse the reasons for the present shape of the response surface and to decide which one - if any - of the two solutions is the correct one. In order to better qualify these two differing results, we will postpone any analysis until we have presented an overview of literature data which will give us a better basis of understanding for the numerous influences that affect the extrusion of rubber compounds.

5.5 Discussion

As the accuracy of the results presented here is of crucial importance for determining a correct set of material parameters, the findings of this work have to be compared critically with research by other authors. Classification of pure rubber or rubber compounds has been attempted many times but an objective comparison of results is complicated by the facts that pure rubber is of reduced interest to the rubber processing industry and that the formulation of commercial rubber compounds is often commercially confidential. As a consequence, no unified approach for the classification of rubber compounds in the domain of process-related rheology is currently in existence.

Apart from the treatment of non-Newtonian behaviour, the author's approach to dealing with wall slip effects has to be a central point of interest in a comprehensive comparison of studies on rubber rheology. The approach most commonly

found (see e.g. Jepsen [7], Geiger [58, 59], Leblanc [43]) is Mooney's [32], making use of a capillary rheometer, described in Section 4.4.1. This approach is well established and allows for the direct calculation of slip velocities at the wall, though its applicability to highly filled rubber compounds used in production lines has recently been questioned (see Leblanc [43]). We will attempt to quantify wall slip phenomena inherent in rubber compounds as thoroughly as possible in this Section.

In the following, we want to give an overview of the results of the preceding chapter as well as putting it in relation to the work of other authors. By making use of the available literature data together with the rheological work done in the scope of this study, we can compile a list of material parameters for EPDM rubber compounds. This list has to be regarded critically as it incorporates different determination methodologies and includes different operating environments but can nonetheless serve as a basis in a compilation of current rubber compound rheology. We will proceed by using the same classification into shear viscosity, extensional viscosity and wall slip used in Chapter 4 as a means of dividing the vast amount of rubber compound data into more convenient sections. As a preliminary note, it has to be mentioned that it will not be possible to numerically compare any parameters found in the literature with the results from the parameter optimisation due to the fact that no previous author has separated the effects of the three phenomena under review simultaneously. It is thus very difficult to separate the similar influence of shear thinning and wall slip for different authors, as both have the same qualitative influence on the flow rate. As a result, we are limited to drawing general conclusions in the form of trends, e.g. when examining a changed extrusion temperature. Under all circumstances, we will be able to numerically compare the results of the response surface evaluation with two free design variables as there are several examples of analyses in the literature that are concerned with a similar setup.

In a preliminary step, we have to classify the rubber compounds used in the studies under survey with regard to their composition. The two materials under examination in this work are very highly filled (190 pphr and 152 pphr carbon black respectively, see Figures 2.2 and 5.9). Most studies are concerned with rubbers filled to a much lower degree. Exceptions to this rule are found in Geiger's work (see [58] and [59]) with 167 pphr and the studies of Markovic [60], which use a compound with 138 pphr. A complete listing of filler levels encountered in this survey is shown in a summary of this literature review, Table 5.10.

	Shear viscosity (Eq. 4.8)				Ext. visc. (Eq. 4.17)			Wall slip (Eq. 4.67)				Experimental setup					
Source	μ_0	n	b	Shear rate range	μ_e	p	d	κ_0	m	c	Wall stress range	pphr carbon black	T	Rheometer	P	L:D, L/D or W:H:L*	Sep. Phen.
	$\left[\frac{Ns^n}{m^2}\right]$	-	$\left[\frac{1}{°C}\right]$	$\left[\frac{1}{s}\right]$	$\left[\frac{Ns^n}{m^2}\right]$	-	$\left[\frac{1}{°C}\right]$	$\left[\frac{Ns^m}{m^{m+2}}\right]$	-	$\left[\frac{1}{°C}\right]$	$\left[\frac{N}{m^2}\right]$	-	[°C]	-	$\left[\frac{N}{m^2}\right]$	$[mm]$	
Aberyst.† $\lvert\eta^*\rvert$	3,301,704	0.109	0.0065	0.06-600	×	×	×	×	×	×	×	190	60	osc.	n.a.	n.a.	no separation
Aberyst.† η'	725,280	0.024	0.0065	0.06-600	×	×	×	×	×	×	×	190	60	osc.	n.a.	n.a.	no separation
Aberyst.† η_s	210,130	0.2	0.0065	10.0-1,000	×	×	×	×	×	×	×	190	60	cap.	n.a.	25:2.0	no separation
Aberyst.† ext. η_e	×	×	0.0065	10.0-1,000	587,942	0.259	×	×	×	×	×	190	60	cap.	n.a.	25:2.0	no separation
Bassi [10] 1	107,950	0.40	×	$10 - 316$	×	×	×	×	×	×	×	×	120	cap.	n.a.	10, 30, 36	no separation
Bassi [10] 2	131,000	0.32	×	$10 - 1 \cdot 10^3$	×	×	×	×	×	×	×	×	120	cap.	n.a.	10, 30, 36	no separation
Bassi [10] 3	184,400	0.16	×	$10 - 1 \cdot 10^4$	×	×	×	×	×	×	×	×	120	cap.	n.a.	10, 30, 36	no separation
Bassi [10] 4	649,000	0.03	×	$100 - 1 \cdot 10^4$	×	×	×	×	×	×	×	×	120	cap.	n.a.	10, 30, 36	no separation
De Laney [61]	24,500	0.408	×	1.5-2,400	×	×	×	×	×	×	×	×	190	cap.	n.a.	15:1, 50:5	mentions ext.
Geiger [58, 59] inc. lubricant 1a)	104,400	0.115	×	0.3-4,000	×	×	×	$1.116 \cdot 10^6$	0.299	×	$7.0 \cdot 10^4 - 2.0 \cdot 10^5$	167	80	slit	n.a.	15:1.069:55	no separation
Geiger [58, 59] inc. lubricant 1b)	104,400	0.115	×	0.3-4,000	×	×	×	$1.206 \cdot 10^6$	0.296	×	$7.0 \cdot 10^4 - 2.0 \cdot 10^5$	167	80	slit	n.a.	15:1.286:55	no separation
Geiger [58, 59] excl. lubricant 2a)	99,600	0.139	×	130-3,000	×	×	×	$6.268 \cdot 10^5$	0.203	×	$1.0 \cdot 10^5 - 2.0 \cdot 10^5$	167	80	slit	n.a.	15:1.069:55	no separation
Geiger [58, 59] excl. lubricant 2b)	99,600	0.139	×	130-3,000	×	×	×	$6.716 \cdot 10^5$	0.204	×	$1.0 \cdot 10^5 - 2.0 \cdot 10^5$	167	80	slit	n.a.	15:1.286:55	no separation
Holzer [62] 1	59,200	0.182	×	$2 - 10^4$	×	×	×	×	×	×	×	83	150	slit	n.a.	×	no separation
Holzer [62] 2	×	×	×	×	×	×	×	$1.237 \cdot 10^6$	0.567	×	$6.0 \cdot 10^4 - 2.2 \cdot 10^5$	83	96	slit	n.a.	×	no separation

Continued on next page

Table 5.10 – continued from previous page

	Shear viscosity (Eq. 4.8)				Ext. visc. (Eq. 4.17)			Wall slip (Eq. 4.67)				Experimental setup					
Source	μ_0	n	b	Shear rate range	μ_e	p	d	κ_0	m	c	Wall stress range	pphr carbon black	T	Rheometer	P	L:D, L/D or W:H:L*	Sep. Phen.
	$\left[\frac{Ns^n}{m^2}\right]$	-	$\left[\frac{1}{°C}\right]$	$\left[\frac{1}{s}\right]$	$\left[\frac{Ns^n}{m^2}\right]$	-	$\left[\frac{1}{°C}\right]$	$\left[\frac{Ns^m}{m^{m+2}}\right]$	-	$\left[\frac{1}{°C}\right]$	$\left[\frac{N}{m^2}\right]$	-	[°C]	-	$[\frac{N}{m^2}]$	$[mm]$	
Holzer [62] 3	×	×	×	×	×	×	×	$3.800 \cdot 10^5$	0.398	×	$6.0 \cdot 10^4 - 2.2 \cdot 10^5$	83	130	slit	n.a.	×	no separation
Holzer [62] 4	×	×	×	×	×	×	×	$2.562 \cdot 10^5$	0.315	×	$6.0 \cdot 10^4 - 2.2 \cdot 10^5$	83	169	slit	n.a.	×	no separation
Holzer [62] 5	×	×	×	×	×	×	×	$1.225 \cdot 10^6$	0.480	×	$6.0 \cdot 10^4 - 2.2 \cdot 10^5$	83	100	slit	n.a.	×	no separation
Jepsen [7]	×	×	×	0.1-1,000	×	×	×	×	×	×	×	45	100	cap.	n.a.	20:1.0, 20:2.0	no separation
Jepsen [7]	×	×	×	×	×	×	×	$6.161 \cdot 10^7$	0.641	×	$1.0 \cdot 10^5 - 2.0 \cdot 10^5$	25	100	cap.	n.a.	30	no separation
Jepsen [7]	×	×	×	×	×	×	×	$1.481 \cdot 10^{10}$	1.313	×	$2.0 \cdot 10^5 - 3.0 \cdot 10^5$	25	120	cap.	n.a.	30	no separation
Jepsen [7]	×	×	×	×	×	×	×	$1.809 \cdot 10^{12}$	1.918	×	$2.5 \cdot 10^5 - 3.5 \cdot 10^5$	25	140	cap.	n.a.	30	no separation
Leblanc [42]	×	×	×	×	×	×	×	×	×	×	×	60	100	cap.	n.a.	1	mentions slip
Leblanc [43]	×	×	×	×	×	×	×	×	×	×	×	30	100	cap.	n.a.	2, 6, 10, 20	mentions slip
Malkin [63] (SBR)	×	×	×	×	×	×	×	$2.070 \cdot 10^6$	0.213	×	$4.75 \cdot 10^5 - 5.25 \cdot 10^5$	55	70	cap.	n.a.	24.3:1.13, 46.8:1.13	no separation
Malkin [63] (SBR)	×	×	×	×	×	×	×	$1.289 \cdot 10^7$	0.407	×	$4.75 \cdot 10^5 - 5.25 \cdot 10^5$	55	70	cap.	n.a.	29.7:1.5, 63.0:1.5	no separation
Markovic [60] S1	75,800	0.22	×	61-1,226	×	×	×	×	×	×	×	138	100	cap.	n.a.	30:1.0	no separation
Markovic [60] S2	72,900	0.23	×	61-1,226	×	×	×	×	×	×	×	138	100	cap.	n.a.	30:1.0	no separation
Markovic [60] S3	62,500	0.26	×	61-1,226	×	×	×	×	×	×	×	138	100	cap.	n.a.	30:1.0	no separation
Markovic [60] S4	73,600	0.23	×	61-1,226	×	×	×	×	×	×	×	138	100	cap.	n.a.	30:1.0	no separation

Continued on next page

Table 5.10 – continued from previous page

	Shear viscosity (Eq. 4.8)				Ext. visc. (Eq. 4.17)			Wall slip (Eq. 4.67)				Experimental setup					
Source	μ_0	n	b	Shear rate range	μ_e	p	d	κ_0	m	c	Wall stress range	pphr carbon black	T	Rheometer	P	L:D, L/D or W:H:L*	Sep. Phen.
	$[\frac{Ns^n}{m^2}]$	-	$[\frac{1}{°C}]$	$[\frac{1}{s}]$	$[\frac{Ns^n}{m^2}]$	-	$[\frac{1}{°C}]$	$[\frac{Ns^m}{m^{m+2}}]$	-	$[\frac{1}{°C}]$	$[\frac{N}{m^2}]$	-	[°C]	-	$[\frac{N}{m^2}]$	$[mm]$	
Montes [64] 1, SBR	52,900	0.36	×	0.03-2.5	×	×	×	×	×	×	×	11	100	osc.	$64.0 \cdot 10^5$, $11.0 \cdot 10^5$	n.a.	mentions slip
Montes [64] 2, SBR	75,150	0.31	×	0.03-2.5	×	×	×	×	×	×	×	25	100	osc.	$64.0 \cdot 10^5$, $11.0 \cdot 10^5$	n.a.	mentions slip
Montes [64] 3, SBR	24,060	0.24	×	0.03-2.5	×	×	×	×	×	×	×	25	100	osc.	0	n.a.	mentions slip
Montes [64] 4, PTT	105,950	0.25	×	0.03-2.5	×	×	×	×	×	×	×	25	44	osc.	$64.0 \cdot 10^5$	n.a.	mentions slip
Montes [64] 5, PTT	45,500	0.28	×	0.03-2.5	×	×	×	×	×	×	×	25	60	osc.	$64.0 \cdot 10^5$	n.a.	mentions slip
Montes [64] 6, PTT	26,650	0.29	×	0.03-2.5	×	×	×	×	×	×	×	25	100	osc.	$64.0 \cdot 10^5$	n.a.	mentions slip
Osanaiye [6]	125,990	0.2	×	$5 \cdot 10^{-7}$ – $5 \cdot 10^3$	×	×	×	×	×	×	×	100	100	cap./osc.	n.a.	7.5:1.5, 15:1.5, 30:1.5	no separation
Song [65]	176,000	0.172	×	0.04-300	×	×	×	×	×	×	×	25	100	cap./osc.	n.a.	7.5:1.5, 15:1.5, 30:1.5	mentions slip
Turner [66] 1	132,470	0.299	×	0.1-10,000	×	×	×	×	×	×	×	filled	100	osc.	×	n.a.	no separation
Turner [66] 2	×	×	×	×	×	×	×	$2.682 \cdot 10^6$	0.417	×	$3.0 \cdot 10^4$ – $5.0 \cdot 10^5$	filled	40	osc.	×	n.a.	n.a.
Turner [66] 3	×	×	×	×	×	×	×	$1,305 \cdot 10^6$	0.353	×	$3.0 \cdot 10^4$ – $5.0 \cdot 10^5$	filled	60	osc.	×	n.a.	n.a.
Turner [66] 4	×	×	×	×	×	×	×	$6.930 \cdot 10^5$	0.289	×	$3.0 \cdot 10^4$ – $5.0 \cdot 10^5$	filled	80	osc.	×	n.a.	n.a.
Turner [66] 5	×	×	×	×	×	×	×	$5.992 \cdot 10^5$	0.302	×	$3.0 \cdot 10^4$ – $5.0 \cdot 10^5$	filled	100	osc.	×	n.a.	n.a.
Turner [66] 6	×	×	×	×	×	×	×	$5.386 \cdot 10^5$	0.312	×	$3.0 \cdot 10^4$ – $5.0 \cdot 10^5$	filled	120	osc.	×	n.a.	n.a.

Continued on next page

Table 5.10 – continued from previous page

	Shear viscosity (Eq. 4.8)				Ext. visc. (Eq. 4.17)			Wall slip (Eq. 4.67)				Experimental setup					
Source	μ_0	n	b	Shear rate range	μ_e	p	d	κ_0	m	c	Wall stress range	pphr carbon black	T	Rheometer	P	L:D, L/D or W:H:L*	Sep. Phen.
	$\left[\frac{N s^n}{m^2}\right]$	-	$\left[\frac{1}{°C}\right]$	$\left[\frac{1}{s}\right]$	$\left[\frac{N s^n}{m^2}\right]$	-	$\left[\frac{1}{°C}\right]$	$\left[\frac{N s^m}{m^{m+2}}\right]$	-	$\left[\frac{1}{°C}\right]$	$\left[\frac{N}{m^2}\right]$	-	[°C]	-	$[\frac{N}{m^2}]$	$[mm]$	
Swansea opt. inc. two param.	138,350	0.35	0.0065	20-420	×	×	×	$1 \cdot 10^{39}$‡	1.0‡	0.000‡	n.a.	152	100	cap.	n.a.	$\infty - 5:1$	n.a.
Swansea opt. inc. nine param. (Table 5.8)	175,727	0.208	-0.0041	20-420	35,173	0.832	0.0042	878,614	0.027	0.0148	n.a.	152	100	cap.	n.a.	$\infty - 5:1$	✓
Swansea opt. inc. nine param. (Table 5.9)	662,856	0.027	0.0148	20-420	7,668	1.149	0.0283	1,135,577	0.208	-0.0041	n.a.	152	100	cap.	n.a.	$\infty - 5:1$	✓

Table 5.10: Summary of EPDM rubber compound material parameters by different authors. '×' denotes an entry which is not available in the respective source. Under the column 'Rheometer', 'cap.' stands for a capillary die, 'slit' for a slit die and 'osc.' for an oscillatory instrument. The entry for P is only valid for oscillatory rheometers under external pressure, as the pressure in capillary dies is determined by the applied extrusion rate. The column 'Sep. Phen.' shows the author's treatment of the interaction between the different phenomena; while 'no separation' represents no separation of wall slip and shear viscosity, a mentioning of the various possibilities without separation is noted by 'mentions...' and a full separation is pointed out by '✓.

*Die dimensions in the format available in the literature. Either L:D (length, diameter), L/D (length to diameter ratio) for capillary dies or W:H:L (width, height, length) for slit dies

†The compound used in Aberystwyth contains no curing agent

‡Parameters fixed to simulate wall stick

Table 5.10 clearly reinforces the view that no concurrent evaluation of all nine possible material parameters is in existence, partly due to the difficulty of a simultaneous determination of all the required data in an experiment. If we try to conceive an experiment for that purpose, it is easily seen that the determination of the extensional viscosity requires a fundamentally different experimental procedure compared to capillary experiments. Once this obstacle has been removed, we are still left with the problem that it proves very difficult to determine wall slip velocities under exclusion of shear thinning effects and vice versa under the condition that both physical effects are to be determined simultaneously.

5.5.1 Shear Viscosity

The field of shear viscosity determination is certainly the one under closest examination due to the fact that experiments for material classification are easily designed from simple shear flows in oscillatory or capillary rheometers and that shear flow was historically considered to be the dominant mode of material flow in a majority of industrial applications. As stated previously, care has to be taken in comparing oscillatory with capillary data, as oscillatory rheometry might or might not exhibit wall slip, depending on the amplitude of the oscillation and the surface of the rheometer discs. Capillary rheometry on the other hand, especially if one is working with highly filled materials, is most certainly influenced by wall slip. In Figure 5.27, a summary of material from different authors regarding shear power law parameters is presented. The power law index n is plotted against the fluid consistency μ_0 to gain an overview of the range of parameters present. This graph is based on the present literature review, details of which are found in Table 5.10.

While Figure 5.27 shows an agreement between Bassi's results and the parameter optimisation values from Table 5.9, these results have to be seen as coincidental, as all of Bassi's data was gathered over arbitrary shear rate ranges from a plot. Changing these ranges will seamlessly change the parameter pairs between the three points given here. The oscillatory data for η' from Aberystwyth on the other hand is very interesting, as it proves very similar to the parameter optimisation, considering that two different materials (see Tables 2.2 and 5.9) have been used. The reason for this similarity between the experimental rheometrical method on the one hand and the material parameter optimisation on the other is clearly found in the probable absence of wall slip (due to small strains below 1 %) for the oscillatory rheometer and the fact that wall slip and shear behaviour are separated in the optimisation process. Furthermore, the comparison is based on

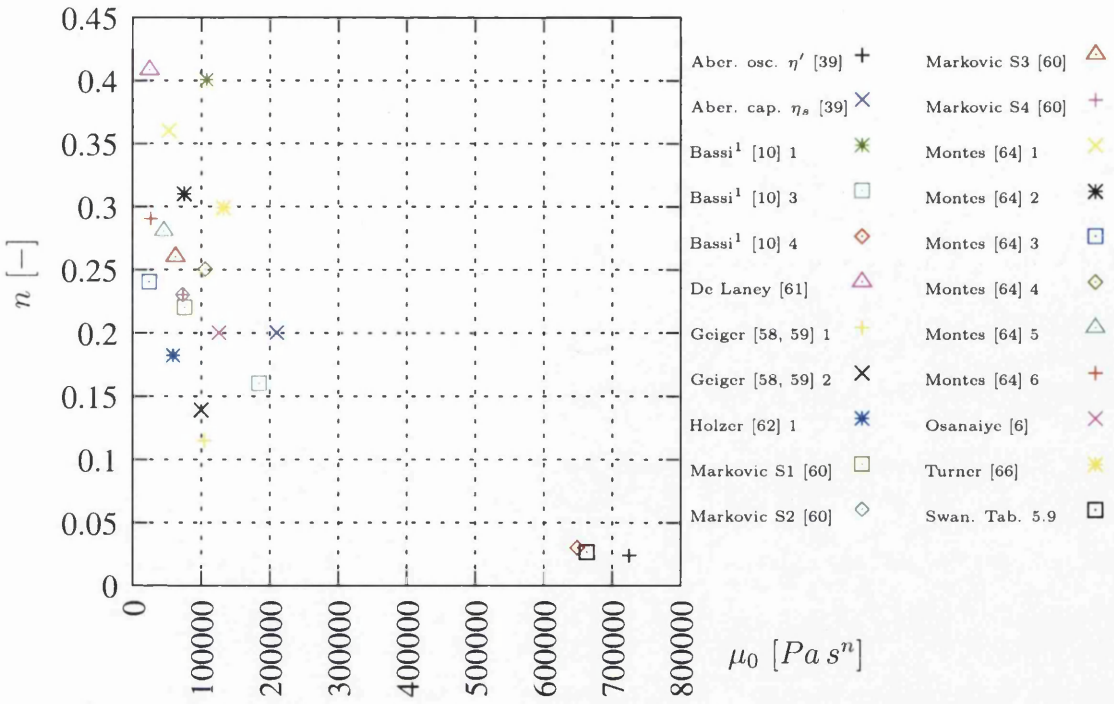

Figure 5.27: Summary of EPDM rubber compound material parameters by different authors at various temperatures (for details see Table 5.10).

[1]The values from Bassi's work present in this graph are determined over several different shear rate ranges, see also Table 5.11

the fact that both η' and the parameter optimisation process do not take into consideration elastic effects.

When judging the literature data, it is necessary to keep in mind that the various authors have used a wide range of experiments and parameters, thus not enabling us to draw direct conclusions. A closer look is needed for classifying the results of this work within the wider frame of contemporary rubber rheology.

Viscosity vs. Shear Rate and Shear Stress

An important feature of many studies on rubber rheology is the double logarithmic viscosity vs. shear rate plot, as it allows for direct extraction of power law parameters. Generally, results can be divided into two classes - either showing constant material parameters and thus a linear plot (at least over the relevant shear rate range, in this case roughly $1\,{}^1/_s$ to $1,000\,{}^1/_s$) or a non-linear plot due to various reasons which will have to be discussed in the following.

A majority of authors (see e.g. Osanaiye [6], Holzer [62], Geiger [58, 59], De Laney [61]) give an indication of constant material parameters, a view which is

consolidated by the rheometrical experiments detailed in Section 5.2, shown in Figure 5.13. For the present investigation, especially the longest die ($L = 5\,mm$) exhibits a very good linearity, this die length also bearing the closest resemblance to the profile extrusion die with regard to geometrical dimensions.

Another argument for constant material parameters is given by the work done by Couch and Binding [39] in the course of this project, reinforcing the expectation of a linear relationship between $\dot{\gamma}$ and η, as can be easily judged from Figure 5.1. The authors of that report use shear rates ranging from $0.006\,{}^1/_s$ to $600\,{}^1/_s$ in the oscillatory case and $10\,{}^1/_s$ to $1,000\,{}^1/_s$ in the capillary case as already mentioned in Table 5.10.

As an illustration for a non-linear plot, we want to cite Bassi's work [10], which shows a varying gradient in the viscosity vs. shear rate plot as shown in Table 5.11. Over the presented shear rate range we observe power law indices from a

$\dot{\gamma}$ range $[{}^1/_s]$	$\mu_0\ [Pa\,s^n]$	n
10-300	108,000	0.40
10-1,000	131,000	0.32
10-10,000	184,000	0.16
100-10,000	649,000	0.03

Table 5.11: Change in shear viscosity power law parameters at different shear rates as extracted from Bassi [10] at $T = 120°C$ (digitised from graph and power law fitted).

moderate $n = 0.40$ at low shear rates to extreme shear thinning with $n = 0.03$ at high shear rates. While it is conceivable that the power law shows variable parameters μ_0 and n, it is more plausible to attribute this curvature to wall slip, an effect not to be confused with the classical transition from constant viscosity at low shear rates to power law behaviour at higher shear rates (see e.g. Figure 5.28 or Tanner [16]), as this transition is seen only at very low shear rates. Under this assumption, higher shear rates involve increased wall slip and thus higher flow rates, an effect which could be interpreted as a non-linearly decreasing viscosity. Thus we have to conclude, that in the example of Bassi, the neglect of the separation of wall slip leads to *combined* shear material parameters. Even if Bassi's work is used as an example of the creation of a material law that incorporates several different physical effects, other sources that practice this method can be found by inspecting Table 5.10 for authors who do not make mention of any extensional or wall slip effects at all.

A further source of non-linearity in the $\dot{\gamma}$ - η plot, not present in Table 5.11,

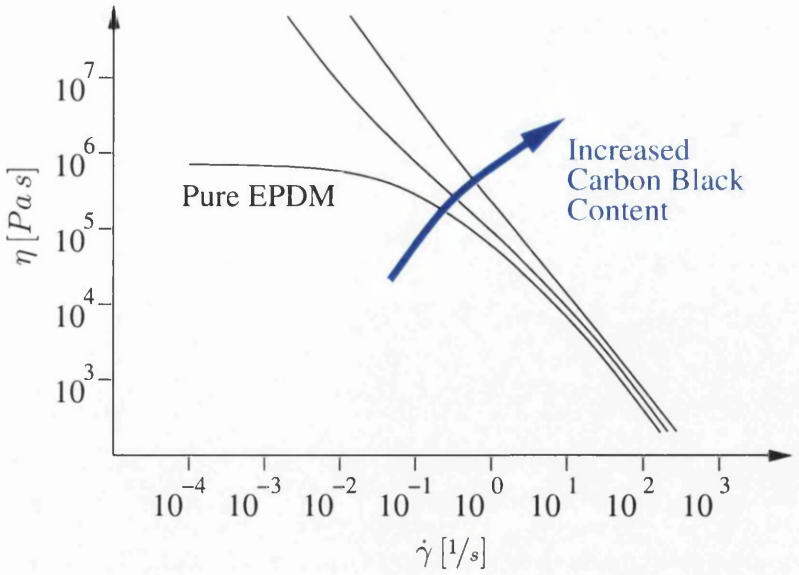

Figure 5.28: Trends in the viscosity under increased carbon black loading according to White [5] and Osanaiye [6]. In this plot, graphs for pure EPDM, a compound filled with 25 pphr and one with 100 pphr are shown.

may be found in the temperature dependence of the material, as it is generally accepted that higher extrusion speeds (i.e. more energy input) and thus higher shear rates lead to reduced viscosity at higher temperatures.

Another major insight concerning the relationship between $\dot{\gamma}$ and η is gained by examining the situation for different levels of carbon black filling. Osanaiye [6], Li [67], Shin [68] and Song [65], working together with White [5], have all documented a clear trend that is demonstrated in Figure 5.28. While this graph shows the relationship between η and $\dot{\gamma}$, the situation is principally the same for a plot of shear stress vs. viscosity as seen from the definition of the viscosity (Equation (4.59)). The latter method of displaying Figure 5.28 is used by a number of authors (see e.g. Shin [68], White [5] and Osanaiye [6]).

The most important fact to notice is that convergence towards a zero shear viscosity η_0 as noticed for pure EPDM is not inherent in compounds including carbon black even in small quantities. Furthermore, the difference between unfilled and filled EPDM is only marked for shear rates well below $\dot{\gamma} = 1\,{}^1/_s$, with values for higher shear rates being almost indistinguishable. As a consequence of this fact, we can assume a behaviour for our highly filled compounds that is similar to other filled materials, even more so as the shear rates of interest are much higher than the ones at which divergence occurs to a significant degree.

Shear Stress vs. Shear Rate

Besides the previous class of plots, a lot of attention is also given to plots of the shear stress τ against the shear rate $\dot{\gamma}$ which are, in fact, very similar to the plots of the viscosity η vs. the shear rate $\dot{\gamma}$ due to the definition of the viscosity $\eta = \tau/\dot{\gamma}$ in Equation (4.59). Figure 5.29 shows the results by a number of authors including the results of the work done in Aberystwyth [39], presented in Section 5.1 and the data collected in the scope of the rheological study, Section 5.2.5.

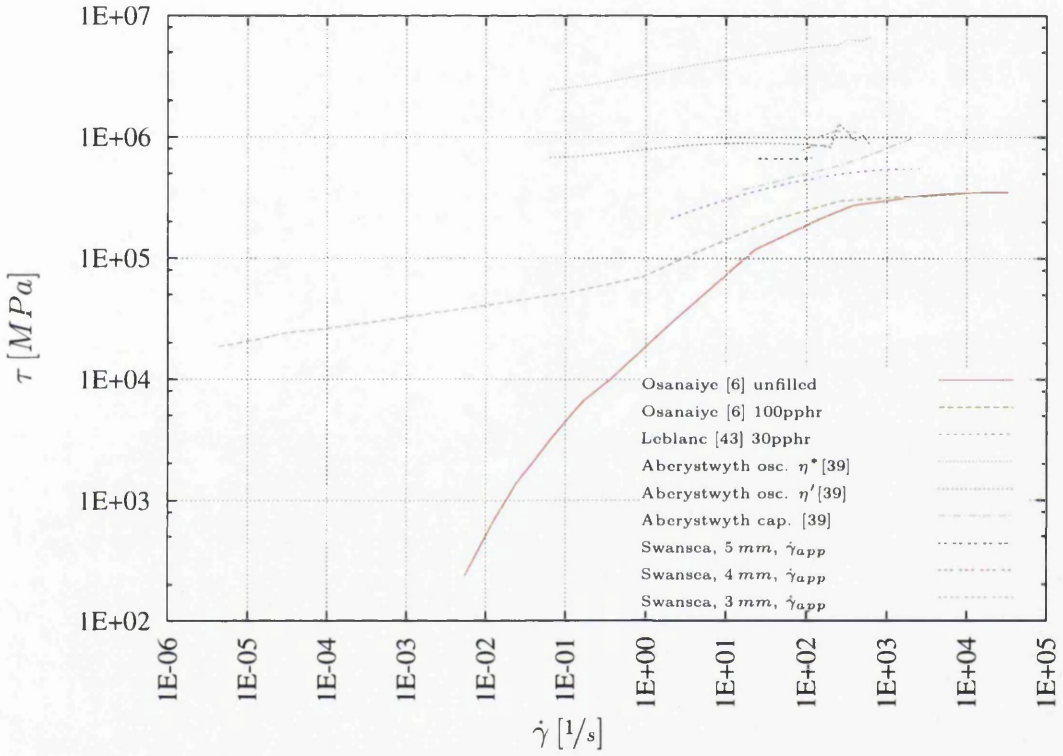

Figure 5.29: Results from various authors for the plot of $\dot{\gamma}$ vs. τ. The data from Swansea is *raw* data, i.e. not temperature corrected, no wall slip extracted and no Rabinowitch correction applied, in order to allow for comparison with other sources.

In Figure 5.29, the data from Aberystwyth, corresponding to the data shown in Figure 5.1, has to be considered with special attention as one of the plots is obtained by oscillatory rheometry under assumption of the Cox-Merz rule and by using the complex viscosity in the calculation of the shear stress, $\tau = \dot{\gamma}|\eta^*|$. Furthermore in comparison with the data from Section 5.2.5, a different rubber compound was used, thus precluding direct conclusions. The capillary results from Aberystwyth, presented for a temperature of 60°C, show a reversed curvature in comparison with other data in that range. When comparing both the complex and the viscous oscillatory data with the capillary data as presented

in Figure 5.29, the need for in-line rheometry is again emphasised by the great range of stresses for a single material under different determination methods. In analogy with Figure 5.27, however, Figure 5.29 shows a very close resemblance between the capillary experiments from Swansea and the viscous part of the oscillatory data, considering the different materials and the use of raw, unshifted data for the capillary experiments. This result reinforces the good match between the real part of the complex oscillatory viscosity η' and the results of the material parameter optimisation.

Osanaiye's data is shown for pure EPDM and for a compound with 100 pphr carbon black, while the intermediate fillings of 25, 43, and 66 %, which are also covered by Osanaiye, are omitted here for reasons of clarity, as they show the expected behaviour in converging from the pure material towards the highly filled one. In the same manner as for the η - $\dot{\gamma}$ relationship (see Figure 5.28), the difference in shear stress between different materials is most pronounced at low shear rates, with rates relevant in the current extrusion process - say in the range from ten to one thousand - showing much less variation.

In comparison with Osanaiye's and also Leblanc's data, it is not surprising that the present material shows higher shear stress, as the filler content for both compounds used in this study is considerably higher at 190 pphr for the oscillatory data and the capillary results from Aberystwyth and 152 pphr for the rheometrical results described in Section 5.2.5 (labelled 'Swansea' in Figure 5.29).

The internal results, shown here for die lengths of three, four and five *mm*, are presented with a certain degree of transient behaviour, due to the unfinished settling of the temperature, which in turn is caused by tight constraints in the trial schedule. As mentioned previously, this fact is of no concern to the parameter optimisation as instantaneous snapshots of all required process parameters ensure consistent results. It would, however, be desirable for the comparability of the different plots to obtain fully stabilised processing conditions before taking any samples. The shear rate values for the three entries are *apparent* values, excluding the extraction of wall slip and entry losses and without the application of the Rabinowitch correction. As a result we have to content ourselves with this limited amount of data in connecting the endpoints of each of the three curves as the best guess for the steady-state. Keeping in mind that we are comparing compounds which are not exactly the same, we can note a definite similarity between the capillary data from Aberystwyth and the internal experiments from Swansea. Much more striking, however, is the aforementioned match between the the viscous part of the complex viscosity as presented by Aberystwyth, η',

and the Swansea results. This result comes as no surprise, as a close resemblance between these two data sets has already been observed for the shear material parameters (see Table 5.10 and Figure 5.27).

Analysis of the Response Surface and Levenberg-Marquardt Results for two Design Parameters, μ_0 and n

As an extensive set of experimental data has been introduced in Table 5.10, the results of the optimisation with two design variables (final parameters $\mu_0 = 138,350$ and $n = 0.350$) can now be reviewed critically. An analysis of Bassi's work [10] over the relevant shear rate range yields $\mu_0 = 131,000$ and $n = 0.32$. As Bassi's results are obtained by making use of a capillary rheometer which exhibits varying material parameters over the shear rate range covered, it is not advisable to compare them directly with the material parameter optimisation of two design variables. De Laney [61] presents a very small μ_0 and high n obtained from capillary data, a result which has to be viewed critically in this comparison as a very high temperature of $T = 190°C$ was used.

Turner [66], however, presents his findings with $\mu_0 = 132,470$ and $n = 0.30$, a result obtained by oscillatory rheology under use of grooved rotor plates, which precludes the occurrence of wall slip. As the simple material parameter optimisation with two design variables uses wall slip values fixed at $\kappa_0 = 1 \cdot 10^{39}$ and $m = 1.0$ in order to create wall stick conditions, a direct comparison is valid for this case. Most authors, making use of capillary rheometry, report smaller values for μ_0 at 50,000 to 100,000, and especially for n, which is commonly determined to be roughly $n = 0.2$ (see e.g. Geiger [58, 59], Holzer [62] and Markovic [60]). This discrepancy is a logical consequence when considering the nature of the capillary data, where wall slip effects are present in the shear law. Thus, it is to be expected that these capillary values are smaller than the oscillatory or the two parameter optimisation results which make a clear distinction between shear thinning and slip effects.

It can be concluded that, when comparing like with like, the material parameter optimisation with two design variables yields results which match the literature well.

5.5.2 Extensional Viscosity

So far, the inclusion of extensional viscosity in the scope of a comprehensive viscous material model has not been attempted in any way due to the circumstance that extensional viscosity is generally considered together with visco-elastic effects, a fact that stems from the observation that extensional flow is the primary cause for die swell effects. This behaviour is also reflected by the scarcity of extensional data in Table 5.10. As we are limiting the modelling to viscous flow due to the extreme computational cost of the simulation of visco-elastic flows, we are not in a position to compare the present material parameters with any literature data.

As the necessity of the inclusion of extensional viscosity parameters only arises for Non-Newtonian fluids where the Trouton ratio significantly diverges from the Newtonian value of three, an analysis of the Trouton ratio in the relevant strain rate range is called for to decide whether a special treatment of extensional viscosity in the simulation code is needed.

Considering the data from Aberystwyth in Figure 5.2, we note a very close distribution of the Trouton ratio around the Newtonian value of three, thus apparently making a special treatment of extensional viscosity in the simulation code unnecessary. Even the material parameters in Table 5.9, which show a much higher Trouton ratio, do not result in a ratio exceeding ten, a value possibly not warranting an inclusion in the simulation code.

5.5.3 Wall Slip

The literature available (see Table 5.10) shows a number of publications dealing with the slip behaviour of rubber compounds, which are, however, primarily focused on experimental results, not expressing the findings in a material law in analogy to Section 5.4, where we express the wall slip in terms of a power law. In consequence, we have to determine the wall slip parameters κ_0 and m in Equation (4.67) from plots of the slip velocity v_s vs. the shear stress τ as presented by the various authors. Nonetheless, a wealth of deductions can be drawn from the sources available, such as effects of the processing conditions and composition, data which proves very valuable in judging the dual nature of the optimum found in Section 5.4.3 in connection with Equation (5.45).

The underlying basic physical concepts of the phenomenon of wall slip are generally attributed to several different causes inherent in the structure of polymers

of high molecular weight. Not commonly seen as significant in rubber processing, some polymers exhibit the formation of a low viscosity layer with high velocity gradients which should correctly be classified as pseudo-slip as the polymer molecules do not physically slip on the wall. Joshi [69] determines two physical causes which he uses as a basis for the development of a simple slip law modelled after de Gennes [34]. On one hand Joshi mentions *disentanglement*, the flow condition where molecules attached to the wall of the flow channel get stretched to the point where their connection with other molecules that are not attached to the wall is broken, resulting in extreme velocity gradients. *Debonding* on the other hand is a veritable slip effect that involves molecules overcoming the adsorption force that keeps them attached to the wall. Several extrusion instabilities such as stick-slip and spurt are associated with these two effects. As they are dependent on the relation between stress levels, adsorption forces and even elastic effects, they sometimes lead to undesirable cyclic phenomena with the result of extremely rough surface finish in the extrudate.

Apart from the data on shear law parameters, Table 5.10 also shows a summary of the findings made during the literature review with respect to wall slip. This data is put in contrast with the results obtained in the present study, generally showing good consistency amongst the different authors. The majority of published results are in the form of τ_w - v_s plots which can be scanned on a flatbed scanner for digital extraction of material parameters, as also presented in Section 5.1.1, where we have extracted shear viscosity power law parameters. The shear stress and slip velocity values of arbitrary points on the scanned curve are obtained by determination of the pixel-coordinates of that point in a graphics manipulation program, and subsequently transformed into shear stress and slip velocity values by aid of a small program. This procedure allows for the rapid acquisition of a large set of graphs which can then be further analysed or plotted. It also has the advantage, with respect to the approach taken in Section 5.1.1, of being suitable as a generic method for the arbitrary fitting of material laws rather than only linear ones. This possibility may prove advantageous in cases where the classical power law is not seen as sufficient for describing the material behaviour accurately (see e.g. Malkin [63]). Once we have gathered a sequence of points on a specific curve, we can make use of a simplified version of the Levenberg-Marquardt algorithm discussed in Section 5.4.3 to perform a curve-fitting exercise. The goal of this exercise is to minimise the least-squares error of the measured data points with respect to the wall slip law (Equation (4.67)) and its two parameters κ_0 and m, which are displayed in Table 5.10.

It has to be mentioned that a number of studies, while very enlightening with

respect to non-Newtonian behaviour, omit the investigation of wall slippage, the most prominent examples emanating from White and his co-workers [5, 65, 68, 6, 67]. While this procedure may be a valid approximation in oscillatory rheology, where only small strains are used or in rotational rheometry if grooved rotors are employed, capillary rheology definitely has to consider wall slippage as a source of non-linear behaviour.

It is generally accepted (see e.g. Agassant[1] [24], Jay [70] and Malkin [63]) that wall slip is a function of the wall shear stress, $v_s(\tau_w)$, with Jepsen [7] indicating that in capillary flow, lower L/D ratios and higher filler contents dramatically increase the slip velocity for elevated shear stress levels. For the temperature dependency, a more complicated situation is found (see Jepsen [7]), as an increase in wall slip with increasing temperatures is noted at low shear stress levels, whereas shear stresses exceeding 0.25 MPa to 0.30 MPa exhibit a reversal of this situation. The complexity of the situation is not reduced when considering the temperature dependence of the wall slip, as the relevant authors show contradictory behaviour, ranging from a certain degree of increase in wall slip when increasing the temperature, to a complete transition from wall slip to wall stick.

Details of Jepsen's extensive study are presented in Figure 5.30, which very clearly demonstrates the complexity of the problems arising in the classification of the different sources of wall slip, as many sudden changes are observed when comparing the data within each of the four plots. This situation, where many different parameters influence the material behaviour again proves the necessity of in-line rheometry as a means for capturing the data required under conditions that are as close as possible to the actual extrusion.

In Table 5.10, we only make use of the plot displayed in Figure 5.30 c), as this plot shows the temperature dependency of the material, the parameter which can be seen as being of most interest in the current context. What is more, the other plots show either very non-linear data or nearly horizontal gradients, both of which are not favourable for fitting with a power law. In the most extreme cases, it might even be called for to introduce an offset value τ_0' in analogy to the Herschel-Bulkeley law (Equation (4.10)) for the shear viscosity. Regarding the shear stress range under review by Jepsen, we have to use caution in comparing the data with the present results, as the shear stresses encountered in the current rheometrical experiments - calculated from Equation (4.45) and the data listed in Appendix C - are found to be significantly higher than Jepsen's data, with shear

[1] Agassant also postulates the existence of an entry length where no slip occurs, a thesis which further reinforces the probability of wall slip being a cause of the offset as seen in Figure 5.13 as for a fixed shear rate, the dies with a smaller L/D ratio show a higher viscosity.

stresses ranging from 0.67 MPa to 1.19 MPa.

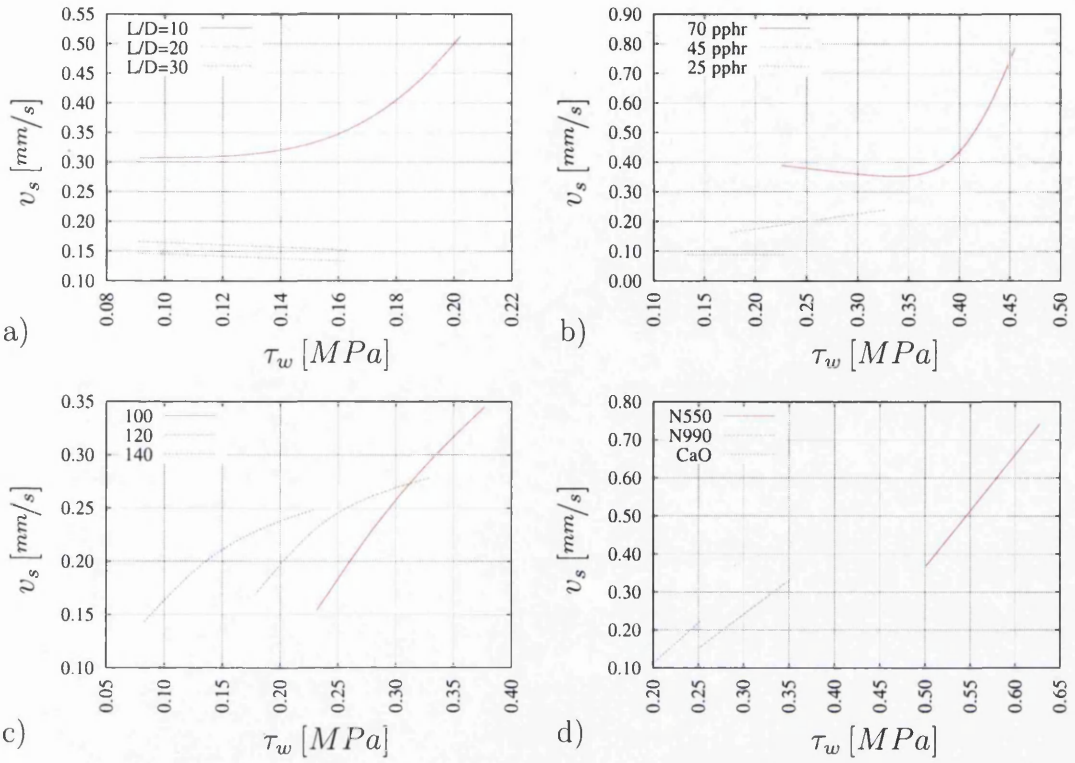

Figure 5.30: Influence of a) L/D ratio, b) carbon black content, c) extrusion temperature and d) carbon black (N550 and N990) and calcium oxide filler in the plot of slip velocity vs. wall shear stress according to Jepsen [7].

In Table 5.10, we have included Malkin's findings [63] in spite of his use of Styrene Butadiene Rubber (SBR), as his work is relevant in the present context due to its close resemblance to the setup chosen in the current work. He uses a power law model as presented in Equation (4.67) which he augments under certain conditions by adding an offset value τ_0' as described above. According to Malkin, this step is necessary when operating at elevated temperatures over 110°C, as under these conditions he notes a distinct critical shear stress threshold at $0.3-0.4\,MPa$ which has to be exceeded before any slippage occurs. A peculiar detail of Malkin's study is found in the strong dependence of the material parameters on the capillary die diameter, see Table 5.10, a result in direct contradiction with Geiger's study on slit dies of different dimensions [58, 59], which, while showing a slight change in κ_0 and m, basically finds constant material parameters. Malkin explains this dependency on the die geometry by the different upstream reservoir to die diameter ratio when changing the die (leading to different levels of elongation) and by differing pressure levels that change the contact area between the compound and the die wall. He argues that in order to create a similar shear stress in dies of different diameter and for otherwise equal processing conditions, a different pressure has

to be applied as demonstrated by Equation (4.45). This changed pressure will then have an influence on the wetted surface in the capillary die and thus the wall slip conditions, a view also expressed by Jepsen. It is doubtful, however, if these effects, which might have an influence at low pressure levels, are still able to produce a significant influence at the pressures encountered in industrial profile extrusion.

Turner's work [66] is set apart from the other authors' research by the fact that he uses a rotational rheometer. Nonetheless, the peculiar behaviour for the slip index m, presented in Table 5.10, has to be noted. In the data presented by Turner, there exists a remarkable temperature dependence, which seems to indicate a minimum for m at around 80°C. While also seen in the work of other authors (see e.g. Holzer [62], who also notes a significant change in m), this would indicate a reversal of how pronounced the wall slip is perceived at a given wall shear stress τ_w.

When comparing the temperature behaviour of the wall slip parameter κ_0 found by the various authors, an overall trend towards decreasing κ_0 (more slip) at elevated temperatures is seen. The numbers we extract from Jepsen's work have to be judged critically in this context as the numbers found show an opposite trend and differ to an extreme degree from the results of other authors. In fact, extrapolating the data found in the plots provided by Jepsen would indicate a complete reversal of the boundary conditions from free slip at 80°C to complete wall stick at 120°C.

Resolution of the Ambiguity in the Results of the Full Parameter Optimisation

It is now left to resolve the ambiguity in the two sets of material parameters obtained by application of the Levenberg-Marquardt algorithm in Section 5.4.3. As shown previously, it is impossible to resolve this ambiguity in an analytical way. Thus, we will have to resort to the data from Aberystwyth and the literature review as a base for a decision on which of the two parameter sets will be chosen for modelling the material flow.

As pointed out previously, the parameter determination strategy most commonly found in the literature, while not wrong in itself, focuses on the determination of one parameter set, thus creating bulk material parameter sets that combine the effects of different physical phenomena into one set. While this can be seen as beneficial in the comparison of different rubber compounds, these material pa-

rameters are not suitable for an accurate simulation that aims to reproduce the three phenomena under investigation. The oscillatory rheometry in Aberystwyth is one of the few incidences where wall slip can be ruled out due to small oscillatory strains and where the viscous part of the complex viscosity is presented, a necessary condition for a meaningful comparison with optimisation data, where elastic behaviour is not considered. This comparison leads to the surprisingly good consistency found for μ_0 and n between the viscous part of the complex viscosity η' and the full parameter optimisation (see Table 5.10 and Figure 5.27) at roughly $\mu_0 = 650,000\, Pa\, s^n$ and $n = 0.025$, a resemblance also observed in the plot of τ vs. $\dot{\gamma}$, shown in Figure 5.29.

It is in the power law indices n and m that the major discrepancy between the results obtained in the current study and the available literature is seen. Both a shear law index or a wall slip index of 0.027 for the two solutions found seems extremely low compared to literature values that are typically situated between 0.2 and 0.4. While it seems that the difference between the literature and the optimisation results is large, it has already been stressed that the present work is not directly comparable with literature data due to the missing separation of effects in the literature.

Furthermore, fully formulated rubber compounds in general are not easily compared as the compounds present in this study (see Tables 2.2 and 5.9) are highly filled compounds not only with regard to the carbon black content but also other components which might influence the material behaviour. As an example, the liquid fillers (Naphtene and Butadiene) might very well form a slip layer at the die wall due to local separation which in turn could result in an effect similar to wall slip in pure EPDM. While not reported in relation with EPDM, this behaviour is often seen in other materials like PVC. Due to the fact that a number of the components in the present rubber compounds are confidential, we can only speculate on any slip-like effects caused by these components.

In the light of these facts it is more sensible to observe the physical meaning of such low material parameters as pointed out in Equations (5.46) and (5.47) and to observe the temperature behaviour as indicated by the change in sign for the shear and power law parameter optimisation results presented in Tables 5.8 and 5.9. The first solution (Table 5.8) shows a very small m which practically leads to wall shear stresses being insensitive to the wall slip velocity or vice versa the wall slip velocity being very sensitive to the wall shear stress, a view not commonly shared by any of the relevant authors (see e.g. Geiger [58, 59], Jepsen [7]). The temperature dependencies show a peculiar behaviour as well, insofar

that commonly an increased temperature is associated with reduced viscosity and reduced wall slip. The second optimum, presented in Table 5.9, shows this more plausible constellation together with a very small n as a sign of a highly shear thinning material, while the wall slip coefficient stays on a reasonable level. As a conclusion, it is obvious that the optimum for the material parameter optimisation presented in Table 5.9 shows a set of parameters that represents more realistically the behaviour of rubber compounds as described in the current literature than the one introduced in Table 5.8.

One more argument in favour of Table 5.9 over Table 5.8 is found in Figure 5.25, which agrees very well with the results in Table 5.9, if it is kept in mind that the wall slip index in Figure 5.25 is fixed at $m = 1.0$.

In summary of the shear rate parameter range covered by the various authors as given in Table 5.10, we can observe, while keeping in mind the differing experimental setups, a division of results. On one hand, we find the oscillatory results (excluding Montes' results due to his use of SBR) in the range of $126,000\,Pa\,s^n \leq \mu_0 \leq 3,302,000\,Pa\,s^n$ and $0.024 \leq n \leq 0.299$, while on the other we find capillary results with $24,500\,Pa\,s^n \leq \mu_0 \leq 210,300\,Pa\,s^n$, with an obvious accumulation around $\mu_0 = 130,000\,Pa\,s^n$ (neglecting the results from the present study, which were obtained under strict parameter separation) and $0.115 \leq n \leq 0.408$. The presentation of these ranges for oscillatory and capillary material parameters is not conclusive in itself. When looking at each of the literature sources in the two classes separately, however, one can find clear signs that indicate a tendency towards lower (μ_0, n) parameter combinations for capillary data in comparison with the oscillatory data. This response can be visualised by plotting the power law for various authors over a shear rate range as shown in Figure 5.31. As an example, De Laney's data, while showing a very high n of 0.408, also has a very small μ_0 of $24,500\,Pa\,s^n$, a combination which results in a small overall viscosity, while the complex viscosity data $|\eta^*|$ from Aberystwyth, with a big μ_0 and a small n, yields a bigger overall viscosity, even up to shear rates of $\dot{\gamma} = 10,000\,1/s$. As a result, it can be deduced that capillary results tend to combine the wall slip effect into the shear material parameters, as already suspected previously.

5.5.4 Conclusions

In summary of the preceding chapter, two main findings should be mentioned. First, the numerical results obtained in the full material parameter optimisation

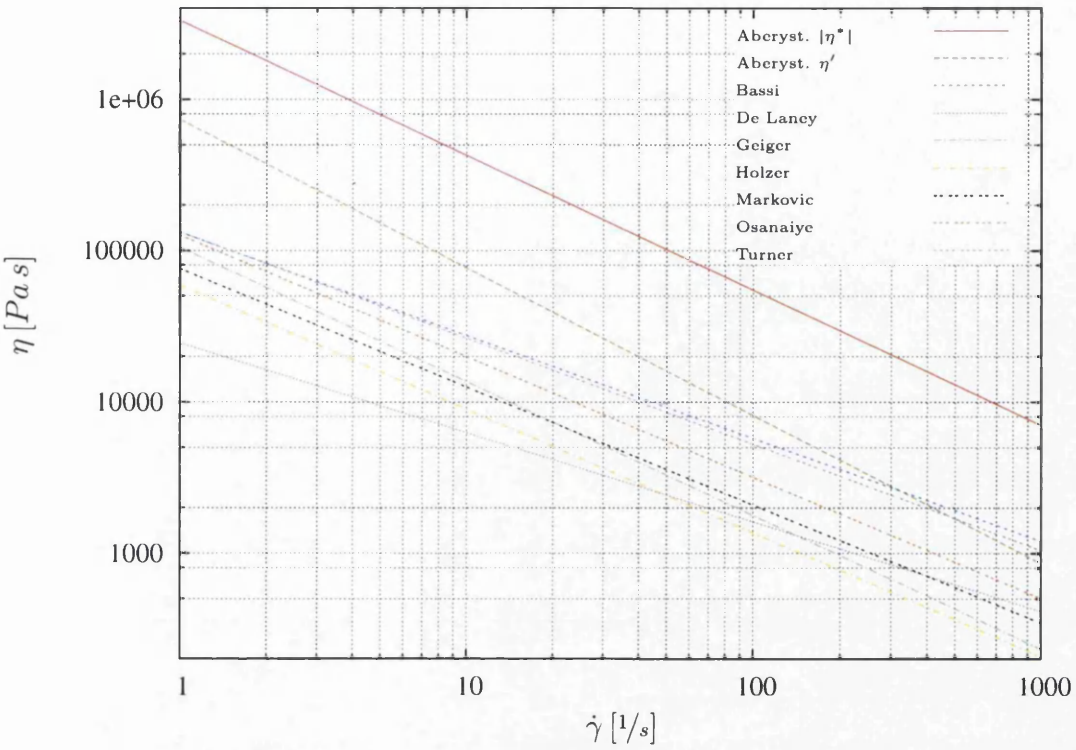

Figure 5.31: Dependency of the viscosity η on the shear rate $\dot{\gamma}$ for various authors.

have to be cited. Though two optima of equal quality are found, strong evidence for the validity of one solution is present. Apart from a clear tendency in the physical behaviour, the optimisation including two free design variables also backs the argumentation for the results given in Table 5.9.

A second major discovery of the material parameter determination is the differentiation between the two types of results that are present in today's data on rubber material parameters. On one hand, *combined* sets of material parameters are present, which are obtained by the (unintentional) combination of the phenomena of non-Newtonian behaviour, wall slip and extensional viscosity, while on the other hand, we see parameter sets produced either by an active separation of effects as in this study, or by a determination method that avoids the mixing of phenomena, e.g. oscillatory rheometry including grooved rotors.

Chapter 6

Simulation

At this point of the study we have assembled all preliminary components for carrying out a numerical simulation, most prominently the fluid mechanics and the material parameters. We are now in a position to combine these elements into a simulation of the material flow in an extrusion die. All results which follow after this point are computed with the material parameters from Table 5.9, except where stated otherwise.

6.1 Pre-Processing

The manual process of the mesh creation is carried out with Altair **HyperMesh** [71], as the meshing capabilities of this program allow for the needed flexibility in creating a highly graduated mesh with large elements being used in the conical entry and small elements for the details of the die. In a first step, a surface representation of the model under investigation is read into **HyperMesh** from a CAD model in IGES format. Subsequently, a triangular surface mesh is created manually under special consideration of a minimum number of elements (to be determined in Section 6.4) across any given section of the flow channel, while maintaining a mesh density as coarse as possible to reduce computation time. Due to the extreme contrast in geometric dimensions between the upstream cone and the die, differences in element size up to a factor of 20 are easily seen. Once an enclosed volume of triangular elements is set up, the creation of a tetrahedral mesh is a trivial task, only requiring the specification of the mesh resizing strategy towards the centre of the computational domain.

Finishing the preparation of the model, boundary conditions are assigned accord-

ing to Figure 6.1. As the inlet velocity v_{in} is easily and accurately calculated

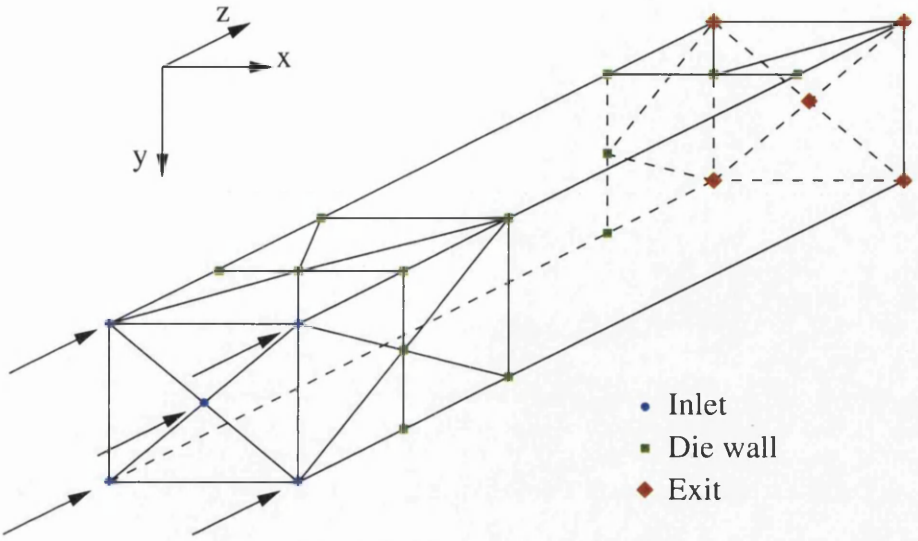

Figure 6.1: Schematic definition of boundary conditions with regard to inlet, die wall and outlet. All interior nodes are free.

from the exit flow rate of the corresponding experiment, velocity boundary conditions are chosen over pressure boundary conditions. The inlet surface nodes are completely constrained by applying $v_x = v_y = 0$ and $v_z = v_{in}$. The exit surface nodes on the other hand are defined by setting $v_x = v_y = 0$ to enforce fully developed flow conditions while keeping v_z free, which, in the finite element formulation results in $\partial v_z/\partial z = 0$. As the use of wall slip is imperative in our model, the die wall requires special attention. Detailed in Section 6.2.2, the nodes on the die wall are fixed by setting the normal velocity v_n to zero as a means to prevent material loss over the boundary of the domain, while using Equation (4.67) to set the tangential velocities v_t in dependence of the shear stress. Due to the fact that no method for defining a wall slip node is implemented in `HyperMesh`, we assign a rotational constraint to wall slip nodes, handling the translation into the proper boundary conditions recognised by the simulation code in a separate script. As a common basis for the translation process the `Nastran` file format [72] is chosen as it is a well documented `ASCII` format and supported as an option for export by `HyperMesh`. After translation, a geometry file containing the nodal coordinates, the boundary of the domain as triangular elements and the connectivities of the tetrahedral elements is created together with a file containing the boundary conditions. These two files, in addition to the master input file that controls the details of the simulation, comprise all the input needed to execute a successful simulation. A typical master input file can be found in Appendix G and a detailed specification of all the required parameters and the mesh representation is found in the manual on the Homepage of `Fantom` [73].

6.2 Simulation Code

The in-house simulation code employed in this study, called '**Fantazt**', has its roots in two separate projects.The fluid mechanics and the finite element treatment are based on a modified version of the publicly available code **Fantom** [73], which is a complete, generic simulation code for computational fluid mechanics. As the linear equation solvers in **Fantom** are not designed to deal with models of the size required in the current context however, an external library is used for that purpose. This library, called **Aztec** [74], is highly optimised for the rapid solving of linear equation systems and displays powerful capabilities in the field of parallelisation.

6.2.1 Physical Problem

As the current project is not concerned with the transient start-up behaviour of the profile extrusion, it is possible to use a reduced form of the full linear momentum equation (see Equation (3.44)), Equation (3.47).

Reynolds Number

The present simulation does not model any turbulent phenomena due to the low Reynolds numbers and the high viscosity encountered in the flow, an indication for laminar flow. An estimate can be obtained either by the classical definition of the Reynolds number for a circular die

$$Re = \frac{Dv\rho}{\eta}, \tag{6.1}$$

where η is the viscosity as determined by the power law, or, preferably,

$$Re_n = \frac{D^n \rho v^{2-n}}{2^{n-3}\mu_0 \left(3 + 1/n\right)^n}, \tag{6.2}$$

the term for the non-Newtonian Reynolds number, derived e.g. by Bird [14]. When considering a typical scenario with $D = 1.0\,mm$, $\rho = 1230\,{}^{kg}/_{m^3}$, $v = 1.0\,{}^{m}/_{s}$ and the power law parameters according to Table 5.9, we find $Re_n = 0.011$, a value which is situated far within the laminary regime, thus confirming the assumption of laminar flow and indicating that inertia effects are negligible.

Exclusion of the Convective Term

When looking at the input file in Appendix G, it can be observed that the convective term

$$\rho v_j \partial_j v_i$$

is neglected in the calculation, leading to Stokes flow. While one indication of the permissibility of this procedure is found in the very low Reynolds number determined above, a confirmation by example is preferable under the present, complex conditions. In correspondence with Appendix D.2, an unoptimised profile model with an inlet velocity of $v_{in} = 5.477^{mm}/_{s}$ (equal to 20 rpm) at $T = 119°C$ was chosen with a number of elements $n_{el} = 308,395$. Two simulations, only differing in their use of the convective term, were conducted. The result of this comparison is displayed in Table 6.1, where the deviation $1 - \dot{V}_{Stokes}/\dot{V}_{conv}$ for each partition is listed. Except for partition five, the difference between Stokes and convective

Partition acc. to Fig. 5.15 a)	1	2	3	4	5
Deviation $\dot{V}_{Stokes}/\dot{V}_{conv}$	-2.0%	4.4%	-1.7%	0.8%	-15.8%

Table 6.1: Divergence in results - deviation between Stokes and convective solution.

flow is very small. As partitions four and five show very small flow rates, a fact which will be detailed shortly, it is thought that this seemingly large deviation is due to the calculation of the average flow rate. Only complete triangular die exit elements are considered, which are added to the side of the partition boundary where the majority of a particular element's area is located. As the accuracy is influenced by the manual process of creating the partition boundaries, and due to the fact that the highest velocities for partition five are found exactly at the boundary of the partition, this could be the cause for the difference found in partition five.

Temperature Dependence

It can easily be seen from Chapter 5 that a degree of temperature dependence exists in all of the flow phenomena. As we would like to make use of iso-thermal conditions for a simplified simulation process, we need to give an indication of the temperature change as the material proceeds through the die. By making use of the specific heat capacity $c_p = 2.01\,\frac{kJ}{kg\,K}$ for rubber as found in standard thermodynamic tables [19], we can calculate the adiabatic temperature increase

ΔT caused by a given pressure drop Δp (see e.g. [75]) as

$$\Delta T = \frac{\Delta p}{\rho c_p}, \tag{6.3}$$

leading, for a pressure drop of $\Delta p = 50\,bar$, to an increase in the temperature over the length of the die of 2°C.

As a pressure of this magnitude will be rarely reached in reality, it is, in consequence, sufficient to adjust the bulk parameters to the temperature of the corresponding experiment, i.e. for the temperature adjusted bulk parameters we simply have

$$\mu_{0,adj} = \mu_0 e^{b(T_{ref}-T)}, \tag{6.4}$$

$$\kappa_{0,adj} = \kappa_0 e^{c(T_{ref}-T)}. \tag{6.5}$$

Inserting the material values from Table 5.9, this leads to a change of 3.0 % for μ_0 and 0.8 % for κ_0.

The above procedure allows us to use an iso-thermal model instead of solving the non-iso-thermal problem, an assumption which also holds for the density, as we have previously determined the insensitivity of the density to temperature changes. Subsequently, the adjusted material parameters are inserted into the master input file, Appendix G.

6.2.2 Implementation of Wall Slip

For the application of wall slip boundary conditions instead of the classical wall stick condition, it is necessary to modify the element stiffness matrix A_{ij}. Details of the assembly of the stiffness matrix are found in the literature, e.g. [76, 77, 20], leading to the basic linear system

$$A_{ij} v_j = f_j. \tag{6.6}$$

In order to display the implementation of wall slip into the simulation code, it is convenient to present a subroutine from the `Fantazt` source code, shown in Figure 6.2. In lines one to four, the slip velocity v_s is calculated in the form of the variable `tang`. After setting a reasonable cut-off value (see line ten), the wall slip power law - Equation (4.67) - is invoked in line 13 in the modified form

$$\tau_w = \kappa_0' \left| v_s \right|^{m-1}, \tag{6.7}$$

```
1       tang=0.0
2       do idime=1,ndime
3        tang=tang+veloc(idime)*veloc(idime)
4       enddo
5
6       do inodb=1,nnodb
7         ievab=(lboel(inodb)-1)*ndime
8         do idime=1,ndime
9           ievab=ievab+1
10          if(tang.lt.1.0e-15) then
11            slpcoe= slip
12          else
13            slpcoe= slip*dsqrt(tang)**(powern-1.0)
14          endif
15          tslip=slpcoe*shapb(inodb)*dtins*dsurf
16          elmat(ievab,ievab)= elmat(ievab,ievab) + tslip
17        end do
18      end do
```

Figure 6.2: Implementation of wall slip in **Fantazt**.

where

$$\kappa_0' = \kappa_0 v_s, \tag{6.8}$$

as this modified expression is favourable for the linearisation of the non-linear system. After multiplying with the shape function, the term **tslip** is added to the stiffness matrix A_{ij} in line 16.

6.2.3 Pressure Interpolation

As the computational cost involved in solving a model of the given size is very high, it is desirable to simplify the complexity of the numerical model as far as possible. We would thus like to make use of linear tetrahedral elements for velocity and pressure.

When using the classical Galerkin formulation however, it is necessary to use a higher order interpolation for the velocity than for the pressure, in this case leading at least to a second order velocity description, to satisfy the Babuška-Brezzi condition, described e.g. in [78]. As this procedure incurs increased computation time, it is preferable to make use of a feature in **Fantazt** which allows for an equal order velocity pressure interpolation under circumvention of the Babuška-Brezzi condition, discussed in detail by Codina in [79].

Another feature in **Fantazt** is the use of an artificial scaling factor determined

at around 10^{-5} to 10^{-7}, introduced in order to scale the pressure and velocity variables present in Equation 6.6 to within the same order of magnitude. As a result, it is found that the solution procedure converges faster than without the application of the scaling parameter. The correct, un-scaled values are recovered in a post-processing step.

6.2.4 Solver

The simulation problem to be solved consists of the traditional computational domain with boundary conditions applied. In an iterative cycle, called the *outer* iterative loop here, the linear system of equations is repetitively solved until the residual of the velocity at each node falls below the desired threshold. Specifically, a Picard iteration is used to handle equation non-linearities (i.e. the shear thinning viscosity). The linear system of equations, within each outer iteration, is also solved by an iterative method, in the present case called the *inner* iterative loop.

While the outer iteration loop is controlled by the simulation code `Fantazt`, the inner iterations are handled by the parallel linear solver `Aztec`. A thorough description of this code can be found in the manual of `Aztec` [80]. At this point, it is sufficient to note that a generalised minimum residual method (GMRES) is employed, together with an incomplete left upper (ILU) factorisation pre-conditioner.

6.3 Post-Processing

The visual post-processing for a general overview of the resulting flow is carried out in a translation from the internal `Fantazt` format to a generic object oriented abstraction of model and results. As this abstraction is stored in memory, extensive transformations can be applied easily, with subsequent translation into the desired target format. At the moment, it is possible to create output for the post-processing packages `GiD` [81], `Tecplot` [82] and the versatile `VTK` library [83], which can be processed further easily. For visualisation purposes, mostly `GiD` was chosen, due to the simple data format.

For the analytical post-processing procedure (as opposed to the visual post-processing introduced above), used to create a valid numerical comparison between experiment and analysis, a different approach was used. This approach is

best demonstrated by presenting an example, namely a parametric study of the transition from wall stick to wall slip, for traditional wall slip parameters.

6.3.1 Determination of Wall Slip - a Parametric Study

In order to get an understanding of the wall slip process and its influence relative to the velocity field across the extruded profile, it is helpful to conduct a simple parametric study. In the present case we will be comparing the results from the profile extrusion trials (discussed in Section 5.3) with a number of simulations that assume different levels of wall slip. The shear thinning behaviour is modelled according to the findings of the experiments in Aberystwyth as described in Section 5.1. In particular, the bulk viscosity parameter is fixed at $\mu_0 = 1.1428 \cdot 10^5 Pa\,s$ and the power law index at $n = 0.27$, values which do *not* represent the current findings in the light of the interaction between the different flow phenomena. Thus, this study has to be seen qualitatively, as a means of understanding the transitional behaviour from wall stick to wall slip.

The experimental partitioning scheme, proposed in Figure 5.15 a) introduces the need for a software tool that allows for a similar partitioning of the exit velocity profile, in the case of the simulation, with subsequent calculation of the average flow rate in each partition. These numbers can then be compared to the ones found in Table 5.6. An in-house tool that meets all needs was found as part of another project of the research group. With this tool it is possible to read a data file containing the two dimensional exit mesh and the corresponding velocities in z-direction. In a second step, the partitioning scheme presented in Figure 5.15 a) is applied by setting a number of markers enabling the program to calculate the average flow rate for each partition. Exit elements which lie on a marker (in this context we have to deal with triangular elements as the simulation is conducted with tetrahedrons) are added to the partition in which the majority of their area lies. A screenshot of the program showing the final result is displayed in Figure 6.3, with the separations and flow rate markers in place. On the numerical side, simulations were run for a range of wall slip parameters as displayed in Table 6.2. The first two entries in this table represent the cross section and the area percentages at 20 rpm as determined in Section 5.3 (see Table 5.6) with all other entries listing the results for the given material parameters. The transition from wall stick to wall slip can easily be visualised by looking at the exit velocity profiles for different parameters. Taking the full range of wall slip bulk parameters κ_0 results in velocity profiles as shown in Figure 6.4. In the present example, the wall slip index m is kept constant but its influence can be judged from the last

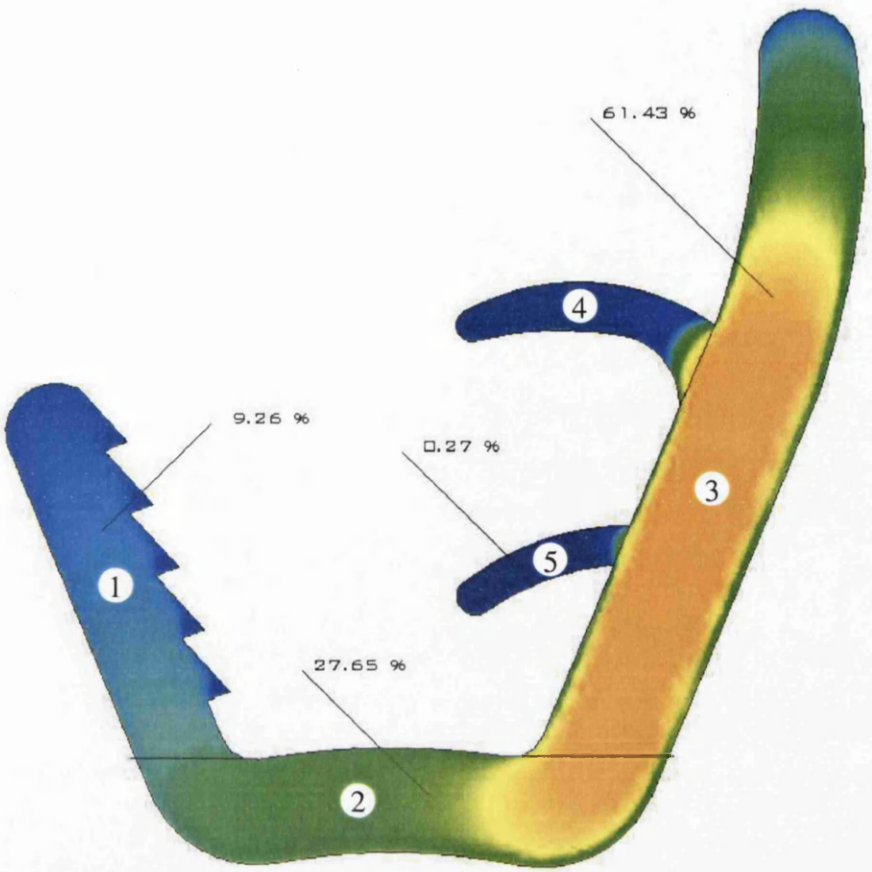

Figure 6.3: Screenshot of program for average flow rate determination in each partition.

two entries in Table 6.2 to be of much less importance compared to the bulk parameter κ_0.

Another important conclusion drawn from these results is the convergence of the flow rate in each partition from an initial unbalanced value (e.g. partition three, the largest one, gets proportionally too much material) for wall stick to exactly the percentage of the exit area for this partition in the case of wall slip. This fact has important implications for the profile optimisation, as a high degree of wall slip will act as a self-regulating mechanism to balance the profile.

With these preliminaries, it is straightforward to find an estimated set of best parameters for matching simulation with experiment. A rough guess locates the wall slip bulk parameter at $\kappa_0 = 1 \cdot 10^6$, meaning that under realistic processing conditions we have to deal with a material which is in full translation between wall stick and wall slip. The minimum and maximum velocities are determined at $v_{min} = 0.0877\frac{m}{s}$ and $v_{max} = 0.1808\frac{m}{s}$. If desired, a grid of simulations could be created, including variations of m, resulting in a manual response surface evaluation similar to the one presented for the material parameter determination in

Wall slip parameters		Partition Nr.				
κ_0	m	1	2	3	4	5
% of total die exit area		19.5	25.3	45.7	6.2	3.3
% of total extr. prof. area		14.3	27.3	49.6	5.0	0.8
no wall slip	no wall slip	8.50	26.96	63.48	0.94	0.11
$\kappa_0 = 2.00e7$	$m = 1.0$	14.63	27.23	53.82	3.10	1.21
$\kappa_0 = 1.00e7$	$m = 1.0$	13.88	27.19	54.97	2.85	1.11
$\kappa_0 = 5.00e6$	$m = 1.0$	14.37	26.99	54.19	3.12	1.32
$\kappa_0 = 4.00e6$	$m = 1.0$	14.67	27.08	53.64	3.24	1.37
$\kappa_0 = 2.50e6$	$m = 1.0$	15.75	26.99	51.98	3.67	1.61
$\kappa_0 = 1.75e6$	$m = 1.0$	16.34	27.04	50.86	3.96	1.79
$\kappa_0 = 1.25e6$	$m = 1.0$	16.82	27.00	49.91	4.26	2.01
$\kappa_0 = 1.00e6$	$m = 1.0$	17.14	26.89	49.47	4.42	2.08
$\kappa_0 = 7.5e5$	$m = 1.0$	17.58	26.67	48.88	4.58	2.29
$\kappa_0 = 5.00e5$	$m = 1.0$	18.21	26.32	47.99	4.95	2.53
$\kappa_0 = 1.00e5$	$m = 1.0$	19.36	25.51	46.13	5.84	3.15
$\kappa_0 = 1.00e-5$	$m = 1.0$	19.36	25.51	45.71	6.11	3.30
$\kappa_0 = 1.00e7$	$m = 0.5$	12.59	27.67	56.73	2.28	0.73
$\kappa_0 = 1.00e6$	$m = 0.5$	13.47	28.07	54.84	2.65	0.97

Table 6.2: Percentages of flow rate and area for experiment and simulation at 20 rpm.

Chapter 5. In the current investigation however, the focus is set on a different method of parameter determination, the inverse parameter optimisation as proposed in Section 5.4, as it proves more powerful and flexible.

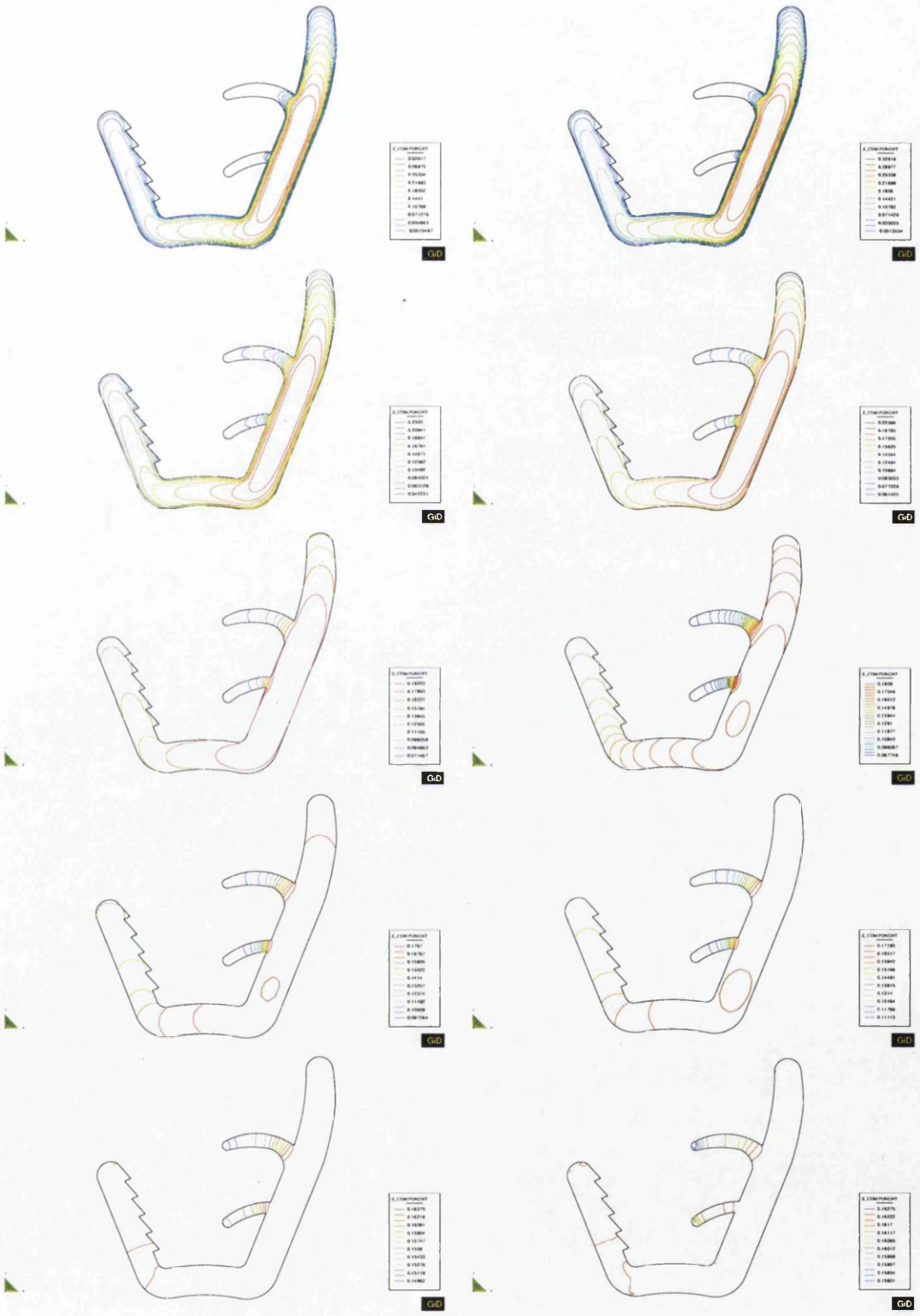

Figure 6.4: Transition from wall stick to wall slip by variation of the wall slip parameter κ_0 ($m = const = 1.0$).

6.4 Mesh Size Study

Before presenting any simulation results with current material parameters, it is necessary to validate the choice of model with regard to the mesh size. Due to the complex shape of the computational domain, shown in Figure 6.5, a highly refined mesh has to be chosen, in order to keep the balance between the number of

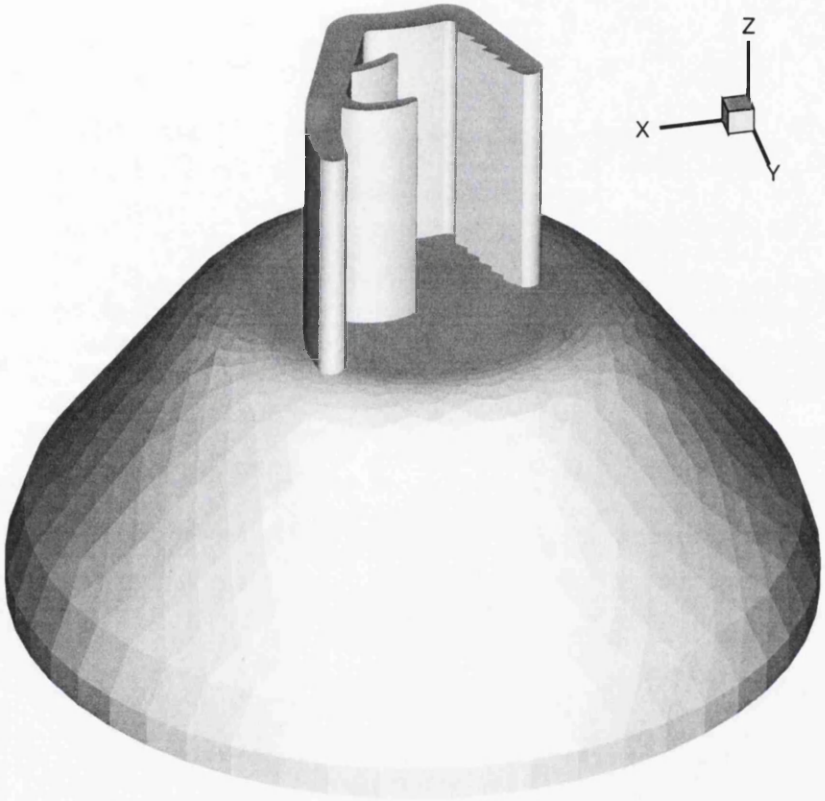

Figure 6.5: Computational domain for the unoptimised, generic profile die.

elements and the resolution of the thin section of the profile. In the implementation for the unoptimised die, over 308,000 tetrahedral elements and an aggressive mesh resizing strategy were necessary to achieve a minimum number of eight elements across all areas of the cross section. An implication of this circumstance is the fact that it is very expensive to verify the convergence of the model with regard to the mesh size, as any mesh with significantly more elements will involve a dramatic increase in simulation time. It is thus indicated to create a simple three dimensional test case for the verification of the minimum number of elements needed for an accurate simulation.

In the present case, a simple cylindrical capillary with $l = 10\,mm$ and $d = 1\,mm$ is

used. Three dimensional tetrahedral meshes of varying refinement are generated with mesh sizes ranging from four elements up to 13 elements over the diameter. As an analytical solution for the flow curve including wall slip and shear thinning has already been given in Equations (5.25) and (5.27), this model is very well suited for verification purposes. This test case makes use of the same linear velocity-pressure elements found in the full simulation, with boundary conditions prescribed according to Figure 6.1 and an inlet velocity $v_{in} = 1.0\,^{m}/_{s}$. Figure 6.6 illustrates the velocity distribution for mesh densities of four, seven and 13 elements across the diameter as well as for the analytical case (see Equation (5.25)). Although a difference of 8.4% is noted between both of the coarser

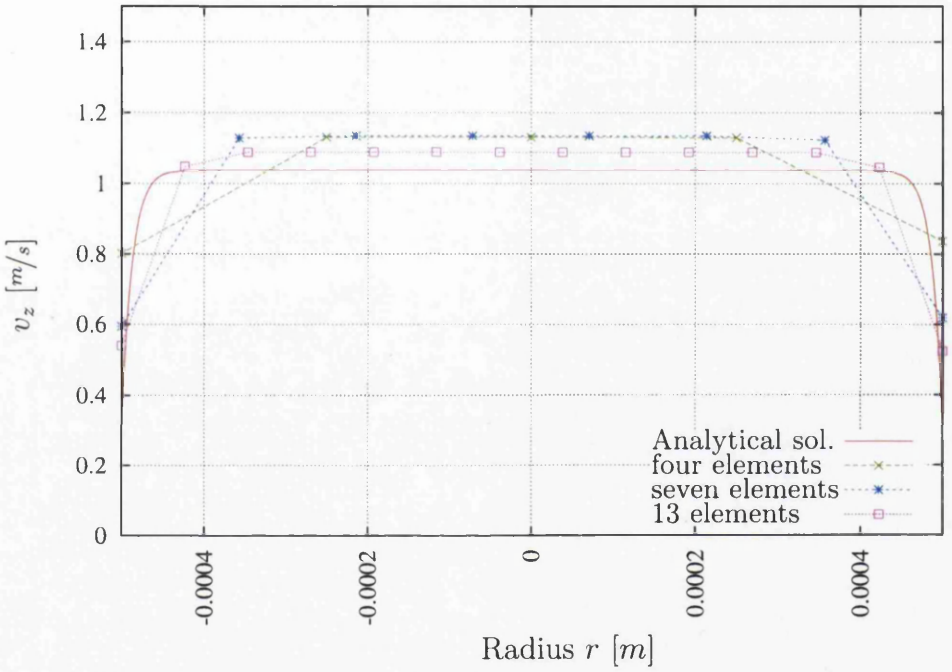

Figure 6.6: Exit velocity profile in flow direction for the simple test case with varying mesh refinement.

meshes and the analytical solution, the overall flow rate ratio $\dot{V}_{in}/\dot{V}_{out}$ is exact to within 0.3% for all cases, with a detailed listing found in Table 6.3. The inequality of the maximum velocity is balanced by varying wall slip velocities v_s. As the wall slip velocity is directly influenced by the shear rate at the wall, for linear elements, the distance of the first node from the wall is of crucial importance for the velocity profile, as wall slip effects are limited to a small zone near the wall and the shear stress distribution can only be determined as a constant within the element.

The analytical pressure value is obtained from Equation (5.27). This equation is

most easily solved for $\mathrm{d}P$ by rearranging into

$$\begin{aligned} f(\mathrm{d}P) = & \left(\frac{\pi^m R^{2m+1}}{2l\kappa_0 e^{c\left(T_{ref}-T\right)}}\right)^{1/m} \mathrm{d}P^{1/m} + \\ & \left(\left(2\pi\frac{n}{n+1}\left(\frac{1}{2}-\frac{n}{3n+1}\right)R^{\frac{3n+1}{n}}\right)\frac{1}{2l\mu_0 e^{b\left(T_{ref}-T\right)}}\right)^{1/n} \mathrm{d}P^{1/n} - \dot{V} \\ = & \quad a\mathrm{d}P^{1/m} + b\mathrm{d}P^{1/n} - \dot{V} = 0, \end{aligned} \tag{6.9}$$

an equation which can easily be solved by the Newton-Raphson method, yielding, in the present case, $\mathrm{d}P = 354.5\,bar$. This result, together with the simulation results of the various mesh densities, is displayed in Table 6.3. This result, showing an asymptotic convergence of the simulation to the analytical solution, is obtained by using the minimum pressure values at the inlet/outlet boundaries, as these values are generally thought to give a more accurate picture of the pressure conditions. Especially at the inlet, a pressure distribution with a peak value at $R = 0.0005$, the die wall, is noted. This peak is thought to be inherent in the numerical scheme and is thus discarded for analysis purposes, a procedure backed by the fact that the pressure quickly drops when moving towards the centre of the die. As an example, the maximum to minimum pressure ratio at the inlet, for a mesh density of thirteen elements, is determined to be $\mathrm{d}P_{max}/\mathrm{d}P_{min} = 1.098$. Alternatively, the data in Table 6.3 may also be displayed in a graph as shown in Figure 6.7.

Mesh density	$\dot{V}_{in}/\dot{V}_{out}$	$\mathrm{d}P$ [bar]	$\Delta\%$
4	99.896 %	431.9	+21.8 %
7	99.669 %	383.2	+8.1 %
13	99.684 %	363.6	+2.6 %
Analytical sol.		354.5	

Table 6.3: Results of mesh size study - flow rate and pressure drop.

In order to exclude any possible inlet/outlet effects, the values in Table 6.3 are verified by cutting an internal section of the die (in the present case, cross sections were taken 2.5 diameters from the entry/exit, resulting in a section of exactly half the total die length) were the flow is known to be stabilised. The average pressure is calculated and the pressure difference is extrapolated to the complete die length, giving the same pressure drops as shown in Table 6.3.

Concluding the mesh size study, we can specify a minimum mesh density of eight elements across any given section of the die with regard to Figure 6.7. Figure 6.8 shows the resulting tetrahedral mesh on the die exit plane. This mesh density is

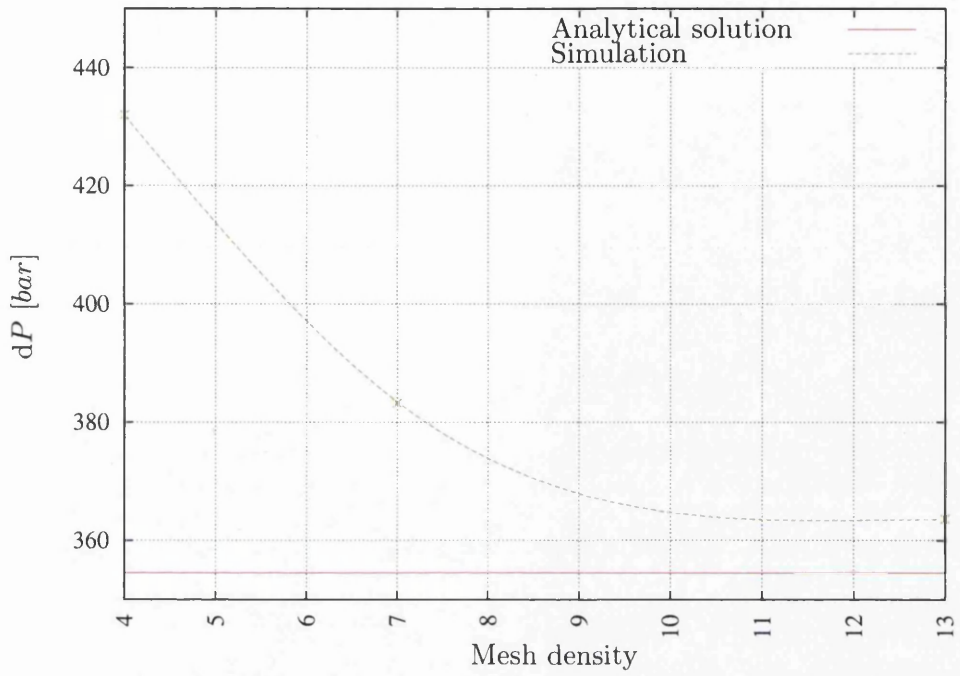

Figure 6.7: Results of mesh size study - visualisation of convergence. The mesh density is expressed in number of elements across the diameter at the exit.

sufficiently fine to restrict the divergence of the pressure drop to acceptable levels, yet coarse enough to result in an acceptable number of tetrahedral elements when meshing the volume of the die.

6.4.1 Mesh Density

In the following, results are presented for simulations of the unoptimised die, Figure 6.5, and the manually optimised die (the same die as the unoptimised one, but with conical openings towards the back of the die, according to Figure 2.9 b)), with a mesh density as seen in Figure 6.8. Given the fact that the latter figure only shows the surface mesh at the die exit, it is necessary to supply additional information regarding the mesh resizing strategy when considering the direction normal to the boundary of the computational domain as from one surface mesh, many different tetrahedral meshes can be created. Considering that a model with ca. one million elements requires around four days and four Gb of memory to solve on the present computer, a four processor `Alpha` system with 16 Gb of memory, it is desirable to reduce the number of tetrahedral elements as far as possible towards the centre of the model. This procedure of element reduction does not give rise to concerns about accuracy, as Figure 6.6 shows a very flat velocity

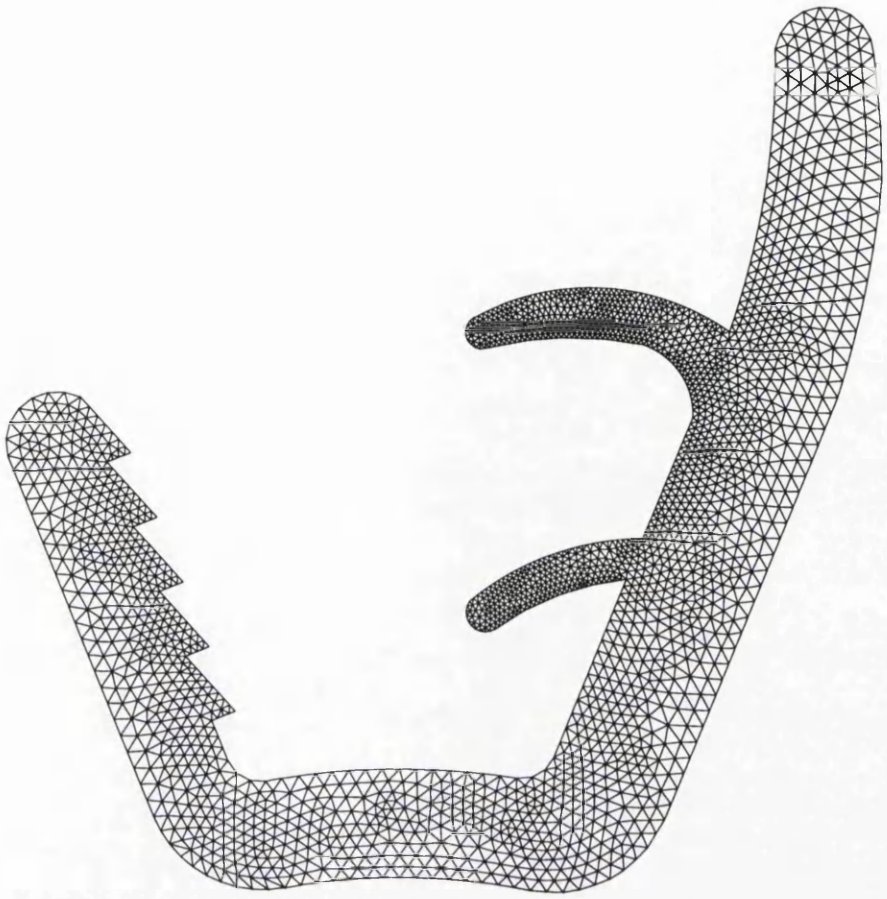

Figure 6.8: Minimum mesh density at the die exit.

profile for the given material parameters, thus leading to a degree of insensitivity of the model to the mesh size at its centre. For better quantification of the flow rate dependency on the mesh refinement, the surface mesh from Figure 6.8 was meshed with tetrahedral elements of varying refinement and the same processing conditions used for obtaining the data in Table 6.1. As a result, the averaged flow rate in the different partitions of the die is shown for the different mesh densities under consideration, Table 6.4. From this table, it can clearly be deduced that

	Partition acc. to Fig. 5.15 a)				
n_{el}	1	2	3	4	5
308,395	5.92	27.57	65.12	1.19	0.19
586,470	6.07	26.49	65.97	1.25	0.22
864,553	5.88	27.11	65.59	1.20	0.21

Table 6.4: Comparison of different mesh densities - Percentage of total flow rate, computed for each partition of the die exit.

there is no pronounced trend when introducing a coarser mesh towards the centre of the model. Also, it can be concluded, that the pressure drop does not influence

the results very much, at least not with respect to the average flow rate in the various partitions. As the medium mesh with 590,000 elements seems to form a reasonable compromise between model size and accuracy, this model is the one chosen for further analysis in Section 6.5.1.

6.5 Unoptimised Die

6.5.1 Influence of Extrusion Velocity

After determination of a suitable mesh refinement strategy, we are now in a position to conduct a series of simulations, modelling the experimental setup used in the trials, Appendix D.2. For each extrusion velocity under investigation, the last measurement for that speed in Table D.2.1 was chosen for temperature and inlet velocity boundary conditions, as these values are the ones most closely resembling the steady state. After the adaptation of the material parameters to the required temperature and the conversion of the inlet flow rate to an inlet velocity, simulations were executed with an input file according to Appendix G. The convergence of the solution for the different extrusion speeds is worthy of closer investigation. Figure 6.9 shows the number of outer iterations needed before the chosen residual of $L^1 = 0.001$ is reached. In this figure, the slowest extrusion

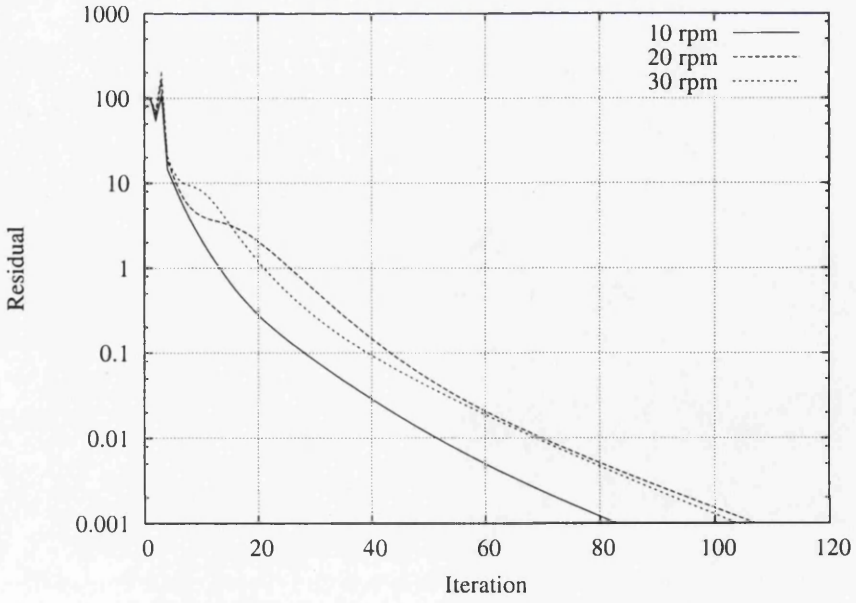

Figure 6.9: Convergence of the solution for different input velocities - unoptimised die.

speed, at 10 rpm, seems to show the fastest convergence, an observation which

is misleading upon closer inspection. For the higher iteration numbers within each of the simulations, where the convergence shows rather linear behaviour in the logarithmic plot, the effort for solving the inner linear system of equations (once for every iteration in Figure 6.9) is not the same at slow and high extrusion speeds. Commonly, five times more iterations were needed for the solution of the linear system of equations at ten rpm than at 20, thus leading to a longer overall computation time for the lower extrusion speeds. Between 20 and 30 rpm, this difference is much less noticeable.

After convergence is achieved, the partitioning procedure yields results according to Table 6.5. In Figure 6.10, the data from Table 6.5 is set in contrast to the ex-

	Partition acc. to Fig. 5.15 a)				
Extrusion speed [rpm]	1	2	3	4	5
10	11.97	29.26	56.68	1.68	0.40
20	6.07	26.49	65.97	1.25	0.22
30	4.40	26.23	68.00	1.17	0.20

Table 6.5: Simulation results at different different extrusion speeds in the unoptimised die - Percentage of total flow rate, computed for each partition of the die exit.

perimental results shown in Appendix D.2.2. Several observations regarding this comparison can be made. Most obvious is an imbalance that favours material flow into the biggest partition, number three, over the smaller ones. Partition number one is also classified with the under-supplied sections due to the ragged saw-tooth pattern on its right border, which leads to increased resistance and reduced flow. In this context, it is interesting to note that partition number two is balanced well for all of the extrusions speeds under consideration, a condition not met by the other partitions. While a general consistency between experiment and simulation can be observed, the gap between the two increases as the extrusion speed is increased. The biggest difference is observed at 30 rpm, and there especially for the small partitions, number four and five.

Regarding the cause of this difference between simulation and experiment, one main factor can be sought in the missing implementation of the extensional viscosity. However, before any further conclusions are drawn from the numbers in Table 6.5, it will be useful to present the results of the simulation of the manually optimised die, as together, the two sets of simulations will give a more complete picture of the situation. In Section 6.7 we will attempt to give a thorough explanation for the difference between the experimental and the simulation results.

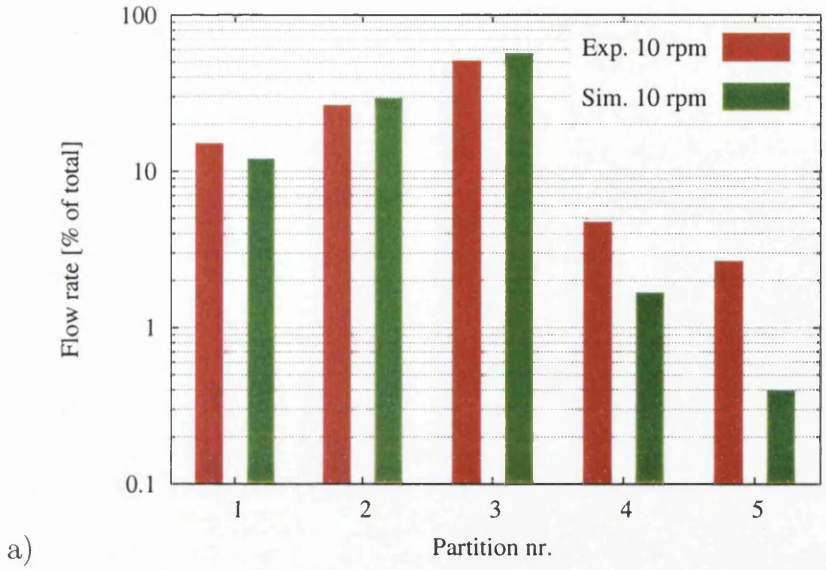

a)

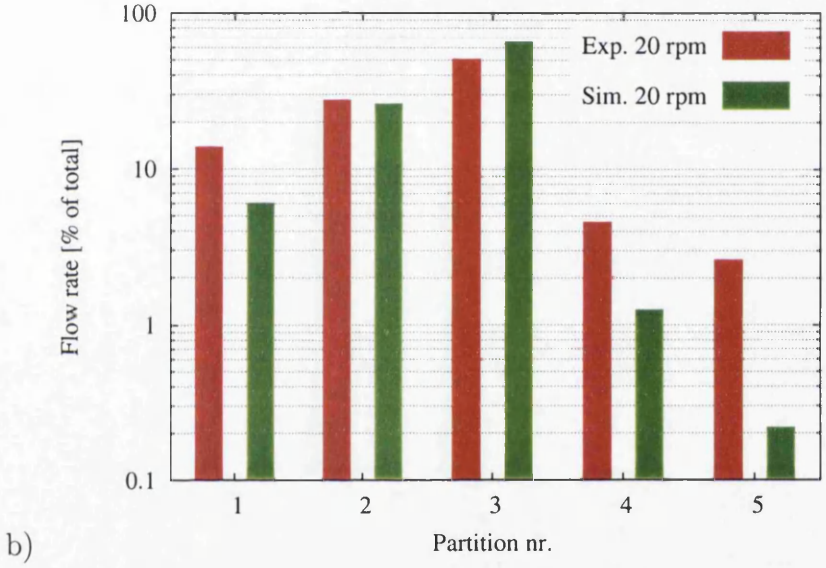

b)

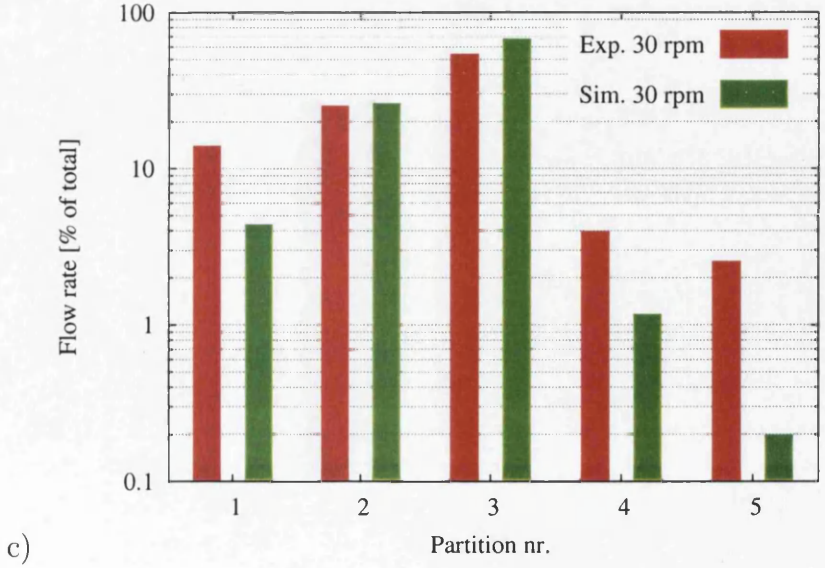

c)

Figure 6.10: Comparison profile extrusion - simulation, unoptimised die; a) ten rpm, b) 20 rpm and c) 30 rpm.

6.6 Manually Optimised Die

The die under investigation in the following simulations is an initial design by the industrial collaborator, manufactured with an optimised flow distribution in mind. As detailed in Section 5.3.2, we want to realize a flow rate distribution that reflects the relative proportion of the exit area for a given partition with respect to the total exit area, shown in Table 5.6 and repeated for convenience here, in Table 6.6. Under ideal conditions, the material distribution should reflect these

	Partition acc. to Fig. 5.15 a)				
	1	2	3	4	5
% of total die exit area	19.5	25.3	45.7	6.2	3.3

Table 6.6: Percentage of exit area.

percentages exactly, with only a minor dependence on the extrusion speed. As the present optimised die represents only a first iteration of the design cycle, we can expect an improved material flow in comparison with the unoptimised die that does, however, not fully match the numbers given in Table 6.6.

6.6.1 Influence of Extrusion Velocity

Following the same procedure as chosen in Section 6.5.1, we conduct a series of simulations at ten, 20 and 30 rpm. Based on the mesh size study, we generate a mesh under use of the same refinement strategy employed for the unoptimised die, resulting in a mesh size of $n_{el} = 413,701$. While smaller than for the unoptimised die, this element number is not considered to be less refined, due to the better volume to surface ratio V_Ω/S_Ω of the computational domain Ω. In the converging sections of the die (see Figures 2.9 a) and b)), all the fine sections of the profile become more wide, leading to more effective creation of a coarse mesh at the centre of the domain. With the processing conditions for the second die, as extracted from Table D.2.1 in the appendix, boundary conditions are applied according to Figure 6.1. The iterative progress of the simulations of the optimised die, shown in Figure 6.11, shows faster convergence compared to the unoptimised die, Figure 6.9. In conformity with the change in the number of elements, this reduction of computational cost is due to a smoother domain Ω, where the extreme differences between the cone and the unoptimised die are reduced.

After performing the partitioning and the analysis of the average flow rate, a situation as outlined in Table 6.7 is found. At this point, it is interesting to compare

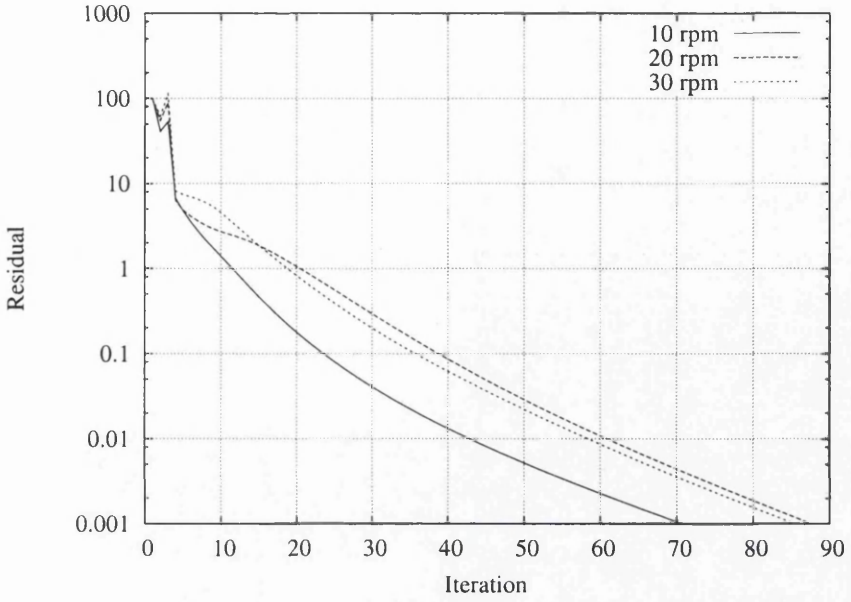

Figure 6.11: Convergence of the solution for different input velocities - manually optimised die.

	Partition acc. to Fig. 5.15 a)				
Extrusion speed [rpm]	1	2	3	4	5
10	22.79	28.64	43.70	4.00	0.87
20	22.86	29.98	44.66	2.19	0.31
30	23.23	30.61	44.19	1.78	0.20

Table 6.7: Simulation results at different different extrusion speeds in the manually optimised die - Percentage of total flow rate.

these results with the exit area values from Table 6.6. A significant improvement of the flow distribution over the numbers given in Table 6.5 is immediately obvious, proving that the manual optimisation process gives satisfying results. Generally, the results differ only slightly from the optimum, with the exception of the small partitions, number four and five. Apart from these two, the comparison with the experimental results from Appendix D.2.2 gives better consistency than for the unoptimised die, as shown in Figure 6.12.

In analogy to the unoptimised die, the best conformity between simulation and experiment for the optimised die is achieved at the slowest extrusion speed, with increasing errors as the extrusion speed is increased.

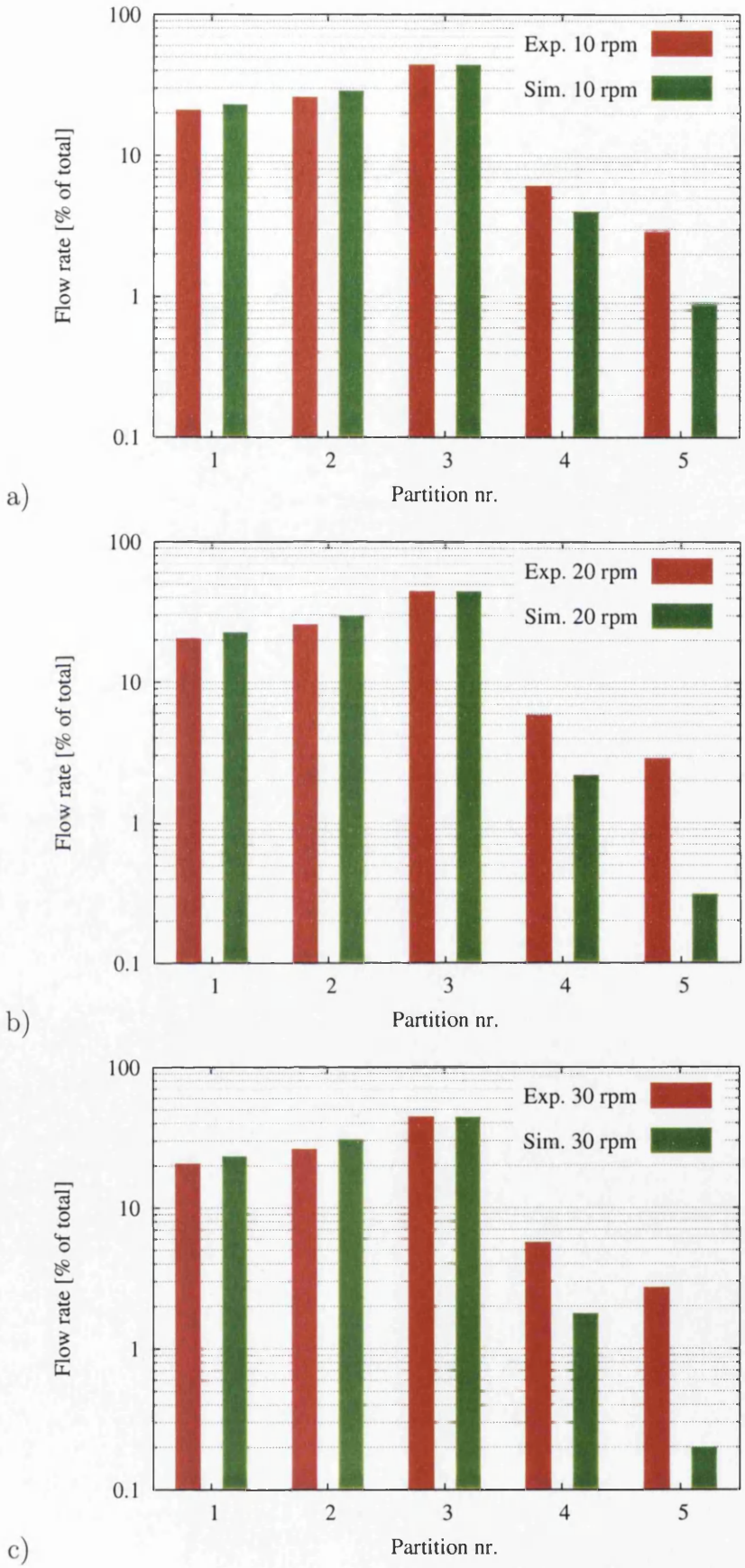

Figure 6.12: Comparison profile extrusion - simulation, manually optimised die; a) ten rpm, b) 20 rpm and c) 30 rpm.

6.7 Conclusions

6.7.1 Convergence

It is necessary to note that the convergence of the present extrusion simulation is considered to be rather slow. While many factors may contribute to this effect, two aspects of the present simulation can be determined as major causes for this behaviour. In Figure 6.13, the convergence for three different simulations at 20 rpm is plotted, clarifying these causes. The fastest convergence is achieved with

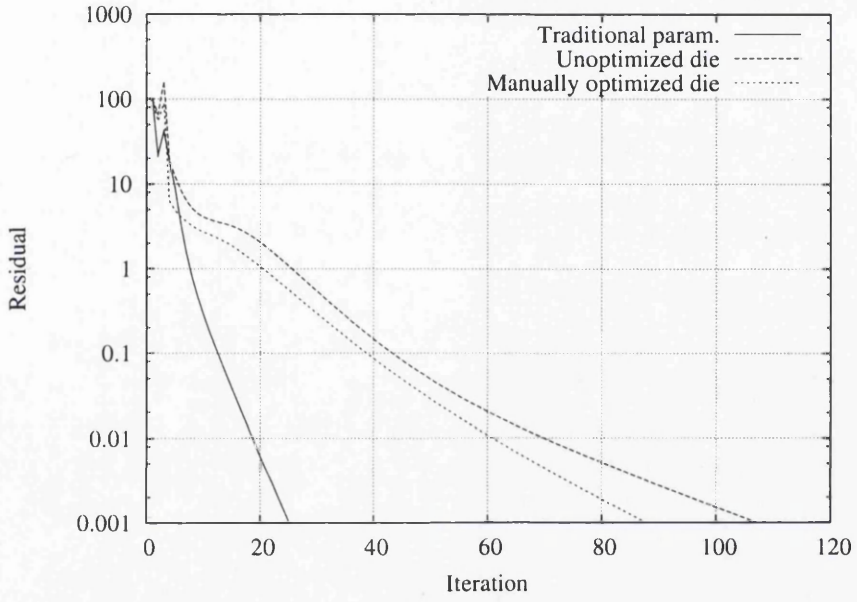

Figure 6.13: Convergence of the solution for different models at 20 rpm. Shown is the convergence for a model with traditional material parameters, the unoptimised die (Section 6.5) and the manually optimised die (Section 6.6).

traditional material parameters ($\mu_0 = 1.1428 \cdot 10^5$, $n = 0.27$, $\kappa_0 = 1.0 \cdot 10^6$ and $m = 1.0$) as found in Section 6.3.1. Next, we find the manually optimised die with the improved computational domain (see Section 6.6) and finally, with the highest number of iterations, the unoptimised die (see Section 6.5). In the light of the simulation results presented previously, it is no surprise that the unoptimised die shows the worst convergence, especially when comparing a shear law index of $n = 0.0266$ with $n = 0.27$. The very low shear law index will result in a highly unfavourable equation system, thus increasing the number of iterations. As convergence is achieved and the usual requirements, like mass conservation ($\dot{V}_{in} = \dot{V}_{out}$), are fulfilled, the high iteration number can be seen as detrimental to the computation time, without any further effect on the simulation in terms

of accuracy.

6.7.2 Influence of Extensional Viscosity

At this point, we are in a position to give reasons for the difference between experiment and simulation, especially as observed in the simulation of the unoptimised die. One main reason can be found in the missing implementation of the extensional material parameters. The derivation of the Trouton ratio in Section 4.2.2 leads to the conclusion that for uniaxial extension and $Tr = 3$, the extensional viscosity does not require any special treatment in the numerical implementation. For differing Trouton ratios however, a growing error is introduced as the deviation from three increases. Thus, the growing error when increasing the extrusion speed, as observed in Figures 6.10 and 6.12, can be explained by an increasing Trouton ratio. It is useful for this purpose to estimate the Trouton ratio for a capillary with spherical converging flow under the conditions encountered in the profile die. In analogy to the profile extrusion simulations, the extrusion speeds of ten, 20 and 30 rpm are used as a basis for the estimation.

Walters [3] derives the conical converging flow into a capillary from the basic equations of fluid mechanics in spherical coordinates, where r denotes the radial direction, θ and χ the angles (see Figure 6.14). As we want to calculate the

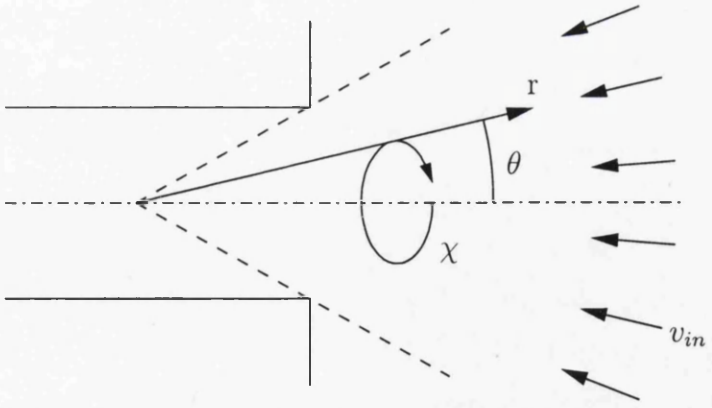

Figure 6.14: Spherical converging flow into a capillary

extension rate $\dot{\varepsilon} = {}^{\partial v_r}/_{\partial r}$, we start with the velocity in radial direction

$$v_r = -\frac{\dot{V}}{r^2}, \tag{6.10}$$

which is differentiated to give

$$\frac{\partial v_r}{\partial r} = \dot{\varepsilon} = \frac{1}{2}\frac{\dot{V}}{r^3}. \tag{6.11}$$

In the following, we will determine an estimated average Trouton ratio for each of the three extrusion speeds and for every partition under consideration, based upon the extensional rate calculated in Equation (6.11). From these 15 values, it will be possible to assess the error introduced by omitting extensional behaviour from the simulation. As an example of the Trouton ratio determination, partition one is chosen at an extrusion speed of 10 rpm. As a preliminary measure, some values are noted as the basis of the calculation:

- Material parameters according to Table 5.9
- Experimental results from Appendices D.2.1 and D.2.2
- $T_{ref} = 100°C$
- $T = 99.53°C$
- Exit area of the profile die $A_{exit} = 182\,mm^2$
- Radius of the capillary die $r_1 = 0.55\,mm$ used in Equation (6.11); this value is determined from the average profile width
- Total flow rate through the profile of $\dot{V}_{tot} = 1.4756 \cdot 10^{-5}\,m^3/s$
- percentage of the total material passing through partition one $R_{M,1} = \dot{V}_1/\dot{V}_{tot}$ (see Appendix D.2.2)

In a first step, it is necessary to calculate the ratio A_{cap}/A_{part} of the capillary (see Figure 6.14) with radius r_1 with regard to the area of partition one. With this ratio, we can calculate the flow rate through the capillary by means of the total flow rate $\dot{V}_{tot}$, the percentage of the total flow rate going through partition one (see Appendix D.2.2) and the aforementioned ratio A_{cap}/A_{part} as

$$\dot{V}_{cap,1} = \underbrace{\dot{V}_{tot} R_{M,1}}_{\dot{V}\text{ part. 1}} \frac{A_{cap}}{A_{part}}. \tag{6.12}$$

This intermediate step is necessary, as we want to get the flow rate in the capillary equivalent to the one in the partition. Using Equation (6.11), we get

$$\dot{\varepsilon}_1 = \frac{1}{2}\frac{\dot{V}_{cap,1}}{r_1^3}, \tag{6.13}$$

which can be used in Equation (4.17). After adapting the material parameters μ and μ_e from the reference temperature to the extrusion temperature, the usual definition of the Trouton ratio, Equation (4.11), can now be used to result in $Tr = 3.93$ for partition one at ten rpm. Following the above steps for all extrusion speeds and partitions results in a matrix as shown in Table 6.8. When

	Partition acc. to Fig. 5.15 a)				
Extrusion speed [rpm]	1	2	3	4	5
10	3.93	1.79	1.48	7.69	10.03
20	5.71	3.00	2.34	11.70	15.70
30	7.37	3.47	3.22	12.83	19.47

Table 6.8: Estimate of the Trouton ratio for different extrusion speeds and partitions.

analysing these Trouton ratios, the errors in the simulation results can be explained easily. The increasing error for increasing extrusion speeds when looking at any given partition is due to higher Trouton ratios, with the most dramatic increase observed for partition five. In the same manner, we can make out the cause for bigger errors in small partitions when comparing different partitions at a given extrusion speed.

In conclusion, the introduction of extensional viscosity in the simulation code should benefit the accuracy greatly, a step left for future work due to time constraints.

Chapter 7

Conclusion

7.1 Main Achievements

The findings of the present work span a range of different subjects, a concentrated summary of which is given in the following paragraphs.

7.1.1 Analysis of the Rheological Data from Aberystwyth

The complex shear modulus and the complex viscosity from the oscillatory experiments conducted at the University of Wales Aberystwyth were used to create viscosity vs. shear rate plots by application of the Cox-Merz rule. In a following step, power law parameters were created from this plot by extracting the gradient and the offset of the graph. Several parameter sets are found by making use of either the complex viscosity, the viscous part of the complex viscosity, the shear viscosity as extracted from capillary data or the extensional viscosity. As oscillatory data was available at four different temperatures ranging from 60°C to 120°C, it was possible to extract a temperature dependence, completing the set of material parameters for the shear power law.

7.1.2 Design of an In-Line Rheometer

In the course of this work, two rheometrical instruments were designed and manufactured. The first of these is a so-called torpedo, located at the point in the flow path were the annular flow, coming from the extruder, gets united into a converging flow towards the die. This semi-spherical dome is instrumented with two

miniature pressure transducers and one thermocouple. As the pressure transducers exhibited a varying drift related to the current temperature, it proved difficult to make use of the numerical values recorded in the data log. The graph, however, still can be used to gain a general idea of the pressure conditions in the die. The thermocouple on the other hand proved very useful in logging the change in temperature. The torpedo was used both in profile and in rheometrical extrusion as its only difference from the standard, non-instrumented torpedo are the slightly protruding sensors.

The second instrument, a generic in-line rheometer, involved a more complicated design process, as several design criteria had to be met for creating a true *in-line* situation. First, and most importantly, the shear rate range covered by the instrument had to be matched with the flow in a typical profile die. This goal was achieved by the use of adjustable overflow valves and the use of capillary dies resembling the geometrical conditions in the die with regard to length and diameter. A further specification to be incorporated into the rheometer was the need for an easily exchangeable capillary die. This requirement was fulfilled by relying on a sliding bar mechanism that allows for a quick change of die after the extruder has been switched off to reduce the pressure on the die bar. As the residence time was another point of concern, a die opening for purging the volume upstream of the die was also incorporated into the sliding bar. The rheometer was fitted with one pressure sensor before the entry to the die, which provided very stable readings, while the temperature was obtained from the sensor in the torpedo.

7.1.3 Rheometer Trials

Several trials were conducted with the new rheometer and two different rubber compounds, all of which were logged on a computer for later analysis. In order to gather data at a range of processing conditions, a trial matrix consisting of different extrusion speeds and die lengths (including zero length dies) and diameters was established. Several initial analyses were performed and the data was presented with regard to flow rate, pressure drop and apparent viscosity.

7.1.4 Profile Die Trials

For the purpose of studying a profile die exhibiting the problems typically encountered, it was necessary to design a generic profile die. This die, including

sections of different width and sharp angles, was manufactured at the industrial collaborators site. Furthermore, a second die was created, showing the improvements proposed by the die designers in order to result in a more balanced flow distribution compared to the first die with straight walls. These two dies were trialled with two different materials under the typical range of extrusion velocities. Flow rate measurements were based on the weight of profile strips collected during pre-determined intervals together with density measurements.

In preparation for the comparison between experiment and simulation, the profile cross sections were scanned on a flatbed scanner and partitioned, separating the various limbs of the profile. This process was repeated for several samples at each extrusion speed. By counting the black pixels for each of the partitions of the profile, it was possible to generate a connection between the area of the cross section and the flow rate in that partition. This data was collected and stored for use in the comparison with simulation results.

7.1.5 Material Parameter Determination

Based on the pressure drop and flow rate data gathered in the rheometer trials, a parameter determination was undertaken, including three relevant material laws. Apart from shear viscosity, wall slip and extensional viscosity were included, each one of them displaying a temperature dependence.

Two analytical equations, describing the flow through a capillary under the aforementioned flow effects, were derived for use in the determination process. On one hand, the entry flow was described for shear and extensional viscosity, on the other the capillary flow including shear behaviour and wall slip. Thus, both flow regimes for the flow through a capillary were covered and use was made of both the zero length and the capillary experimental data.

In the following, two concepts were used to obtain material parameters after a suitable objective function was defined for fitting the experimental data with the analytical equations. First, a response surface calculation was performed, where nested iterative loops were used to vary all of the design variables, i.e. the material parameters under investigation, resulting in a matrix of objective function values of the order of the number of material parameters. At the minimum of this set of objective values, the correct set of material parameters can be found. This approach, while very simple and convenient, has two drawbacks. Besides the fact that a full response surface calculation takes a large amount of computational time, due to the nested iterative loops, the resolution of the grid created by

the calculations needs to be small enough to resolve every detail of the response surface. The latter requirement was found to be an issue in the current context, as the response surface proved to exhibit a very shallow optimum. In consequence, the response surface method was used to present results for the case of wall stick, under variation of the shear power law parameters. It was later possible to classify the result with regard to the literature.

For the full parameter optimisation, another optimisation strategy, the Levenberg-Marquardt algorithm, was used. By combining the evaluation of the analytical entry and capillary flow equations into one objective function, it was possible to create a flexible optimisation framework. After validation of the method in comparison with the response surface results for two free material parameters, a full analysis with nine material parameters was executed. In result of this analysis, two optima, depending on the initial values for the material parameters, were found. The reason for this duality was found in the composition of the objective function, where an addition of two analytical terms occurs. As a wide variation of starting conditions always results in one of the two optima, further optima can confidently be dismissed as non-existent. After a thorough investigation of the literature available on the rheology of rubber, one of the two optima was clearly dismissed, leading to a unique solution for the material parameters. This solution lead to the conclusion that a separation of shear and wall slip effects is imperative for the accurate simulation of the flow of rubber compounds.

7.1.6 Comparison of Experimental and Simulation Results

A number of simulations, taking into account shear viscosity changes and wall slip, were conducted on the basis of the newly found material parameters, after the physical problem and the numerical conditions were well established. Both the unoptimised and the manually optimised die were compared with experimental results. Differences between experiment and simulation were explainable after an estimate of the Trouton ratio was obtained for the flow in the different sections of the profile. A strong connection between high Trouton numbers and underprediction of flow into narrow partitions of the die was established, leading to the recommendation that extensional viscosity effects should be included in the simulation code.

7.2 Future Work

Although this work is conclusive with regard to its initial goals, there is a number of areas where further investigation is needed, either because more significant results could be obtained without much effort, or because the time frame did not allow any further study.

7.2.1 Inclusion of Extensional Effects into the Simulation Code

The consideration of extensional effects would be the next logical step in advancing the accuracy of the simulation. Even if it is believed that neglecting the extensional viscosity might result in acceptable optimisation results due to an improved Trouton ratio distribution between the different partitions, an implementation of extensional viscosity would result in accurate results from the start of the optimisation procedure. Thus, the introduction of extensional behaviour is considered, in the light of the findings of this work, to be a necessity for accurate results under all circumstances.

The use of extensional viscosity in finite element simulation was under investigation within the research group as part of a related project (see [84]) which yields interesting conclusions regarding the treatment of extensional viscosity. At the highest level, visco-elastic and viscous material descriptions have to be distinguished. Visco-elastic models include, in the form of the deformation history, extensional effects. While of high accuracy, visco-elastic models have, due to the consideration of this deformation history, an unacceptable numerical cost, as detailed in Section 4.1. Viscous models on the other hand, do not incur this penalty, at the cost of reduced accuracy. As a result, these models, which are based on the instantaneous, local deformation rates, are easier to implement. Several such implementations have been developed, based on experimental observation.

- Mitsoulis [85] proposes a model which, while directly implemented in the finite element formulation, displays dependence on the frame of reference. This results in difficulties when applying this approach to generic flow problems and is the reason why no further investigation was considered.
- Schunk [86] presents a scheme based on the relative rotation rate of the

strain rate tensor, where a combined viscosity η_c is defined as

$$\eta_c = W\eta_s + (1 - W)\,\eta_e. \tag{7.1}$$

The weighting function W is usually based on the relative rotation rate and has to range from zero for pure extension to one for the case of pure shearing. The combined viscosity η_c replaces the traditional shear viscosity in the numerical formulation and η_s and η_e are calculated by a convenient non-Newtonian model.

- A third model is indicated by Song [87], who bases his phenomenological investigations on the third Invariance of the strain rate tensor, III_ε. In defining a combined viscosity η_c similar to the one given by Schunk, it is established that

$$\eta_c = \eta_s Tr\,(III_\varepsilon)\,. \tag{7.2}$$

The extensional viscosity is considered via the use of the Trouton ratio in this context and an indifference to the frame of reference is given. The Trouton ratio has to be defined such that it becomes one for simple shear, given through $III_\varepsilon = 0$ and $Tr\,(III_\varepsilon) = 1$. For increasing levels of extension on the other hand, $Tr\,(III_\varepsilon)$ will increase according to the importance of extension in relation to shear.

Both Schunk's and Song's work show potential viability with regard to an inclusion into the simulation code. The major benefit of these models is the use of η_c, which is likely to reduce the number of changes to the existing code to a minimum.

7.2.2 Realisation of the Automated Optimisation Framework

Clearly, it would be desirable to further advance the development of the framework for the automated optimisation of a profile die from initial CAD model to optimised CAD model (as presented in Figure 2.10). It is unfortunate that this final step in rounding off the present work could not be taken, especially as the remaining work for the creation of a functioning optimisation is not estimated to be more than three months. All the basic blocks for the optimisation loop are already existent within the research group (see [88]), thus mainly requiring an effort in including the simulation code in the framework.

- Beginning with the unoptimised CAD model in IGES format, a pre-processor (based on the Open Cascade library [89]) is available, which is able to read two dimensional slices of the die, from the entry of the cone to the exit of the profile die. After these slices are connected semi-automatically by ruled surfaces, colour-coded parametrisation variables are added to specific features such as lines, arcs or splines. These variables specify in which direction, and within which boundaries the design variables of the optimisation problem are allowed to vary. No further preparation work is required up to this stage, as some manual work in preparation for the central optimisation cycle is unavoidable.

- An automatic mesher is in existence, capable of tetrahedral mesh creation with some capabilities regarding graduated mesh creation. These refinement capabilities, which are based upon the variation of the mesh size according to the z-coordinate of the model, require some enhancement in order to deal with the complex geometry encountered in the profile die.

- The simulation code Fantazt is ready for use at the centre of the optimisation problem, subject to inclusion of extensional viscosity, as seen above.

- Automatic post-processing capabilities have been developed in the course of this work. Missing is an automated scheme for the extraction of the flow rates in the various partitions of the die, as this data is collected manually at the moment.

- An optimisation algorithm is ready for adaptation from a two dimensional optimisation, described as part of a parallel project to the current one (see [88]). A suitable objective function, based on the flow rate distribution in the different partitions and the average flow rate of the whole die presents itself as an obvious candidate for solving this optimisation problem.

- As the CAD model is updated throughout the optimisation process, the extraction of the CAD geometry after convergence of the optimisation is a trivial task, a considerable advantage over schemes based purely on finite element models.

The tasks presented above show, that the process of creating an automated optimisation framework is at an advanced stage and could be completed within a reasonable time frame. The major work lies in combining the various stages of the scheme and further automation of present steps that are currently carried out manually.

7.2.3 Further Studies with the In-Line Rheometer

As the design effort in creating the rheometer described in Section 5.2 has already been spent, it would be a simple task to establish a series of trials for the further characterisation of rubber compounds. As the two standard rubber compounds used at the industrial collaborators site have been studied fairly extensively, it would now be possible to enlarge the spectrum of processing conditions to more uncommon situations regarding pressure conditions (by adjusting the overflow valves, see Figure 5.5) and extrusion speeds. Furthermore, it would be interesting to study the extrusion of other rubber compounds, including pure EPDM.

Bibliography

[1] E. A. Muccio. *Plastics Processing Technology.* ASM International, Materials Park, Ohio, 1994.

[2] C. M. Blow and C. Hepburn. *Rubber Technology and Manufacture.* Butterworth Scientific, London, second edition, 1982.

[3] K. Walters. *Rheometry.* Chapman and Hall Ltd, London, 1975.

[4] W. H. Press, S. A. Teukolsky, W. T. Vetterling, and B. P. Flannery. *Numerical Recipes in C.* Cambridge University Press, Cambridge, UK, 1993.

[5] J. L. White, Y. Wang, I. Isayev, N. Nakajima, F. C. Weissert, and K. Min. Modelling of Shear Viscosity Behaviour and Extrusion through Dies for Rubber Compounds. *Rubber Chemistry and Technology*, 60:337–360, 1987.

[6] G. J. Osanaiye, A. I. Leonov, and J. L. White. Investigations of the Rheological Behaviour of Rubber-Carbon Black Compounds over a wide Range of Stresses including very low Stresses. *Journal of Non-Newtonian Fluid Mechanics*, 49:87–101, 1993.

[7] C. Jepsen and N. Räbiger. Untersuchungen zum Wandgleitverhalten von Kautschukmischungen an einem Hochdruck-Kapillar-Viskosimeter. *Kautschuk + Gummi Kunststoffe*, 41:342–352, 1988.

[8] J. L. White. *Rubber Processing: Technology, Materials, Principles.* Hanser-Gardner, Cincinnati, 1995.

[9] H. A. Barnes, J. F. Hutton, and K. Walters. *An Introduction to Rheology.* Elsevier Science Publishers B.V., Amsterdam, 1989.

[10] A. C. Bassi and U. Della Piane. Misure su Materiali Elastomerici con il Reometro Capillare. *Industria della Gomma*, 203:37–48, 1974.

[11] Z. Tadmor and I. Klein, editors. *Engineering Principles of Plasticating Extrusion.* Robert E. Krieger Publishing Company, Huntington, 1978.

[12] C. Bernhardt, editor. *Processing of Thermoplastic Materials.* Reinhold Publishing Corporation, New York, 1959.

[13] H. J. Ettinger, J. Sienz, J. F. T. Pittman, and I. Szarvasy. Parameterization Techniques for Two- and Three-Dimensional Automated Optimization of PVC Extrusion Dies. In *Polymer Processing Society PPS 18*, Guimarães, June 2002.

[14] R. B. Bird, W. E. Stewart, and E. N. Lightfoot. *Transport Phenomena.* John Wiley and Sons, Inc., New York, 1960.

[15] J. M. Powers. *Lecture Notes on Intermediate Fluid Mechanics.* Lecture Notes.

[16] R. I. Tanner. *Engineering Rheology.* Oxford University Press, New York, 1992.

[17] F. S. Sherman. *Viscous Flow.* Mc-Graw-Hill, New York, 1990.

[18] R. Aris. *Vectors, Tensors, and the Basic Equations of Fluid Mechanics.* Prentice-Hall, London, 1962.

[19] W. Blanke. *Thermophysikalische Stoffgrößen.* Springer, Berlin, 1989.

[20] M. J. Crochet, A. R. Davies, and K. Walters. *Numerical Simulation of Non-Newtonian Flow.* Elsevier, Amsterdam, 1984.

[21] C. D. Han. *Rheology in Polymer Processing.* Academic Press, New York, 1976.

[22] J. A. Dantzig and C. L. Tucker III. *Modeling in Materials Processing.* Cambridge University Press, Cambridge, 2001.

[23] T. A. Osswald and G. Menges. *Materials Science of Polymers for Engineers.* Hanser, Munich, 2003.

[24] J.-F. Agassant. *Polymer Processing.* Hanser, Munich, 1991.

[25] S. A. McGlashan and M. E. Mackay. Comparison of Entry Flow Techniques for Measuring Elongation Flow Properties. *Journal of Non-Newtonian Fluid Mechanics*, 85:213–227, 1999.

[26] F. N. Cogswell. Measuring the Extensional Rheology of Polymer Melts. *Transactions of The Society of Rheology*, 16:383–403, 1972.

[27] D. Sarkar, T.-H. Wu, P. Beaupre, M. Gupta, and F. A. Morrison. Estimation of Elongational Viscosity from Contraction Flow. In *XIIIth International Congress on Rheology*, Cambridge, UK, 2002.

[28] D. M. Binding. An Approximate Analysis For Contraction And Converging Flows. *Journal of Non-Newtonian fluid Mechanics*, 27:173–189, 1988.

[29] W. L. Wilkinson. *Non-Newtonian Fluids.* Pergamon Press, New York, 1960.

[30] F. A. Holland and R. Bragg. *Fluid Flow for Chemical Engineers.* Edward Arnold, London, 1995.

[31] H. Schlichting. *Boundary-Layer Theory.* Mc-Graw-Hill, New York, 1979.

[32] M. Mooney. Explicit Formulas for Slip and Fluidity. *Journal of Rheology*, 2:210–222, 1931.

[33] J. L. Leblanc. Rubber-filled Interactions and Rheological Properties in Filled Compounds. *Progress in Polymer Science*, 27:627–687, 2002.

[34] P. G. de Gennes. Wetting: Statistics and Dynamics. *Reviews of Modern Physics*, pages 827–863, 1985.

[35] F. Brochard and P. G. de Gennes. Shear-Dependent Slippage at a Polymer/Solid Interface. *Langmuir*, 8:3033–3037, 1992.

[36] K. Walters, editor. *Rheometry: Industrial Applications.* Research Studies Press, Chichester, 1980.

[37] A. G. Fredrickson. *Principles and Applications of Rheology.* Prentice-Hall, Englewood Cliffs, 1964.

[38] F. N. Cogswell. *Polymer Melt Rheology.* George Godwin Limited, London, 1981.

[39] M. A. Couch and D. M. Binding. E8246 Rubber Rheology - Experimental Results. Internal Report.

[40] S. Montes, J. L. White, and N. Nakajima. Rheological Beahviour of Rubber Carbon Black Compounds in Various Shear Flow Histories. *Journal of Non-Newtonian Fluid Mechanics*, 28:183–212, 1988.

[41] U. Fischer. *Tabellenbuch Metall.* Verlag Europa-Lehrmittel, Haan-Gruiten, 1997.

[42] J. L. Leblanc. Pertinent Rubber Extrusion Experiments with an Instrumented Extruder. *Journal of Elastomers and Plastics*, 22:97–115, 1990.

[43] J. L. Leblanc. Wall Slip and Compressibility like Effects in Capillary Rheometer Tests on Complex Polymer Systems. *Plastics, Rubber and Composites*, 30:282–291, 2001.

[44] U. Eisele. Einflüsse der Molekülstruktur auf Verabeitungs- und Festigkeitseigenschaften von hauptvalenzmäßig vernetzten Polymeren. *Kautschuk + Gummi Kunststoffe*, 33:165, 1980.

[45] M. Gupta. Estimation of Elongational Viscosity of Polymers from Entrance Loss Data Using Individual Parameter Optimization. *Advances in Polymer Technology*, 85:98–107, 2002.

[46] O. H. Nouatin, L. Gavrus, T. Coupez, B. Vergnes, and J.-F. Agassant. Inverse Method for the Identification of the Rheology of Molten Polymers. In *The* 4^{th} *international ESAFORM Conference on Material Forming*, pages 395–398, 2001.

[47] T. Dal Negro, L. D'Alvise, Y. Chastel, and E. Massoni. Inverse Technique for Automatic Identification of Rheological Parameters in Combined Tension-Torsion and Compression Conditions. In *The* 4^{th} *international ESAFORM Conference on Material Forming*, pages 419–422, 2001.

[48] N. Billon, E. Gorlier, and J. M. Haudin. Characterisation of Polyethylene Terephtalate close to glass transition using Inverse Analysis. In *The* 4^{th} *international ESAFORM Conference on Material Forming*, pages 390–393, 2001.

[49] E. Mitsoulis. Determination of Elongational Viscosity in a Spin-line Rheometer by Inverse Analysis. In *The* 5^{th} *international ESAFORM Conference on Material Forming*, pages 179–182, 2002.

[50] J. P. Ponthot and J. P. Kleinermann. Optimization methods for inverse modeling of forming processes. In *The* 4^{th} *international ESAFORM Conference on Material Forming*, pages 387–390, 2001.

[51] G. Astarita and M. E. Mackay. The Generalised Engineering Bernoulli Equation (GEBE) and the first and second laws of thermodynamics for viscoelastic fluids. *Journal of Rheology*, 40, 1996.

[52] M. E. Mackay and G. Astarita. Analysis of entry flow to determine elongation flow properties revisited. *Journal of Non-Newtonian Fluid Mechanics*, 70:219–235, 1997.

[53] R. B. Bird, R. C. Armstrong, and O. Hassager. *Dynamics of Polymeric Liquids.* John Wiley & Sons, Inc., New York, 1977.

[54] E. Massoni, R. Forestier, T. Dal Negro, Y. Chastel, and M. Bellet. Inverse Analysis for the Identification of Thermal and Mechanical parameters of Materials. In *The 5^{th} international ESAFORM Conference on Material Forming*, pages 159–162, 2002.

[55] E. Kreyszig. *Advanced Engineering Mathmematics.* John Wiley & Sons, Inc., New York, 1993.

[56] O. Ghouati and J.-C. Gelin. A Finite Element-based Identification Method for Complex Metallic Material Behaviours. *Computational Materials Science*, 21:57–68, 2001.

[57] `SciPy` Library of scientific tools for Python. `http://www.scipy.org/`.

[58] K. Geiger. Rheologische Charakterisierung von EPDM-Kautschukmischungen mittels Kapillarrheometer-Systemen. *Kautschuk + Gummi Kunststoffe*, 42:273–283, 1989.

[59] K. Geiger. Fließ- und Wandgleitverhalten von EPDM-Kautschukmischungen. *Kautschuk + Gummi Kunststoffe*, 42:663–664, 1989.

[60] M. G. Markovic, N. R. Choudhoury, M. Dimopoulos, J. G. Matisons, N. K. Dutta, and A. K. Bhattacharya. Rheological Behaviour of Highly Filled Ethylene Propylene Diene Rubber Compounds. *Polymer Engineering and Science*, 40:607–617, 2000.

[61] D. E. De Laney, V. Morrow, and J. Greene. Broad Spectrum On-Line Rheology. In *Proceedings of the SPE Annual Technical Conference (ANTEC)*, pages 1095–1099, 1996.

[62] C. H. Holzer. Praxisnahe Rheologische Untersuchungen an einer EPDM-Mischung. *Kautschuk + Gummi Kunststoffe*, 50:648–652, Sept. 1997.

[63] A. Y. Malkin, A. V. Baranov, and M. E. Vickulenkova. Experimental Estimation of Wall Slip for Filled Rubber Compounds. *Rheologica Acta*, 32:150–155, 1993.

[64] S. Montes, J. L. White, N. Nakajima, F. C. Weissert, and K. Min. An experimental Study of Slippage of Rubber Compounds using a modified Mooney Viscosimeter with Application to Extrusion. In *132nd Meeting, Rubber Division, American Chemical Society*, pages 1–44, 1987.

[65] H. J. Song, J. L. White, K. Min, N. Nakajima, and F. C. Weissert. Rheological Properties, Extrudate Swell and Die Entry Extrusion Flow Marker Experiments for Rubber-Carbon Black Compounds. *Advances in Polymer Technology*, 8:431–449, 1988.

[66] D. M. Turner and M. D. Moore. The Contribution of Wall Slip in the Flow of Rubber. *Plastics and Rubber: Processing*, pages 81–84, 1980.

[67] L. L. Li and J. L. White. Rheological Behaviour of Highly Filled EPDM Compounds with Calcium Carbonate, Carbon Black, Silica and Zinc Oxide. *Rubber Chemistry and Technology*, 69:628–636, 1996.

[68] K. C. Shin, J. L. White, R. Brzoskowski, and N. Nakajima. Rheological Behaviour and Extrudate Shrinkage of Rubber-Carbon Black Compounds. *Kautschuk + Gummi Kunststoffe*, 43:181–188, 1990.

[69] Y. M. Joshi, A. K. Lele, and R. A. Mashelkar. A Unified Wall Slip Model. *Journal of Non-Newtonian Fluid Mechanics*, 94:135–149, 2000.

[70] P. Jay, J. M. Piau, N. El Kissi, and J. Cizeron. Numerical Simulation of the Transition from Adhesion to Slip with Friction in generalized Newtonian Poiseuille Flow. *Journal of Non-Newtonian Fluid Mechanics*, 77:233–251, 1997.

[71] Altair `Hypermesh`. `http://www.altair.com/software/hw_hm.htm`.

[72] MSC.Software Corporation, Los Angeles. *MSC.*`Nastran` *Quick Reference Guide.*

[73] R. Codina. `Fantom`. Flow Analysis Numerical Techniques Organized Moduli. `http://www.rmee.upc.es/homes/codina/`.

[74] R. S. Tuminaro, J. N. Shadid, and M. Heroux. `Aztec`. A Massively Parallel Iterative Solver Library for Solving Sparse Linear Systems. `http://www.cs.sandia.gov/CRF/aztec1.html`.

[75] H. Kuchling. *Taschenbuch der Physik.* Fachbuchverlag Leipzig, Leipzig, 1995.

[76] O. C. Zienkiewicz and R. L. Taylor. *The Finite Element Method. Volume 3. Fluid Dynamics.* Butterworth-Heinemann, Oxford, 2000.

[77] C. L. Tucker III, editor. *Computer Modeling for Polymer Processing.* Hanser, Munich, 1989.

[78] F. Brezzi and M. Fortin. *Mixed and Hybrid Finite Element Methods.* Springer, Berlin, 1991.

[79] R. Codina and J. Blasco. Analysis of a Pressure-Stabilized Finite Element Approximation of the Stationary Navier-Stokes Equations. *Numerische Mathematik*, 87:59–81, 2000.

[80] R. S. Tuminaro, M. Heroux, S. A. Hutchinson, and J. N. Shadid. *Official* `Aztec` *User's Guide, Version 2.1.* Massively Parallel Computing Research Laboratory, Sandia National Laboratories.

[81] R. Ribó, M. de Riera Pasenau, E. Escolano, J. S. P. Ronda, L. F. González, and E. G. de la Rosa. `GiD`. *The Personal Pre and Postprocessor. User Manual.* International Center for Numerical Methods in Engineering, Barcelona.

[82] `Tecplot` User's Manual, 2003.

[83] W. J. Schroder, K. M. Martin, L. S. Avila, and C. C. Law. `VTK` *User's Guide.* Kitware Inc., 2000.

[84] H. J. Ettinger. Measurement and Determination of Elongational Viscosity Effects during the Extrusion of uPVC using an On-Line Rheometer.

[85] E. Mitsoulis, J. Vlachopoulos, and F. A. Mirza. A Numerical Study of the Effect of Normal Stresses and Elongational Viscosity on Entry Vortex Growth and Extrudate Swell. *Polymer Engineering and Science*, 25:677–689, 1984.

[86] P. R. Schunk and L. E. Scriven. Constitutive Equation for Modeling Mixed Extension and Shear in Polymer Processing. *Journal of Rheology*, 34:1085–1119, 1990.

[87] W. N. Song and Z. M. Xia. A Phenomenological Viscosity Model for Polymeric Fluid. *Journal of Non-Newtonian Fluid Mechanics*, 53:151–163, 1994.

[88] H. J. Ettinger. *Development of Optimization and Parameterization Techniques applied to Extrusion Die Design Optimization of PVC Profile Dies.* PhD thesis, University of Wales Swansea.

[89] `Open Cascade. http://www.opencascade.org/.`

Appendix A

Experiments Aberystwyth

A.1 Aberystwyth - Oscillatory Results; Complex Shear Modulus and Complex Viscosity

$\omega\left[\frac{\text{rad}}{s}\right]$	Osc. σ $\left[\frac{N}{m^2}\right]$	Strain $\left[\frac{m}{m}\right]$	$\delta\,[°]$	$G'\left[\frac{N}{m^2}\right]$	$G''\left[\frac{N}{m^2}\right]$	$\lvert\eta^*\rvert\,[Pa\,s]$	$\eta'\,[Pa\,s]$
628.3	3260	5.28E-04	7.27	6.61E+06	8.44E+05	1.06E+04	1.35E+03
499.0	5940	1.00E-03	9.48	6.16E+06	1.03E+06	1.25E+04	2.09E+03
396.5	6050	9.99E-04	8.52	6.19E+06	9.26E+05	1.58E+04	2.36E+03
314.9	6230	9.99E-04	10.07	6.26E+06	1.11E+06	2.02E+04	3.59E+03
250.1	5730	1.01E-03	12.69	5.58E+06	1.26E+06	2.29E+04	5.15E+03
198.7	5710	1.01E-03	8.26	5.63E+06	8.17E+05	2.86E+04	4.15E+03
157.8	5600	9.99E-04	8.56	5.57E+06	8.39E+05	3.57E+04	5.38E+03
125.4	5520	9.98E-04	8.84	5.48E+06	8.52E+05	4.42E+04	6.87E+03
99.57	5430	9.99E-04	9.2	5.38E+06	8.71E+05	5.47E+04	8.86E+03
79.11	5300	9.98E-04	9.35	5.25E+06	8.65E+05	6.73E+04	1.11E+04
62.81	5210	9.99E-04	9.58	5.15E+06	8.68E+05	8.31E+04	1.40E+04
49.91	5100	9.98E-04	9.83	5.04E+06	8.73E+05	1.02E+05	1.77E+04
39.65	4990	9.99E-04	10.08	4.92E+06	8.75E+05	1.26E+05	2.24E+04
31.49	4880	9.99E-04	10.32	4.81E+06	8.76E+05	1.55E+05	2.83E+04
25.02	4770	9.99E-04	10.59	4.69E+06	8.78E+05	1.91E+05	3.57E+04
19.87	4660	9.98E-04	10.83	4.59E+06	8.78E+05	2.35E+05	4.50E+04
15.78	4550	1.00E-03	11.08	4.47E+06	8.75E+05	2.89E+05	5.65E+04

Continued on next page

Table A.1 – continued from previous page

$\omega\left[\frac{\text{rad}}{s}\right]$	Osc. σ $\left[\frac{N}{m^2}\right]$	Strain $\left[\frac{m}{m}\right]$	$\delta\,[^\circ]$	$G'\left[\frac{N}{m^2}\right]$	$G''\left[\frac{N}{m^2}\right]$	$\lvert\eta^*\rvert\,[Pa\,s]$	$\eta'\,[Pa\,s]$
12.54	4440	9.99E-04	11.34	4.36E+06	8.74E+05	3.54E+05	7.11E+04
9.96	4330	9.98E-04	11.57	4.25E+06	8.70E+05	4.36E+05	8.92E+04
7.91	4230	9.98E-04	11.79	4.15E+06	8.65E+05	5.35E+05	1.12E+05
6.28	4119	9.99E-04	12.04	4.03E+06	8.60E+05	6.56E+05	1.40E+05
4.99	4016	9.98E-04	12.22	3.93E+06	8.52E+05	8.06E+05	1.75E+05
3.97	3906	9.99E-04	12.49	3.82E+06	8.45E+05	9.86E+05	2.18E+05
3.15	3793	1.00E-03	12.77	3.70E+06	8.39E+05	1.21E+06	2.73E+05
2.50	3701	9.99E-04	12.76	3.61E+06	8.18E+05	1.48E+06	3.35E+05
1.99	3589	9.99E-04	12.97	3.50E+06	8.07E+05	1.81E+06	4.17E+05
1.58	3485	9.99E-04	13.23	3.39E+06	7.98E+05	2.21E+06	5.20E+05
1.25	3379	9.99E-04	13.41	3.29E+06	7.84E+05	2.70E+06	6.43E+05
1.00	3276	9.99E-04	13.6	3.19E+06	7.71E+05	3.29E+06	7.97E+05
0.79	3184	9.99E-04	13.76	3.10E+06	7.59E+05	4.03E+06	9.87E+05
0.63	3092	9.99E-04	13.94	3.01E+06	7.46E+05	4.93E+06	1.22E+06
0.50	3007	9.98E-04	14.13	2.92E+06	7.35E+05	6.03E+06	1.52E+06
0.40	2921	9.97E-04	14.24	2.84E+06	7.21E+05	7.39E+06	1.87E+06
0.32	2845	9.99E-04	14.42	2.76E+06	7.09E+05	9.04E+06	2.33E+06
0.25	2772	9.98E-04	14.63	2.69E+06	7.01E+05	1.11E+07	2.90E+06
0.20	2704	9.97E-04	14.68	2.62E+06	6.88E+05	1.37E+07	3.58E+06
0.16	2640	9.96E-04	14.85	2.56E+06	6.79E+05	1.68E+07	4.45E+06
0.13	2578	9.95E-04	14.97	2.50E+06	6.69E+05	2.07E+07	5.53E+06
0.10	2526	9.95E-04	15.21	2.45E+06	6.66E+05	2.55E+07	6.93E+06
0.08	2476	9.96E-04	15.41	2.40E+06	6.61E+05	3.14E+07	8.66E+06
0.06	2426	9.93E-04	15.55	2.35E+06	6.55E+05	3.89E+07	1.08E+07

Table A.1: Aberystwyth complex shear modulus and complex viscosity.

A.2 Aberystwyth - Temperature Dependence of Complex Viscosity

$\omega\left[\frac{1}{s}\right]$	$\eta^*\,[Pa\,s]$ (120°C)	$\eta^*\,[Pa\,s]$ (100°C)	$\eta^*\,[Pa\,s]$ (80°C)	$\eta^*\,[Pa\,s]$ (60°C)
628.318	7238	8676	9752	10610
499.010	8567	10200	11360	12520
396.468	10610	12670	14200	15780
314.913	13170	15910	18020	20200
250.133	15530	18240	21070	22880
198.737	19090	22830	25680	28620
157.833	23500	28140	31880	35700
125.412	28760	34560	39400	44210
99.5884	35180	42400	48380	54730
79.1053	43010	51730	59450	67260
62.8130	52630	63350	73210	83070
49.9136	64180	77360	89680	102400
39.6531	78340	94540	110100	126100
31.4850	95560	115300	135200	155300
25.0196	116400	140600	165700	190900
19.8737	141500	171700	203200	235000
15.7833	172700	209400	248700	288600
12.5343	210500	255200	304300	354400
9.9588	257300	311600	373000	435600
7.9105	312600	380300	455600	535300
6.2831	383100	463800	557800	656200
4.9907	467100	565500	683500	806000
3.9653	568800	688700	833600	986100
3.1497	684600	836600	1015000	1205000
2.5013	843500	1023000	1248000	1480000
1.9867	1033000	1245000	1527000	1809000
1.5783	1261000	1513000	1857000	2210000
1.2534	1544000	1847000	2268000	2697000
0.9958	1887000	2247000	2767000	3294000
0.7910	2282000	2731000	3381000	4030000
0.6283	2813000	3300000	4137000	4927000
0.4991	4004000	5050000	6032000	
0.3965	4862000	6194000	7389000	

Continued on next page

Table A.2 – continued from previous page

$\omega\left[\frac{1}{s}\right]$	$\eta^*\,[Pa\,s]\,(120°C)$	$\eta^*\,[Pa\,s]\,(100°C)$	$\eta^*\,[Pa\,s]\,(80°C)$	$\eta^*\,[Pa\,s]\,(60°C)$
0.3149	5970000	7606000	9042000	
0.2501	7288000	9335000	11100000	
0.1986	8905000	11430000	13650000	
0.1578	10840000	14120000	16780000	
0.1253	13220000	17430000	20670000	
0.0995	16010000	21590000	25500000	
0.0791	19640000	26620000	31440000	
0.0628	23650000	33170000	38880000	

Table A.2: Temperature dependence of complex viscosity.

Appendix B

Rheometer Design - Technical Drawings

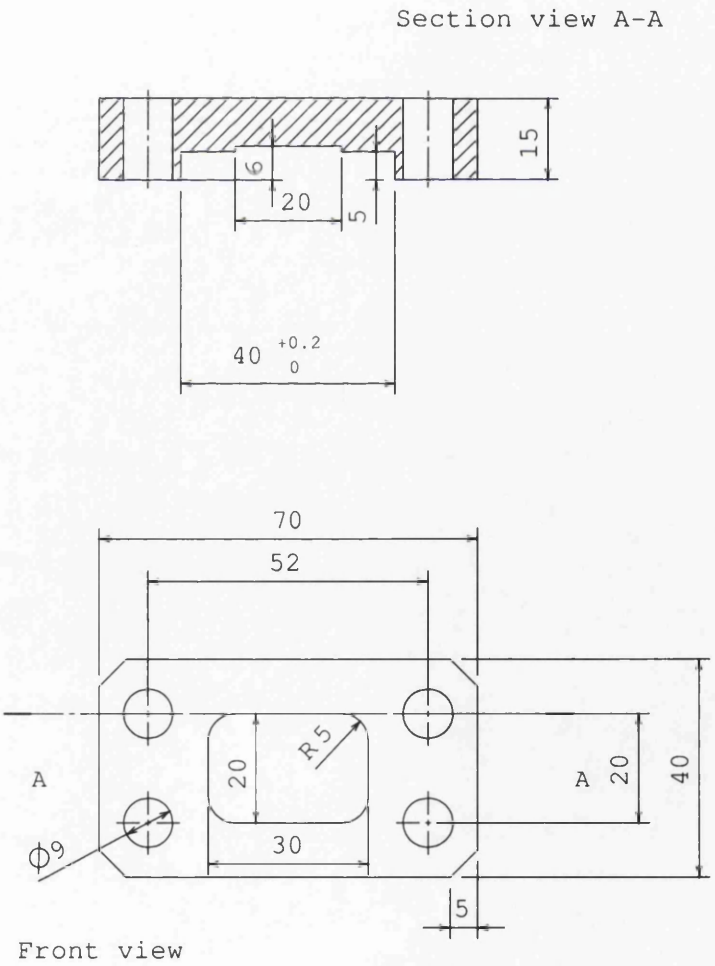

Figure B.1: Clamp for adjustable die bar.

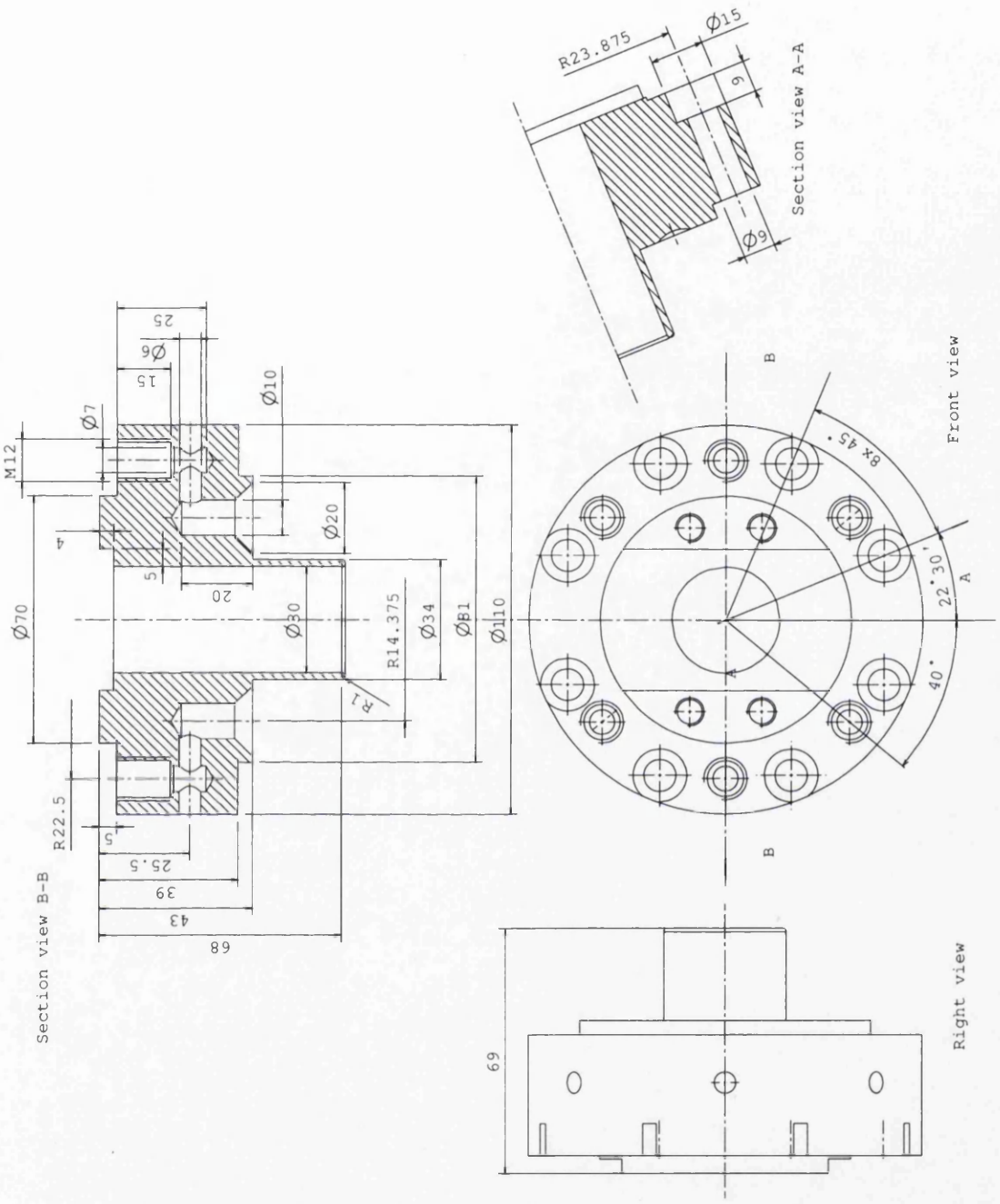

Figure B.2: Main rheometer body.

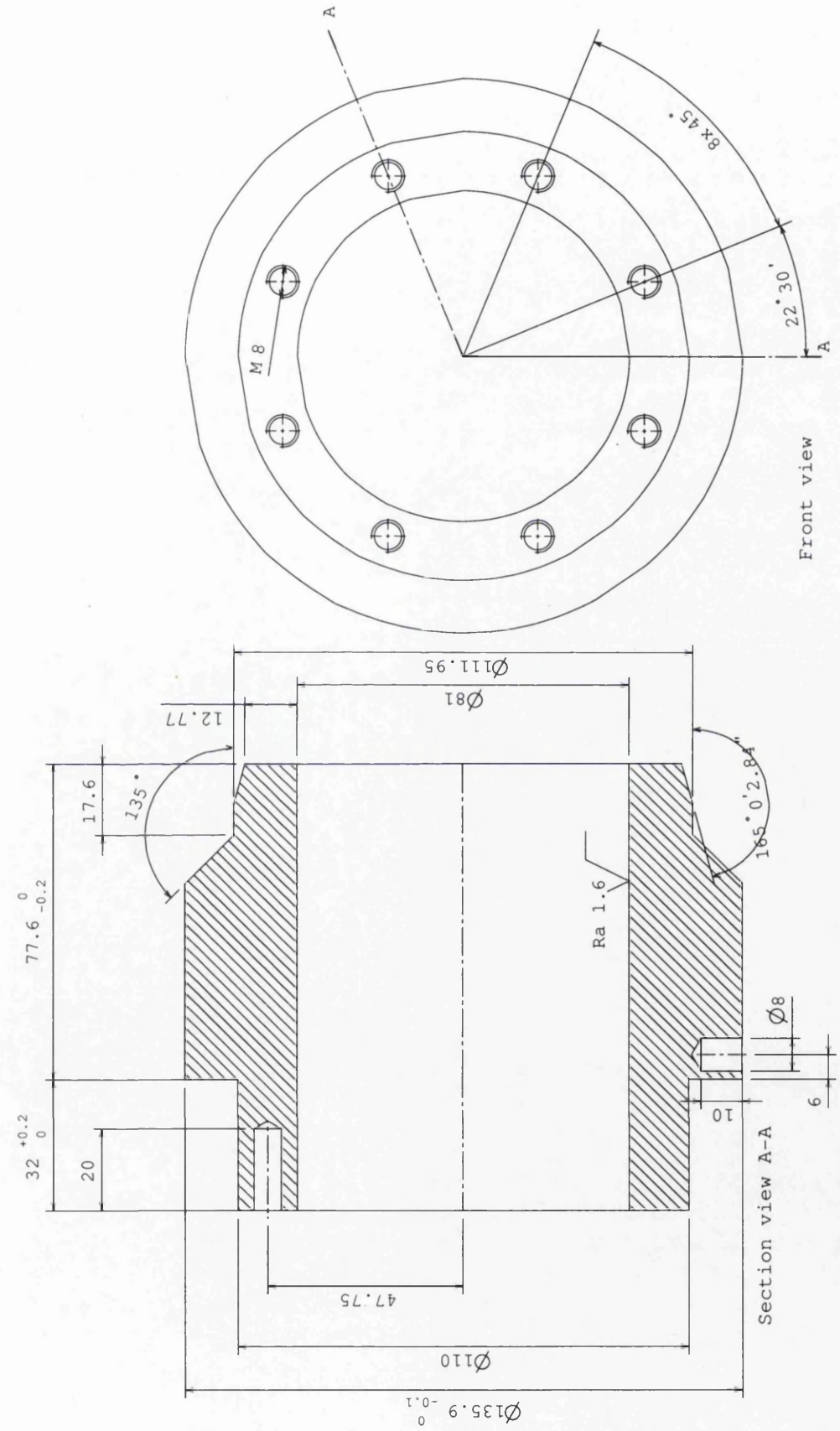

Figure B.3: Rheometer base.

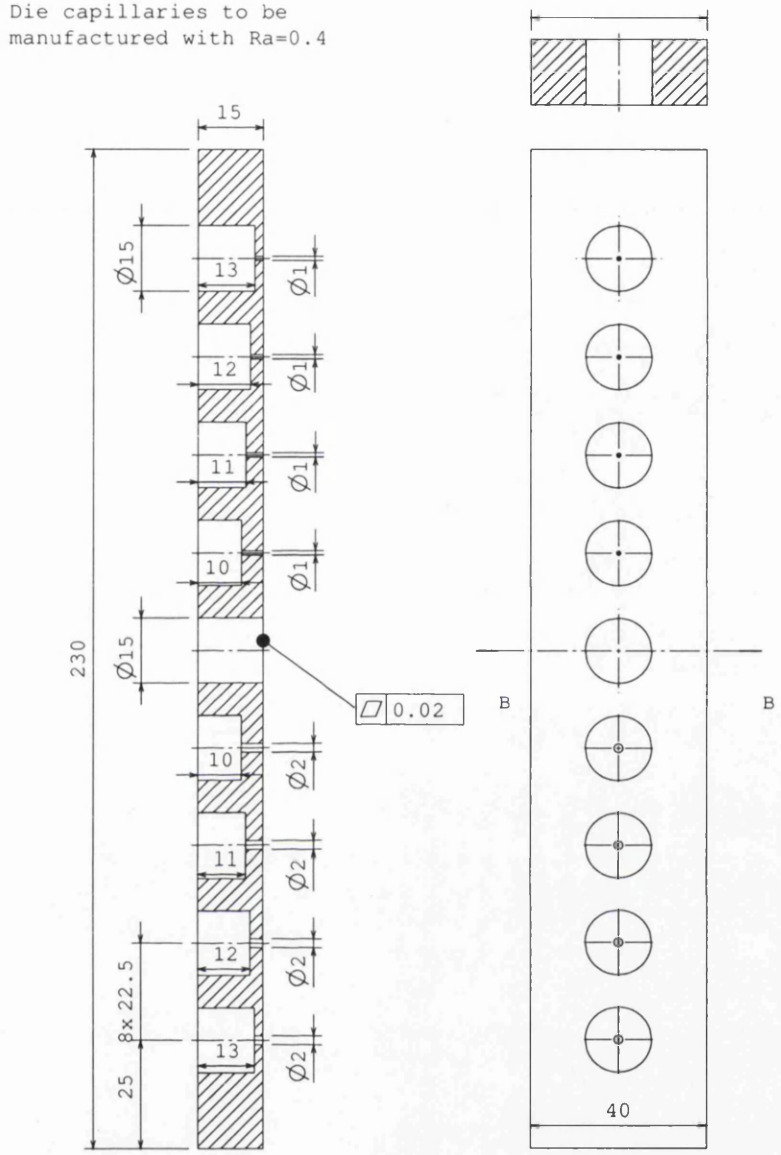

Figure B.4: Adjustable die bar.

Appendix C

Results of Capillary Die Trials

C.1 Rheometry Trial 1

C.1.1 Results of Trial no. 1 - ten rpm

Extr. speed $\left[\frac{1}{min}\right]$	Die dia. $[mm]$	Die length $[mm]$	Output vel. $\left[\frac{m}{s}\right]$	Input vel. $\left[\frac{m}{s}\right]$	Pressure drop $[bar]$
10	2	5	$9.25 \cdot 10^{-3}$	$4.11 \cdot 10^{-5}$	89.84
10	2	5	$7.76 \cdot 10^{-3}$	$3.45 \cdot 10^{-5}$	87.59
10	2	5	$8.37 \cdot 10^{-3}$	$3.72 \cdot 10^{-5}$	86.42
10	2	5	$8.80 \cdot 10^{-3}$	$3.92 \cdot 10^{-5}$	85.50
10	2	5	$9.34 \cdot 10^{-3}$	$4.15 \cdot 10^{-5}$	85.30
10	2	5	$9.68 \cdot 10^{-3}$	$4.30 \cdot 10^{-5}$	85.25
10	2	5	$1.01 \cdot 10^{-2}$	$4.50 \cdot 10^{-5}$	85.02
10	2	5	$0.01 \cdot 10^{-2}$	$4.46 \cdot 10^{-5}$	84.61
10	2	5	$0.01 \cdot 10^{-2}$	$4.49 \cdot 10^{-5}$	84.11
10	2	5	$0.01 \cdot 10^{-2}$	$4.46 \cdot 10^{-5}$	83.80
10	2	4	$2.74 \cdot 10^{-2}$	$1.22 \cdot 10^{-4}$	82.84
10	2	4	$2.29 \cdot 10^{-2}$	$1.02 \cdot 10^{-4}$	82.22
10	2	4	$2.16 \cdot 10^{-2}$	$9.60 \cdot 10^{-5}$	82.16
10	2	4	$2.06 \cdot 10^{-2}$	$9.14 \cdot 10^{-5}$	82.18
10	2	4	$1.98 \cdot 10^{-2}$	$8.82 \cdot 10^{-5}$	81.81
10	2	3	$7.15 \cdot 10^{-2}$	$3.18 \cdot 10^{-4}$	81.96
10	2	3	$7.08 \cdot 10^{-2}$	$3.15 \cdot 10^{-4}$	81.97
10	2	3	$6.75 \cdot 10^{-2}$	$3.00 \cdot 10^{-4}$	80.82

Continued on next page

TableC.1 – continued from previous page

Extr. speed $[\frac{1}{min}]$	Die dia. $[mm]$	Die length $[mm]$	Output vel. $[\frac{m}{s}]$	Input vel. $[\frac{m}{s}]$	Pressure drop $[bar]$
10	2	3	$6.29 \cdot 10^{-2}$	$2.79 \cdot 10^{-4}$	80.02
10	2	3	$5.86 \cdot 10^{-2}$	$2.60 \cdot 10^{-4}$	79.48
10	2	2	$1.26 \cdot 10^{-1}$	$5.61 \cdot 10^{-4}$	81.44
10	2	2	$1.31 \cdot 10^{-1}$	$5.83 \cdot 10^{-4}$	79.82
10	2	2	$1.31 \cdot 10^{-1}$	$5.81 \cdot 10^{-4}$	79.04
10	2	2	$1.30 \cdot 10^{-1}$	$5.77 \cdot 10^{-4}$	78.61
10	2	2	$1.24 \cdot 10^{-1}$	$5.53 \cdot 10^{-4}$	77.92
10	2	2	$1.24 \cdot 10^{-1}$	$5.50 \cdot 10^{-4}$	77.85
10	2	1	$3.98 \cdot 10^{-1}$	$1.77 \cdot 10^{-3}$	78.66
10	2	1	$3.82 \cdot 10^{-1}$	$1.70 \cdot 10^{-3}$	77.90
10	2	1	$3.75 \cdot 10^{-1}$	$1.67 \cdot 10^{-3}$	76.73
10	2	1	$3.70 \cdot 10^{-1}$	$1.65 \cdot 10^{-3}$	75.89
10	2	1	$3.80 \cdot 10^{-1}$	$1.69 \cdot 10^{-3}$	75.38

Table C.1: Results of trial no. 1 - ten rpm.

C.1.2 Results of Trial no. 1 - 15 rpm

Extr. speed $[\frac{1}{min}]$	Die dia. $[mm]$	Die length $[mm]$	Output vel. $[\frac{m}{s}]$	Input vel. $[\frac{m}{s}]$	Pressure drop $[bar]$
15	2	5	$2.41 \cdot 10^{-2}$	$1.07 \cdot 10^{-4}$	91.52
15	2	5	$1.55 \cdot 10^{-2}$	$6.88 \cdot 10^{-5}$	86.06
15	2	5	$1.26 \cdot 10^{-2}$	$5.62 \cdot 10^{-5}$	84.79
15	2	5	$1.22 \cdot 10^{-2}$	$5.44 \cdot 10^{-5}$	84.09
15	2	5	$1.23 \cdot 10^{-2}$	$5.48 \cdot 10^{-5}$	83.30
15	2	4	$3.68 \cdot 10^{-2}$	$1.64 \cdot 10^{-4}$	85.18
15	2	4	$2.51 \cdot 10^{-2}$	$1.12 \cdot 10^{-4}$	82.63
15	2	4	$2.25 \cdot 10^{-2}$	$1.00 \cdot 10^{-4}$	81.56
15	2	4	$2.26 \cdot 10^{-2}$	$1.01 \cdot 10^{-4}$	80.64
15	2	4	$2.26 \cdot 10^{-2}$	$1.01 \cdot 10^{-4}$	80.28
15	2	3	$6.02 \cdot 10^{-2}$	$2.68 \cdot 10^{-4}$	84.30

Continued on next page

TableC.2 – continued from previous page

Extr. speed $[\frac{1}{min}]$	Die dia. $[mm]$	Die length $[mm]$	Output vel. $[\frac{m}{s}]$	Input vel. $[\frac{m}{s}]$	Pressure drop $[bar]$
15	2	3	$5.31 \cdot 10^{-2}$	$2.36 \cdot 10^{-4}$	82.66
15	2	3	$5.28 \cdot 10^{-2}$	$2.35 \cdot 10^{-4}$	81.77
15	2	3	$5.26 \cdot 10^{-2}$	$2.34 \cdot 10^{-4}$	80.73
15	2	3	$5.38 \cdot 10^{-2}$	$2.39 \cdot 10^{-4}$	80.42
15	2	2	$1.70 \cdot 10^{-1}$	$7.56 \cdot 10^{-4}$	91.95
15	2	2	$1.52 \cdot 10^{-1}$	$6.75 \cdot 10^{-4}$	86.38
15	2	2	$1.44 \cdot 10^{-1}$	$6.41 \cdot 10^{-4}$	82.87
15	2	2	$1.25 \cdot 10^{-1}$	$5.56 \cdot 10^{-4}$	81.35
15	2	2	$1.26 \cdot 10^{-1}$	$5.61 \cdot 10^{-4}$	79.35
15	2	1	$4.62 \cdot 10^{-1}$	$2.05 \cdot 10^{-3}$	81.82
15	2	1	$4.36 \cdot 10^{-1}$	$1.94 \cdot 10^{-3}$	78.83
15	2	1	$4.70 \cdot 10^{-1}$	$2.09 \cdot 10^{-3}$	77.00
15	2	1	$4.94 \cdot 10^{-1}$	$2.19 \cdot 10^{-3}$	75.49
15	2	1	$5.07 \cdot 10^{-1}$	$2.25 \cdot 10^{-3}$	74.64

Table C.2: Results of trial no. 1 - 15 rpm.

C.2 Rheometry Trial 2

C.2.1 Results of Trial no. 2 - five rpm

Extr. speed $[\frac{1}{min}]$	Die dia. $[mm]$	Die length $[mm]$	Output vel. $[\frac{m}{s}]$	Pressure drop $[bar]$	Temperature $[°C]$
5	2.0	5.0	$4.80 \cdot 10^{-3}$	72.59	86.24
5	2.0	5.0	$4.88 \cdot 10^{-3}$	70.51	87.53
5	2.0	5.0	$5.33 \cdot 10^{-3}$	69.00	88.38
5	2.0	5.0	$5.73 \cdot 10^{-3}$	67.88	88.68
5	2.0	5.0	$6.30 \cdot 10^{-3}$	66.89	89.11
5	2.0	4.0	$2.08 \cdot 10^{-2}$	60.42	93.75
5	2.0	4.0	$2.14 \cdot 10^{-2}$	61.00	92.45
5	2.0	4.0	$2.16 \cdot 10^{-2}$	61.54	91.47

Continued on next page

TableC.3 – continued from previous page

Extr. speed $[\frac{1}{min}]$	Die dia. $[mm]$	Die length $[mm]$	Output vel. $[\frac{m}{s}]$	Pressure drop $[bar]$	Temperature $[°C]$
5	2.0	4.0	$2.16 \cdot 10^{-2}$	62.11	90.76
5	2.0	4.0	$2.17 \cdot 10^{-2}$	62.37	90.56
5	2.0	3.0	$3.90 \cdot 10^{-2}$	57.95	99.37
5	2.0	3.0	$3.80 \cdot 10^{-2}$	58.26	97.32
5	2.0	3.0	$3.88 \cdot 10^{-2}$	58.70	95.73
5	2.0	3.0	$3.85 \cdot 10^{-2}$	59.67	93.59
5	2.0	3.0	$3.85 \cdot 10^{-2}$	60.24	92.82
5	2.0	3.0	$3.88 \cdot 10^{-2}$	60.60	92.27
5	2.0	3.0	$3.69 \cdot 10^{-2}$	60.84	91.86
5	2.0	3.0	$3.64 \cdot 10^{-2}$	61.11	91.72
5	2.0	3.0	$3.71 \cdot 10^{-2}$	61.37	91.65
5	2.0	0.0	$1.52 \cdot 10^{-1}$	53.16	102.81
5	2.0	0.0	$1.57 \cdot 10^{-1}$	53.78	101.37
5	2.0	0.0	$1.66 \cdot 10^{-1}$	53.82	99.67
5	2.0	0.0	$1.71 \cdot 10^{-1}$	54.27	98.17
5	2.0	0.0	$1.73 \cdot 10^{-1}$	54.75	96.90

Table C.3: Results of trial no. 2 - five rpm.

C.2.2 Results of Trial no. 2 - ten rpm

Extr. speed $[\frac{1}{min}]$	Die dia. $[mm]$	Die length $[mm]$	Output vel. $[\frac{m}{s}]$	Pressure drop $[bar]$	Temperature $[°C]$
10	2.0	5.0	$1.05 \cdot 10^{-2}$	69.75	97.08
10	2.0	5.0	$1.12 \cdot 10^{-2}$	68.44	99.10
10	2.0	5.0	$1.22 \cdot 10^{-2}$	67.55	100.10
10	2.0	5.0	$1.33 \cdot 10^{-2}$	67.06	100.50
10	2.0	5.0	$1.42 \cdot 10^{-2}$	66.72	100.71
10	2.0	4.0	$3.79 \cdot 10^{-2}$	71.55	93.00
10	2.0	4.0	$3.41 \cdot 10^{-2}$	70.28	94.66
10	2.0	4.0	$3.27 \cdot 10^{-2}$	69.66	96.10
10	2.0	4.0	$3.19 \cdot 10^{-2}$	68.95	97.36

Continued on next page

TableC.4 – continued from previous page

Extr. speed $\left[\frac{1}{min}\right]$	Die dia. $[mm]$	Die length $[mm]$	Output vel. $\left[\frac{m}{s}\right]$	Pressure drop $[bar]$	Temperature $[°C]$
10	2.0	4.0	$3.20 \cdot 10^{-2}$	68.64	98.42
10	2.0	3.0	$6.91 \cdot 10^{-2}$	71.25	93.01
10	2.0	3.0	$6.69 \cdot 10^{-2}$	70.63	94.15
10	2.0	3.0	$6.52 \cdot 10^{-2}$	69.49	95.31
10	2.0	3.0	$6.18 \cdot 10^{-2}$	68.93	96.42
10	2.0	3.0	$6.08 \cdot 10^{-2}$	68.23	97.32
10	2.0	3.0	$5.82 \cdot 10^{-2}$	67.84	98.07
10	2.0	3.0	$5.74 \cdot 10^{-2}$	67.45	98.79
10	2.0	0.0	$2.52 \cdot 10^{-1}$	65.76	95.72
10	2.0	0.0	$2.46 \cdot 10^{-1}$	65.29	96.20
10	2.0	0.0	$2.28 \cdot 10^{-1}$	64.64	96.87
10	2.0	0.0	$2.28 \cdot 10^{-1}$	64.13	97.56
10	2.0	0.0	$2.26 \cdot 10^{-1}$	63.86	98.26

Table C.4: Results of trial no. 2 - ten rpm.

C.2.3 Results of Trial no. 2 - 15 rpm

Extr. speed $\left[\frac{1}{min}\right]$	Die dia. $[mm]$	Die length $[mm]$	Output vel. $\left[\frac{m}{s}\right]$	Pressure drop $[bar]$	Temperature $[°C]$
15	2.0	5.0	$1.85 \cdot 10^{-2}$	68.51	105.39
15	2.0	5.0	$1.85 \cdot 10^{-2}$	67.84	106.97
15	2.0	5.0	$1.88 \cdot 10^{-2}$	67.30	107.86
15	2.0	5.0	$1.97 \cdot 10^{-2}$	67.08	108.45
15	2.0	5.0	$2.04 \cdot 10^{-2}$	66.87	108.91
15	2.0	5.0	$2.12 \cdot 10^{-2}$	66.84	108.96
15	2.0	5.0	$2.22 \cdot 10^{-2}$	66.77	109.05
15	2.0	5.0	$2.27 \cdot 10^{-2}$	66.77	109.17
15	2.0	5.0	$2.39 \cdot 10^{-2}$	66.68	109.16
15	2.0	4.0	$4.19 \cdot 10^{-2}$	71.44	102.55
15	2.0	4.0	$4.01 \cdot 10^{-2}$	70.56	104.10
15	2.0	4.0	$3.95 \cdot 10^{-2}$	69.81	105.42

Continued on next page

TableC.5 – continued from previous page

Extr. speed $[\frac{1}{min}]$	Die dia. $[mm]$	Die length $[mm]$	Output vel. $[\frac{m}{s}]$	Pressure drop $[bar]$	Temperature $[^oC]$
15	2.0	4.0	$3.92 \cdot 10^{-2}$	69.36	106.53
15	2.0	4.0	$3.95 \cdot 10^{-2}$	69.18	107.27
15	2.0	4.0	$3.96 \cdot 10^{-2}$	68.92	108.05
15	2.0	4.0	$4.01 \cdot 10^{-2}$	68.37	109.19
15	2.0	4.0	$4.08 \cdot 10^{-2}$	68.27	109.45
15	2.0	3.0	$7.07 \cdot 10^{-2}$	69.50	103.98
15	2.0	3.0	$6.73 \cdot 10^{-2}$	68.58	105.29
15	2.0	3.0	$6.73 \cdot 10^{-2}$	67.93	106.42
15	2.0	3.0	$6.82 \cdot 10^{-2}$	67.55	107.41
15	2.0	3.0	$6.99 \cdot 10^{-2}$	67.26	108.20
15	2.0	3.0	$7.12 \cdot 10^{-2}$	66.90	108.76
15	2.0	3.0	$7.40 \cdot 10^{-2}$	66.75	109.16
15	2.0	0.0	$2.83 \cdot 10^{-1}$	68.44	100.85
15	2.0	0.0	$2.83 \cdot 10^{-1}$	67.33	102.63
15	2.0	0.0	$2.83 \cdot 10^{-1}$	66.31	104.13
15	2.0	0.0	$2.94 \cdot 10^{-1}$	65.54	105.37
15	2.0	0.0	$3.04 \cdot 10^{-1}$	65.03	106.45

Table C.5: Results of trial no. 2 - 15 rpm.

C.2.4 Results of Trial no. 2 - 20 rpm

Extr. speed $[\frac{1}{min}]$	Die dia. $[mm]$	Die length $[mm]$	Output vel. $[\frac{m}{s}]$	Pressure drop $[bar]$	Temperature $[^oC]$
20	2.0	5.0	$2.82 \cdot 10^{-2}$	68.29	112.45
20	2.0	5.0	$2.76 \cdot 10^{-2}$	67.87	114.03
20	2.0	5.0	$2.83 \cdot 10^{-2}$	67.44	115.51
20	2.0	5.0	$2.89 \cdot 10^{-2}$	67.55	115.79
20	2.0	5.0	$2.92 \cdot 10^{-2}$	67.62	115.98
20	2.0	4.0	$4.79 \cdot 10^{-2}$	68.98	114.24
20	2.0	4.0	$4.78 \cdot 10^{-2}$	68.67	115.08
20	2.0	4.0	$4.78 \cdot 10^{-2}$	68.27	115.81

Continued on next page

TableC.6 – continued from previous page

Extr. speed $\left[\frac{1}{min}\right]$	Die dia. $[mm]$	Die length $[mm]$	Output vel. $\left[\frac{m}{s}\right]$	Pressure drop $[bar]$	Temperature $[^oC]$
20	2.0	4.0	$4.75 \cdot 10^{-2}$	68.12	116.33
20	2.0	4.0	$4.85 \cdot 10^{-2}$	67.98	116.64
20	2.0	3.0	$9.34 \cdot 10^{-2}$	67.45	113.31
20	2.0	3.0	$9.34 \cdot 10^{-2}$	67.06	114.26
20	2.0	3.0	$9.59 \cdot 10^{-2}$	66.88	115.05
20	2.0	3.0	$9.76 \cdot 10^{-2}$	66.57	115.58
20	2.0	3.0	$1.01 \cdot 10^{-1}$	66.37	116.00
20	2.0	3.0	$1.02 \cdot 10^{-1}$	66.26	116.40
20	2.0	3.0	$1.05 \cdot 10^{-1}$	66.07	116.67
20	2.0	0.0	$3.78 \cdot 10^{-1}$	66.44	110.47
20	2.0	0.0	$3.90 \cdot 10^{-1}$	65.51	112.16
20	2.0	0.0	$4.42 \cdot 10^{-1}$	64.32	114.51
20	2.0	0.0	$4.74 \cdot 10^{-1}$	63.92	115.15
20	2.0	0.0	$4.78 \cdot 10^{-1}$	63.67	115.75

Table C.6: Results of trial no. 2 - 20 rpm.

Appendix D

Results of Profile Die Trials

D.1 Profile Trial 1

D.1.1 Results of Trial no. 1 - Processing Conditions

ID	Time $[s]$	RPM $[\frac{1}{min}]$	Die ID	$\dot{V}$ $[\frac{m^3}{s}]$	T [°C]
1	1705	10	1	$1.35 \cdot 10^{-5}$	109.37
2	1765	10	1	$1.32 \cdot 10^{-5}$	109.46
3	2220	15	1	$1.98 \cdot 10^{-5}$	121.61
4	2280	15	1	$1.98 \cdot 10^{-5}$	122.16
5	2340	15	1	$2.00 \cdot 10^{-5}$	122.40
6	2820	20	1	$2.58 \cdot 10^{-5}$	131.31
7	2880	20	1	$2.62 \cdot 10^{-5}$	131.37
8	2910	20	1	$2.62 \cdot 10^{-5}$	131.32

Table D.1: Results of trial no. 1 - Processing conditions.

D.1.2 Results of Trial no. 1 - Partitioning

ID	Part. 1 %	Part. 2 %	Part. 3 %	Part. 4 %	Part. 5 %	Total %
1	15.29	26.50	50.13	5.13	2.94	99.99
2	15.30	26.89	49.63	5.20	2.98	100.00

Continued on next page

TableD.2 – continued from previous page

ID	Part. 1 %	Part. 2 %	Part. 3 %	Part. 4 %	Part. 5 %	Total %
3	15.27	26.83	49.89	5.11	2.90	100.00
4	14.27	28.00	49.84	4.95	2.94	100.00
5	14.31	27.48	50.31	4.98	2.93	100.01
6	14.54	27.04	50.44	5.02	2.97	100.01
7	14.34	27.92	49.71	5.06	2.97	100.00
8	14.43	27.71	50.00	4.97	2.88	99.99

Table D.2: Results of trial no. 1 - Percentage of total area in partitions (see Figure 5.15 a)).

D.2 Profile Trial 2

D.2.1 Results of Trial no. 2 - Processing Conditions

ID	Time $[s]$	RPM $\left[\frac{1}{min}\right]$	Die ID	$\dot{V}$ $\left[\frac{m^3}{s}\right]$	T [°C]
1	2882	10	1	$1.5515 \cdot 10^{-5}$	98.72
2	2976	10	1	$1.4734 \cdot 10^{-5}$	99.11
3	3059	10	1	$1.4756 \cdot 10^{-5}$	99.53
4	3556	15	1	$2.2257 \cdot 10^{-5}$	109.92
5	3578	15	1	$2.1221 \cdot 10^{-5}$	110.10
6	3599	15	1	$2.1956 \cdot 10^{-5}$	110.30
7	4248	20	1	$2.9154 \cdot 10^{-5}$	119.06
8	4268	20	1	$2.7387 \cdot 10^{-5}$	118.00
9	4288	20	1	$2.8122 \cdot 10^{-5}$	119.01
10	4701	25	1	$3.5089 \cdot 10^{-5}$	124.40
11	4721	25	1	$3.3278 \cdot 10^{-5}$	124.37
12	4741	25	1	$3.4208 \cdot 10^{-5}$	124.49
13	5400	30	1	$4.1300 \cdot 10^{-5}$	129.85
14	5424	30	1	$3.9964 \cdot 10^{-5}$	129.75
15	5444	30	1	$4.0591 \cdot 10^{-5}$	129.75
16	6939	10	2	$1.6082 \cdot 10^{-5}$	102.02
17	6974	10	2	$1.4253 \cdot 10^{-5}$	102.05

Continued on next page

TableD.3 – continued from previous page

ID	Time $[s]$	RPM $[\frac{1}{min}]$	Die ID	$\dot{V}$ $[\frac{m^3}{s}]$	T [°C]
18	7003	10	2	$1.4547 \cdot 10^{-5}$	102.06
19	7790	15	2	$2.1279 \cdot 10^{-5}$	112.29
20	7807	15	2	$2.1394 \cdot 10^{-5}$	112.37
21	7828	15	2	$2.1584 \cdot 10^{-5}$	112.47
22	8323	20	2	$2.7778 \cdot 10^{-5}$	120.07
23	8343	20	2	$2.7158 \cdot 10^{-5}$	120.15
24	8363	20	2	$2.8283 \cdot 10^{-5}$	120.27
25	8765	25	2	$3.5928 \cdot 10^{-5}$	126.14
26	8785	25	2	$3.3631 \cdot 10^{-5}$	126.26
27	8805	25	2	$3.4008 \cdot 10^{-5}$	126.27
28	9247	30	2	$4.4465 \cdot 10^{-5}$	130.70
29	9267	30	2	$4.1345 \cdot 10^{-5}$	130.82
30	9287	30	2	$4.0878 \cdot 10^{-5}$	131.06

Table D.3: Results of trial no. 2 - Processing conditions.

D.2.2 Results of Trial no. 2 - Partitioning

ID	Part. 1 %	Part. 2 %	Part. 3 %	Part. 4 %	Part. 5 %	Total %
1	14.79	27.11	50.68	4.75	2.69	100.02
2	14.99	26.46	51.05	4.80	2.70	100.01
3	15.08	26.51	51.01	4.75	2.67	100.02
4	14.64	26.49	51.58	4.66	2.65	100.02
5	14.89	25.56	52.25	4.63	2.68	100.01
6	15.12	25.57	52.08	4.58	2.68	100.03
7	14.06	26.89	51.76	4.58	2.72	100.01
8	14.27	27.40	51.12	4.58	2.65	100.02
9	13.94	27.79	51.05	4.58	2.64	100.00
10	14.22	25.62	53.40	4.17	2.62	100.04
11	13.83	26.72	52.49	4.32	2.64	100.00
12	14.16	24.92	54.04	4.27	2.64	100.04
13	14.07	25.62	53.60	4.16	2.57	100.02
14	14.11	25.10	54.14	4.08	2.57	100.01

Continued on next page

TableD.4 – continued from previous page

ID	Part. 1 %	Part. 2 %	Part. 3 %	Part. 4 %	Part. 5 %	Total %
15	14.01	25.30	54.17	3.98	2.56	100.02
16	21.04	25.68	44.05	6.31	2.94	100.02
17	21.98	25.52	43.56	6.10	2.85	100.01
18	20.94	26.04	44.07	6.09	2.88	100.02
19	20.63	26.40	44.25	5.92	2.82	100.01
20	19.97	27.20	44.11	5.89	2.84	100.02
21	20.80	26.21	44.28	5.86	2.86	100.00
22	20.61	26.49	44.07	5.93	2.90	100.01
23	20.95	26.01	44.24	5.91	2.89	100.00
24	20.63	25.93	44.67	5.89	2.88	100.00
25	20.80	26.28	44.18	5.91	2.83	100.00
26	20.86	26.07	44.38	5.86	2.83	100.00
27	20.96	26.13	44.22	5.87	2.83	100.01
28	20.62	26.44	44.48	5.74	2.73	100.01
29	20.91	25.97	44.68	5.74	2.70	100.00
30	20.70	26.33	44.54	5.71	2.72	100.01

Table D.4: Results of trial no. 2 - Percentage of total area in partitions (see Figure 5.15 a)).

Appendix E

Program Code Response Surface Calculation

E.1 Program Code Response Surface Calculation - two free Parameters

```
#!/usr/bin/python

import os
import math
import sys
import string
from file import File
from Numeric import *
import Gnuplot, Gnuplot.funcutils

input   = sys.argv[1:]
r       = []
l       = []
vexp    = []
pexp    = []
texp    = []

k0      = 1e39
m       = 1.0
b       = 0.0065
tref    = 100
```

```
nmin    = 0.1
nmax    = 1.0
ninc    = (nmax-nmin)/500
mumin   = 10000
mumax   = 1000000
muinc   = (mumax-mumin)/500

for case in input:
   infile     = open(case)
   line       = infile.readline()
   words      = string.split(line)
   vexp.append(float(words[0]))
   pexp.append(float(words[1]))
   texp.append(float(words[2]))
   r.append(float(words[3]))
   l.append(float(words[4]))
   infile.close()
vexp = array(vexp)
pexp = array(pexp)
texp = array(texp)
r    = array(r)
l    = array(l)

outfile = open("response_ana.data","w")
for n in arange(nmin, nmax, ninc):
   for mu in range(mumin, mumax, muinc):
      obj = 0
      vana = pi*(((pexp*r)/(2*l*k0))**(1/m))*r**2+2*pi*(n/(n+1))\
             *((pexp/(2*l*mu*e**(b*(tref-texp))))**(1/n))*((0.5-\
             (n/(3*n+1)))*r**((3*n+1)/n))
      obj  = sum((vexp-vana)**2)
      scribble = "%10.9f   %14.9f   %14.9e \n" % (n, mu, obj)
      outfile.write(scribble)
   outfile.write("\n")
outfile.close()
os.system('./getminobj.py response_ana.data')
os.system('gnuplot response_surf2.gnu')
os.system('gv response_surf.eps')
```

Appendix F

Program Code Parameter Optimisation

F.1 Simultaneous Parameter Optimisation

F.1.1 Program Code Simultaneous Parameter Optimisation

```
#!/usr/bin/python

"""Optimisation both zero and cap in one routine using lsq
   and concatenating the two resulting vectors.
"""

import sys
from matpam import Matpam
from scipy.optimize import leastsq

iniparams = [100000.0,0.5,0.01,100000.0,0.5,0.01,100000.0,0.5,0.01]
param = Matpam(sys.argv[1],iniparams)

tol = 1e-18
plsq = leastsq(param.rescalc,param.outparams,\
       ftol=tol,epsfcn=1e-36,xtol=tol,gtol=tol,\
       maxfev=100000,full_output=1)
print "NUMBER OF ITERATIONS: ",plsq[1]['nfev']
if plsq[2]!=1:
```

```
   print "ERRORS: ",plsq[2], plsq[3]
param.outparams = plsq[0]
print param.outparams
#param.movplot("test1.eps")
param.print_results()
param.save_log()
```

F.1.2 Class Code Simultaneous Parameter Optimization

```
"""
   Class that defines the matpam object consisting of

   - execname
   - code_exec
   - code_class
   - infiles
   - iniparams
   - zparams
   - cparams
   - outparams
   - stats
   - plot

"""

class Matpam:

   def __init__(self,basedir,iniparams):

      import os
      import sys
      import string
      from Numeric import array
      import copy

      self.inz,self.inc                = [],[]

      self.execname    = str(os.getcwd())+str(sys.argv[0])[1:]
      infile           = open(self.execname,"r")
      self.code_exec   = infile.readlines()
      infile.close()
```

```
infile          = open(__file__,"r")
self.code_class = infile.readlines()
infile.close()

zerodir   = basedir+"/200603_zero"
capdir    = basedir+"/200603_cap"

inzero   = os.listdir(zerodir)
incap    = os.listdir(capdir)
for i in range(len(inzero)):
   if inzero[i][-3:]=="exp":
      self.inz.append(zerodir+"/"+inzero[i])
for i in range(11,len(incap)):
   if incap[i][-3:]=="exp":
      self.inc.append(capdir+"/"+incap[i])
self.infiles   = [self.inz, self.inc]
self.iniparams = iniparams
self.outparams = copy.deepcopy(self.iniparams)
self.stats     = [[],[]]

rz,lz,vexpz,pexpz,texpz = [],[],[],[],[]
rc,lc,vexpc,pexpc,texpc = [],[],[],[],[]

vanaz,vanac             = [],[]

for case in self.infiles[0]:
   infile     = open(case)
   line       = infile.readline()
   words      = string.split(line)
   vexpz.append(float(words[0]))
   pexpz.append(float(words[1]))
   texpz.append(float(words[2]))
   rz.append(float(words[3]))
   lz.append(float(words[4]))
   infile.close()
vexpz = array(vexpz)
pexpz = array(pexpz)
texpz = array(texpz)
rz    = array(rz)
lz    = array(lz)

for case in self.infiles[1]:
```

```
            infile     = open(case)
            line       = infile.readline()
            words      = string.split(line)
            vexpc.append(float(words[0]))
            pexpc.append(float(words[1]))
            texpc.append(float(words[2]))
            rc.append(float(words[3]))
            lc.append(float(words[4]))
            infile.close()
         vexpc = array(vexpc)
         pexpc = array(pexpc)
         texpc = array(texpc)
         rc    = array(rc)
         lc    = array(lc)

         tref    = 100

         self.zparams = [rz,lz,vexpz,pexpz,texpz,tref]
         self.cparams = [rc,lc,vexpc,pexpc,texpc,tref]

#-------------------------------------------------------------
      def rescalc(self,inparams):

         from Numeric import sort
         from Numeric import array

         try:
            self.outparams        = inparams

            errcomb = []

            vanazero = self.reszero(inparams)
            if len(inparams) == 9:
               print "IN CLASSIC"
               vanacap  = self.rescap_classic(inparams)
            elif len(inparams) == 10:
               print "IN TAU0"
               vanacap  = self.rescap_tau0(inparams)
            errzero  = sort(self.zparams[2]-vanazero)
            errcap   = sort(self.cparams[2]-vanacap)
            for i in range(len(errzero)):
               errcomb.append(abs(errzero[i]))
```

```
            for i in range(len(errcap)):
               errcomb.append(abs(errcap[i]))
            errcomb = array(errcomb)

         except KeyboardInterrupt:
            self.print_results()
            sys.exit(0)

         return errcomb

#-------------------------------------------------------------
   def reszero(self,inparams):

      from scipy.special import gamma
      from Numeric import exp
      from Numeric import pi

      rz                   = self.zparams[0]
      lz                   = self.zparams[1]
      vexpz                = self.zparams[2]
      pexpz                = self.zparams[3]
      texpz                = self.zparams[4]
      tref                 = self.zparams[5]
      ratioz               = rz/15.

      if len(inparams) == 9:
         mu,n,b,mue,p,d,k0,m,c      = inparams
      elif len(inparams) == 10:
         mu,n,b,mue,p,d,k0,tau0,m,c = inparams
      mu,n,mue,p           = abs(mu),abs(n),abs(mue),abs(p)

      Imn  = (p*n*(p+1)*(n+1)*gamma(p)*gamma(2*n/(n+1)))/\
             ((p*(n+1)+2*n)*((p+1)*(n+1)+2*n)*gamma(p+\
             (2*n/(n+1))))

      vana = (pexpz*3*p/((16*n*mu*exp(b*(tref-texpz)))*((p+\
             1)/(n+1))**2*(mue*exp(d*(tref-texpz))*Imn*(3*n+\
             1)/(mu*exp(b*(tref-texpz))*(4*p)**p*4*n))**\
             (1/(p+1))*(1-ratioz**(3*p*(n+1)/(p+1)))))**((p+\
             1)/(p*(n+1)))*(n*pi*rz**3)/(3*n+1)
      return vana
```

```
#-------------------------------------------------------------
   def rescap_classic(self,inparams):

      from scipy.special import gamma
      from Numeric import exp
      from Numeric import pi

      rc                    = self.cparams[0]
      lc                    = self.cparams[1]
      vexpc                 = self.cparams[2]
      pexpc                 = self.cparams[3]
      texpc                 = self.cparams[4]
      tref                  = self.cparams[5]
      ratioc                = rc/15.

      mu,n,b,mue,p,d,k0,m,c = inparams
      mu,n,mue,p,k0,m       = abs(mu),abs(n),abs(mue),\
                              abs(p),abs(k0),abs(m)

      Imn  = (p*n*(p+1)*(n+1)*gamma(p)*gamma(2*n/(n+1)))/((p*\
             (n+1)+2*n)*((p+1)*(n+1)+2*n)*gamma(p+(2*n/(n+1))))

      gdot = (3*n+1)*vexpc/(n*pi*rc**3)

      pent = 16*n*mu*exp(b*(tref-texpc))/(3*p)*((p+1)/(n+1))**\
             2*(mue*exp(d*(tref-texpc))*Imn*(3*n+1)/(mu*exp(b*\
             (tref-texpc))*(4*p)**p*4*n))**(1/(p+1))*gdot**\
             (p*(n+1)/(p+1))*(1-ratioc**(3*p*(n+1)/(p+1)))

      vana = pi*((((pexpc-pent)*rc)/(2*lc*k0*exp(c*(tref-\
             texpc))))**(1/m))*rc**2+2*pi*(n/(n+1))*(((pexpc-\
             pent)/(2*lc*mu*exp(b*(tref-texpc))))**(1/n))*\
             ((0.5-(n/(3*n+1)))*rc**((3*n+1)/n))

      print "#CAPILLARY---------#---------#---------#---------"
      print "mu,n,b =", mu,",",n,",",b
      print "mue,p,d =", mue,",",p,",",d
      print "k0,m,c =", k0,",",m,",",c

      return vana

#-------------------------------------------------------------
```

```
   def rescap_tau0(self,inparams):

      from scipy.special import gamma
      from Numeric import exp
      from Numeric import pi

      rc                    = self.cparams[0]
      lc                    = self.cparams[1]
      vexpc                 = self.cparams[2]
      pexpc                 = self.cparams[3]
      texpc                 = self.cparams[4]
      tref                  = self.cparams[5]
      ratioc                = rc/15.

      mu,n,b,mue,p,d,k0,tau0,m,c = inparams
      mu,n,mue,p,k0,tau0,m       = abs(mu),abs(n),abs(mue),abs(p),\
                                   abs(k0),abs(tau0),abs(m)

      Imn  = (p*n*(p+1)*(n+1)*gamma(p)*gamma(2*n/(n+1)))/((p*\
             (n+1)+2*n)*((p+1)*(n+1)+2*n)*gamma(p+(2*n/(n+1))))

      gdot = (3*n+1)*vexpc/(n*pi*rc**3)

      pent = 16*n*mu*exp(b*(tref-texpc))/(3*p)*((p+1)/(n+1))**2*\
             (mue*exp(d*(tref-texpc))*Imn*(3*n+1)/(mu*exp(b*\
             (tref-texpc))*(4*p)**p*4*\n))**(1/(p+1))*gdot**(p*\
             (n+1)/(p+1))*(1-ratioc**(3*p*(n+1)/(p+1)))

      vana = pi*((((pexpc-pent)*rc)/(2*lc*k0*exp(c*(tref-\
             texpc)))-tau0/k0)**(1/m))*rc**2+2*pi*(n/(n+1))*\
             (((pexpc-pent)/(2*lc*mu*exp(b*(tref-texpc))))**\
             (1/n))*((0.5-(n/(3*n+1)))*rc**((3*n+1)/n))
      print "#CAPILLARY---------#---------#---------#---------"
      print "mu,n,b      =", mu,",",n,",",b
      print "mue,p,d     =", mue,",",p,",",d
      print "k0,tau0,m,c =", k0,",",tau0,",",m,",",c

      return vana

#-------------------------------------------------------------
   def movplot(self,filename):
```

```
      import scipy.xplt

      vanaz = self.reszero(self.outparams)
      if len(self.outparams) == 9:
         vanac = self.rescap_classic(self.outparams)
      if len(self.outparams) == 10:
         vanac = self.rescap_tau0(self.outparams)

      scipy.xplt.plot(self.zparams[2],vanaz,'x',\
                      self.cparams[2],vanac,'o',\
                      [float("0"),float("1.6e-6")],\
                      [float("0"),float("1.6e-6")])
      scipy.xplt.xlabel("vexp")
      scipy.xplt.ylabel("vana")
      scipy.xplt.title('Vexp vs. Vana')
      scipy.xplt.gridxy(1)
      scipy.xplt.legend(['Data Points Zero Length',\
                         'Data Points Capillary',\
                         'Exact Solution'])
      scipy.xplt.gist.eps(filename)   # Make epsi file.

#-------------------------------------------------------------
   def print_results(self):

      from Numeric import array
      from Numeric import concatenate
      from statistics import mean
      from statistics import stddev
      import copy

      sepzeroarr = []
      sepcaparr  = []
      sepcombarr = []

      vanaz = array(self.reszero(self.outparams))
      if len(self.outparams) == 9:
         vanac = array(self.rescap_classic(self.outparams))
      elif len(self.outparams) == 10:
         vanac = array(self.rescap_tau0(self.outparams))

      sepzeroarr = (vanaz-self.zparams[2])/self.zparams[2]
      sepcaparr  = (vanac-self.cparams[2])/self.cparams[2]
```

```
      sepcombarr = concatenate((sepzeroarr,sepcaparr))

      print "TOT STATS-------------------------------------"
      print "MEAN, STDDEV TOT: ",mean(sepcombarr+1),\
                                stddev(sepcombarr)

#-------------------------------------------------------------
   def save_log(self):

      from os import getcwd
      from sys import argv
      from Numeric import concatenate
      from statistics import mean
      from statistics import stddev

      sepcaparr  = []
      sepzeroarr = []
      sepcombarr = []

      vanaz = self.reszero(self.outparams)
      if len(self.outparams) == 9:
         vanac = self.rescap_classic(self.outparams)
      if len(self.outparams) == 10:
         vanac = self.rescap_tau0(self.outparams)

      outfile    = open("full_log.txt","a")
      for i in range(80):
         outfile.write("#")
      outfile.write("\n")
      outfile.write(str(getcwd())+str(argv[0])[1:]+"\n\n")
      infiles_comb = self.infiles[0]+self.infiles[1]
      for i in range(len(infiles_comb)):
         outfile.write(str(infiles_comb[i])+"\n")
      outfile.write("\n")

      infile     = open(argv[0],"r")
      lines      = infile.readlines()
      infile.close()
      for line in lines:
         outfile.write(line)

      scribble = "\n#MATERIAL PARAMETERS ------------------------------\n"
```

```
scribble = scribble+"mu, n, b  = "+str(self.outparams[0])+", "+\
                                   str(self.outparams[1])+", "+\
                                   str(self.outparams[2])+"\n"
scribble = scribble+"mue, p, d = "+str(self.outparams[3])+", "+\
                                   str(self.outparams[4])+", "+\
                                   str(self.outparams[5])+"\n"
scribble = scribble+"k0, m, c  = "+str(self.outparams[6])+", "+\
                                   str(self.outparams[7])+", "+\
                                   str(self.outparams[8])+"\n\n"
outfile.write(scribble)

sepzeroarr = (vanaz-self.zparams[2])/self.zparams[2]
sepcaparr  = (vanac-self.cparams[2])/self.cparams[2]
sepcombarr = concatenate((sepzeroarr,sepcaparr))

scribble = "#TOT STATS ----------------------------------------------"
scribble = scribble+"\nMEAN TOT  : "+str(mean(sepcombarr+1))
scribble = scribble+"\nSTDDEV TOT: "+str(stddev(sepcombarr))
scribble = scribble+"\nMAXERR    : "+str(max(abs(sepcombarr)))+"\n\n"
outfile.write(scribble)
outfile.close()
```

Appendix G

Sample Input Master File for Fantazt

```
FANTOM TEST
$-----------------------------------------------------------------------
RUN_DATA
  RUN_TYPE:  NEW
  CPU_LIMIT: 1.0e6
  LENGTH: 8
END_RUN_DATA
$-----------------------------------------------------------------------
PHYSICAL_PROBLEM
$***********************************************************************
  NAVIER_STOKES_EQUATIONS: ON
    TEMPORAL_DERIVATIVES:  OFF
    CONVECTIVE_TERM:       OFF
    VISCOUS_TERM:          DIVERGENCE_FORM
    CORIOLIS_TERMS:        OFF
    BODY_FORCES:           OFF
    LAW_DENSITY:           CONSTANT
    LAW_VISCOSITY:         POWER_LAW
    TURBULENCE_MODEL:      LAMINAR
  END_NAVIER_STOKES_EQUATIONS
  HEAT_EQUATION: OFF
  END_HEAT_EQUATION
  PROPERTIES
    DENSITY:    1230
    VISCOSITY:    500206.0, 0.0266, 0.0, 0.0, 0.0, 0.0, 0.001
  END_PROPERTIES
```

```
END_PHYSICAL_PROBLEM
$-------------------------------------------------------------------
MESH_DATA
$*******************************************************************
   DIMENSIONS
     NODAL_POINTS:   179733
     ELEMENTS:      864553
     NODES_PER_ELEMENT:  4, SIMPLEX
     SPACE_DIMENSION:    THREE
     BOUNDARY:       137434
   END_DIMENSIONS
   GEOMETRY
    INCLUDE ../d1n7a.geo
   END_GEOMETRY
END_MESH_DATA
$-------------------------------------------------------------------
FIXITY_CONDITIONS
$*******************************************************************
   PRESCRIPTIONS
     FIX_ONE_PRESSURE: ON
     INITIAL, CONSTANT
     INCLUDE ../d1n7a.ini
     END_INITIAL
   END_PRESCRIPTIONS
END_FIXITY_CONDITIONS
$-------------------------------------------------------------------
NUMERICAL_TREATMENT
$*******************************************************************
  GENERAL
    INTERPOLATION:              STANDARD
    INTEGRATION_RULE:           OPEN, QUADRATURE_POINTS: 4
     SMOOTHING_REQUIRED:         QUADRATURE
    TIME_DATA: INITIAL_TIME:    0.0, FINAL_TIME: 1.5,/
                                     TIME_STEP_SIZE: 0.005
    ORDER_OF_BLOCK_ITERATIONS: MOMENTUM
    GOVERNING_PROBLEM:          MOMENTUM
    OTHER_PARAMETERS:           NATURAL_LENGTH: 0.7
    FREEP: 0.0,2.0,1.0E-09,0.0,1.0,57.0,228.0,0.0,/
       2.0,1.0E-05,200,50,0,2.0,1.0,/
       1226686.6, 0.2082
    SENDV
  END_GENERAL
```

```
$-------------------------------------------------------------------
  NAVIER_STOKES_EQUATIONS
    SPATIAL
      PRESSURE_INTERPOLATION:  NUM_NODES: 4, STANDARD, CONTINUOUS
       PENALTY_STRATEGY:       ITERATIVE, PARAMETER: 1.0E-6
       STABILITY_FUNCTIONS:     MAX_PRESS: 1.0
       PERTURB_FUNCT:           ALL
    END_SPATIAL
    TEMPORAL_TREATMENT
      WEIGHTING_OF_DERIVATIVE: ALL
      INCREMENTAL_QUOTIENT:   ONE_STEP
      ORDER_OF_APPROXIMATION:  1
      CONVECTION_TREATMENT:    IMPLICIT
      EULER_TIME_STEPS:        1
      STEADY_STATE_TOLERANCE:  1.0e-5
    END_TEMPORAL_TREATMENT
    SOLUTION
    LINEARIZ_TECHNIQUE:      PICARD
     CONVERGENCE_STRATEGY:    L1, MAX_ITER: 500, TOLERANCE: 0.001 %
     ALGEBRAIC_SOLVER:        SK_GMRES, MAX_ITER=3000,TOLER=1E-10,/
                              KRYLOV=100
     PRECONDITIONING_STRATEGY: DIAGONAL
    END_SOLUTION
  END_NAVIER_STOKES_EQUATIONS
END_NUMERICAL_TREATMENT
$-------------------------------------------------------------------
OUTPUT_&_POST-PROCESS
  POSTPROCESS VELOCITY,        STEPS: 1
  POSTPROCESS PRESSURE,        STEPS: 1
  POSTPROCESS DENSITY,         STEPS: 1
  POSTPROCESS VISCOSITY,       STEPS: 1
END_OUTPUT_&_POST-PROCESS
```

Index